Time Resolved Optical Tomography for the Detection and Specification of Breast Disease.

Tara D. Yates

Department of Medical Physics and Bioengineering
University College London

Supervisors:
Professor Jeremy C. Hebden
Dr Adam P. Gibson

Thesis submitted for the degree of Doctor of Philosophy (Ph.D.) at the University of London.

January 2005

ProQuest LLC
789 East Eisenhower Parkway
P.O. Box 1346
Ann Arbor, MI 48106-1346

Abstract

This thesis describes the evaluation of time-resolved optical tomography for detecting and specifying breast disease. Optical tomography involves transilluminating the breast using near infrared (NIR) light. Characteristic absorption by oxy- and deoxy- haemoglobin at NIR wavelengths can be exploited to yield oxygen saturation and blood volume information. This information may provide a distinction between the high vascularisation often associated with malignant lesions and benign or normal breast tissue.

A 32 channel time-correlated single photon counting system is utilised to perform a series of investigations on both healthy volunteers and patients with pre-diagnosed lesions. Specific datatypes, extracted from a histogram of the times of flight of photons across the breast, are used to reconstruct images of the optical properties (absorption μ_a and reduced scattering coefficient μ_s'). The reconstruction is performed using a non-linear, finite element based algorithm.

Two patient interfaces are assessed. The first system is based on two rings of different diameters to which source and detector bundles are attached. A study involving 24 volunteers is performed. Images displaying heterogeneous features that are unique to specific healthy volunteers, and reproducible over time, are presented. Pre-diagnosed benign lesions are identified in most cases, although they are not always the most dominant feature. A single tumour is identified as a dominant increase in absorption. Additionally, the recovery of tissue post Interstitial Laser Photocoagulation (ILP) treatment of a fibroadenoma is successfully monitored in a single study.

A second system based on a hemisphere filled with a coupling fluid is investigated. Preliminary investigations into the optimal optical properties of the coupling fluid and reconstruction techniques are also performed. The first investigations on healthy volunteers are presented. Initial findings suggest that this method provides superior information to the ring system due to its three dimensional capability and its ability to provide consistent coupling.

Acknowledgements

First, I would like to thank my supervisors Professor Jeremy Hebden and Dr. Adam Gibson for all their guidance, encouragement, support and friendship throughout my PhD.

The work in this thesis has been part of a much larger project and I would like to thank all the people who have contributed. In particular I would like to thank: Dr. Nick Everdell, Dr. Elizabeth Hillman, Professor David Delpy, and Louise Enfield as well as all the other members of the Biomedical Optics Research Laboratory both past and present who have contributed to the building, maintaining and experimentation of MONSTIR; Dr. Wayne Chicken and Dr. Micheal Douek from the Department of Surgeons at the Royal Free and University College London Hospitals, for allowing me to recruit their patients to this study and for providing me with the necessary medical information; Professor Simon Arridge, Dr. Martin Schweiger and Dr. Jason Riley from the theoretical imaging team for all their help in this area and Dr. Norma Morris for obtaining constructive feedback from volunteers.

Additionally I would like to thank all the members of the OPTIMAMM project. I will very much miss the open and friendly environment of the European meetings.

This project was generously funded by the Commission for the European Communities (OPTIMAMM) grant (contract QLG1-2000-00690), The Wellcome Trust, and by Cancer Research UK.

I would also like to give special thanks to all the volunteers who have taken part in this study. Without their contribution this project would not have been possible and I have been amazed at the help and encouragement we have received from them all.

Most of all I would like to thank all my family who, as always, have given me endless love and support throughout my PhD. In particular I would like to thank my husband Tim, without whom I simply would not have finished this PhD. I dedicate this thesis to Tim with all my love.

Publications Resulting From This Work

Forthcoming Peer Reviewed Publications

- **Yates, T D.** et al, '*Optical Tomography of the Breast Using a 32-channel Time-resolved Imager.*', Physics in Medicine and Biology, (In press)
- **Yates, T D.** et al,'*Time-resolved optical mammography using a liquid coupled interface.*',Journal of Biomedical Optics, (Under review).
- Hebden J C, **Yates T D.** et al, *'Monitoring recovery following laser surgery of the breast using optical tomography: a case study'*, Applied Optics, (In press)

Conference Proceedings

- **Yates, T. D.**, Hebden J.C., Gibson A., Everdell N., Arridge S. R., Douek M, Chicken W, Delpy D. T. '*Clinical Results from a 32-channel time resolved system used to image the breast.*', OSA Technical Digest, Biomedical Topical Meetings, Miami, April 2004
- **Bland, T.D** *'Three Dimensional optical imaging of the breast and infant brain'*, Symposium on Terahertz imaging, Rank Prize funds, Grasmere, March 2003.
- Morris, N, Hebden J C, **Bland, T D** and Balmer B. *'Role of patient feedback in the design and implementation of clinical trials of optical tomography of the breast.'* Proc SPIE 5138 12-22, 2003.
- **Bland T. D.** , Hebden J.C., Hillman E.M.C. , Gibson A., Everdell N. , Delpy D.T., Arridge S. R., Douek M., *'Optical tomography of the breast using a 32-channel time-resolved imager'*, OSA Technical Digest, Biomedical Topical Meetings, Miami, April 2002.

Table of Contents

List of Figures

List of Tables

Part 1

Introduction

1.1 Introduction

1.1.1 Motivation

The female breast or mammary gland is a complex and sensitive organ, which is susceptible to a range of pathologic conditions. The most serious of these is breast cancer. With more than 1 million people worldwide being diagnosed with breast cancer in 2000 (Ferlay et al 2001), breast cancer is widely recognised as the most common cancer in women and is the cause of around 13000 deaths a year in the UK alone. Other breast conditions include mastalgia, which is the term given to variety of conditions that cause breast pain, and benign lesions such as fibroadenomas and cysts. Though these in themselves are not fatal they can still cause undesirable symptoms and anxiety.

Improved methods for early detection and diagnosis of breast disease are essential to decrease mortality rates due to cancer (Foster 2003). In addition a greater understanding of the physiology of the breast is needed to aid in the diagnosis of disease and in improving treatments. The principal imaging modality used to detect breast disease at present is x-ray mammography, which while it has a high sensitivity, suffers from a relatively poor specificity for some tumours and breast types, leading to unnecessary biopsies (Keith et al 2002). Thus there is a need for an imaging technique that can non-invasively distinguish between malignant and benign lesions. At present both Magnetic Resonance Imaging (MRI) and ultrasound can provide extra diagnostic information for this purpose. The disadvantages of MRI are that a contrast agent is required to provide adequate specificity and that it is immobile, expensive, and unsuitable for some women (Schnall 2000). Ultrasound, while relatively inexpensive and versatile, is dependent on operator expertise and provides relatively poor specificity between certain solid breast masses (Pavic et al 2003).

1.1.2 Optical Imaging

A potential alternative to these modalities is optical imaging. Optical tomography provides a distinction between tissues based on their optical properties obtained from measurements of transmitted light (Ntziachristos et al 2000). Of particular interest is the facility to exploit the differences between the absorption spectra of oxy-haemoglobin and deoxy-haemoglobin at near infrared wavelengths to produce images of blood volume and oxygen saturation (Cheng et al 2003; Jiang et al 2003). It is anticipated that this physiological information can add to the anatomical information gained from x-ray mammography to produce a better diagnosis (Dehghani et al 2003; Li et al 2003).

The idea of using light for breast imaging was first demonstrated by Cutler in 1929 (Cutler 1929), but it was not until the mid 1980s that interest in the subject became widespread. This was stimulated by the emergence of new source and detector technologies (Hebden et al 1997) along with substantial developments in computing technology allowing the use of algorithms to reconstruct images representing the optical properties contained within a three-dimensional volume (Arridge et al 1997; Arridge 1999). Since then many researchers have built and begun clinical evaluations of breast imaging systems that exploit one or both of these developments. The constant improvement in processing speeds and detectors has led to a realistic potential of their use for detecting and specifying breast disease.

In 1996 a team here at University College London began development of a 32 – channel time resolved system for optical tomography. This system is described in detail in (Schmidt et al 2000). It records the temporal distribution of transmitted light at up to 32 locations on the surface simultaneously in response to illumination by picosecond pulses of light at wavelengths of 780 nm and 815 nm. Meanwhile, our reconstruction package known as TOAST (Temporal Optical Absorption and Scattering Tomography) determines the optical parameters that describe a finite-element model of photon migration within an object by comparing its predictions with the measured data (Arridge et al 2000). The model is then adjusted iteratively to minimize the difference between the two.

1.1.3 Aim

The purpose of the work presented in this thesis is to assess the ability of optical tomography to diagnose breast disease by using the 32 –channel time resolved system and TOAST reconstruction algorithm. This has involved a series of initial tests on volunteers. These volunteers were separated into three groups. First, healthy volunteers were scanned to assess the viability of the patient interface in a clinical situation and to provide a comparison for scans on patients. Second, volunteers with known benign conditions were scanned and the images produced were analysed. Finally, patients with malignant lesions were scanned and compared with previous results.

Alongside the clinical tests, constant improvements of the patient interface, imaging protocol and image reconstruction method were performed to optimise the quality of the images produced using this technique.

Ultimately it is hoped that optical tomography may provide a safe alternative imaging technique that, in combination with conventional imaging techniques, can provide greater specificity and so reduce the need for biopsy. In addition there is a potential niche for optical tomography in situations where functional imaging of tissue is needed and other modalities are inferior or unavailable, for example the monitoring of tissue after surgery.

1.1.4 Structure of thesis.

This thesis is divided into three parts. The first part is an introduction to the field of optical imaging and its contribution so far to imaging breast disease. In particular, chapter 1.2 describes the basic interactions of light with tissue and concludes with a review of the measured optical properties of the various tissues present in the breast. A further in detailed discussion of light propagation in tissue is given in chapter 1.7, along with a presentation of various image reconstruction techniques. The anatomy, physiology and pathology of the breast and their relevance to optical imaging of the breast are discussed in chapter 1.3. A detailed review of existing breast imaging techniques and alternative optical imaging devices are presented in chapters 1.4 and 1.5 respectively. Finally an overview of the UCL 32-channel imaging system is presented in chapter 1.6.

Part 2 is a presentation of various clinical studies performed using an initial patient interface based on two rings of different diameters to which the sources and detectors are attached, mounted onto a frame. The scanning protocol and image reconstruction technique are described in depth. This is followed by a review of the results obtained to date, from the studies on 23 volunteers with different breast conditions. Although this initial interface was designed and constructed prior to my involvement with this work, I have been the principal researcher involved in the clinical studies, image reconstruction and data analysis.

Part 3 describes the design and construction of a new liquid coupled patient interface. This is followed by initial analysis of the system in terms of spatial resolution, contrast, spatial accuracy and sensitivity. The first images of healthy volunteers are also presented. The design, construction and analysis presented in this section have largely been of my own initiative.

1.2 Fundamentals of Tissue Optics

In this section the basic interactions of light with tissue are discussed. This is followed by a summary of the bulk optical properties of tissue and a review of the origins of the specific optical properties of the breast.

When travelling through tissue, light experiences two main types of interaction: absorption and scatter. Other forms of radiation are also absorbed by tissue. Indeed it is the absorption of x-rays that enables an image to be created. Scatter, however, is a property that is far more dominant for light and so cannot be ignored as it is for other imaging modalities (Cheong et al 1990b). The principal optical properties to be discussed in this chapter are:

1. Absorption.
2. Scatter.
3. Refractive index.

Tissue does exhibit other optical properties such as fluorescence and inelastic scatter. Although important, these properties are not related to the measurements and analysis presented within this thesis and so are not discussed here. Detailed discussion of the principles presented below can be found in (Ishimaru 1978) and (Bohren et al 1983).

1.2.1 Absorption

Absorption is the transfer of energy from incident radiation to the surrounding tissue. If a non-scattering medium is illuminated with a collimated beam of light with intensity I_o (as illustrated in figure 1.2.1) and wavelength λ, the intensity of the emerging light is given by:

$$I = I_0 e^{-\mu_a d} , \qquad (1.2.1)$$

where $\mu_a(\lambda)$ is the absorption coefficient of the medium and d is the thickness of the sample as shown in figure 1.2.1:

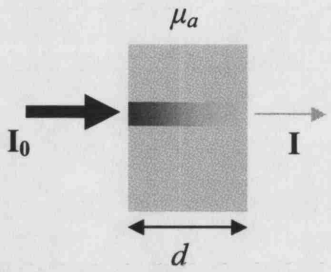

Figure 1.2.1: Attenuation of light through a non-scattering medium.

The absorption coefficient is the number of absorption events per unit length (mm^{-1} or cm^{-1}). It follows that its reciprocal $1/\mu_a$, often called the absorption mean free path, is the distance required for the intensity to fall to $1/e$ of the original value. If we define the particle density (or volume density), ρ, of an absorber as the number of absorbing particles per unit volume, and the absorption cross section, σ_a, as the cross section area that a perfect absorber would have to cause the equivalent attenuation to a collimated light beam, then we can also express the absorption coefficient as the cross-sectional area of absorption per unit volume of medium:

$$\mu_a = \rho\sigma_a \quad . \tag{1.2.2}$$

Thus by substituting equation 1.2.2 into equation 1.2.1 we obtain:

$$I = I_o e^{-\rho\sigma_a d} . \tag{1.2.3}$$

It also follows that for an absorbing substance dissolved in a non-absorbing medium the absorption coefficient is proportional to the concentration (c) of the solution. The constant of proportionality is known as the specific absorption coefficient, α. Thus:

$$\mu_a = \alpha c \quad . \tag{1.2.4}$$

The specific absorption coefficient represents the level of absorption for a unit absorber concentration per mole of compound per unit volume of solution per unit length of optical path. It should be noted that the specific absorption coefficient is described using natural logarithm units. A similar quantity can be defined using base 10 logarithm units, which is known as the specific extinction coefficient. From equations 1.2.4 and 1.2.1 we can thus obtain:

$$I = I_o e^{-\alpha c d} \quad . \tag{1.2.5}$$

This is known as the Beer-Lambert law.

Biological tissues generally contain a number of different substances that contribute to the overall absorption of light. These substances are known as chromophores. The overall absorption coefficient $B(\lambda)$ at a specific wavelength can be expressed as the sum of the contributions by all chromophores within the tissue:

$$B(\lambda) = \sum_n \alpha_n(\lambda) c_n \ . \tag{1.2.6}$$

1.2.2 Scatter

Scatter is the phenomenon that causes the direction of radiation within a medium to be changed. Just as the absorbing properties of a medium can be described by its absorption coefficient μ_a so the scattering coefficient μ_s can describe its scattering properties. In the case of a collimated source and single scattering this is given by:

$$I = I_0 e^{-\mu_s d} \ , \tag{1.2.7}$$

where I is the non- scattered component of light after traversing a non-absorbing medium of thickness d. The scattering coefficient can also be described in terms of the particle density ρ and the scattering cross section σ_s such that:

$$\mu_s = \rho \sigma_s \ . \tag{1.2.8}$$

The scattering coefficient μ_s represents the probability per unit length of a photon being scattered. It can be shown that the reciprocal of the scattering coefficient, $1/\mu_s$, or scattering mean free path, is the average distance a photon travels between consecutive scattering events.

The scattering case, however, differs from that of absorption, as the photons no longer travel in a direct line across the medium and can be scattered through any angle in three dimensions. To treat the scattering of light in tissue correctly, we must consider the probability of a photon being scattered in a given direction by a particular scatterer. If a photon is incident along a unit vector **p** then the probability that it is scattered into direction **q** is described by the phase function $f(\mathbf{p},\mathbf{q})$.

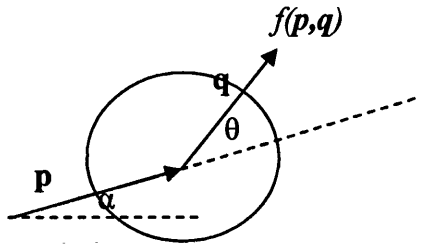

Figure 1.2.2: Representation of the phase function *f(p,q)*.

In random media, it is assumed that the phase function is a function of the angle between the incident and scattered light and so is independent of the orientation of the scatterer (i.e. independent of **p**). While true in most cases, this assumption does not hold for some tissues such as muscle and white matter where there is a difference in the scattering properties in different orientations. Using this assumption, the phase function can be expressed as a function of the scalar product of the unit vectors in the initial and final directions (***p,q***) which is equal to the cosine of the scattering angle cos(θ). The anisotropy factor, g, is then defined as the mean cosine of the scattering angle θ:

$$g = \int_{4\pi} d(\cos\theta)\cos\theta d\theta .$$

(1.2.9)

The anisotropy factor depends on the size, shape and refractive index mismatches of the scatterers: if $g = 0$ then the scatter is isotropic, if $g = 1$, the scatter is entirely forward and if $g = -1$ the light is backscattered.

In biological tissues the anisotropy factor varies between about 0.69 and 0.99 (Cheong et al 1990b). This implies that the scatter occurs mainly in a forward direction. However the typical values of the scattering coefficient within the breast ensure that beyond a few millimetres penetration the light loses its initial directionality. This means that it is appropriate to assume isotropic scatter where the scatter coefficient has been reduced by the factor (1-*g*):

$$\mu_s' = \mu_s(1-g),$$

(1.2.10)

where μ_s' is known as the transport scattering coefficient. The reciprocal of μ_s' is the distance over which a collimated beam has a *1/e* probability of undergoing an isotropic scattering event. The extra distance travelled by light in tissue as a result of scatter will lead to a greater chance

that the photon is absorbed. The distance now travelled is known as the differential pathlength and can be obtained from the differential pathlength factor (*DPF*), given by

$$DP = DPF\, d,$$

(1.2.11)

where *DP* is the true optical pathlength, (differential pathlength) and *d* is the geometrical distance between the source and detector. The differential pathlength factor will depend on the number of scattering events that occur. The *DPF* will in practise be a function of the scattering coefficient μ_s, the anisotropy *g*, the absorption of the medium, and the geometry of the medium and must be included in the Beer Lambert law to describe attenuation in a scattering medium (Matcher et al 1993). It is also necessary to introduce an additive term *G*, which represents the scattering losses due to the geometry of the media. Thus we can modify equation (1.2.7) to give:

$$I = I_0 e^{-\mu_a(\lambda) DPF d + G} \quad .$$

(1.2.12)

This is known as the modified Beer Lambert law. *G* is dependent on the measurement geometry and the scattering coefficient of the tissue under study and is largely unknown. Consequently, spectroscopic measurements generally assume that *G* is constant during the measurement period and attempt to quantify changes in the absorption instead of absolute values:

$$\Delta A_{(2-1)} = Log\left(\frac{I_1}{I_2}\right) = DPFd(\Delta\mu_{a(2-1)}),$$

(1.2.13)

where $\Delta A_{(2-1)}$ is the change in attenuation measured between state 2 and state 1 corresponding to an absorption change of $\Delta\mu_{a(2-1)}$.

The DPF can be approximately calculated from the μ_a, μ_s' and the geometry of the object or determined via measurement of the mean time $< t >$ taken for light to traverse a scattering medium using

$$DPF = \frac{c_{vacuum} < t >}{dn} \quad ,$$

(1.2.14)

where *n* is the refractive index of the material and c is the speed of light.

For a more complete description of light propagation through complex scattering media analytical and numerical models can be derived. These are presented in more detail in chapter 1.7.

1.2.3 Refractive index

The speed of light, c, within a specific medium of refractive index n is given by:

$$c = \frac{c_{vacuum}}{n}, \tag{1.2.15}$$

where c_{vacuum} is the speed of light in a vacuum.

Light arriving at a non-normal angle of incidence, θ_1, to a boundary of two media with different refractive indices will be refracted causing the light to change direction and emerge at angle θ_2. This is illustrated in figure 1.2.3.

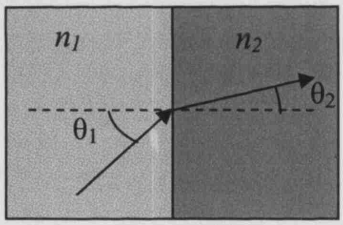

Figure 1.2.3: The behaviour of light at a boundary between two media with different refractive indices. $n_1 < n_2$.

Snell's law states that:

$$n_1 sin\theta_1 = n_2 sin\theta_2 \tag{1.2.16}$$

The refractive indices of individual tissue constituents at optical wavelengths vary from about 1.33 for water to approximately 1.55 for fat and concentrated protein solution (Bennett et al 1951). The overall refractive index is considered typically to be around 1.40 for most tissue types (Bolin et al 1989).

1.2.4 Optical properties of tissue

Within biological tissue there are various substances that contribute to the absorption of light, known as chromophores. Figure 1.2.4 shows the absorption spectra of some common

chromophores from the UV to the mid infrared region of the electromagnetic spectrum. The main chromophores in breast tissue within the region of interest (NIR window) are water, lipids, haemoglobin and melanin. Figure 1.2.4 also includes a representation of the scatter coefficient of tissue across this region.

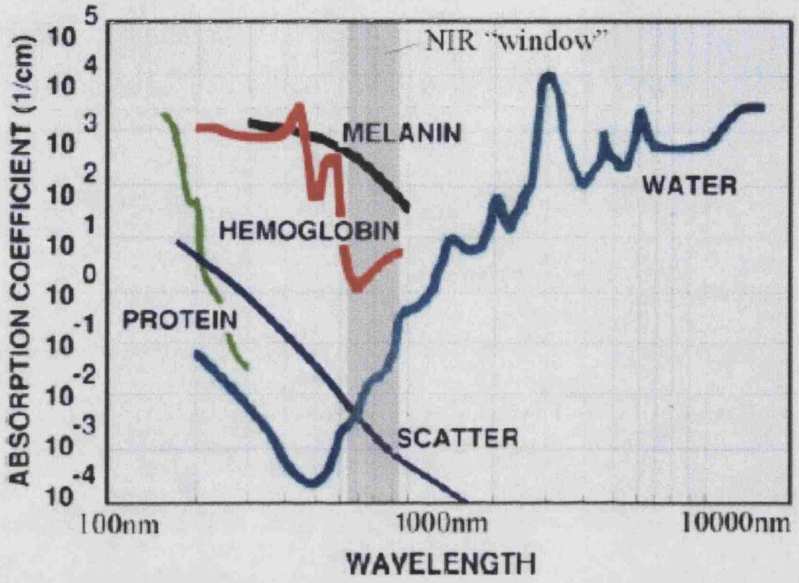

Figure 1.2.4: The absorption spectra for the main chromophores found within tissue.

1.2.4.1 Water

The absorption spectrum of water is shown in figure 1.2.5.

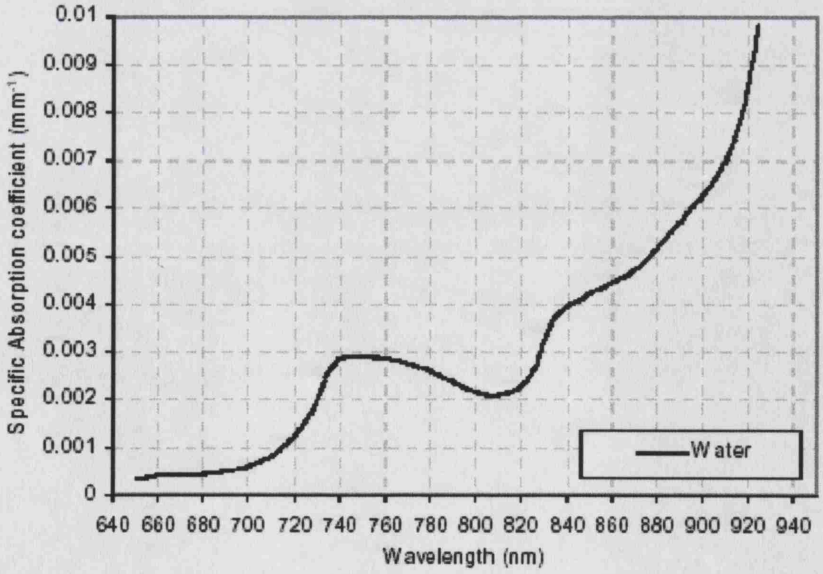

Figure 1.2.5: The absorption spectra of water in the near infrared region (Hollis et al 2001).

As can be seen water has a low absorption over the NIR range. At the specific wavelengths used for the work described in this thesis (780nm and 815nm) the absorption is only 0.0026 and 0.0021 mm^{-1} respectively. Water can, nevertheless, strongly influence measurements due to the high concentration. In most tissues water is the major constituent with 30 – 60% (Grosenick et al 2003; Srinivasan et al 2003) of the breast being made up of water, depending on the time from menstruation. This means that the accumulative absorption effect cannot be ignored.

1.2.4.2 Lipids

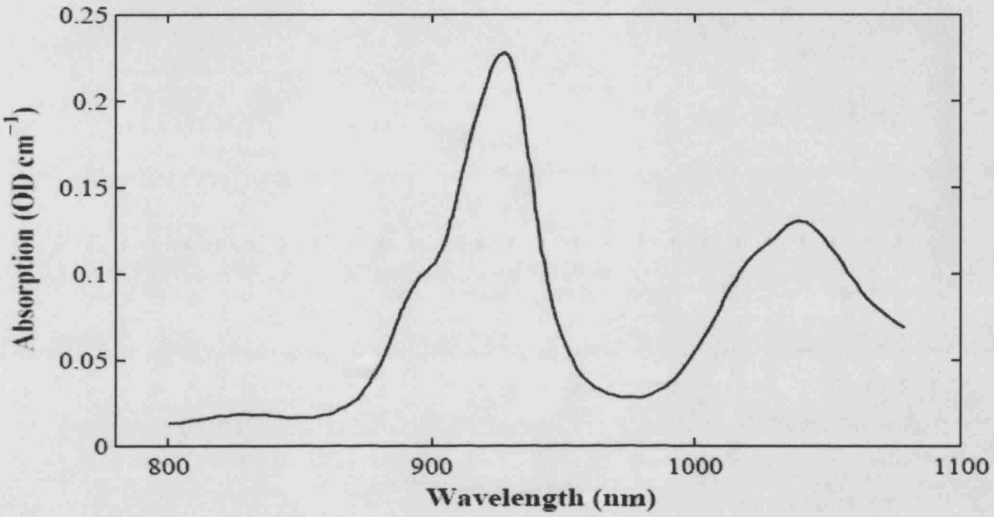

Figure 1.2.6: The absorption spectrum of lipids (pork fat) in the near infra red region (Conway et al 1984)

Adipose tissue (fatty tissue) is a second dominant constituent of breast tissue (chapter 1.3) and so the absorption by lipids must be considered. The absorption spectrum of lipids is similar to that of water and is relatively flat between 780 and 815 nm (figure 1.2.6). As with water the absorption of lipids can be considered constant for the purposes of this thesis, but the high concentration of lipids in the breast leads to an accumulative absorption effect making lipids one of the dominant absorbers within breast tissue (Cerussi et al 2002). This effect will increase with the age of women as older women tend to have less fibrous tissue and more adipose tissue. However, it should be noted that glandular tissue has an increased vascularity in comparison to adipose tissue and that the resulting increase in haemoglobin (see 1.2.4.3) means that the absorption coefficient of breast tissue is likely to be higher in the breasts of younger women.

1.2.4.3 Haemoglobin

Haemoglobin is a compound found within red blood cells and consists of four haeme (iron containing) groups. In the lungs oxygen attaches itself to the iron within these groups to form

oxy-haemoglobin. As blood is circulated around the body the oxygen is released and the haemoglobin is returned to its deoxygenated state, deoxy-haemoglobin. The absorption spectra of oxy- and deoxy- haemoglobin are shown in figure 1.2.7.

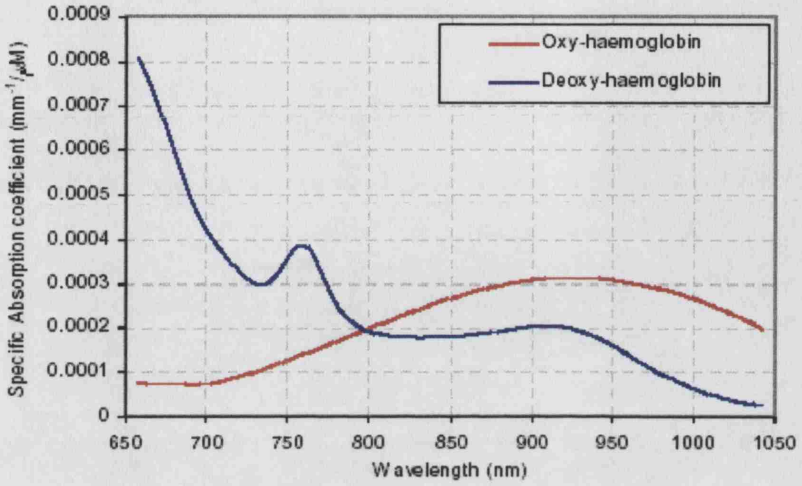

Figure 1.2.7: The absorption spectra of oxy- and deoxy-haemoglobin within the near infra-red region (Cope 1991).

Within the visible region the difference shown accounts for the appearance of arterial blood (flowing away from the lungs so highly oxygenated) as bright red and venous blood (flowing back towards the lungs so deoxygenated) as a bluish - red.

The relatively low absorption by both haemoglobin and water at NIR wavelengths provides a transparency window enabling transmittance measurements over several centimetres of tissue and hence the NIR region is chosen for the study of the breast.

The differences between the absorption spectra of oxy- and deoxy-haemoglobin at the two wavelengths used in this study (780nm and 815nm) can be used to determine the oxygen saturation (the percentage of blood that is oxygenated) and blood volume of the tissue. Oxygen saturation (SO_2) is given by:

$$SO_2 = \frac{[HbO_2]}{[HbO_2 + Hb]} \times 100 . \qquad \textit{(1.2.17)}$$

From equation 1.2.6 we can determine the absorption coefficient of blood at two wavelengths as follows:

$$\mu_{780nm} = \alpha_{HbO_2}(780nm) \times [HbO_2] + \alpha_{Hb}(780nm) \times [Hb]$$

$$\mu_{820nm} = \alpha_{HbO_2}(820nm) \times [HbO_2] + \alpha_{Hb}(820nm) \times [Hb].$$

(1.2.18)

By solving the simultaneous equations in 1.2.18 and using 1.2.17 we can now obtain:

$$SO_2 = \frac{\alpha_{Hb}(780nm) \times \mu_{820nm} - \alpha_{Hb}(820nm) \times \mu_{780nm}}{(\alpha_{Hb}(780nm) \times \mu_{820nm} - \alpha_{Hb}(820nm) \times \mu_{780nm}) + (\alpha_{HbO_2}(820nm) \times \mu_{780nm} - \alpha_{HbO_2}(780nm) \times \mu_{820nm})} \times 100$$

(1.2.19)

We can obtain the values of the specific absorption coefficients of oxy- and deoxy-haemoglobin (α_{HbO2} and α_{Hb}) from figure 1.2.6 and so by measuring the absorption coefficient at two different wavelengths it should be possible to determine the oxygen saturation.

1.2.4.4 Melanin

Melanin is found in the epidermis layer of the skin in cells called melanosomes. In the region of interest for this study melanin is a relatively high absorber. However its' absorption can be considered to be constant and oxygen independent within the near infra-red region. In addition its overall concentration in the breast is low and so although it is a relatively high absorber it will not contribute significantly to the absorption of breast tissue.

It should be noted, however, that melanin granules are arranged in a periodic structure so also lead to high scatter. The effect of this is that the light is distributed throughout the cell avoiding local regions of high absorption and potential for cell damage. In terms of optical imaging this means that the concentration of melanin in the skin will affect the reflectance of the light from the skin and therefore will also effect the transmission of light into the tissue below.

1.2.5 Optical properties of breast tissues

Various groups have measured the optical properties of biological tissue including breast tissue, although most measurements have been in vitro (Bevilacqua et al 1997; Cheong et al 1990a; Gayen et al 1999; Nair et al 2002; Peters et al 1990; Troy et al 1996). The values from one such study (Peters et al 1990) for healthy and diseased (both malignant and benign) breast tissue at different wavelengths are shown in table 1.2.1.

Breast tissue	Wavelength	μ_a (mm^{-1})	μ_s' (mm^{-1})	Sample number
Glandular	700	0.047 ± 0.011	1.42 ± 0.30	3
	900	0.062 ± 0.005	0.99 ± 0.20	3
Adipose	700	0.070 ± 0.008	0.86 ± 0.13	7
	900	0.075 ± 0.008	0.79 ± 0.11	7
Fibrocystic	700	0.022 ± 0.009	1.34 ± 0.19	8
	900	0.027 ± 0.011	0.95 ± 0.17	8
Fibroadenoma	700	0.052 ± 0.047	0.72 ± 0.17	6
	900	0.072 ± 0.053	0.53 ± 0.14	6
Ductal carcinoma	700	0.045 ± 0.012	1.18 ± 0.31	9
	900	0.050 ± 0.015	0.89 ± 0.26	9

Table 1.2.1: The in vitro optical properties of the tissue types found within the breast as provided by (Peters et al 1990).

The results presented show a slight variation between malignant and benign lesions, and between malignant and healthy tissues, although in some cases the variation proved to be statistically insignificant. Other values quoted for the absorption of the breast in vitro range from 0.0040 ± 0.0010 mm^{-1} at 700 nm (Zacharakis et al 2001) to 0.056 mm^{-1} at 590 nm (Nair et al 2002). However, such values are not representative of the contrast between the optical properties in this thesis as the measurements are made in vitro and the samples are prepared in such a way that the majority of the blood is removed from the sample. The work presented in this thesis is based on in vivo measurements and so the optical properties of the tissues will have a high dependence on their physiology (e.g. oxygen saturation and blood volume) due to the high absorption of haemoglobin as described previously. Indeed it is proposed that a likely origin of contrast between malignant and benign or healthy tissue will be a result of the high vascularisation of tumours (see chapter 1.3) and this may not be revealed by in vitro measurements.

Various in-vivo measurements have been made. These studies have focused on the bulk optical properties of the breast and have included measuring variation in optical properties with the menstrual cycle (Cubeddu et al 2000), menopausal status (Cerussi et al 2001a; Chance et al 1998; Suzuki et al 1996), age (Cerussi et al 2001a; Cerussi et al 2002; Chance et al 1998; Cubeddu et al 2000; Durduran et al 2002; Suzuki et al 1996; Tromberg et al 1997) and body

mass index (BMI)[1] (Pogue et al 2001; Suzuki et al 1996; Cerussi et al 2002; Durduran et al 2002).

The study by (Suzuki et al 1996) involved 30 Japanese women and was performed using a time-resolved optical system in the transmission geometry. In their study they used a single wavelength 753nm source and a single detector. They concluded that the value of μ_a, for the volunteers ranged from 0.0024 to 0.0078 mm^{-1} and that the value of μ_s' ranged from 0.63 to 1.08 mm^{-1}. They also reported a strong correlation between absorption and scatter and age, BMI and menstrual status. They also reported no correlation between the optical properties of the breast and breast thickness or the number of pregnancies. It should be noted that 30 women is clearly too few to extrapolate to all women and that measurements made at 753nm will vary from those made in this thesis at 780 nm and 815nm.

The study by (Cerussi et al 2001a) involved 28 volunteers, measured with a multi wavelength, multi modulation frequency optical system. Once again a single source and detector pair were used with a relatively small separation and so only around 1 cm of the tissue surface would be sampled. As the tissue directly below the surface of the skin is known to contain a greater concentration of fat this is likely to affect the results. In this work a substantial change in breast tissue properties with menopausal status, age, blood volume (BV) and water content were reported. It was also reported that older breast tissue contained a different water and lipid content to younger breast tissue. A further study by (Cerussi et al 2002) involved the same system and a further 30 volunteers. In this second paper a relationship between scatter and body mass index was reported. Once again both studies involved a small sample of women. Furthermore the wavelengths used (672, 800, 806, 852, 896, 913, and 978 nm) in this study, although over a broader range, are not exactly the same as those used in this thesis.

Meanwhile (Cubeddu et al 2000) investigated breast optical properties at multiple wavelengths between 610 and 1010 nm throughout the menstrual cycle and quantified changes for one volunteer. Although this study indicated that changes in optical properties occur across the menstrual cycle, these findings were based on only one volunteer. A more recent study by (Pogue et al 2004) focused on the oxygenation and blood volume properties of the breast in seven premenopausal women. Their results revealed an average increase in the heamoglobin concentration of 13% of the background properties towards the end of the cycle.

[1] BMI = weight/height^2

An earlier study by (Pogue et al 2001) on 16 women, using a cylindrical Diffuse Optical Tomography (DOT) system (see chapter 1.5), reported a correlation between blood volume and BMI, but no other correlations.

Bulk optical properties of healthy female breast tissue as published by (Durduran et al 2002) are given in table 1.2.2. This work involved the use of a compressed breast geometry with a single intensity-modulated source centrally located on one plate and 153 detectors on the opposite plate. Three wavelengths of 830, 786 and 759 nm were used.

λ(nm)	830	786	750
μ_a (mm^{-1})	0.0046 ±0.0027	0.0041 ± 0.0025	0.0046 ± 0.0024
μ_s' (mm^{-1})	0.83 ± 2.0	0.85 ± 2.1	0.87 ± 2.2

Table 1.2.2: Bulk optical properties of the breast (Durduran et al 2002).

This study represents an improvement on most of the studies mentioned previously as multiple measurements are made to probe the entire volume of the breast and not just the surface layers. The wavelengths used, though not identical, are close to those used in the work of this thesis. However, the use of a compressed breast geometry could lead to a reduction in blood volume in comparison to the non-compressed geometry adopted in the work of this thesis.

To my knowledge there is only one published work quoting properties of breast tumours in vivo (Fantini et al 1998) although various studies have indicated that tumours can be distinguished from healthy tissue as areas of increased absorption and scatter (Grosenick et al 2003; Taroni et al 2004a). There are no published values of the in vivo properties of benign lesions, although a study by (Taroni et al 2004a) has shown that cysts exhibit low scatter in comparison to healthy tissue, whereas fibroadenomas exhibit no distinguishing optical properties. The reason for this lack of in vivo data is the difficulty of measuring such values and the present uncertainty in the accuracy of reconstructed values. The values quoted by (Fantini et al 1998) for a tumour in vivo at two wavelengths (690 and 825 nm) are:

- $\mu_a(690nm) = 0.0084 \pm 0.0014\ mm^{-1}$
- $\mu_a(825nm) = 0.0085 \pm 0.0017\ mm^{-1}$
- $\mu_s'(690nm) = 1.50 \pm 0.3\ mm^{-1}$
- $\mu_s'(825nm) = 1.27 \pm 0.3\ mm^{-1}$

These values indicated that the tumour had higher absorption and scatter than the surrounding healthy tissue, although they only represent one measurement, and once again are measured at different wavelengths to those used in this thesis. This means that the only comparative information for the optical properties of malignant and benign tissue are in vitro measurements such as those presented in table 1.2.1.

1.2.5.1 Conclusion

As a result of the work in these previously published studies I am going to use the following values as estimates of the typical bulk optical properties of the pre-menopausal breast at 780nm:

- $\mu_a = 0.007 mm^{-1}$
- $\mu_s' = 0.8\ mm^{-1}$

The value for the reduced scatter coefficient is based on the results obtained by (Durduran et al 2002) presented in table 1.2.2. It is assumed that the wavelength dependence of μ_s' is negligible. The value for absorption is based on the results presented by (Suzuki et al 1996). A value towards the higher end of the values quoted has been chosen as the results from the pre-menopausal volunteers were generally higher than those for the post-menopausal volunteers. The results in (Durduran et al 2002) were not used to estimate typical absorption as it is likely that the compression of the breast and subsequent reduction in blood volume will produce a lower absorption than that of the uncompressed breast.

The determination of both coefficients is subject to ongoing debate and published estimates are likely to involve inaccuracies. However the values selected above are chosen as typical in order to construct suitable phantoms and reference media. Nevertheless it should be noted from the findings presented above that the optical properties of the breast can vary significantly from volunteer to volunteer and are dependent on their BMI and menopausal status (and age). These parameters should be taken into account during the interpretation of images.

1.3 Anatomy, Physiology and Pathology of the Breast

1.3.1 Anatomy

The breast, or mammary gland, is a glandular organ unique to mammals. On the surface of the breast is a round, pigmented area called the areola. At the centre of this lies a raised area known as the nipple. In mature women 10 to 15 tubes, or ducts, lead from the nipple to the interior of the breast. At the end of the ducts are situated clusters of rounded cells called lobules. It is these lobules that are the site of milk production (Hall-Craggs 1995; website 1; Peters 1989). Figure 1.3.1 illustrates the basic anatomy of the breast:

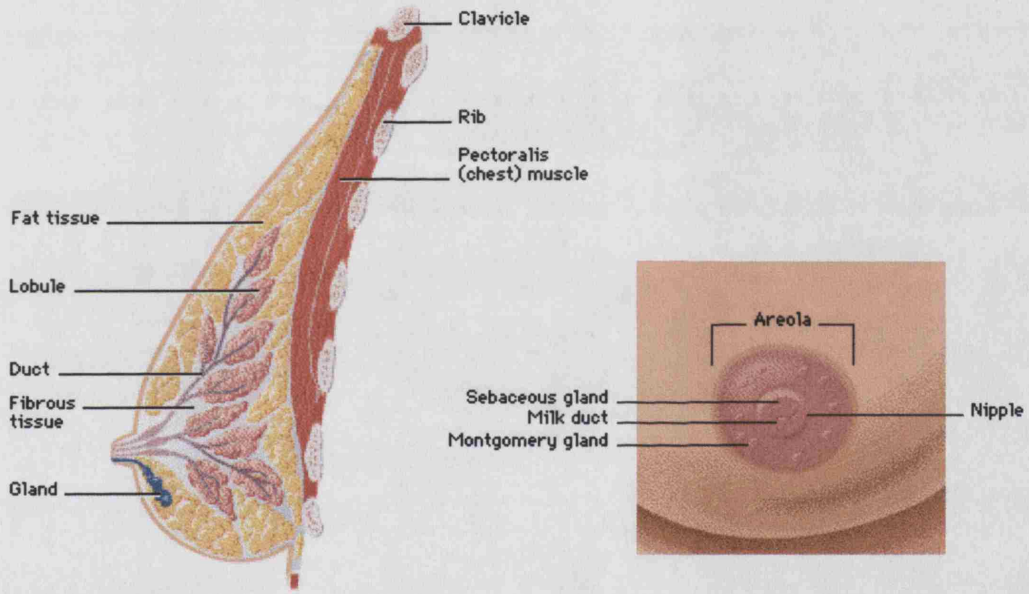

Figure 1.3.1: The anatomical structure of the female breast (website 2).

The main groups of tissue known to have distinct characteristic optical properties are adipose (fat) tissue, glandular tissue and fibrous tissue.

1.3.2 Physiology

It is important to consider the physiology of the breast, as the changes seen in the breast during a woman's life will have an effect on the optical properties of the tissues. It is also important to understand the stages at which there is a higher risk of breast cancer, as an imaging device needs to be tailored accordingly.

The growth of breast tissue is mainly influenced by the relative concentrations of progesterone and oestrogen in the body. Human breast tissue begins to develop in the sixth week of foetal life due to oestrogen and progesterone being absorbed by the foetus from the mother. All human babies, both male and female, are in fact born with very small breasts and can experience some nipple discharge during the first few days after birth (witch's milk). Although not unknown, breast cancer in children is extremely rare and so any imaging technique will not have to be tailored for use in children.

The female breast does not fully develop until the onset of puberty, when hormonal changes (especially increases in oestrogen and progesterone) stimulate the growth of breast tissue. During this time, fat and fibrous tissue becomes more elastic and the breast ducts begin to grow. This growth continues until menstruation begins (typically one or two years after breast development has begun).

The shape and appearance of the breast continues to change as a woman ages. In young women, the breast skin stretches and expands as the breasts grow, creating a rounded appearance. Young women tend to have denser breasts (more glandular tissue) than older women. The denser breasts lead to poorer contrast between healthy and diseased tissue in x-ray mammography, although it should be noted that the occurrence of breast cancer in younger women is low, with 80 % of breast cancers occurring in women over the age of 50 (Cancer Research UK 2003). The last significant change in the female breast occurs at the menopause. During the menopause the production of hormones is reduced to below that necessary for menstruation to occur. It is these hormonal changes that are linked to the change in the constituency of the breast as a woman ages. The occurrence of the most common breast lesions with age is illustrated graphically in figure 1.3.2.

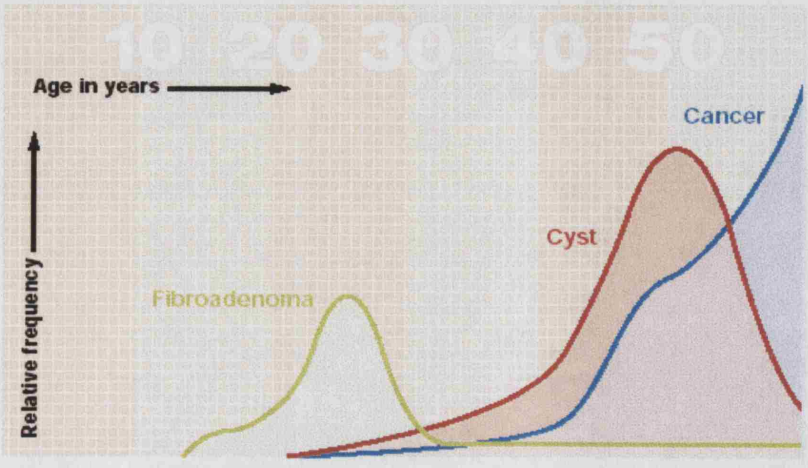

Figure 1.3.2: Incidence of common breast lesions with age (Kothari 2003).

During each menstrual cycle, breast tissue tends to swell as a result of changes in the body's levels of oestrogen and progesterone. The milk glands and ducts enlarge, and in turn, the breasts retain water. During menstruation, breasts may temporarily feel swollen, painful, tender, or lumpy. The effect of this on optical imaging is that the bulk absorption properties of the tissue are likely to change over the course of the menstrual cycle (Cubeddu et al 2000; Pogue et al 2004), especially in relation to the retention of water (see section 1.2.4.1). For this reason it may be considered desirable that women returning for a repeated scan should be imaged at the same point in her menstrual cycle. This is particularly true if, like in x-ray mammography, images are compared with previous images to look for changes as a matter of routine diagnosis. A further consideration is that there are potential problems with imaging larger breasts. In some cases the breasts can swell significantly over the menstrual cycle and so it may be an advantage to image a patient at a point just after menstruation when the breasts are at their smallest.

1.3.3 Male Breast Cancer

Male breast cancer, although rare, is potentially more lethal than the female form (Perkins et al 2003). At present there is no designated imaging technique for male breast cancer. X-ray mammography is not suitable as there is typically not enough tissue in the male breast for compression (see chapter 1.4). Other imaging modalities such as ultrasound will be limited due to the close proximity of the ribs and lungs. However it should be noted that male breast cancer is more easily detected by physical examination than female breast cancer, although due to social influences it is not always reported when first detected. This is one potential area where optical topography (section 1.5.1.2) may be able to provide the diagnostic information required whilst using a safe non-ionising technique.

1.3.4 Pathology

1.3.4.1 Benign conditions

There are many lesions and conditions that are non-cancerous but still affect the health of the breast (Kothari 2003) and could be mistaken for cancer. In this thesis studies on fibroadenomas, cysts and mastalgia are presented and so these conditions are discussed in depth below. Other benign conditions include breast calcifications, duct ectasia and periductal mastitis, fat necrosis, hyperplasia, intraductal papilloma, phyllodes tumour and sclerosing adenosis. Further details of these conditions can be found in Appendix A.

1.3.4.1.1 Fibroadenomas

A fibroadenoma is a fibrous lump of tissue that occurs most commonly in younger women. In fact the majority of lumps in a young breast turn out to be fibroadenomas (figure 1.3.2) and it is not unusual for more than one to be found. They are thought to result from an increased sensitivity to the hormone oestrogen. They are highly palpable and move easily under the skin, which has given rise to their nickname the 'breast mouse' (website 1, website 2).

Fibroadenomas are not in themselves harmful but may be tender or painful. Most are 1-3cm in size and this group are referred to as 'common' fibroadenomas. Occasionally they can grow to over 5cm and these are known as 'giant' fibroadenomas. In most cases fibroadenomas will not change in size, or will disintegrate naturally over time and so are simply left. In some cases the fibroadenoma can become larger, especially during pregnancy or breast-feeding. If the fibroadenoma becomes larger than 3cm or is extremely painful then it may be removed by surgery. At present this is mainly through conventional surgery, however research is under way to develop a technique to remove fibroadenomas by laser surgery (Bown 1998).

1.3.4.1.2 Cysts

Breast cysts are fluid-filled sacs that develop within the breast tissue. They are often palpable, but are not harmful and are not associated with an increased risk of developing cancer. They most frequently occur in the upper half of the breast and are most common in women over 35. Cysts do not normally occur in post-menopausal women unless they are undergoing hormone replacement therapy (HRT).

Cysts can often disappear naturally. If the cyst is large or does not go away on its own, the usual treatment is to draw off the fluid with a fine needle and syringe. Once the fluid has been drawn off the cyst usually disappears. The fluid drawn off from the cyst can vary in appearance, from clear to very dark, which will affect its optical properties. If it is bloodstained, it may be sent to a laboratory for testing, as there is a small risk that this may be due to breast cancer.

1.3.4.1.3 Mastalgia

Mastalgia is the name given to a wide variety of conditions that cause breast pain. Although not associated with a lesion, it is a very common condition affecting two out of three pre-menopausal women at some point in their lives. There are two categories of mastalgia: cyclical and non-cyclical. Cyclical mastalgia varies in severity at regular times throughout the menstrual

cycle, and it usually manifests as a discomfort and lumpiness in the breast around a week before menstruation. Meanwhile non-cyclical mastalgia is a lasting pain that is not related to the menstrual cycle.

The exact cause of cyclical breast pain is not known. The latest research suggests that it may be a result of extremely low levels of an essential fatty acid called gamolenic acid (GLA) (Cheung 1999). It can also be associated with starting to take the contraceptive pill, and with certain anti-depressant drugs and herbal remedies.

There are in fact two types of non-cyclical mastalgia:

1. True breast pain that has its origin within the breast but is not linked to the menstrual cycle;
2. Pain that is felt in the area of the breast but is actually caused by a condition elsewhere such as within the muscles, bones and joints. This may be referred to as musculoskeletal pain.

Both of these can result in continuous pain and can affect women both before and after the menopause. The pain tends to be in a specific area and can be in both breasts at the same time. The cause of non-cyclical mastalgia is often unknown. It can sometimes be related to specific benign breast conditions or underlying conditions that are not directly related to the breasts.

1.3.4.2. Malignant lesions

Cancer is caused by a defect in the normal process of cell division. Cells rapidly multiply with no variation and so form a lump that can invade and damage the normal tissue. There are several different types of tumours that can affect the breast. Over 70% of breast cancers are ductal carcinomas, which are associated with the milk ducts, 10% - 15% are lobular carcinomas associated with the lobes, and the rest are relatively rare forms of cancer such as of the connective tissue. While the cancer remains in the duct or lobule it is known as localised cancer, which is easier to treat. It can however extend beyond the duct or lobule infiltrating into the surrounding tissue and so become invasive.

As tumours grow some develop the ability to produce their own capillary system of blood vessels. This process is known as vascularisation and is linked to rapid tumour growth and the ability for a tumour to metastasize, when tumour cells travel to other parts of the body. Thus vascularisation of a tumour is an indication that a tumour is likely to become invasive. As described in chapter 2, optical imaging has the ability to determine blood volume, so it is

anticipated that the increase in blood volume caused by the vascularisation of tumours will be an indicator of a malignant tumour as compared with a benign lesion where no vascularisation occurs.

The percentage of cancer occurrence within each of the four quadrants of the breast is shown in figure 1.3.3. Studies have shown that cancers are most likely to occur in the upper outer quadrant of the breast (under the armpit) so it is important for any imaging system to be able to sample this region.

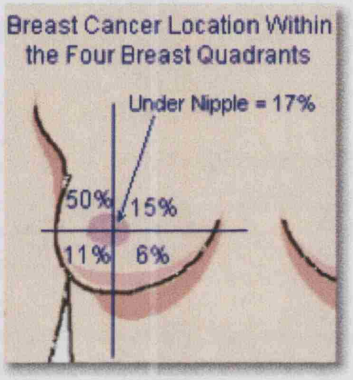

Figure 1.3.3: The percentage occurrence of cancers in each section of the breast (website 2)

There are several systems by which malignant lesions can be classified. One-way is to categorise all cancers into one of four stages with stage four being the most advanced case. Another popular system is the TNM system. This separately assesses the tumour (T), nodes (N) and secondary spread or metastases (M). A detailed description of both systems is given in Appendix B. Diagnosing a cancer at an early stage significantly increases the chances of survival for a patient as shown in figure 1.3.4. This is why methods of early detection and diagnosis are so important in the management of breast cancer. The onset of vascularisation, which is the primary basis of the contrast of optical tomography, generally occurs when tumours reach a size greater than a few cubic millimetres and vascularisation is required prior to the onset of metastasis, thus vascularisation occurs in the majority of tumours in all stages (Sainsbury et al 2000).

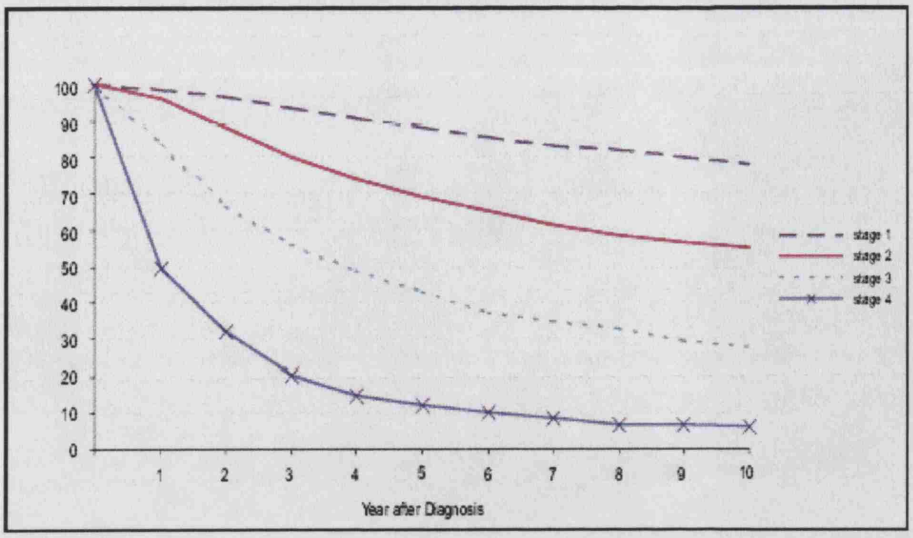

Figure 1.3.4: 0-10 year survival for cases of breast cancer by stage diagnosed in the West Midlands 1985-1989 followed up to the end of 1999 (Cancer research uk 2003).

Treatment of cancer depends on the type and stage of the cancer along with other issues such as the individual circumstances of the patient. The most common treatments are surgery followed by radiotherapy, hormone treatment, or chemotherapy. Surgery can be either conservative, where only the lesion and a small amount of surrounding tissue is removed, or a mastectomy, which involves removing the whole of the breast. In both cases the tissue following surgery is particularly sensitive and so the conventional method of imaging the breast, x-ray mammography, which uses compression (see chapter 1.4) is unsuitable for assessing the effectiveness of the surgery. Radiotherapy can be used before surgery to reduce the size of the cancer but is more commonly used following surgery to destroy any remaining cancer cells. Hormone therapy is often used to lower the levels of oestrogen in the breast. Oestrogen can often stimulate the proliferation of cancer cells so blocking or reducing its levels can stunt cancer growth. The most common drug prescribed for hormone therapy is tamoxifen. Monitoring the effectiveness of radiotherapy, hormone therapy and chemotherapy is again an area where optical imaging has a potential to fill a vacant niche due to its use of non-ionising radiation, the lack of necessity for compression and its ability to display functional information.

1.3.5 Possible appearance of lesions using Optical Mammography

As described in section 1.2.5, there has been no thorough, systematic collection of information on the optical properties of all malignant and benign conditions. Nevertheless, the following table is an attempt to predict the appearance of each lesion based on the physiology and information of the optical properties of the lesions where available.

Condition	Summary	Possible appearance in Optical mammography
Malignant cancer	Rapidly dividing cells causing lesion that can invade surrounding tissue	High absorption due to high vascularisation. High scatter. High blood volume and low oxygen saturation. (Fantini et al 1998)
Fibro adenoma	Fibrous benign lesion. Highly palpable	Low scatter, possibly high absorption (Peters et al 1990), normal vasculature.
Cyst	Liquid filled sac.	Similar properties to water. Low scatter and low absorption (Taroni et al 2004a). Low (zero) blood volume and oxygen saturation. Bloodstained cases may exhibit higher absorption and blood volume. Difficult to model as it is a non-scattering region and so the diffusion approximation does not apply (see chapter 1.7).
Mastalgia	Cyclical/non-cyclical breast pain.	Possible change in optical properties related to water retention and other unknown physiological process. Possible cyclical changes.
Calcifications.	Collection of calcium salts	High scatter, however likely to be too small in size to be detected using optical tomography.
Duct Ectasia and periductal mastitis.	Blockage and inflammation of ducts.	Similar to cyst. Low scatter.
Fat necrosis	Firm round lump in area of damage adipose tissue.	Normal vasculature. Concentration of adipose tissue - High scatter. Absorption of adipose tissue similar to water therefore low absorption.
Hyperplasia.	Increased growth in size and number of normal cells.	No significant effect.
Intraductal papilloma.	Wart like lump in duct behind areola.	Possible high scatter. No excess vascularisation so no change in absorption. Location behind nipple important.
Phyllodes Tumour.	Large benign tumour.	Large feature. Possible high scatter. No significant absorption change due to vascularisation.
Sclerosing Adenosis.	Extra tissue in breast lobule.	Possible high scatter.

Table 1.3.1: Summary of pathological conditions of the breast and their predicted appearance in optical mammography.

1.4. Existing Breast Imaging Techniques

1.4.1 X-ray Mammography

X-ray mammography is the most common method of imaging the breast at present. The technique involves the breast being compressed between two plates with an x-ray film placed underneath (figure 1.4.1). Low energy (~17 keV) x-rays are then passed through the breast and recorded on the film (website 1; website 5; Peters 1989).

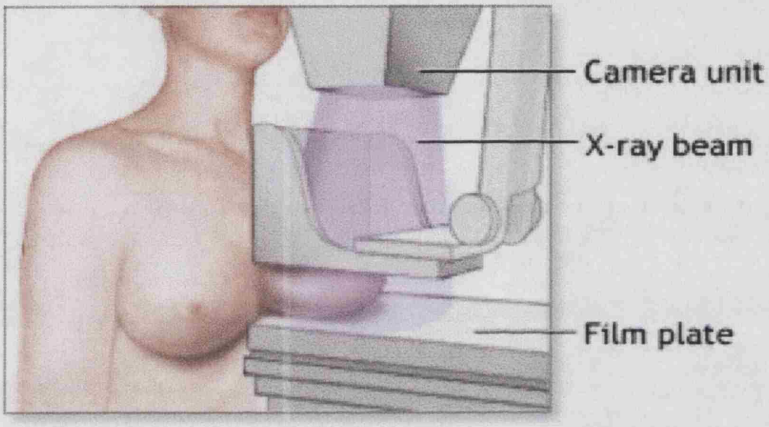

Figure 1.4.1: A diagram illustrating the use of x-ray mammography (website 1)

The attenuation of x-rays through tissue is given by:

$$I = I_o e^{-\mu d}, \tag{1.4.1}$$

where I and I_o are the intensities of an x-ray beam entering and leaving a slab of material of thickness d and μ is the linear attenuation coefficient (Barker 1996). The value of μ is dependent on the atomic number of the material. Thus tissues with higher atomic numbers (such as calcium in bone (Douglas and Williamson 1980) and microcalcifications) will produce a higher attenuation than others. However, there is very little difference between the atomic number of the tissues in the breast and hence little difference in the attenuation of x-rays. The best contrast between soft tissues is achieved at low energies and hence these are used in x-ray mammography. The x-rays are produced by an electron beam irradiating either a tungsten or molybdenum target depending on the size of the breast to be imaged. Contrast is dependent on the thickness of the breast and the difference in linear attenuation coefficients between the tissue types. Figure 4.2 shows the dependence of contrast on photon energy for glandular tissue and calcifications. As can be seen the contrast decreases rapidly with increasing photon energy.

However, at low energies, the transmission is low causing a high dose to the patient. Thus a compromise between contrast and dose is necessary. This problem is reduced by compression of the breast. The breast is compressed to between 2 and 8 cm enabling a high contrast whilst keeping the dose within an acceptable level. Compression of the breast also spreads out the layers of the breast so that it is less likely that a feature could be hidden behind a more dominant layer. The disadvantages of compressing the breast are that it is, at best, uncomfortable and for many women with sensitive breasts it can be very painful. This limits the maximum time feasible for the imaging process. Also the spatial accuracy of the image can be distorted so that it is difficult to exactly locate an identified lesion.

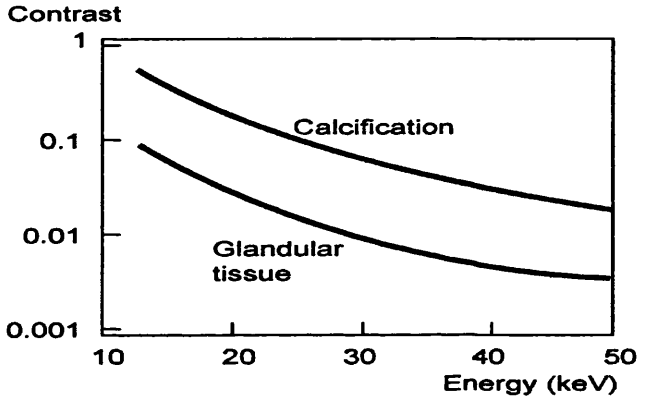

Figure 1.4.2: The contrast of glandular tissue and calcifications against photon energy (website 7).

The sensitivity of mammography is as high as 91.4% (Brem et al 2003), which out performs any other imaging modality for breast cancer detection and is the reason why mammography is so widely used in screening programmes. Its specificity, however, varies across studies with a typical value being 72% (Bone et al 1997) which means that roughly 1 out of 4 benign lesions are diagnosed as suspicious leading to unnecessary biopsies. The sensitivity of mammography for younger women is lower than that for older women. Younger women have denser breasts and less adipose (fatty) tissue (see chapter 1.3). Adipose tissue provides a greater contrast to calcifications than denser fibrous tissue and so mammography is more successful. It is for this reason, combined with the risk associated with using ionising radiation in mammography, that the screening of younger women is a controversial topic and in general is not performed (Dershaw 2000; Kerlikowske et al 1993; Kopans 1994; Kopans 1999; Miller 2003; Tabar et al 2003).

There have been several recent advances to improve x-ray mammography including digital mammography and computer aided detection (CAD) (for further details see Appendix C) but at present due to their high expense and limited improvement (if any) to cancer detection rates neither are yet in widespread clinical use.

1.4.1.3 Screening mammography

Mammography is the only approved screening technique for breast cancer. It is suitable for this purpose because of its very high sensitivity and fast image acquisition time. In a breast screening examination the breast is imaged both in the craniocaudal and mediolateral directions so that the whole breast can be imaged.

A typical x-ray mammogram is shown in figure 1.4.3 with a malignant region highlighted. This image indicates the difficulty involved in interpreting such images. Typical features to look for are clusters of white dots that can indicate calcifications or contrast regions that exhibit finger-like structures into the surrounding tissues. To aid in such interpretation it is common to compare the mammogram with a previous mammogram and look for changes. Comparisons are also made with a mammogram of the opposite breast.

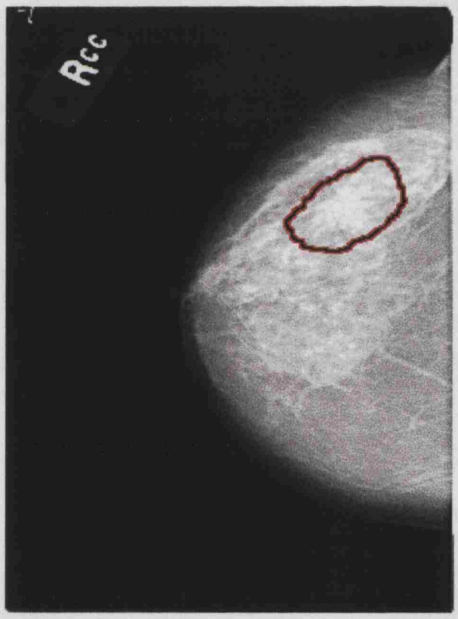

Figure 1.4.3: A mammogram indicating a malignant lesion.

1.4.1.4 Summary

The advantages and disadvantages of x-ray mammography are summarised in table 1.4.1

Advantages	Disadvantages
Good resolution (Säbel et al 1996) – micro calcifications are easy to see.	Uses ionising radiation and so is potentially harmful.
High Sensitivity (91.4% (Brem et al 2003))	Sensitivity is not 100%.
Quick imaging time allows many women to be scanned in one screening session	Interpreting mammograms can be difficult due to differences in the appearance of the normal breast for each woman
	Specificity is relatively low for some tumour types
	Sensitivity is lower for women with dense breast tissue (e.g. younger women)
	Breast implants can affect the accuracy of mammography, as silicone implants are not transparent to X-rays.

Table 1.4.1: The advantages and disadvantages of x-ray mammography.

1.4.2 Magnetic resonance imaging (MRI)

1.4.2.1 Theory

The nuclei of some atoms have a property known as spin. Such nuclei act like tiny current loops and consequently generate a magnetic field M (or magnetic moment), along the spin axis. Under normal circumstances these moments have no fixed orientation so there is no overall magnetic field. If, however, an external magnetic field, B_o, is applied they will align in given directions dictated by the laws of quantum physics. In the case of hydrogen nuclei (a proton), which is the most abundant nuclei in the human body, two discrete energy levels are created: a lower energy level in which the magnetic moment has a component parallel to the magnetic field, E_1 and a higher energy level where the magnetic moment has a component anti-parallel to the external magnetic field, E_2. These energy states are illustrated in figure 1.4.4. In equilibrium slightly more nuclei are found in the lower energy state E_1 and so a net magnetisation is created, which is aligned parallel to the applied field B_o. Increasing the applied magnetic field can increase this net magnetisation and so MRI devices employ strong magnets with fields in the range of 0.5 to 3.0 Tesla.

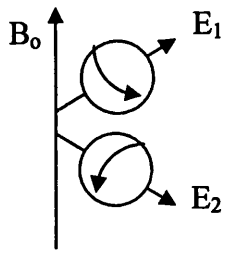

Figure 1.4.4: The two possible energy states of a hydrogen nucleus within a magnetic field.

As the moments are not exactly aligned with the magnetic field they steadily precess about it with an angular frequency (ω) that is directly proportional to B_o (Pope 1998).

$$\omega = \gamma B_o ,$$

(1.4.2)

where γ is the gyromagnetic ratio.
This can be expressed in terms of frequency as:

$$f = \frac{\gamma B_o}{2\pi}.$$

(1.4.3)

This is known as the Larmour frequency and for a hydrogen nucleus is 42.57 B_0 MHz, where B_0 is given in units of Tesla.

In order to detect a signal using MRI a second magnetic field is introduced, B_1 as a radio frequency (rf) pulse. This field is applied perpendicular to B_o and is at the Larmor frequency. Appropriate radio frequency coils are used to transmit B_1, which acts to tip the spins out of alignment with B_o. The nuclei are then forced to precess in phase with the rf pulse. If the pulse is applied for long enough the spins are flipped into the transverse plane and so a '90° RF' pulse has been applied. After the rf pulse is applied the nuclei still precess in phase and so induce a current in the MR coil (either the same one or a different one). Eventually the nuclei will relax back to their original energy state. The induced current that is detected will thus decay, but the way in which this happens will depend on the type and surroundings of the nucleus. This information is used to produce an image.

The signal in MRI arises from the rotating magnetisation, but it decays due to two different relaxation processes. First, is the spin-lattice relaxation. This is due to the return of the relative

populations of spin states to their original (non-equal) distribution. Some nuclei lose energy to their molecular environment, which allows them to switch from E_2 to E_1. The consequence of this is that the magnetisation returns to its original orientation. The time taken for this relaxation to occur is characterised by a constant known as T_1. The second relaxation process is the spin-spin relaxation. This is due to individual nuclear moments no longer rotating in phase with one another. Instead they will rotate at slightly different speeds and eventually point in random directions meaning that the net magnetisation perpendicular to B_o is zero. This can be caused by local variation in the strength of the field B_o. During spin-spin relaxation, the detected signal decays over a period of time characterised by T_2. However, the spins are also subject to inhomogeneities in the magnetic field B_o causing the signal to decay faster than the 'natural' T_2. Thus the term T_2^* is often used.

Some of the signal can be obtained by what is known as the spin-echo. This involves the application of a further RF pulse which causes the spins to be flipped by 180°. This means that the phase-position of each spin has been inverted and so nuclei that were precessing faster are now behind spins that were precessing at a slower rate. At the echo time T_E, the spins will catch each other up and a peak in the signal will be detected. The signal at this point is smaller than the original peak as only the decay due to T_2^* is recovered.

One of the advantages of MRI is that it has very good soft-tissue contrast. It is also easy to manipulate the contrast to highlight specific features. In a typical image acquisition a basic sequence (i.e. the 90° -180° -signal detection) is repeated hundreds of times. By altering the echo time (T_E) or repetition time (T_R), i.e. the time between successive 90° pulses, the signal contrast can be altered or weighted. For example if a long T_E is used, differences in the T_2 times of tissues will be highlighted. Tissues with a long T_2 (e.g. water) will take longer to decay and their signal will be greater (or appear brighter in the image) than the signal from tissue with a short T_2 (e.g. fat). Similarly, T_R governs T_1 contrast. Tissue with a long T_1 (e.g. water) will take a long time to recover back to B_o, and so using a short T_R will make this tissue appear dark compared to tissue with a short T_1 (e.g. fat). If T_E and T_R are chosen to minimise both these weightings, the signal obtained arises only from the number or density of spins in the tissue. Such images are said to be 'proton-density weighted' (PD). The different weightings are summarised as follows:

- T_2-weighting requires long T_E, long T_R
- T_1-weighting requires short T_E, short T_R
- PD-weighting requires short T_E, long T_R

For a quantum mechanical description of MRI imaging see (Webb 1993). A classical overview is given in (Keevil 2001).

1.4.2.2 MRI of the breast

In a breast MRI examination the patient is positioned on a special table as shown in figure 1.4.5. A benefit of MRI is that it can easily acquire direct views of the breast in any orientation while mammography requires re-orientation of the breast and mammography system for each view desired. An MRI exam of the breast typically takes between 30 and 60 minutes (website 1).

Figure 1.4.5: A photograph of a breast array coil (Seimens Medical) for MRI breast examinations (website 1).

1.4.2.3 Diffusion and Perfusion MRI

Diffusion and perfusion MRI are relatively new procedures (Sinha et al 2002). Diffusion MRI measures the mobility of water protons whereas perfusion MRI measures the rate at which blood is delivered to tissue. Both of these factors vary in malignant tissues as compared with benign tissue so can be used as an indicator for cancer.

1.4.2.4 Contrast Agents

The injection of a contrast agent can further the ability of MRI to detect a specific feature or, in the case of dynamic contrast-enhancement MRI, study the functionality of tissue. The contrast agents used are paramagnetic agents with gadolinium (website 1) (Gd-DTPA) being the most common. The effect of this agent is to shorten the relaxation time of local spins causing a decrease in signal in T_2 weighted images and an increase in T_1 weighted images.

The increased vascularity of tumours produces a preferential uptake of contrast agent and the technique can be used to improve their contrast from surrounding normal tissue. Furthermore if MRI scans are repeatedly acquired following the contrast injection, the dynamic nature of contrast uptake can be examined, which may improve the differentiation of benign and malignant disease. This is called dynamic contrast-enhancement MRI.

1.4.2.3 Summary

Advantages	**Disadvantages**
Can be used on women with denser breasts	Expensive
Non-ionising	Requires injection of a contrast agent for functional imaging.
Can take images in any orientation.	Specificity can be limited.
Highly sensitive to small abnormalities.	Cannot image calcifications.
Can determine multi-focal cancers.	Can induce feelings of claustrophobia
Useful in determining if the cancer has spread to the chest wall.	Long scan times in comparison to x-ray mammography.
Could be used to check for recurrence of cancer in women who have undergone lumpectomy.	
MRI can assess if a newly inverted nipple is a sign of retroareolar cancer.	
Can see breast implants and ruptures	

Table 1.4.2: The advantages and disadvantages of MRI as a breast-imaging device.

1.4.3 Ultrasound

Ultrasound is defined as a frequency of sound above the threshold of human hearing (i.e. > 20 kHz). The frequency range used in medical ultrasound imaging, is 1 – 15 MHz. This allows wavelengths less than 1 mm to be measured and so produces good spatial resolution. Ultrasound waves interact with tissue in a variety of ways but it is the reflection and transmission at interfaces between tissues of different acoustic impedance that is utilised in medical imaging. If there is a large acoustic mismatch between two tissues then a large fraction of the ultrasound intensity will be reflected. If there is a small difference in the acoustic impedance then most of the intensity will be transmitted. The time between pulse generation and the detection of an echo provides the depth of the reflecting interface, and thus images can be generated. Measuring the magnitude and time difference between different reflected signals can be used to determine the type, depth and size of different tissues (Hughes 2001; Pope 1998).

Ultrasound pulses are generated and detected by a hand-held transducer, based on an array of small piezoelectric crystals (figure 1.4.6). The very low acoustic impedance of air means that any boundary between air and tissue results in a near 100% reflection, so to ensure that the

ultrasound waves are coupled into the body an impedance matching gel is used between the breast and the transducer.

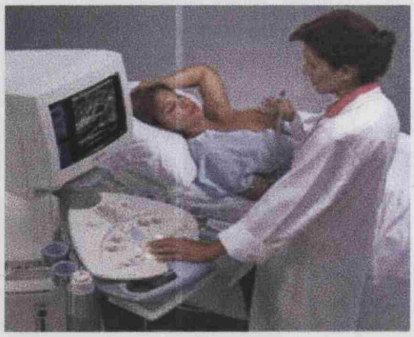

Figure 1.4.6: A breast ultrasound scan (website 1).

As there is a large difference between the acoustic impedance of a liquid filled cyst and normal breast tissue, around 23% of the ultrasound wave is reflected at such a boundary, making this technique particularly useful for the diagnosis of such a lesion. The small differences in acoustic impedance between adipose tissue and glandular tissue mean that this technique is of particular use for younger women with denser breasts, where x-ray mammography is often unsuitable (Houssami et al 2003).

1.4.3.1 Doppler ultrasound

Doppler ultrasound utilises Doppler shifts from Rayleigh backscattered ultrasound waves to determine the velocity at which red blood cells are moving. Doppler ultrasound can be used to monitor blood flow and so can be an indicator of vascularisation of a malignant tumour in the breast.

1.4.3.2 Summary

Advantages	**Disadvantages**
Excellent contrast resolution, which means suspicious areas are easy to differentiate from normal tissue	Lacks fine detail
Can be used for younger women and women with breast implants	Cannot always detect micro calcifications
Entirely safe, and can be used regularly	Effectiveness depends on the ability of the technician
	Cannot differentiate between certain solid masses
	Poor ability to see deep lesions.

Table 1.4.3: The advantages and disadvantages of using ultrasound to image the breast.

1.4.4 Nuclear Medicine Breast Imaging (Scintimammography)

Nuclear medicine breast imaging or scintimammography is sometimes used alongside x-ray mammography in the diagnosis of breast disease as it has the ability to determine if a located lesion is malignant (website 1). Nuclear medicine imaging involves injecting a radioactive tracer into the patient. The tracer emits radiation, which is detected using a gamma camera. Appropriate image reconstruction algorithms enable the distribution of the tracer within the body to be reconstructed. Since the tracer accumulates differently in malignant and benign tissues it can be used to distinguish between the two.

A nuclear medicine investigation of the breast usually takes between 45 and 60 minutes. To perform an exam the radioactive tracer (Tc-99m sestamibi) is injected into the patient's arm. The patient is then asked to lie face down on a special table and suspend her breast through a hole. Approximately five minutes after the injection, images of the breast are taken from several angles using a gamma camera.

An example of a nuclear medicine image of the breast is shown in figure 1.4.7 b). In this case an abnormal breast mass was discovered in the right breast of a 40 year old woman. The x-ray mammograms showed extremely dense breasts and no suspicious masses or calcifications. The technetium sestamibi images, however, showed focal uptake in the right breast in the area of the palpable mass. A breast biopsy was then performed and the pathology results showed the lesion to be an infiltrating ductal carcinoma (website 1).

a)

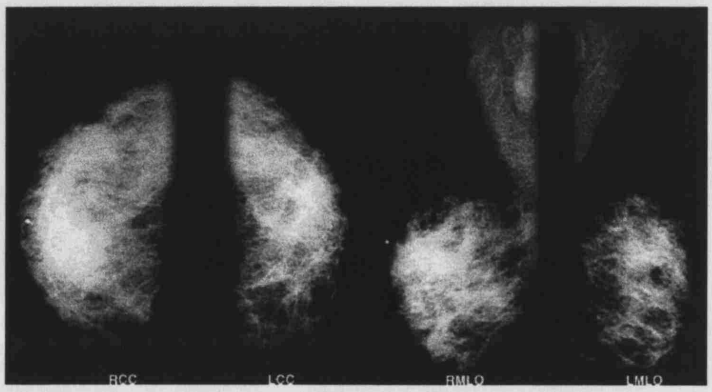

b)

Figure 1.4.7: The a) x-ray mammogram and b) scintimammogram of a woman with an infiltrating ductal carcinoma. In this case the lesion was seen in the scintimammogram but not in the x-ray mammogram.

1.4.4.1 Summary

Advantages	Disadvantages
Can be used on patients with dense breasts.	Ionising radiation
Is able to determine multifocal breast cancers	Involves injecting a substance into a patient (invasive)
It can image large palpable lesions that do not appear using other imaging modalities.	Whilst it is 90% accurate for abnormalities over 1cm it is only 40- 60% accurate for smaller abnormalities.
It can be used to test tissue remaining from a mastectomy	Long examination time
It can be used to check for metastases in the auxiliary lymph nodes	

Table 1.4.4: Advantages and disadvantages of Nuclear medicine

1.4.5 Developing breast imaging techniques

Along with optical imaging there are other emerging imaging modalities being developed in the hope of filling the potential niche left by the limitations of x-ray mammography and other conventional imaging modalities described previously.

1.4.5.1 Thermography

Thermography is based on the principle that metabolism and blood vessel proliferation in both pre-cancerous tissue and the area surrounding a developing breast cancer is almost always higher than in normal breast tissue. As described in section 1.3.2 developing tumours increase circulation to their cells by enlarging existing blood vessels and creating new ones in a process called vascularisation. This process frequently results in an increase in regional surface temperatures of the breast. Thermography uses ultra-sensitive infrared cameras and PCs to generate high-resolution diagnostic images of these temperature variations.

Although thermography is an appealing method of screening for breast cancer, research over the past 20 years has failed to produce a system that is reliable for such a purpose and so thermography is not widely used (Belliveau et al 1998; Gros et al 1980; Keyserlingk 1997; Nyirjesy 1986). Advances such as computerised thermal imaging may provide significant improvement in the cancer detection rate but this remains to be seen. It should also be noted that attenuation of infrared radiation in tissue is high. For this reason thermography will only

ever be able to provide information on the surface temperature variations and so no depth information is available. This is a severe limitation of thermography in detecting breast cancer.

1.4.5.2 Electrical Impedance Tomography (EIT) and T-scan

Electrical Impedance imaging is based on the idea that tissues have different conductivities depending on their cell structure and pathology. Cancerous tissue causes alterations in the intracellular and extra cellular fluid compartments, cell membrane surface area, ionic permeability, and membrane associated water layers. These histological biochemical changes within the cancerous tissue give rise to measurable changes in tissue electrical impedance. When a small alternating current is placed across the breast, the increase in electrical conductance and capacitance of the cancer tissue distorts the electric field within the breast and the resulting impedance map can be used to highlight a malignant area (Jossinet 1996; Radai et al 1999).

1.4.5.2.1 T-scan

A T-scan is a simple device that utilises measurements of electric impedance to distinguish between benign and malignant lesions. A T-scan measures low-level bioelectric currents to produce real-time images of the electric impedance properties of the breast. It is proposed that a T-scan used in addition to x-ray mammography can increase the specificity of a diagnosis (website 1).

There are currently 36 T-scan centres worldwide. A T-scan imaging system is similar in size and appearance to an ultrasound system. During a T-scan 1.0 to 2.5 mA of AC electrical current are generated by the system and conducted through the body via a metallic wand that is held by the patient. The scanning probe is then moved over the breast, and the current at the surface is measured. This information is then used to reconstruct an image, which is immediately displayed on a computer screen. A gel is used between the skin and the scanning probe to improve the conductivity.

The T-scan produces images of the electrical impedance profile of the breast in real-time and displays them as a 256-level grey scale map of capacitance and conductivity. The image is divided into 9 sectors on a 3 x 3 sector matrix and targeted electrical impedance views may be recorded using an anatomical screen. The only white object that should occur in T-scan examination of a normal breast is the nipple. Skin marks such as moles, insect bites, or recent

biopsy locations can also show as bright spots and must be annotated by the operator so they are not confused with cancerous abnormalities. Under normal conditions, the nipple image should be the same size and symmetrical for both breasts.

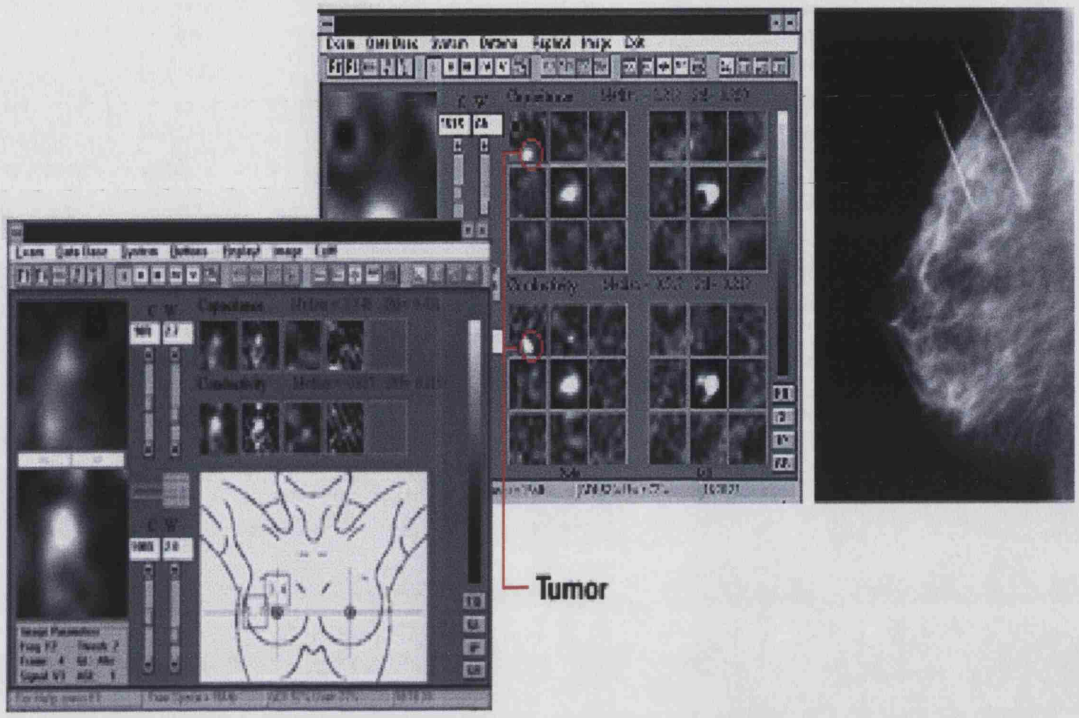

Figure 1.4.8: A clinical example of a t-scan. The left hand images show the screen for a t-scan during an investigation, with the right hand image showing a mammogram of the same breast (website 1).

A clinical example of the use of a T-scan is shown in figure 1.4.8. In this case the x-ray mammogram showed evidence of microcalcifications and a 10 mm tumour in the upper, outer quadrant of the right breast (right hand image in figure 1.4.8). The T-scan images show bright spots in the upper, outer quadrant of the right breast, corresponding to the microcalcifications and mass seen in the mammogram. The white focal spot in the centre of each display corresponds to the patient's nipple. A biopsy performed after the mammography and T-scan confirmed that the lesion seen was an invasive ductal carcinoma and ductal carcinoma in situ.

T-scans are becoming more widespread in conjunction with x-ray mammography. The technique employs relatively small and inexpensive devices and can detect small cancers down to 1 mm. The limitations of T-scans are that depth information is not available, microcalcifications cannot be detected, they cannot be used on patients with pacemakers, and they are less sensitive to larger tumours. The sensitivity and specificity of the T-scan have not yet been fully investigated, although a preliminary trial quotes values of 78% and 53 % respectively (Tetlow et al 2000). The rate of false positives appears to be associated with

hormone levels in the blood and so can be affected by time since menstruation and the use of hormone replacement therapy.

1.4.5.2.3 EIT

EIT uses the same principles as a T-scan but utilises a number of measurements obtained by applying different current distributions to reconstruct an image of the electric impedance of the whole breast. The quantities measured by EIT (i.e the voltage and current at certain points on the breast) are related to the electric impedance at low frequencies via the Laplace equation:

$$\nabla \cdot \sigma \nabla \phi = 0,$$

(1.4.4)

where σ is the conductivity, and Φ is the potential. The solution of the Laplace equation, in practise, is very sensitive to noise in the measurements and so normalisation techniques are used. Most in-vivo images produced so far use linearised, approximating techniques which attempt to find a solution for a small change in resistivity from a known starting value. Until recently, this change in resistivity was measured over time, and so EIT images displayed physiological function. Anatomical images have now been produced using the same reconstruction technique, but by imaging changes with frequency (Osterman et al 2000).

1.4.5.2.4 Summary

The advantages of using electric impedance devices are that they are much smaller and cheaper than other imaging modalities and use non-ionising radiation. Also in principle it is possible for EIT to produce thousands of images per second. Its limitations have been seen to be a low resolution and a large variability of images between subjects. Thus except for the simple T-scan case, electric impedance techniques are still undergoing further research and development before they become widely used (website 4).

1.4.6 Other Breast diagnostic techniques

1.4.6.1 Fine Needle Biopsy

If a breast lesion appears to be suspicious or is undefined following examination using the imaging methods described then the patient will undergo a biopsy. There are two degrees of biopsy: fine needle aspiration cytology (FNAC) and core biopsy. In a FNAC a fine needle and syringe are used to obtain a small sample of cells from the suspicious area. If this sample is insufficient or the diagnosis remains inconclusive a core biopsy may be needed which requires a

larger needle to remove a larger sample of cells. In both cases the procedure is painful and involves the extraction of potentially diseased tissue through healthy tissue. Hence the desire for a non-invasive imaging techniques with greater specificity that can reduce the need for biopsy.

1.4.6.2 Visual qualitative examinations

One of the primary methods for detection of breast disease is self examination, with 80 % of breast lumps first being detected by the individual or their partner (website 1). The first diagnosis and inspection used by a doctor is also a visual and tactile inspection. This along with described symptoms and subsequent images contribute towards the final diagnosis.

1.4.6.3 Ductal Lavage

It is estimated that over 95% of breast cancers begin in the cells lining the breast ducts. Ductal Lavage involves analysing cells that have effectively been washed out from the breast ducts using a breast pump (or aspirator). The cells are studied under a microscope to determine whether they have malignant characteristics before they develop into breast cancer. This technique is still in its experimental stages and is a similar idea to the Pap smear used to test for cervical cancer (website 1).

1.4.7 Summary

At present x-ray mammography is the most common breast imaging technique and is the only technique used for routine screening. The reason x-ray mammography has become the "gold-standard" for breast imaging is that it has a remarkably high sensitivity and is able to detect very small tumours and calcifications. The main limitations of x-ray mammography are that it has a poor specificity for some tumour types and that it is unsuitable for use on women with dense breasts. In addition, x-ray mammography uses ionising radiation and usually causes considerable discomfort to the patient. Thus there is potential for an alternative technique to replace x-ray mammography or to be used as an additional resource to improve the overall specificity of the diagnosis. As discussed MRI, ultrasound and Nuclear medicine are currently used to provide additional diagnostic information, but all have their limitations and are certainly not contenders to replace mammography. Other techniques are currently being investigated such as EIT and thermography but as yet these have severe limitations in resolution and specificity. Thus there still remains a niche for an additional imaging modality to aid in the detection and diagnosis of breast disease.

1.5. The Development and Current state of Optical Imaging of the Breast

1.5.1 General optical imaging geometries

1.5.1.1 Near infrared spectroscopy

Near infrared spectroscopy (NIRS) is the most straight-forward method to determine the optical properties of tissue. It involves placing a light source onto the surface of the tissue and detecting the diffusely reflected light via a fibre/ detector placed some distance from the source. As described in chapter 1.2, measurements made in this manner can be used to determine the concentration of different chromophores such as oxy (HbO_2) and de-oxy (Hb) haemoglobin within tissue (Yodh et al 1995).

NIRS was originally employed to measure the Hb and HbO_2 concentrations of in-vitro blood samples. It was later developed as a means of measuring in-vivo arterial haemoglobin oxygenation (known as oximetry measurements). The first oximetry measurements were used to measure the oxygenation of pilots in unpressurised cockpits during the second World War (Severinghaus 1986). The next breakthrough came in the 1970's with the development of the pulse oximeter. Pulse oximeters measure the change in light attenuation, usually across the fingertip or ear, due to arterial blood volume changes across each cardiac cycle. If light at two different wavelengths are used then absolute arterial haemoglobin saturation values can be obtained. NIRS is now used in a variety of clinical studies such as investigation of acute brain injury, strokes, autonomic failure and sleep disorders in adult brains (Leung et al 2002). One particular area of interest is to monitor the cerebral oxygenation in the newborn infant. A stylised representation of NIRS in use on a baby's head is shown in figure 1.5.1 a). Figure 1.5.1b) shows the changes in [HbO_2], [Hb] and total haemoglobin concentration measured during delivery. The measurements were taken by placing optodes against the foetal scalp and recording data using the continuous intensity Hamamatsu NIRO 500 instrument. The results show the changes in the foetal brain during the transition from foetal to postnatal life and also show periodic changes due to uterine contractions (Peebles et al 1992).

a)

b)

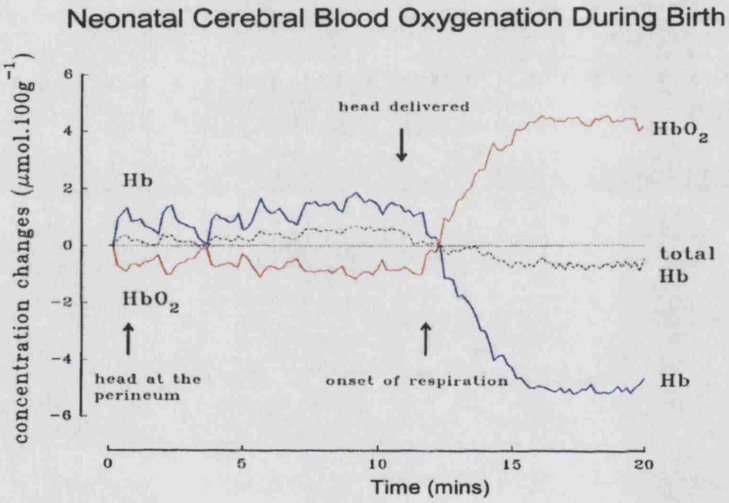

Figure 1.5.1: a) a source and detector placed on a babies head to perform optical spectroscopic measurements. b) The global HbO_2, Hb and total Hb concentration changes in a baby's head during labour measured using optical spectroscopy.

A further application of NIRS is to correlate changes in chromophore concentrations with the stimulation of a particular region of the brain (e.g. the motor or visual cortex). This is known as localised functional NIRS.

NIRS has been widely employed to determine the optical properties of breast tissue (Cerussi et al 2001b; Kang et al 1993; Peters et al 1990). This can either be performed in vitro on a sample of tissue or in vivo by the means of a fibre on the skin or inserted down a needle during surgery. Various studies involving these techniques are described in depth in section 1.2.5. One focus of work in this area has been spectroscopic investigation of breast tissue in vivo to study the physiology of the breast and the dependence of optical properties on hormonal status, and age.

These investigations use time-domain (Cubeddu et al 2000), frequency-domain (Cerussi et al 2002) or continuous wave (Quaresima et al 1998) (see section 1.5.2) instrumentation and many wavelengths to determine tissue composition. Additionally, (Tromberg et al 2000) have shown that near-infrared spectroscopy can be used to characterise known lesions situated close to the surface of the breast by using a hand held probe.

NIRS can accurately determine the optical properties of a homogenous sample of tissue, although it only provides globally averaged values when applied to heterogeneous tissues.

1.5.1.2 Optical topography

Optical topography involves acquiring multiple reflectance measurements at small source-detector separations over a large area of tissue simultaneously or in rapid succession. The absorption and scatter for each source detector pair are determined and constructed into a matrix. The matrix can then be used to create a map of the HbO_2 and Hb concentrations of the tissue directly beneath the array. The penetration depth of detected light depends on the distance between the sources and detectors with a typical depth of sensitivity being about half the source detector distance. Thus close source and detector pairs tend to sample only the surface layers of an object. When using distant source and detector pairs, however, the light must travel further through the tissue and so experiences greater attenuation leading to a lower signal. Therefore a compromise must be made when selecting appropriate optode spacing. Typically topographic systems employ optode spacings of the order of a couple of centimetres (Koizumi et al 2003; Strangman et al 2002). Topography is therefore used in situations where there is likely to be a change in optical properties close to the surface of the body e.g. mapping changes on the surface of the brain due to stimuli (Hebden 2003; Peña et al 2003), or imaging tumours on or just beneath the skin. Figure 1.5.2 shows a topography system developed by Hitachi employed to measure signals originating within the brain. Physical movement such as a finger tapping exercise stimulates the motor cortex causing an increase in the local arterial blood flow and increase in oxygen consumption. The two mechanisms provide opposing effects on the concentration of HbO_2 and Hb but in adults an overall increase in [HbO_2] and decrease in [Hb] is typically seen (Villringer et al 1993).

Figure 1.5.2: A topography system attached above the motor cortex region of the brain (website 6).

The main disadvantage of this method is that it only provides surface maps with no depth information. However it may be of significant use in imaging women with small breasts or in imaging the male breast where other imaging devices are inappropriate (see chapter 1.4).

1.5.1.3 Optical tomography

Optical tomography again uses multiple sources and detectors only in this case they are placed in such a manner that sampling can occur across the whole volume of the tissue. Two alternative source and detector arrangements for tomography of the breast are illustrated in figure 1.5.3. The slab geometry is most commonly used in combination with compression of the breast as will be discussed later in section 1.5.4.1. In the second arrangement, data is acquired between sources and detectors arranged in one or more rings around the breast and generally all detectors acquire data simultaneously for each source.

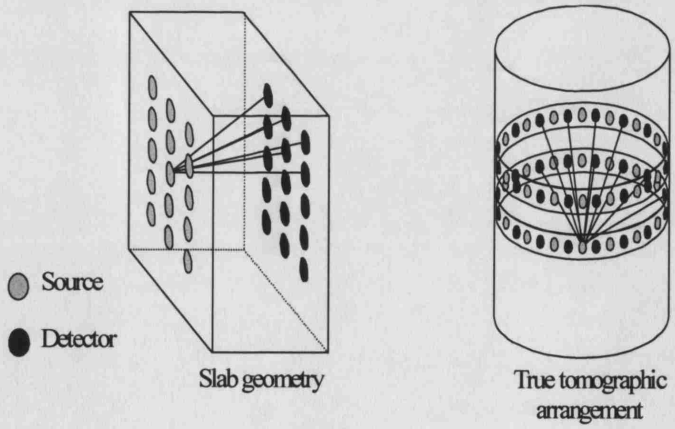

Figure 1.5.3: Different source and detector arrangements in optical tomography (Hillman 2002).

Acquiring data for one source position at a time increases the overall scan time, which may result in movement artefacts or prolonged discomfort for the patient. The main advantage of

using this technique is that structural and functional information can be gained about the whole volume of the tissue (e.g. a brain or breast) and so diagnosis is not limited to features near the surface.

1.5.2 Optical instrument types.

Researchers have built, and begun clinical evaluations of a variety of different optical imaging systems. Some groups (He et al 1990; Jiang et al 2003; Nioka et al 1997; Schmitz et al 2001) have developed optical tomography systems that perform straightforward intensity measurements. Other groups (Culver et al 2003; Francheschini et al 1997; Grosenick et al 1999; Kaschke et al 1994; Pogue et al 1997; Schmidt et al 2000) have followed a more technically complex approach using time and frequency domain systems to measure the characteristic response of tissues to illumination by pulsed and intensity modulated sources, respectively. The following section introduces the various different systems and discusses their merits and disadvantages.

1.5.2.1 Continuous intensity instruments

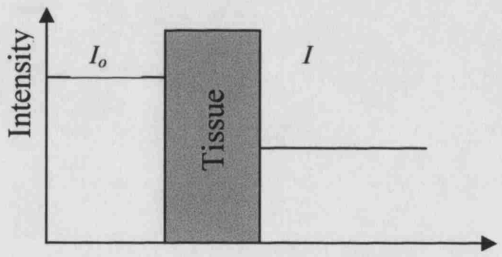

Figure 1.5.4: An illustration of the measurements made by continuous intensity instruments.

Continuous intensity instruments measure changes in attenuation by recording the change in the intensity of light leaving the tissue surface (Jöbsis 1977). Intensity measurements alone are insufficient to distinguish between changes in absorption and scatter (Arridge et al 1998). A common approach to overcome this is to assume that scatter is homogenous throughout the tissue and estimate its average value. The average distance travelled by the photons (the pathlength) through the tissue is then estimated and thus the absorption can be derived from the measured decrease in intensity.

There are several different ways to determine the pathlength. If we have an arrangement involving a simple monochromatic source at a fixed source-detector spacing then we can define an effective optical pathlength (differential pathlength (*DP*)) such that:

$$DP = -\frac{\delta \ln I}{\delta \mu_a} .$$

(1.5.1)

The *DP* is related to the geometrical pathlength (inter-optode spacing) d by the differential pathlength factor (*DPF*) (see equation 1.2.11). If the *DPF* is known and can be assumed to be constant over a narrow wavelength range, it is possible to determine the absorption. If the absorption is determined at two or more wavelengths, depending on the number of chromophores, then it is possible to determine changes in chromophore concentrations.

A common way to perform continuous intensity measurements is to use a fibre coupled CCD spectrometer. If the water concentration of the tissue is known accurately it is possible to use spectral measurements and the known optode spacing to determine the optical pathlength. This allows the absorption coefficients at multiple wavelengths to be derived simultaneously and so the functional state of the tissue under study can be determined (chapter 1.2). However, the scatter will be dependent on the wavelength used and so the assumption that scatter is constant may introduce significant errors. The absorption and therefore the pathlength also have a wavelength dependence, which makes the method of solving for chromophore concentrations non-linear. A significant advantage of CW measurement devices is their speed, with a CCD spectrometer being able to operate at up to 100 Hz.

Continuous intensity measurements can be made using any geometry. The continuous wave CCD spectrometer has also been adapted to perform measurements on multiple channels, to enable tomography to be performed (Schmitz et al 2000). If the technique is extended to several source and detector pairs then, by using several spectral measurements, it is possible to separate μ_a and μ_s' by fitting data to a light transport model.

The limitations of continuous intensity measurements are that the pathlength must be determined and, as with other methods, the signal to noise ratio is limited by the thickness of the tissue, placing a limitation on the results that can be achieved in performing optical tomography of large volumes.

1.5.2.2 Frequency domain

Lakowicz developed the first frequency domain instrument in 1990 (Lakowicz et al 1990). A frequency domain measurement involves using a light source that is intensity modulated at radio frequencies (rf) (Chance et al 1998). Using an intensity modulated light source enables a

measure of the average time taken for light to pass through tissue to be extracted as well as a measure of the emerging intensity. This requires that we measure the phase shift between the original signal and the transmitted signal (figure 1.5.5). The scatter and the absorption of the tissue will have separate affects on both the measured intensity and phase shift of the transmitted signal. Therefore, by measuring both the amplitude and phase difference of the signals, we can separate absorption and scatter without requiring a priori knowledge of the pathlength unlike in the continuous intensity case.

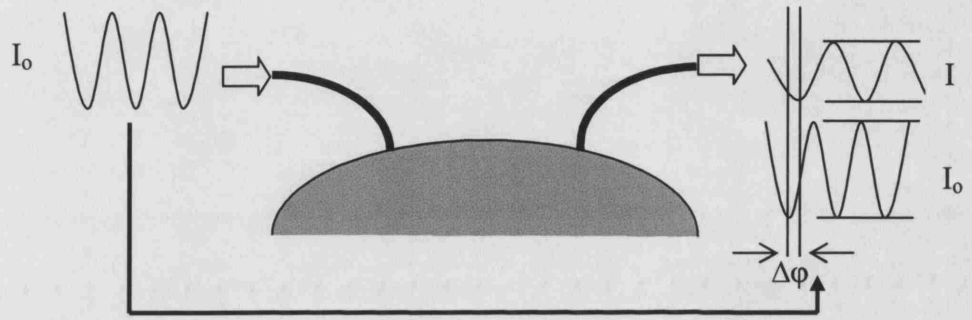

Figure 1.5.5: An illustration of the amplitude and phase measurements made with frequency domain instruments (Hillman 2002).

The sensitivity to absorption and scatter, and the spatial resolution of the system is dependent on the frequency chosen. Frequencies of around 100 MHz are most commonly used and can usually be achieved using laser diodes. The frequency bandwidth of the detectors is also important and in general PMTs or photodiodes are used.

In order to use several wavelengths to determine the chromophore concentration, the tissue is illuminated serially by each wavelength. This adds to the overall scan time and also could introduce errors if the object/tissue has altered significantly between each wavelength acquisition.

1.5.2.3 Time – resolved instruments

Time – resolved measurements may be made by illuminating the tissue with a very short (ps) pulse of light and measuring the time of flight for each individual photon travelling between the source and the detector. A histogram of the times of flight, or temporal point spread function (TPSF), can then be generated (figure 1.5.6a). Various datatypes can be extracted from a TPSF, such as the mean flight time or integrated intensity. The integrated intensity is the same as a continuous intensity measurement. A measured TPSF contains a range of information and so provides a better measurement to characterise tissue than cw or frequency-domain methods.

The way in which a TPSF is influenced by both scatter and absorption is shown in figure 1.5.6b and 1.5.6c.

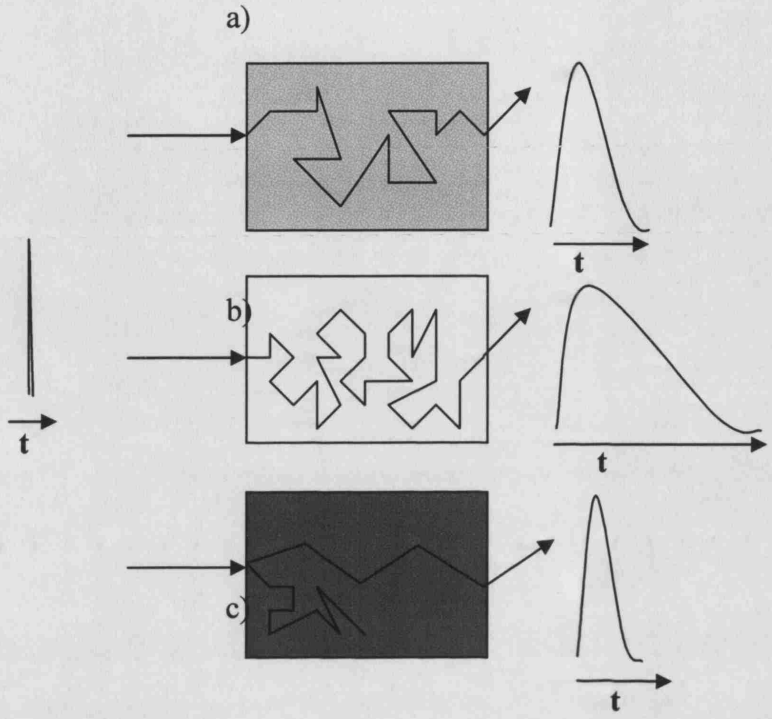

Figure 1.5.6: a) An illustration of a TPSF b) A scattering medium will cause the TPSF to broaden because on average the photons will have travelled further c) An absorbing medium will cause the TPSF to narrow because photons with longer paths are more likely to be attenuated.

One disadvantage of a time resolved system is that the instrumentation is expensive. For this reason time resolved systems are rarely used in spectroscopy or topography.

Frequency domain data can be obtained by calculating the Fourier transform of time-resolved measurements and so similar information can be obtained from both. However, time-domain measurements obtain data at all frequencies simultaneously.

1.5.2.3.1 Detection methods for time-resolved imaging

Detection methods for time-resolved imaging can be split into two categories:

1. The use of gating methods to isolate shorter flight time photons.
2. Methods in which the whole TPSF is recorded.

The principle behind gating methods is that photons with shorter flight times are more likely to have travelled in a direct line between the source and detector and therefore provide higher

spatial resolution. An in depth review of various gating techniques is given in (Hebden et al 1997). A simple technique involves using a collimator aligned co-axially with the incident beam. It effectively spatially filters the light leaving the tissue surface and so weakly scattered photons that exit the tissue at angles greater than a given threshold from the normal, are removed. A scanning laser beam system that employs a degree of collimated detection has been used in breast studies by (Kaneko et al 1989). Despite the fact that published results (He et al 1990) claimed a degree of detection of certain tumours the reported spatial resolution and specificity were poor. The spatial resolution of collimated detection is hindered by photons scattered back along the original line of sight. It is also only suitable for imaging tissue samples with a thickness of a few mm (Hebden et al 1990).

1.5.2.3.1.1 Analogue detection methods: Streak Camera.

A streak camera can be used to record the whole TPSF. In the streak camera the detected photons are converted into electrons by a photocathode. These electrons are then accelerated through two deflection plates that are subject to a variable applied potential so that they are scanned across a phosphor screen at the same frequency as the laser repetition rate. The phosphor screen can then be viewed using a CCD (charged coupled device) camera.

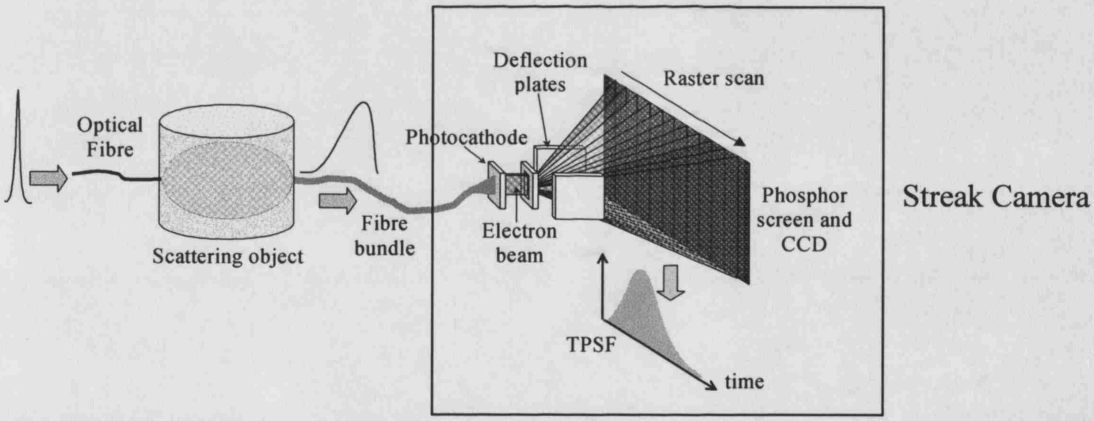

Figure 1.5.7: Schematic of a streak camera (Hillman 2002).

The positions at which the electrons arrive at the phosphor screen depend on the magnitude of the deflecting potential. Thus electrons in each scan reaching a particular horizontal position across the image will always have taken the same time relative to the input pulse. The TPSF is constructed by summing the values in each pixel column of the CCD after a sufficient number of scans. Illuminating the photocathode directly by the laser can create a reference pulse. This reference enables absolute flight times to be measured.

The streak camera is a popular method of temporal measurement, outside of tissue optics, due to its excellent temporal resolution, and has been used by (Mitic et al 1994) to obtain a series of in vivo measurements of TPSFs on the breast. However it does have certain disadvantages. Streak cameras are normally bulky and very expensive. They require a long acquisition time. They have a low dynamic range and require subjective gain adjustment. Finally, they have a small aperture size and so are inefficient. For these reasons the streak camera method is generally unsuitable for optical imaging applications.

1.5.2.3.1.2 Time correlated single photon counting (TCSPC)

In a time correlated single photon counting (TCSPC) system the arrival times of individual photons are measured in comparison to a reference pulse, by a device such as a time to amplitude converter (TAC). Such measurements are recorded for many photons, enabling a histogram to be built up representing the whole TPSF. An example of how TCSPC can be employed is shown schematically in figure 1.5.8. In this case a pulsed laser source at 80 MHz is incident on a tissue sample. Every incident pulse will emerge from the tissue as a broadened pulse. This broadened pulse is transferred to a fast detector that then detects a maximum of one single photon from each broadened pulse. The illumination is kept sufficiently low so that the probability of detecting two photons per pulse is negligible (usually $< 10^{-4}$). The signal corresponding to the detected photon is then converted into a digital pulse and the temporal delay between this pulse and a reference pulse, derived directly from the laser, is determined and recorded. After multiple laser repetitions a recorded histogram of flight times represents the full TPSF.

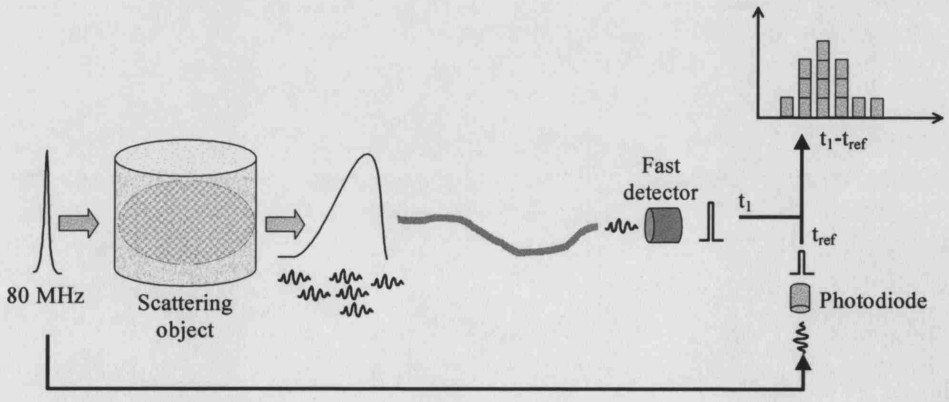

Figure 1.5.8: A schematic of a TCSPC system (Hillman 2002).

The advantages of a TCSPC system are that they have a very high dynamic range and excellent temporal linearity. Additionally, they usually employ PMT or MCP-PMT detectors, which have

the advantage of a large collection area. The main disadvantage of a TCSPC system is a comparatively low temporal resolution (typically of the order of tens to hundreds of picoseconds). The optical tomography system at UCL (Schmidt et al 2000) involves TCSPC and will be described in detail in chapter 1.6.

1.5.3The Development of optical breast imaging

Optical imaging of the breast is not a new concept and dates back to a paper presented by Cutler in 1929 (Cutler 1929). This describes an experiment which involved simple 'transillumination' by shining white light from a lamp through a pendant breast and viewing the absorption patterns on the other side. This first attempt revealed attenuation changes for tumours due to high vascularization, but also revealed similar changes for benign lesions that exhibited a high haemoglobin concentration. It was also seen in this very basic study that the images appeared blurred even for lesions located close to the surface of the breast due to the high scattering of light. Because no absorption quantification or high-resolution structural information was available, the method did not appear to offer sufficient specificity for clinical use.

Technological advances in the 1970s, specifically the development of video cameras able to observe light in the visible or NIR parts of the spectrum, revived an interest in transillumination of the breast. In 1972 the first differentiation between a benign and malignant tumour was made using a variation of this method. This technique was called diaphanography and malignant lesions were found to be more attenuating than the surrounding tissue or other lesions (e.g. some types of cysts) (Profio et al 1989). The contrast of lesions was seen to be improved by recording a photographic image using transilluminated light at NIR wavelengths (Ohlsson et al 1980). Furthermore it was discovered that most visible wavelengths did not penetrate the breast and so it was more appropriate to use wavelengths in the NIR region. Despite these advances the basic limitations encountered by Cutler remained. The resolution was still poor, and only very large tumours (or those near the surface) were detectable, and consequently conventional transillumination techniques yielded a low sensitivity and specificity. The sensitivity of transillumination was initially claimed to be as high as 96% by (Bundred et al 1987). This contradicted other studies that recorded sensitivities (Lafreniere et al 1986) as low as 60% (Brenner 1982; Drexler et al 1985; Sickles 1984). Hence transillumination is a poor competitor with other breast imaging modalities (see chapter 1.4).

Perhaps the biggest breakthrough in optical mammography came in the 1990s when further advances in source and detector technologies were combined with advances in computers and

computer algorithms that allowed the effects of scatter and absorption to be modelled and separated into distinct images. Such advances have led to the development of diffuse optical tomography (DOT). DOT uses measurements of diffuse light that propagates through tissue, between multiple positions on the surface, to yield three-dimensional tomographic images of the internal optical properties. Depending on the specific technique used, DOT has the potential to produce three-dimensional maps of absorption, scattering, blood volume, oxygenation and contrast agent uptake (in either fluorescence or absorption mode). DOT has many advantages over simple transillumination. First, it offers superior quantification, which could lead to an increase in the sensitivity. Second, the ability to produce independent absorption and scatter images provides additional diagnostic information. Third, it has the ability to produce three-dimensional images and so the spatial accuracy is improved. Finally, the resolution is improved due to the multiple-projection information. All these points are leading to a greater specificity and sensitivity being achieved.

1.5.4 Recent optical breast imaging systems.

Since the early 1990s, interest in so-called optical mammography has increased as many research groups entered the field. The first imaging systems were based on the frequency-domain approach using a single modulation frequency (Francheschini et al 1997; Götz et al 1998; Moesta et al 1998). More recent systems have investigated advances in time-correlated single photon-counting techniques. This has particularly been the case in the European consortium known as OPTIMAMM of which the work in this thesis has been a part. OPTIMAMM was established in 2000, and has involved nine research groups in six EU countries who have worked together to develop new optical techniques for imaging breast cancer, and specifying the optical properties of breast tissues, including tumours. The following summarises the instrumentation that is currently being developed and evaluated for optical mammography in various laboratories throughout the world.

1.5.4.1 Compression and scanning geometries

A geometry employed by several groups (Chance et al 1998; Durduran et al 2002; Grosenick et al 1999; Grosenick et al 2003; Li et al 2003; Pifferi et al 2003) involves compressing the breast and scanning one or more detectors and sources over the surface of the breast. The projected image is then reconstructed. This technique involves using the slab geometry described in section 1.5.1.3. The advantages of such a method are that the source and detector separations are kept to a minimum and the geometry is simple so reconstruction problems are reduced. Furthermore this geometry allows optical tomography to be combined directly with x-ray

mammography (Li et al 2003) so that the functional information available from optical images can be combined with the anatomical information derived from x-ray images. The present problem with such a combination is that optical tomography usually requires a longer scan time than is acceptable for the compression force used in x-ray mammography. Further potential problems with such a geometry are that a reduction in blood volume could potentially lead to a reduction in contrast, and that prolonged compression can produce significant discomfort (Morris et al 2003). There will also be a reduction in the spatial accuracy due to the deformation of tissue layers similar to that seen in x-ray mammography.

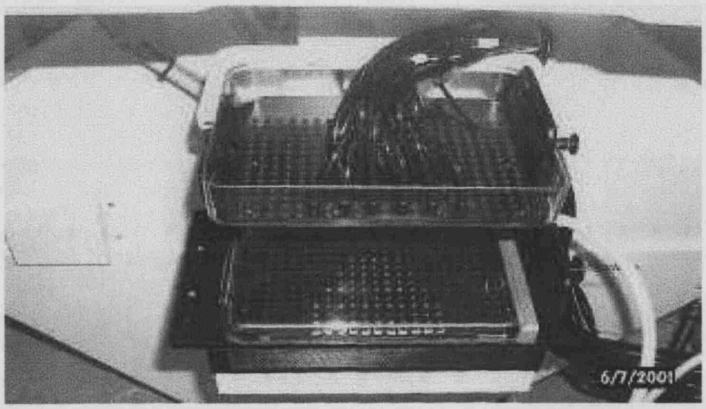

Figure 1.5.9: The compressed breast geometry as employed by (Li et al 2003).

OPTIMAMM partners in Berlin (Grosenick et al 2003) and Milan (Taroni et al 2004a; Taroni et al 2004b) both employ this technique. The laser pulse scanning mammograph developed in Berlin measures the times of flight of scattered photons through the breast at a large number of scan positions. As with all scanning geometries the breast is gently compressed between two parallel glass plates. The mammograph is equipped with two picosecond laser diodes (PDL-800, PicoQuant, Berlin) and images are recorded at 670 and 785 nm. Typically a step size of 2.5mm is employed allowing 1000-2000 scan positions, and mammograms are recorded in both the craniocaudal and mediolateral projections consistent with x-ray mammograms.

In Milan several versions of an instrument named MAMMOT (Mammograph for Optical Tomography) have been developed. In each version time-resolved measurements are collected from the breast placed between plane Plexiglass plates in the craniocaudal and mediolateral views, to produce projection images. The initial instrument included four pulsed diode lasers emitting at 683, 785, 913 and 975 nm. Continuous acquisition is performed and data is stored every 25 ms. More recent versions were developed to change the number and/or spectral position of the illumination wavelengths and to allow for technical improvements such as higher collection efficiency. Additional wavelengths investigated in subsequent MAMMOT systems

are 637, 656, 905, 916, 975, and 985 nm. The maximum number of wavelengths employed by any one MAMMOT system was 7. A significant feature of this work is that they are the only group to employ wavelengths above 900nm.

1.5.4.2 Other tomographical geometries

Other groups have developed more traditional tomographic geometries. For example, a group in Dartmouth (USA) has developed a frequency domain tomographic instrument. This employs three circular arrays of linear translation stages, holding 32 fibre bundles (16 sources and detectors) each that can be adjusted between diameters of 45 and 200 mm according to breast size (Pogue et al 1997). In this system six laser diodes emitting at 661, 761, 785, 808, 826 and 849 nm are used consecutively.

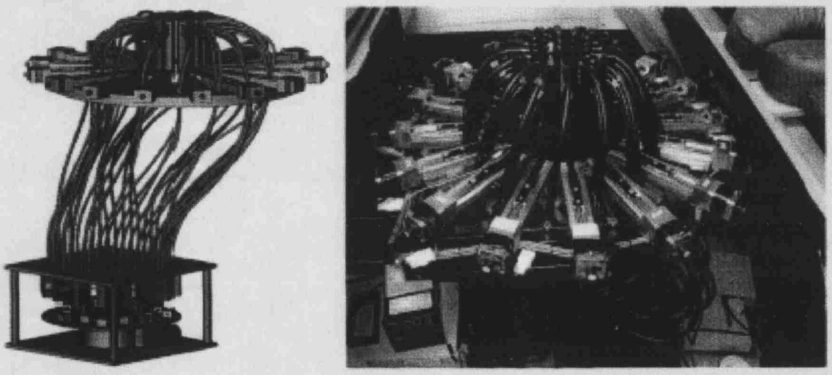

Figure 1.5.10: The experimental arrangement used by a group in Dartmouth, USA. This is a frequency domain instrument and utilises three linear translation stages to move the source and detector fibres into close contact with the breast (website 3 (Pogue et al 2004)).

Meanwhile a group at the Philips Research laboratory developed a system based on continuous wave measurements with the sources and detectors distributed around a conical shaped cup that was filled with a fluid. The highly scattering fluid overcomes problems associated with coupling the sources and detectors to the breast (Colak et al 1997) (figure 1.5.11). Their system employs a semiconductor laser source that operates at 680, 780 and 870 nm.

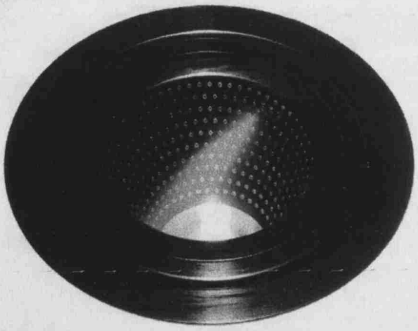

Figure 1.5.11: The cup used by Philips in their continuous wave instrument. This is filled with a coupling fluid during a scan (Philips Research laboratories 1997).

A group at SUNY (USA) have developed a CW system with interchangeable measurement heads for different basic geometries with the breast imaging head consisting of a folding hemisphere (Schmitz et al 2000; Schmitz et al 2001). This system employs two or more laser diodes operating in the 800 nm range. The basic device is now marketed by NIRX Medical Technologies (www.nirx.net).

At UCL we have developed a 32-channel time-resolved optical tomography instrument. As described in chapter 1.6 and part 2 the sources and detectors were initially connected around the edge of three interconnecting rings. Recently, this patient interface has been replaced, having adopted an approach similar to that of Philips where the fibres are connected to the outside of a hemispherical cup that is filled with a coupling fluid. The new configuration is discussed in more detail in part 3.

1.6 The MONSTIR System

1.6.1 System Description

The optical tomography instrument at UCL is known as the Multichannel Optoelectronic Near infrared System for Time resolved Image Reconstruction (MONSTIR) (Schmidt 2000; Schmidt et al 2000). This TCSPC -based system is designed to measure the times of flight of photons travelling through the tissue under study (see section 5.2.3.1.2). MONSTIR emits two interlaced picosecond pulses of light at 780nm and 815nm. These pulses travel through the breast and experience a series of scattering and absorbing interactions (as described in chapter 1.3). The emerging photons are collected by up to 32 detectors distributed across the surface of the breast. The times of flight for the emerging photons are then calculated relative to a reference pulse. For each detector a histogram of the times of flights for all the detected photons is generated in the form of a TPSF. It is the TPSF that provides the information that is used to reconstruct three-dimensional images of scatter and absorption as described in chapter 1.7. Figure 1.6.1 shows a schematic diagram of the MONSTIR system.

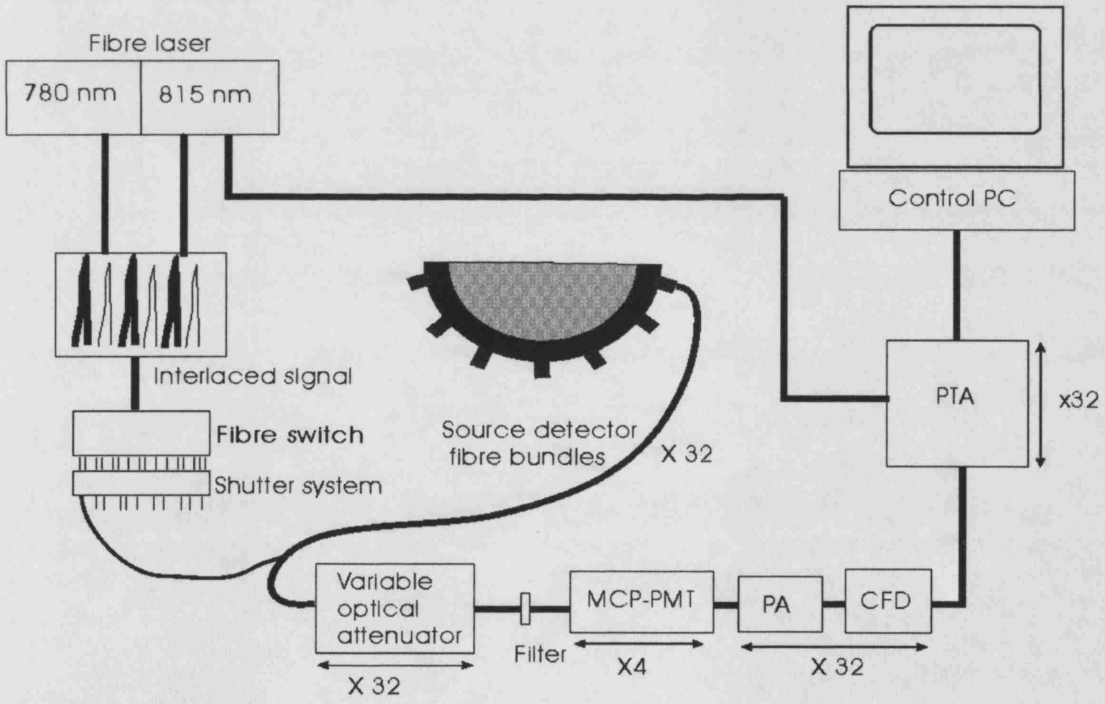

MCP-PMT – Micro-Channel Plate PhotoMultiplier Tube

PA- Pre-Amplifier

CFD – Constant Fraction Discriminator

PTA – Picosecond Time Analyser

Figure 1.6.1: A schematic diagram of the MONSTIR system.

1.6.2 Components of MONSTIR

A complete description of the MONSTIR system is given in (Schmidt et al 2000) and (Schmidt 2000). The following sections provide an overview of some of the more important features, some of which have been introduced/re-designed since these earlier descriptions.

1.6.2.1. Laser

The MONSTIR source was custom-built for the project by IMRA America, and consists of two fibre lasers driven by a single 40 MHz oscillator. It produces two laser pulses, at 780nm and 815nm, which are either interlaced or pulsed alternately as required. This is illustrated in figure 1.6.2.

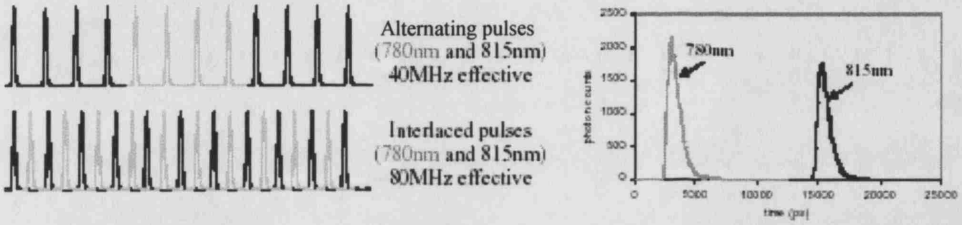

Figure 1.6.2: A representation of the two different operation modes of the fibre laser (Hillman 2002).

The maximum temporal window over which we can display a TPSF is determined by the interval between the pulses. If we collect light from both lasers simultaneously, this will be 1/80 MHz = 12.5 ns (i.e. the maximum temporal window to acquire two TPSFs, one at each wavelength is 25 ns).

The laser has a digital synchronisation output taken from either laser that can be used as a robust reference signal. This signal originates from a photodiode which is illuminated within the laser. The TCSPC electronics (see section 1.6.2.4) determines the interval of time between the photon detected by the MCP-PMT and the reference pulse from the photodiode.

1.6.2.2 Optical fibres

The laser pulses are transmitted down 32 source fibres to illuminate the breast. These multi-mode, graded index, fibres are multiplexed from the laser via a fibre switch (DiCon (Berkeley, CA) VX500). The transmitted light is then detected by 32 detector fibre bundles. The fibre bundles were designed to provide a larger collection area than that achievable using a single fibre, whilst ensuring a low temporal dispersion. Originally the source and detector fibres were

separate but could be coupled so that illumination and detection occurred at the same point on the surface. This allows optimal use of limited surface area and also provides an in-situ calibration technique (Hebden et al 2003)(see section 1.6.5). Second generation fibres have since been developed where the source is integrated permanently along the central axis of the detector fibre bundle. These coaxial bundles consist of a 62.5 / 125 μm graded index single source fibre, with a numerical aperture value of 0.275, which is sheathed by an inner ferrule of outer diameter 1.0mm. Tightly packed detector fibres with an outer diameter of 3.2 mm surround the source fibre and are contained within an outer ferrule. The whole unit is then sheathed in a protective plastic cover. The advantages of using these fibre bundles over the previous, separate fibres are:

- The collection area for the detectors has been increased from 2.5 mm to 3 mm and so the light collection is increased by 44%;
- The source profile is more evenly distributed as the source and detector share a common axis;
- The source fibres are protected within the surrounding bundles and therefore are less likely to become damaged;

The new fibre bundles are shown schematically in figure 1.6.3.

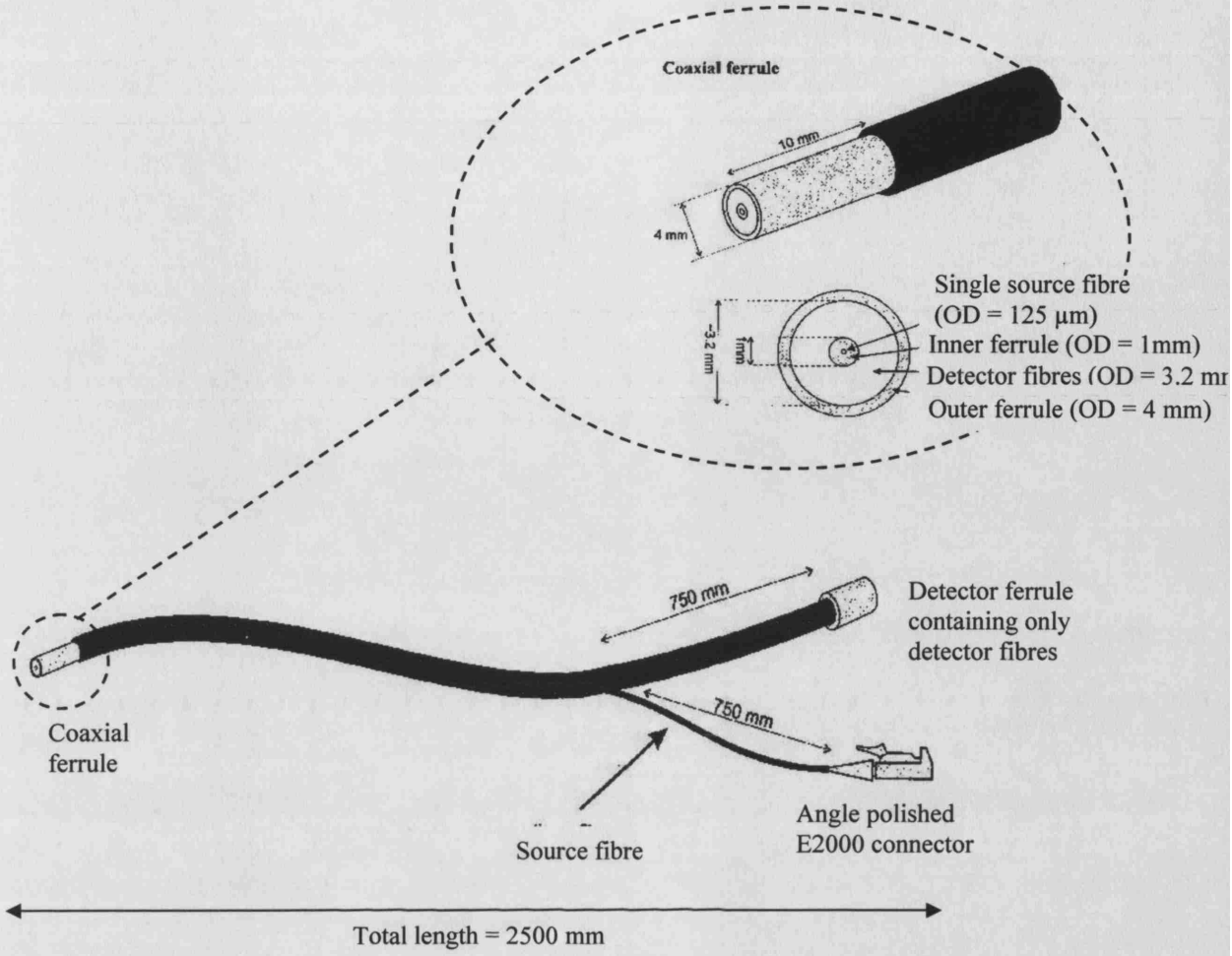

Figure 1.6.3: A schematic diagram of the coaxial fibre bundles.

In order to couple these fibres to the breast, connectors like the one shown in figure 1.6.4 were constructed from black, NIR absorbing plastic. As shown there is a gap of 12 mm between the surface of the tissue and the source. This is to allow divergence of the source so that a greater laser power can be used without exceeding safety limits for skin exposure.

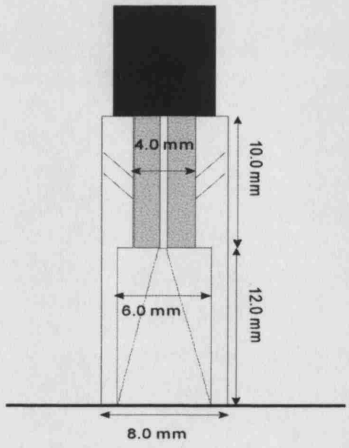

Figure 1.6.4: A Schematic diagram of the connector used to couple the coaxial fibre bundles to the breast.

1.6.2.3 Variable Optical Attenuators (VOAs)

Due to the attenuation of near infrared light through tissue, detected intensity falls off rapidly with increasing source – detector separation. Thus there is a large dynamic range of signal intensities incident on the detectors. This can lead to several potential problems:

- The pulse processing electronics have a maximum count rate of ~300 kcps and may saturate at very high-count rates;
- Excessive illumination levels may damage the MCP-PMT;
- Cross-talk between physically adjacent channels of the same 8-anode MCP-PMT may become significant if the corresponding count rates are very different.

For these reasons it is necessary to control the amount of light incident on the detectors. This is done through the use of variable optical attenuators (VOAs). The VOAs are thin blackened metal discs with a series of eight holes of different sizes etched around the edge as shown in figure 1.6.5. The largest hole allows all the light collected by the detector bundles to enter a 4 mm diameter polymer fibre that delivers light to the MCPs. The smallest hole allows the signal to be attenuated by ~ 10^2 (Schmidt 2000). Each VOA is mounted onto a stepper motor and is positioned between the incoming detector bundle and the polymer fibre. Each stepper motor can be pre-programmed to ensure the optimal VOA positions for a specific data acquisition. The information on the optimal positions is stored in what is known as an aquisition definition file (ADF). Prior to any data acquisition a small photoswitch is used to detect a reference hole in each disc to determine its orientation and so 'initialise' the position of the VOAs. The stepper motor then moves the VOAs relative to this point according to the positions stored in the ADF. In the case of a breast scan, the optimum VOA positions are calculated in advance using a conical resin phantom with properties of μ_a = 0.007 mm^{-1} and μ_s' = 0.8 mm^{-1}, (see chapter 2.2). The ADF file is generated automatically by illuminating each source in turn and systematically measuring the illumination at each detector with different VOA positions. The ADF file records the VOA position for each source detector combination that allows maximum illumination of the detector without exceeding a pre-defined maximum count rate (normally 150 000 cps). Ultimately it would be desirable to perform an ADF generation on the patient prior to performing the scan. However, this process would lengthen the overall time that the patient would be required to remain stationary to about 30 minutes, which would be unacceptable for most patients.

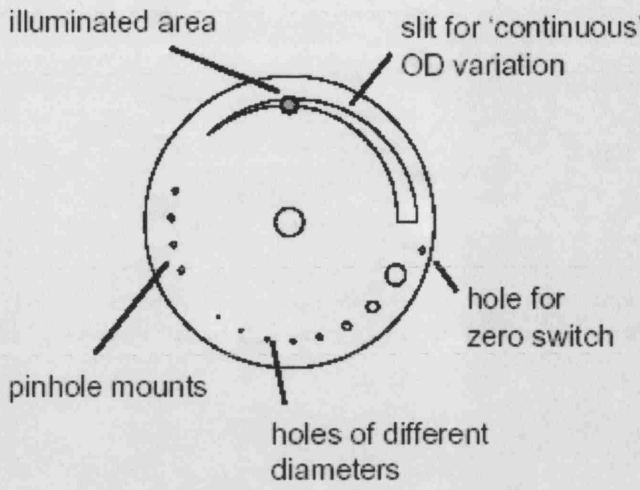

Figure 1.6.5: Diagram of a VOA (Schmidt 2000).

Another function of the VOAs is to set the transmission to zero when neccessary. This is essential for very close source and detector separations as they produce very high signal intensities and yet provide little or no useful tomographic information. In addition, all of the VOAs can be set to zero transmission to protect the MCPs from room light when an acquisition is not being performed.

One disadvantage of using a variable aperture to attenuate light from a fibre bundle is that specific fibres in the bundle will be preferentially selected when the aperture is small. As each fibre collects light from a different point on the surface of the tissue, only selecting light from a small number fibres may effectively move the position of the detector, thus producing a different temporal measurement across the tissue. A further disadvantage is that the VOA system is subject to slight variability in the alignment between the fibre bundles and the holes on the VOAs, and this can affect the repeatability of the attenuation produced. Additionally, movement of the VOAs to their correct position takes just less than one second per source position, which adds to the acquisition time and is more than is desirable for evoked response studies of the brain.

Alternative designs of VOA are currently being investigated to overcome these problems. These include using a) a distribution of microscopic pinholes (diameter ~ 10 μm) created using a YAG laser, b) attenuating filters based on photographic film, or c) arrays of dots printed on acetate (Jennions et al 2003).

1.6.2.4 Detectors and pulse processing electronics

A short single polymer fibre collects the light that passes through each VOA. It is then relayed to the photocathode of one of four 8-anode ultrafast microchannel plate photomultiplier tube (MCP-PMT) detectors via a visible light blocking long pass filter. The MCP-PMTs, which are supplied by Hamamatsu Photonics, were custom built for this application and have a lower temporal dispersion than conventional PMTs. Apertures in front of the MCP-PMTs ensure that illumination of the photocathode is only 5.5mm in diameter and $\geq$ 1.0 mm from the individual anode boundaries (Schmidt 2000).

The resulting analog electronic pulses are preamplified and fed into EG&G Ortec Model 935 quad 200-MHz Constant-Fraction Discriminator (CFD) units. Each CFD unit contains four separate and independently adjustable timing discriminators that convert the input analogue pulses into fast nuclear instrument module (NIM) logic pulses with high timing accuracy (Schmidt 2000). The CFDs determine the temporal position of the arriving pulse independent of its amplitude.

The fast NIM logic output pulse and the digital sync output pulse are then used by EG&G Ortec picosecond time analysers (PTAs) to measure the relative arrival time of individual photons. The measured photon flight times are automatically recorded and stored in histograms (TPSFs) by the picosecond time analysers. These are transferred to the control PC following illumination at each source position. There are, however, some features of the detectors and pulse electronics that must be taken into account as they may lead to errors in the final TPSF.

Detector cross talk occurs between the 8 channels of the MCP-PMTs. It has a magnitude of $\leq$ 0.3% in terms of count rate and is generally strongest between physically adjacent channels. There are two possible causes of this cross talk. These are electronic cross talk inside the MCP-PMT itself, and optical cross talk in front of, and possibly within, the window covering the photocathode. It should be noted that this problem becomes more significant if there is a large variation in the dynamic range of the detected intensities of physically adjacent MCP-PMTs.

1.6.2.5 MIDAS

A software package known as the MONSTIR Image Data Acquisition Software (MIDAS), written originally by Florian Schmidt and adapted by Adam Gibson, is used to control the hardware and data read-out of the MONSTIR system. MIDAS controls the data acquisition by

the use of the ADF. The ADF contains information on the required VOA settings, the exposure time and the order in which individual sources are to be illuminated.

1.6.2.6 Peltier Coolers

Peltier coolers are used to reduce dark counts in the detectors to a few events per second. They cool the MCP-PMTs to -25°C. Peltier coolers are heat pumps so one side will cool while the other side gets hot. It is important to remove this heat as it could cause damage to the MCPs and surrounding casing and it will affect the performance of the peltiers. In MONSTIR a water-cooling system is used to remove this heat by circulating water through all four MCP units before returning to a chiller unit. Failure to run this system whilst operating the peltiers could damage the peltier surroundings and units. In addition a leak in the system could cause substantial damage to the electronics in MONSTIR. For these reasons a system is used to monitor the flow of water.

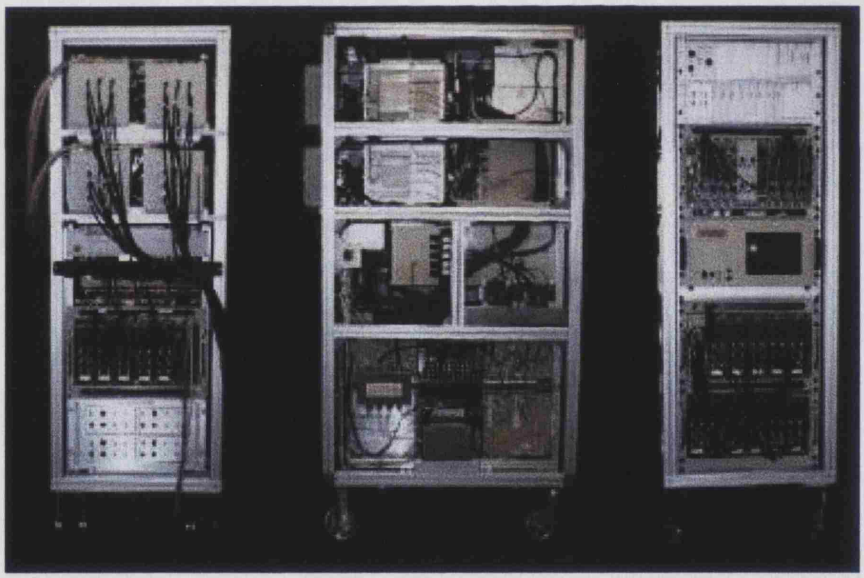

Figure 1.6.6: Photograph of the MONSTIR system. This shows the back, side and front view (from left to right)

1.6.3 Development of a clinical interface

Attaching the fibres onto the breast to produce meaningful data is not a trivial task. Different groups have attempted it in a variety of different ways as described in chapter 1.5. The design constraints on such a system are as follows:

1. The system must have a rigid geometry so that the precise locations of the sources and detectors are known for image reconstruction.
2. The sources and detectors should be placed in a uniform arrangement around the breast and across three dimensions. This enables optimum sampling of the breast.
3. The system needs to encompass a large range of sizes and shapes of breast. This means that it must provide good contact between the breast and all the source/detector bundles for every patient.
4. The system must provide maximum comfort given the constraints imposed.

1.6.3.1 Ring system

Our first patient interface consists of a series of three interconnecting rings that can be mounted into a frame. When all three rings are interconnected a conical shape is formed. This design was based on a system used for Electrical Impedance Tomography (EIT) studies (Holder D S 1995) where a vacuum pump was used to conform the breast to the shape of the cone. In this study the vacuum was not considered desirable, but it was hoped that a combination of the rings would produce geometries suitable for a wide range of patients. This system is described in depth in part 2.

Unfortunately during our studies it became apparent that combining two or three rings together is not a suitable geometry for the breast. For all the women that have been studied, it has only been possible to achieve constant contact around the breast by using just one of the rings. This limits the collection of data to one plane. It is important to image the whole volume of the breast to ensure that lesions are not missed. Sampling the whole breast also provides more information, including more extensive coverage of the background tissue, to enable a better comparison with the appearance of the lesion and the ability to determine further information on the location of the lesion relative to other anatomical features.

1.6.3.2 Thermoplastic design

One idea that was considered as an alternative to the rings was to have a range of rigid cups constructed from thermoplastic that corresponded to different bra sizes. The sources and detectors would be attached at known positions across the surface of the cup. Given that the bra size of a patient can be known in advance of a study, the appropriate cup can be selected. A prototype cup was made by coating a bra in adhesive (UniBond super PVA adhesive and sealer) and allowing it to dry into a rigid shape. This was then filled with plaster of Paris to create a mould of the bra shape. The plaster of Paris shape was then used to mould the thermoplastic

(illustrated in figure 1.6.7). This is a similar technique to that used by our group's parallel project, which involves imaging the neonatal head. In this project a helmet is constructed using thermoplastic for each individual baby, based on photographs taken of the infants head (Hebden et al 2002).

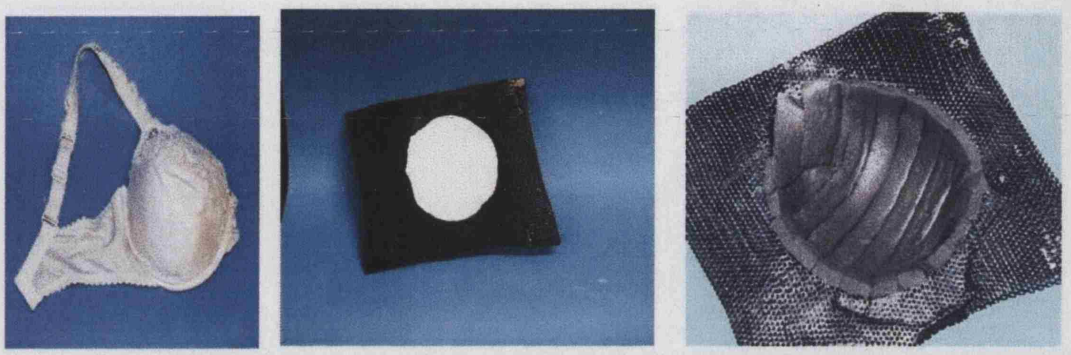

Figure 1.6.7: An individual patient interface modelled from a bra.

Although successful for imaging the irregular shape of a neonate's head, this technique was considered to be too complicated for use in breast imaging. The reconstruction would be more complex and less accurate using this geometry than if a simple standard shape could be employed.

1.6.3.3 3D liquid coupled system

Currently under development is a new coupling mechanism that will hopefully overcome some of the limitations associated with the ring system. The new system is based on the approach adopted by Philips (Hoogeraad et al 1997) which employs a container filled with a coupling liquid and the sources and detectors are attached around the surface of the container. The development of this system is described in detail in part 3. It consists of a plastic hemisphere to which the source and detector bundles are attached by means of small plastic tubes. Highly scattering windows are attached to the end of each tube to provide a diffuse light source. The windows also enable a watertight seal to be achieved.

1.6.4 Data noise characteristics

As with all imaging systems the data produced by the MONSTIR system is subject to various sources of noise. During its development care was taken to optimise the temporal stability and to minimise the sources of noise as much as possible (Schmidt et al 2000). However a certain

amount of temporal drift and noise are to be expected. The principal causes of noise that can affect a TPSF are listed and discussed below.

1.6.4.1 Background noise

There is inherently always some temporally un-correlated noise measured on all TPSFs due to thermal noise within the MCPs, electronics, and incident room light. Cooling the MCP-PMTs to -25°C reduces the magnitude of this 'background' noise by reducing dark counts within the MCPs.

1.6.4.2 Cross talk

Light leakage into the deactivated channels of the fibre switch is quoted to be $<10^{-8}$ by the manufacturers. The light leaking into a given source fibre can then migrate directly into the corresponding detector bundle via reflection off the surface. Although this so-called source cross-talk is small, light from the active source can be attenuated by tissue by at least a factor of 10^6 for large source-detector separations, and so this leakage can have a significant effect on the signal recorded, manifesting as a pre-peak before the main TPSF. The occurrence and magnitude of this pre-peak is determined by the source-detector pair in use, the intensity delivered by the particular source and the amount of attenuation across the object being imaged. To reduce this effect an auxiliary bank of fibre shutters, which provides an additional factor of 10^4 attenuation for each source fibre, has been introduced. This system is shown in figure 1.6.8.

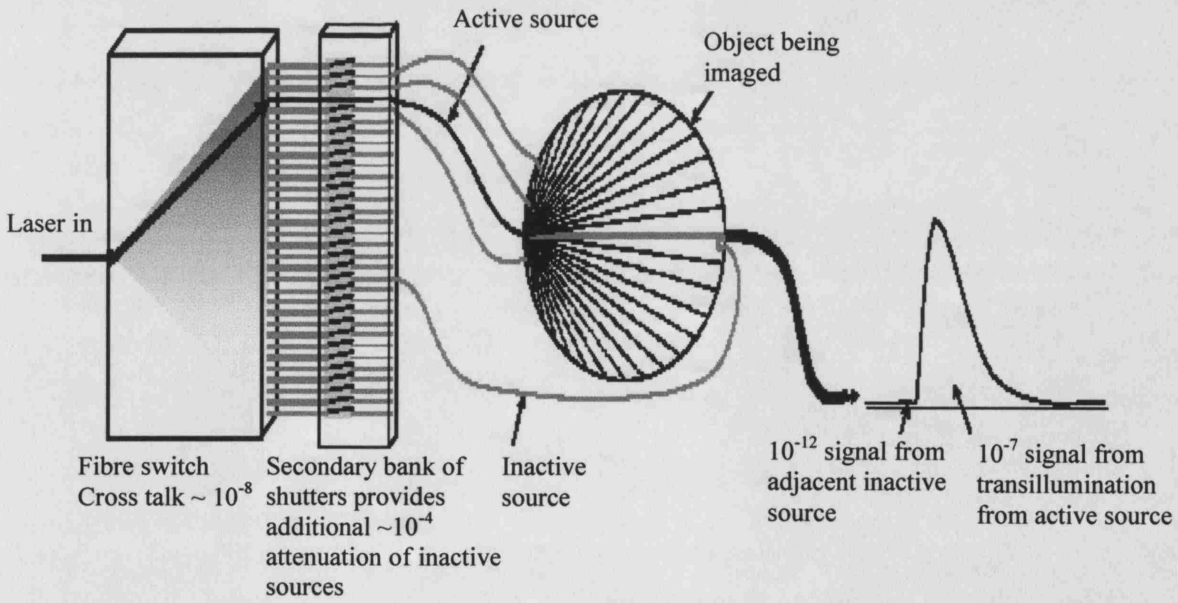

Figure 1.6.8: The shutter system introduced to reduce the amount of light reaching the object via inactive sources (Hillman 2002).

A further form of cross talk in the MONSTIR system is that occurring between neighbouring detector bundles coupled to one single MCP unit. This was described in section 1.6.2.4.1 and occurs as light leaks from one channel into a neighbouring channel. This appears as a superposition of the TPSFs of the adjacent detector channels and the magnitude of this effect is dependent on the relative intensities of the TPSFs for each detector.

1.6.5 Calibration methods

The impulse response function (IRF) of a system is the output obtained when the input is a delta function. For MONSTIR the IRF can be assumed to represent the measurement of a TPSF when a source and a detector bundle are in direct contact with each other and the input is a perfect delta function of laser light. The IRF will be different for each source-detector pair and will convolve with any signal measured by the system thus influencing the measured TPSF. For further details see (Hillman 2002). As described above the measured TPSF also contains features that are a result of various noise mechanisms. All these temporal characteristics will be different for each individual source-detector measurement and will also vary over a period of time. It is possible to eliminate the variability over time, to a large degree, by performing appropriate temporal calibration measurements immediately before or after each data acquisition. The variations between separate source-detector measurements arise due to differences between the lengths and dispersion properties of detector and source fibre bundles and electronic cables, and between the pulse-sampling characteristics of electronic components. Appropriate calibration techniques can also be employed to reduce these source-detector effects.

Originally data calibration was achieved through the use of a so-called calibration tool consisting of a clear resin cylinder in which a small scattering target is embedded, attached to an optical fibre. This technique described by (Hillman et al 2001) allowed both the differences in source fibre properties and detector characteristics to be measured. So-called source calibration involved illuminating the target using each source fibre in turn, with a single detector coupled to the target, whereas for detector calibration a beam of pulses is delivered to the target and the emitted light is collected with each detector bundle simultaneously. Additionally an absolute calibration measurement was required to perform a full temporal calibration of the experimental data. This was obtained by recording a single TPSF when just one source was connected directly to one detector.

The main disadvantage of this method was that it required the sources and detectors to be transferred from the object under investigation to the calibration phantom. This can be

extremely time-consuming and so calibration of temporal instabilities would be affected. Instead a method involving in situ calibration was developed.

The new method was inspired by an approach reported by (Eda et al 1999) where an assumption is made that the measurement of the time of arrival of the back-reflected pulse (using co-axial fibre bundles) is a good approximation for the mean flight time measured if the source and detector were held in contact. For MONSTIR this assumption was extended to the entire shape of the TPSF and thus providing a way to acquire 32 absolute calibrations measurements. This required the use of the new coaxial source detector bundles and the connector described in section 1.6.2.2. The absolute calibration measurements are obtained by illuminating each source in turn and measuring the light reflected at the surface of the object using the corresponding detector. The illuminating power is attenuated for this measurement to a few picowatts (or a few tens of millions of photons per second). After further reduction due to the detection efficiency of the system, this provides a few thousand detected counts per second, depending on the reflectivity of the surface.

In practise this method of measuring the absolute temporal response corresponding to a given source-detector pair requires two assumptions to be made. First, that the light entering the detector bundle uses the same transmission modes in the fibres as those used by diffuse light detected during an imaging experiment. This can be reasonably assumed if the surface is a diffuse reflector. Second, that the detected signal is dominated by reflection occurring at a flat air/object boundary, and is not significantly influenced by scattering within tissue beneath the surface.

To obtain the total temporal calibration it can be shown (Hebden et al 2003) that the calibrated TPSF for source n and detector m, $T_{n,m}$ can be acquired from the measured TPSF $M_{n,m}$ as follows:

$$T_{n,m} = (M_{n,m} * S_m) \otimes (A_m * S_n) \qquad (1.6.1)$$

where S_i represents a source calibration measurement for source i, A_j represents an absolute calibration measurement for source j and detector j coupled together, * represents a convolution operation and $\otimes$ represents a deconvolution operation.

Thus it is necessary to perform a source calibration as well as the absolute calibration described above. This is performed using the calibration tool and so requires the sources to be set up

separately. The source calibration allows for differences in the lengths and dispersing properties of the source fibres to be taken into account. Fortunately these properties do not vary significantly over time (unless the fibres are repaired or replaced) and so it is only necessary to acquire a source calibration occasionally. A detailed discussion of this in situ calibration method is given in (Hebden et al 2003).

1.6.6 Data Types

As described in previous sections the data extracted from MONSTIR is in the form of a series of TPSFs. In theory the whole TPSF could be used directly in image reconstruction, although it would be very computationally intensive, and it is also likely that there would be some redundancy in using this method. Instead we extract characteristic datatypes from the TPSF and use these for the reconstruction. In figure 1.6.9 the common datatypes are illustrated. These are the mean flight time, integrated intensity and variance (about the mean). These datatypes are used, as they are generally the most robust in the presence of noise as described in 1.6.5, and in combination they provide good differentiation between absorption and scatter. They have also been shown to be effective in simulated reconstructions (Arridge et al 1993; Schweiger et al 1999). In general, meantime and intensity are most often used since meantime and variance hold very similar information, and variance is more susceptible to noise. Intensity, however, has been shown to be very sensitive to surface coupling (Arridge et al 1998) and so can generally only be used in difference imaging, as described in section 1.6.7, where the unknown coupling coefficient will cancel if it is constant for successive measurements.

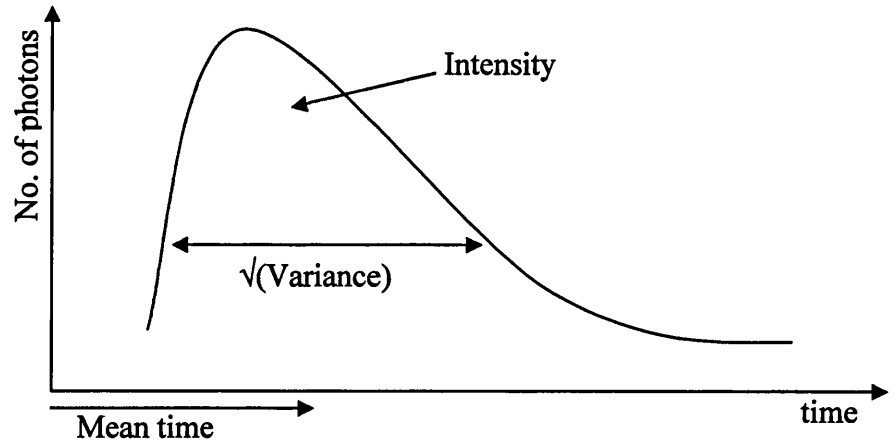

Figure 1.6.9: The common datatypes extracted from a TPSF for image processing.

The extraction of these datatypes is summarised in (Hillman et al 2000). If we define the discrete data acquired by MONSTIR as *y(t)* then we can express the more common datatypes in the following manner:

$$Intensity[y(t)] = \sum_t y(t) \tag{1.6.2}$$

$$Meantime[y(t)] = \frac{\sum_t y(t) \times t}{\sum_t y(t)} \tag{1.6.3}$$

$$Variance[y(t)] = \frac{\sum_t y(t) \times [t - < t >]^2}{\sum_t y(t)} \tag{1.6.4}$$

1.6.7 Difference imaging

An alternative approach to calibration is to perform difference imaging which involves reconstructing the differences between the optical properties of the object of interest and those of a suitable reference medium. The reference medium will either be a homogenous phantom with similar properties to the object being imaged, the object itself with a change imposed (e.g. the breast in a different state, a liquid phantom with and without a suspended object) or the same object imaged at a different wavelength.

Reference measurements are frequently used in optical tomography as the most simple image reconstruction techniques, such as linear reconstruction, rely on differences between measurements made on the object under study and those of a similar object or the same object in a different state (see section 1.7.6.5). A further advantage of difference imaging is that systematic contributions and model errors usually cancel and additional calibration measurements are unnecessary as shown below.

We can make the assumption that the IRF of a particular source-detector combination does not change between object and reference measurements and so any data acquired with that source and detector pair would be affected by their unique IRF. Thus if we acquire data on both an object and a reference object with the same source and detector we will effectively acquire the following two expressions:

$$y_1(t) = D_1(t) * I(t) \tag{1.6.8}$$

$$y_2(t) = D_2(t) * I(t),$$

(1.6.9)

where y_1 represents the measured TPSF and D_1 represents the true TPSF for object 1, y_2 and D_2 represent the equivalent parameters for object 2, and *I(t)* represents the system IRF. As described in 1.6.6 we can express the datatypes commonly extracted from a TPSF via discrete summations expressed by equations 1.6.2 and 1.6.3.

From these equations we can derive simple relations between transformed convolved functions for meantime and intensity as follows:

$$Meantime[y(t)] = \frac{\sum_t y(t) \times t}{\sum_t y(t)} = \frac{\sum_t D(t) * I(t) \times t}{\sum_t D(t) * I(t)}$$

(1.6.10)

and also show that

$$Meantime[y(t)] = Meantime[D(t)] + Meantime[I(t)]$$

(1.6.11)

and

$$Intensity[y(t)] = \sum_t y(t) = Intensity[D(t)] \times Intensity[I(t)] \ .$$

(1.6.12)

Therefore if we extract the meantime and intensity for both an object and a reference object we can use the ratios between the two and the relations given in 1.6.13 and 1.6.14 to derive the following expression:

$$\frac{Intensity[y_1(t)]}{Intensity[y_2(t)]} = \frac{Intensity[D_1(t)] \times Intensity[I(t)]}{Intensity[D_2(t)] \times Intensity[I(t)]} = \frac{Intensity[D_1(t)]}{Intensity[D_2(t)]}$$

(1.6.13)

In practise our calculations are based on the log intensity and so

$Log(Intensity[y_1(t)]) - Log(Intensity[y_2(t)]) = Log(Intensity[D_1(t)]) - Log(Intensity[D_2(t)])$

Whereas, for meantime:

$Mean[y_1(t)] - Mean[y_2(t)] = (Mean[D_1(t)] + Mean[I(t)]) - (Mean[D_2(t)] + Mean[I(t)])$

$= Mean[D_1(t)] - Mean[D_2(t)]$

(1.6.14)

In both cases the *I(t)* terms cancel and so by measuring such differences we can obtain the real differences without the need for calibration. It should be noted however that the values obtained relative to the reference medium are not absolute values for the object being studied. This means that an accurate determination of the reference properties is required in order to estimate the object values. In general, however, difference imaging produces fewer systematic artefacts than absolute imaging with the calibration techniques described earlier.

The ideal reference for optical imaging of the breast is still the subject of ongoing investigations. Possible approaches for difference imaging include:

- Using a solid phantom with similar properties to the breast and a similar geometry (e.g. a conical phantom);
- Recording data for the breast in two different states such as before and after the injection of a contrast agent such as ICG;
- Employing a liquid coupled device where the breast submerged in liquid is measured relative to the device filled with liquid alone.

The first approach has been employed successfully for imaging phantoms as the reference phantom can be made with exactly the same geometry and background properties as the object phantom. When imaging the breast, however, this method may introduce errors due to a mismatch in optical properties and geometry. If this mismatch is great, linear reconstruction will almost certainly fail. Non-linear reconstruction will attempt to reconstruct these large differences, but the values obtained are likely to be inaccurate as a result.

Various groups are investigating the second approach (Hawrysz et al 2000; Ntziachristos et al 2002). The advantage of this technique is that the reference will have exactly the same geometry, properties and structure as the object, except for the areas where the contrast agent is concentrated. If the contrast agent is preferentially absorbed by a malignant lesion as opposed to a benign lesion, then this method may prove to be useful in the diagnosis of breast disease. However, the disadvantages of using a contrast agent such as ICG are that the technique then becomes invasive, and the scan time for the patient is increased as the breast must be scanned twice, so it is unlikely that this could be used for screening programs. A potential non-invasive technique is to increase the blood volume in the breast through a global temperature rise, but this requires investigation.

The third approach has been used previously by (Colak et al 1997) and is to be discussed in detail in part 3. This approach benefits the reconstruction in two significant ways. First, the exterior geometry of the reconstructed volume is known exactly, so an accurate model can be generated. And second, the coupling of the source-detector optics at the surface is constant and independent of the subject. Its disadvantages are that sampling must be performed over a larger volume than necessary, the effects of a refractive index mismatch between the breast and the liquid are unknown, and that the technique is messy for routine clinical use.

1.7 Image Reconstruction

Image reconstruction is based on the solution of both the inverse and forward problems (sections 1.7.7.4 and 1.7.7.1). For other imaging modalities such as those involving x-rays the path of the radiation can be assumed to be linear and so simple back projection techniques can be employed (Webb 1993). A common method is to employ the Radon transform (Barret et al 1981). Imaging involves recording a series of 1 dimensional projections of the object at different angles (such as those taken in a CT scan). A 1-D projection at an angle θ, $g(\theta)$, can be defined as the line integral of the image intensity, $f(x,y)$, along a line that is a distance s from the origin and at angle θ:

$$g(\theta,s) = \int_l f(x,y)dl \qquad (1.7.1)$$

The collection of $g(\theta,s)$ at every angle θ is the Radon transform of the image $f(x,y)$. Inverting the transformation enables, $f(x,y)$ to be recovered, e.g. by filtered back projection.

Such techniques, however, fail to describe the forward problem for optical tomography due to the scattering nature of photons as described in chapter 2. Instead an alternative method must be employed. Recent reviews of image reconstruction in optical imaging are given in (Arridge 1999; Kohlemainen 2001; Schweiger et al 2003). The following sections give a summary of the main principles involved.

1.7.1 Radiative Transfer Equation

The radiative transfer equation (RTE) describes the transport of particles through a medium (Arridge et al 1997; Patterson et al 1992). The radiative transfer equation is a balance equation describing the change of energy radiance in time due to changes in energy flow and so can be derived by considering the gains and losses to the specific intensity, $I(r,\hat{s},t)$ for photons travelling from point r in direction $\hat{s}$ at time t (figure 1.7.1).

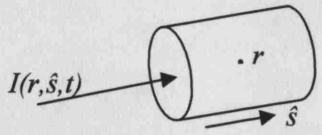

Figure 1.7.1: The specific intensity $I(r,\hat{s},t)$ for photons travelling from point r in direction $\hat{s}$.

The factors which reduce the specific intensity in a small volume around r are:

$\frac{1}{c}\frac{\partial I(r,\hat{s},t)}{\partial t}$ — the number of photons entering the volume minus the number of photons leaving it per unit time,

$\hat{s}\cdot\nabla I(r,\hat{s},t)$ — the photon flux at r at time t travelling in direction ŝ,

$(\mu_a+\mu_s)I(r,\hat{s},t)$ — the attenuation of light from the volume of interest,

whereas the factors which lead to an increase in the specific intensity are:

$\mu_s\int_{4\pi}p(\hat{s},\hat{s}')I(r,\hat{s}',t)\partial\hat{s}'$ — the light scattered from direction ŝ into direction ŝ',

$q(r,\hat{s},t)$ — the source term (i.e. the number of photons per unit time emitted at position r at time t in direction $\hat{s}$),

where

$p(\hat{s}\cdot\hat{s}')=$ — the normalised phase function representing the probability density of scattering from direction ŝ to direction ŝ'.

Thus in the time domain, the radiative transfer equation (or Boltzmann transport equation) is:

$$\left(\frac{1}{c}\frac{\partial}{\partial t}+\hat{s}\cdot\nabla+\mu_a(r)+\mu_s(r)\right)I(r,\hat{s},t)=\mu_s(r)\int_{4\pi}p(\hat{s}\cdot\hat{s}')I(r,\hat{s}',t)d\hat{s}'+q(r,\hat{s},t).$$

(1.7.2)

Two important parameters that can be extracted from equation 1.7.2 are the photon density $\Phi(r,t)$ and photon flux or current $J(r,t)$. These are the measurable parameters that can allow us to solve for μ_a and μ_s':

$$\Phi(r,t)=\int_{4\pi}I(r,\hat{s},t)d\hat{s},$$

(1.7.3)

$$J(r,t)=\int_{4\pi}\hat{s}.I(r,\hat{s},t)d\hat{s}.$$

(1.7.4)

The frequency domain version of the radiative transfer equation can be obtained by exchanging $\frac{\partial}{\partial t}$ with $i\omega$.

The radiative transfer equation relies on the following assumptions:

1) electromagnetic wave properties such as polarization are ignored;
2) particle properties such as inelastic collisions are ignored;
3) the refractive index is constant.

1.7.2 P_1 Approximation

In order to solve the radiative transport equation in a reasonable amount of computer time approximations and simplifications need to be made. One such approximation is the P_N approximation. If the parameters I, q and p in equation 1.7.2 are expanded in spherical harmonics, we obtain an infinite set of coupled equations. The P_N approximation is derived by taking the first N spherical harmonics, which gives $(N+1)^2$ coupled partial differential equations (PDEs). If we take the first spherical harmonic we therefore obtain four PDEs, which combine to form the P_1 approximation. The photon density and photon current as given in equations 1.7.3 and 1.7.4 can also be expanded into spherical harmonics. Substitution of these terms into the equations for the P_1 approximation leads to the following expressions (Arridge 1999):

$$\left(\frac{1}{c}\frac{\partial}{\partial t}+\mu_a(r)\right)\Phi(r,t)+\nabla\cdot J(r,t)=q_0(r,t)\,,$$

(1.7.5)

and

$$\left(\frac{1}{c}\frac{\partial}{\partial t}+\frac{1}{3\kappa(r)}\right)J(r,t)+\frac{1}{3}\nabla\Phi(r,t)=q_1(r,t)\,,$$

(1.7.6)

where q_0 and q_1 are the first two terms of the expansion of the source function and describe the isotropic and dipole-like anisotropic component of the source, respectively and the following definitions apply:

$$q_1(r,t)=\int \hat{s}q(r,\hat{s},t)d\hat{s}\ ,$$

$$\kappa=\frac{1}{3(\mu_a+\mu_s')}=\text{the diffusion coefficient.}$$

Therefore two simplified equations relating the measurables Φ and J to the optical properties μ_a and κ have been obtained. It should be noted that equation 1.7.6 can include an anisotropic source term but equation 1.7.5 includes only an isotropic source term.

1.7.3 The Diffusion Approximation

If we now assume that the source is isotropic in all cases and that the photon flux changes slowly, i.e.

$$q_1 = 0 \text{ and } \frac{\partial J}{\partial t} = 0,$$

(1.7.7)

equation (1.7.6) becomes:

$$J(r,t) = -\kappa(r)\nabla\Phi(r,t) .$$

(1.7.8)

This is known as Fick's Law for the diffusion of gases or molecules and states that the rate of diffusion is proportional to the product of the diffusion coefficient with the concentration gradient.

If we now substitute 1.7.8 into 1.7.5 we obtain the time domain form of the diffusion approximation to the radiative transfer equation (or diffusion equation):

$$\mu_a(r)\Phi(r,t) + \frac{1}{c}\frac{\partial\Phi(r,t)}{\partial t} - \nabla\cdot\kappa(r)\nabla\Phi(r,t) = q_o(r,t) .$$

(1.7.9)

The diffusion equation is also an energy conservation equation, where absorption + flow + diffusion = sources.

The main assumptions of the diffusion equation are:

1. The angular dependence of the source, phase function and specific intensity are all almost uniform in order to be modelled as first order spherical harmonics.

In practise this means that the photons must be isotropically scattered. This will be true away from the source if $\mu_s' >> \mu_a$. As was shown in section 1.2.5 the transport scatter coefficient for breast tissue is around 100 times greater than the absorption coefficient. This assumption is invalid for non-scattering (void) regions or regions of strongly absorbing media. One place where this is of concern is in optical tomography of the neonatal brain as void regions are found in the head such as the ventricles and the cerebral spinal fluid (CSF) layer. Research is being performed to develop models which include void regions within a diffusing domain (Riley et al 2000) but is largely irrelevant in the case of the breast, except in the case of cysts.

2. The rate of change of the photon flux is zero.

To ensure that this is true we must assume that the flux variations occur more slowly than the time between scattering events. In our system, the flux variations can never exceed the duration of the laser pulse = 3ps. For a medium of $\mu_s' = 0.8$ mm^{-1} (typical for breast tissue (section 1.2.5)) the time between isotropic scattering events is again in the order of 3ps. This means that it is possible that the diffusion equation is not valid in such a study. However as $\mu_s' >> \mu_a$ the TPSF will experience substantial broadening as it travels through the tissue and so the flux variations will quickly drop below 3ps. This means that whilst this assumption may not hold close to the source, it will hold within the bulk of the breast tissue.

1.7.5 Numerical Solutions

Various numerical methods can be used to solve the diffusion equation. These rely on repeatedly applying the rules of light propagation through a medium. Analytical solutions to the diffusion equation do exist through the use of Greens functions (Arridge et al 2000) although these require more computational time and memory and can not be applied to as wide a range of geometries as the numerical solutions.

1.7.5.1 Monte Carlo Modelling

In Monte Carlo modelling, a model is created with a specific geometry and optical property distribution. A simulation is then performed where photons are emitted one by one (or in packets) from a modelled source into the system. As a photon travels through the system, the probability it is scattered (determined by the μ_s of the local region) is combined with the probability that it will be absorbed (dependent on the μ_a of the region). The direction in which the light is scattered is then determined from the modelled phase function. Each photon is assigned a 'weight' that represents its statistical probability of not having been absorbed. The weights of all the photons that reach the modelled detector are summed, and information about the distance that each has travelled (and hence the time it has taken) can be retrieved. This method is at present seen as the gold standard of numerical modelling techniques, and is used extensively in such areas as radiotherapy and atmospheric modelling, although it is very slow and computer intensive. Typically a photon can have several hundred interactions as it propagates between a source and detector, and many millions of photons are needed to obtain adequate statistics. This means that such models applied to large (>several cm) thickness of tissue typically require several days to run on a PC. Thus other methods may be more efficient

for use in our application although investigations have been performed using Monte Carlo methods (Boas et al 2002).

1.7.5.2 Finite Element Method

The finite element method is another established numerical method that can be used to solve partial differential equations (PDEs) for complex geometries. It is currently widely used in engineering to study the heat transfer, strains and stresses within a structure, fluid mechanics, and has also been used in medical imaging in such areas as EIT (Lionheart 2004).

The finite element method involves dividing the domain (region of interest), Ω, into a finite number of elements that have a set number of corners or nodes. The photon density, $\Phi i(t)$, is then calculated at each node i and summed over all D nodes in the domain. This can be expressed mathematically by representing the photon density $\Phi(r,t)$ using the piecewise polynomial function:

$$\Phi^h(r,t) = \sum_i^D \Phi_i(t) u_i(r) .$$

(1.7.14)

The h superscript relates to the fact that the solution is calculated at the nodes and so is an approximate solution. $u_i(r)$ is a basis function that describes the way that the function is allowed to vary over an element. The simplest form is for the basis to be constant, but a variety of basis functions can be used (Arridge et al 1995).

A finite element mesh can be used to define the location of each node. A typical mesh shown in figure 1.7.2 was generated using software developed by (Schöberl 1997), and was created to reconstruct the data collected from the female breast by the system described in part 3.

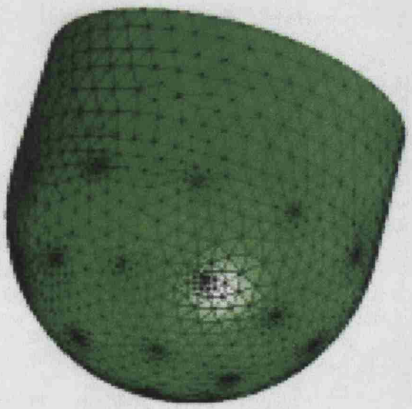

Figure 1.7.2: A finite element mesh used in finite element modelling.

1.7.6 Image reconstruction using models

The basis of optical image reconstruction is to determine the optical properties of a theoretical model that produces the same measurements as are obtained experimentally. These are then considered to be the optical properties of the object under study. To do this we must therefore consider two different problems: the forward problem and the inverse problem.

1.7.6.1 Forward problem

The forward problem can be described by the equation:

$$y = Jx, \tag{1.7.15}$$

where y are the measurements, x are the optical properties of the object and $\boldsymbol{J}$ is the sensitivity matrix (otherwise known as the Jacobian of the forward operator or the weight matrix). Measurements y can be computed if we know the geometry of the object, the location of the sources and detectors and the transport of light according to the diffusion equation.

Solutions to the forward problem can be used to generate model data for comparison with experimental data during image reconstruction, or used to generate simulated data to test reconstruction techniques or expected outcomes of a phantom study. Naturally such forward calculations depend on knowledge and determination of the sensitivity matrix $\boldsymbol{J}$. As can be seen from equation 1.7.15 this is a matrix that relates changes in the optical properties (μ_a, μ_s') at specific positions within the object to perturbations in the measurement.

1.7.6.2 Perturbation theory and PMDFs

The perturbation theory is based on the approximation that a change in the state of an object results in a change in the measurement that can be expressed as a series based on known functions describing the original state of the object. A measurement $Y_{n,m}(x,t)$ made at frequency ω, using source n and detector m on an object with optical properties x can be expressed (via a Taylor series) as:

$$Y_{n,m}(x_1(r),\omega) = Y_{n,m}(x_0(r),\omega) + \frac{\partial Y_{n,m}(x_0(r),\omega)}{\partial x}[x_1(r)-x_0(r)] + \frac{1}{2!}\frac{\partial^2 Y_{n,m}(x_0(r),\omega)}{\partial x^2}[x_1(r)-x_0(r)]$$
$$(+ \textit{higher orders})$$

where $$x(r) = \begin{pmatrix} \mu_a(r) \\ \kappa(r) \end{pmatrix} \tag{1.7.16}$$

represents the distribution of optical properties over the object. $x_o(r)$ denotes the initial state and $x_1(r)$ a perturbed state. If we ignore the terms above the first derivative and rearrange equation 1.7.16 then we get:

$$\frac{Y_{n,m}(x_1(r),t) - Y_{n,m}(x_0(r),t)}{x_1(r) - x_0(r)} = \frac{\partial Y_{n,m}(x_0(r),t)}{\partial x} = J_{n,m}(x_0(r),t) \quad . \tag{1.7.17}$$

If the values of $J_{n,m}(x_0(r),t)$ are plotted over the volume or area of the object of interest then a photon measurement density function (PMDF) is obtained (Arridge 1995; Arridge et al 1995). This shows the magnitude of the change in the measurement $Y_{n,m}(x,t)$ that will result from a unit change in optical properties x at position r for a given source detector pair n,m. A PMDF obtained for the mesh shown in figure 1.7.2 for κ is shown for both intensity and meantime for one source and detector in figure 1.7.3. As can be seen the PMDF forms a tight band between the source and detector. If a localised perturbation in optical properties is placed outside this band then virtually no change in the measurements will be detected. The sensitivity varies significantly within this band and also includes negative values. This means that there are some positions within this object that will result in a decrease in the measurements if a perturbation is introduced and other positions where the same perturbation will lead to an increase.

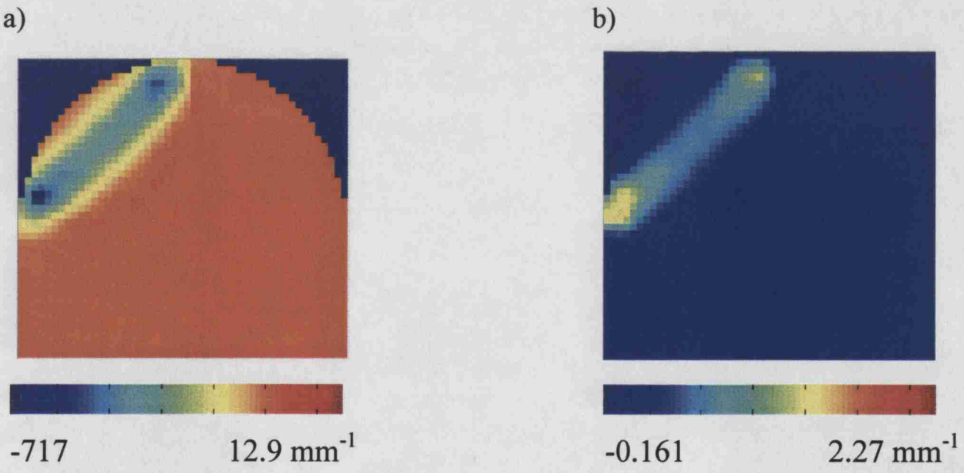

Figure 1.7.3: A plot of the photon measurement density function for source n and detector m, with a) intensity and b) meantime as the measurement type and κ as the optical property varying on the mesh shown in figure 1.7.3. The optical properties allocated to the mesh were μ_a = 0.007 mm^{-1}, μ_s' = 0.8 and n = 1.56.

The sensitivity matrix is composed of all the derivatives of $J_{nm}(x_0(r),t)$ for all source and detector combinations at all mesh nodes. $\boldsymbol{J}$ can be determined numerically using FEM or Monte Carlo modelling, analytically, or experimentally by placing a small absorber (and/or scatterer) at

discrete positions within the domain. These different methods will be explored in more detail for our specific breast imaging system in part 3.

1.7.6.4 Inverse problem

The second problem to be considered in image reconstruction is the inverse problem. This can be expressed by the equation:

$$x = J^{-1}y.$$

(1.7.18)

In the case of the work in this thesis, y represents the datatypes obtained from MONSTIR as described in chapter 1.6. It can be seen that in order to solve this equation we must first invert the sensitivity matrix. There are several features of the sensitivity matrix, however, that complicate the inversion process:

- The matrix is ill posed – this means that there are fewer independent measurements than there are unknown pixel values.
- The matrix is ill conditioned – the condition number is typically very large, resulting in the magnification both of measurement errors and numerical errors on inversion.

1.7.6.5 Linear Reconstruction

The simplest way to reconstruct an image is to use linear reconstruction. If we rewrite equation 1.7.17 in the form of equation 1.7.15, the change in measurements, $\Delta Y_{n,m}(x(r),\omega)$, can be expressed as the product of the Jacobian and the change in optical properties:

$$\Delta Y_{n,m}(x_0(r),\omega) = J_{n,m}(x_0(r),\omega)\Delta x(r),$$

(1.7.19)

in the limit where Δx is small. Therefore in order to solve the forward problem and determine measurements given the optical properties we must first calculate the sensitivity matrix for the model. Alternatively in order to determine the optical properties Δx corresponding to the measurement $\Delta Y_{n,m}(x(r),\omega)$, we must invert the sensitivity matrix $J_{n,m}(x_0(r),\omega)$.

As described earlier inversion of the sensitivity matrix is non-trivial and various methods exist such as singular value decomposition (Isaacson et al 1992; Press et al 1992) although the Tikhonov regularisation is more commonly used in optical imaging. The Tikonov regularisation improves the matrix's condition by adding an identity matrix I weighted by a

factor $\tilde{\lambda}$. Improving the condition of the matrix concentrates the information on its diagonal, which then aids the inversion. The Tikonov regularisation is given by:

$$\Delta x = \left[J^T J + \tilde{\lambda} I\right]^{-1} J^T \Delta y, \qquad \textit{(1.7.20)}$$

where $\tilde{\lambda} = \lambda * Fmax$. *Fmax* is the maximum main diagonal element value of the matrix $J^T J$ and λ is a regularisation parameter, which determines the accuracy of the match between the model and the data.

An advantage of linear reconstruction is that it does not require a good forward model to be derived for reasonable results to be achieved. Its main disadvantage is that it can only reconstruct small changes in the optical properties and so reconstruction of breast tissue relative to a reference phantom is likely to fail, especially if the reference phantom has optical properties that are not close to those of the breast.

1.7.6.6 Non-linear reconstruction

Non-linear reconstruction involves generating a forward model, comparing its predictions with the experimental data and updating the sensitivity matrix to minimise the difference. This process is then repeated iteratively until the model data is within an acceptable degree of the experimentally measured data.

1.7.6.7 TOAST

The computer programme used to reconstruct images at UCL is known as temporal optical absorption and scattering tomography (TOAST). TOAST employs a non-linear algorithm and an FEM forward model based on the diffusion approximation.

The method for computing the updated estimate of the sensitivity matrix and the method of inversion will affect the way in which the reconstruction proceeds and converges. Reconstructions can be constrained by using a-priori information, for example about tissue boundaries. The following sections describe some of the specific features that can be employed in TOAST to aid the reconstruction and presentation of images.

1.7.6.7.1 Boundary conditions

The finite element model used in TOAST must be based on a mesh that has the same geometry as the object we are attempting to image. The boundaries of this mesh must also model the real characteristics of our measurement geometry. There are various different boundary conditions that can be implemented in TOAST. The Dirichlet boundary condition requires that the function $\Phi^h(r_{boundary}, t)$ = constant at the boundary. A Neumann boundary condition requires that the derivative of the function $\delta\Phi^h(r_{boundary}, t)/\delta r$ = constant. A Robin boundary condition imposes a combination of the two such that $\alpha\Phi^h(r_{boundary}, t) + \beta\delta\Phi^h(r_{boundary}, t)/\delta r$ = constant. In the cases presented in this thesis the boundary has been made to be absorbing (i.e. black surface) and so the total inward photon current at the boundary is zero. However the boundary condition must also incorporate diffuse reflection that will occur at the boundary due to the refractive index mismatch between the domain and the surrounding medium. Thus we use a Robin boundary condition of the form:

$$\Phi(m) + 2A\kappa(m)\frac{\partial\Phi(m)}{\partial\nu} = 0, \qquad \textit{(1.7.21)}$$

where ν is the vector normal to the surface, $A = (1+R)/(1-R)$, where $R(\hat{s})$ is a directionally varying refraction parameter. The choice of the value of A is often determined from Monte Carlo data (Arridge 1999). We must also include information about the properties of the sources and detectors used and the source size and profile (e.g. point source or Gaussian) must be adequately modelled.

1.7.6.7.2 Cholesky and Conjugate gradient methods for linear inversion

To solve the forward problem and so produce model data, TOAST can employ either of two linear inverse solvers:

1. Cholesky (direct) solver
2. Conjugate-gradient solver.

The Cholesky factorisation is a direct method that requires the calculation and storage of a factorisation matrix. The advantage of this method is that it is fast for two-dimensional modelling as it does not involve an iterative process. In three-dimensional modelling, however, it requires a lot of memory to store the factorisation matrix and so the reconstruction becomes slower, making this method most appropriate for 2D modelling. The conjugate-gradient solver

uses an iterative process to solve equation 1.7.15. It is slower than the Cholesky solver, but requires less memory and so is generally used for 3D reconstructions.

1.7.6.7.4 Mapping to local basis functions

In order to produce an image of μ_a and μ_s' we need to define the way in which the values assigned to the continuous FEM are mapped to an image. This can be done through a local basis function:

$$\kappa(r) = \sum_{p=1}^{N_\kappa} \kappa_p \nu_p{}^{(\kappa)}(r)$$

$$\mu_a(r) = \sum_{p=1}^{N_{\mu_a}} \mu_{ap} \nu_p{}^{(\mu_a)}(r)$$

(1.7.23)

There are many different forms that such a basis can take, for example the so-called pixel basis or forward mesh basis. The forward mesh basis uses the existing basis function for each node and so effectively maps the values of μ_a or μ_s' directly, whereas the pixel basis maps the values of μ_a or μ_s' generated on the FEM mesh to a regular grid of $N\mu_a$ or $N\mu_s'$ pixels. The interpolation used in the pixel basis occurs throughout the image reconstruction. It should be noted that the basis for μ_s' does not have to be the same as the basis for μ_a and so a different resolution for each image could be obtained. The different local basis functions that can be implemented in TOAST are illustrated in figure 1.7.4. Conventionally, pixel basis would be a series of piecewise constant functions (e.g. each pixel has one single value throughout), although in TOAST pixel basis refers to a piecewise linear basis.

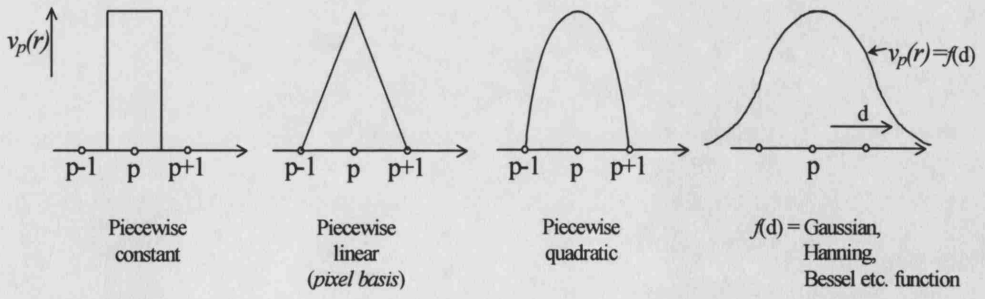

Figure 1.7.4: The different local basis functions that can be implemented in TOAST (Hillman 2002).

A successful non-linear reconstruction and hence a reconstruction using TOAST requires a good fit to be achieved between the data and the model. It has the advantage over linear reconstruction that large changes in the optical properties between an object and a reference can be made so long as an accurate model of the reference can be made. It is also possible to

reconstruct absolute images instead of difference images using non-linear reconstruction, although calibration factors, such as the IRF of the system and systematic noise from the electronics, have to be accounted for (see section 1.6.5).

Part 2

Experimental studies performed using a single ring of optodes.

The main focus of this project has been to perform clinical studies with the novel instrument described in chapter 1.6. This part describes the studies that have been performed to date and the results obtained. The purpose of these studies have been: first, to develop the optimum data collection and image reconstruction techniques for optical imaging using this system; second, to investigate the appearance of the reconstructed images in relation to specific breast tissues; and third, to assess the effectiveness of optical mammography as a clinical tool.

2.1 Clinical Protocol

2.1.1 Imaging procedure

The initial patient interface for studies on volunteers utilises three interconnecting rings as shown in figure 2.1.1. These rings are based on a probe designed for EIT where a vacuum pump was used to conform the breast to the geometry of the rings (Holder D S 1995). For this study it is important to maximise patient comfort during a scan. This is because a significant advantage that optical imaging possesses over other techniques is that it can be used repeatedly (or even continuously) and does not require the compression needed for x-ray mammography. In addition the acquisition time required to perform a study is around 5 minutes to ensure that a sufficient number of photons have been detected (see section 2.5), for these reasons the use of a vacuum pump was not considered. The rings are lined with black felt to provide close contact between the breast and the source/detector bundles and are mounted onto an adjustable frame (figure 2.1.1). It was originally anticipated that a combination of two rings would allow three-dimensional imaging of the breast. The rings are of different diameters (A = 56 mm, B = 82 mm and C = 110 mm) to accommodate a variety of breast sizes. However, as will be discussed later, it was discovered that we were only able to fit a single ring (B or C) to any patient. Pairs of source and detector fibre bundles are attached to the rings via connectors, which provide a common circular illumination and detection area with a diameter of 6 mm (chapter 1.6). Each ring can hold up to 16 fibre bundles, which are distributed evenly around the circumference.

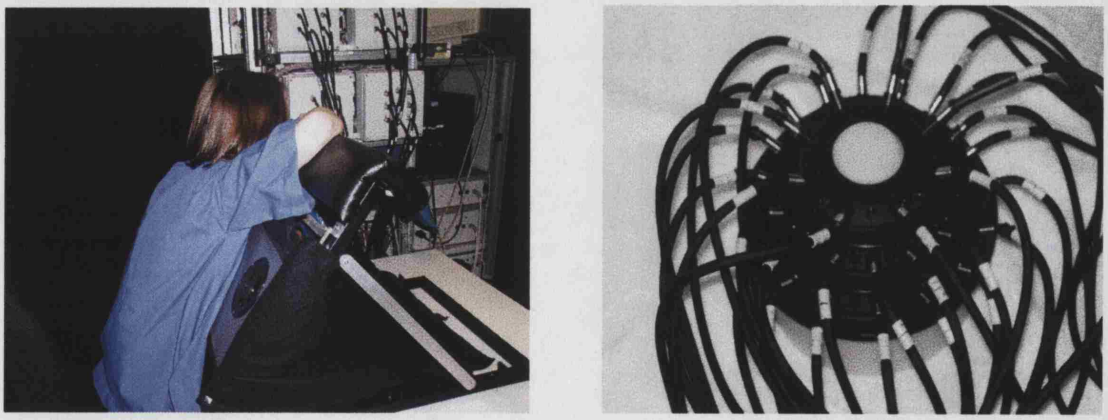

Figure 2.1.1: A patient interface based on a ring system mounted into a frame.

The scan procedure requires the patient to wear a specially made front opening gown, and then position herself by adjusting the frame and chair so that her left or right breast is at a height where it can be placed into one of the two rings. The patient is also required to wear safety

goggles with a minimum of 1 OD (at 800nm) attenuation to conform to the laser safety guidelines.

Prior to every full scan, illumination of the breast at one source position is performed and the TPSFs are viewed. This enables the data to be checked for any errors. The errors that commonly occur are:

- Light passing directly between adjacent optodes due to insufficient contact between the breast and the source/detector connectors, which manifests as a large pre-peak within the TPSFs (figure 2.1.2).
- The pre-determined ADF file (chapter 1.6) is not appropriate due to a mismatch between the properties of the breast tissue and the properties of the phantom. This can lead to significant cross talk between adjacent detectors and/or saturation of the detectors. Both will cause serious deterioration of the data (figure 2.1.3).

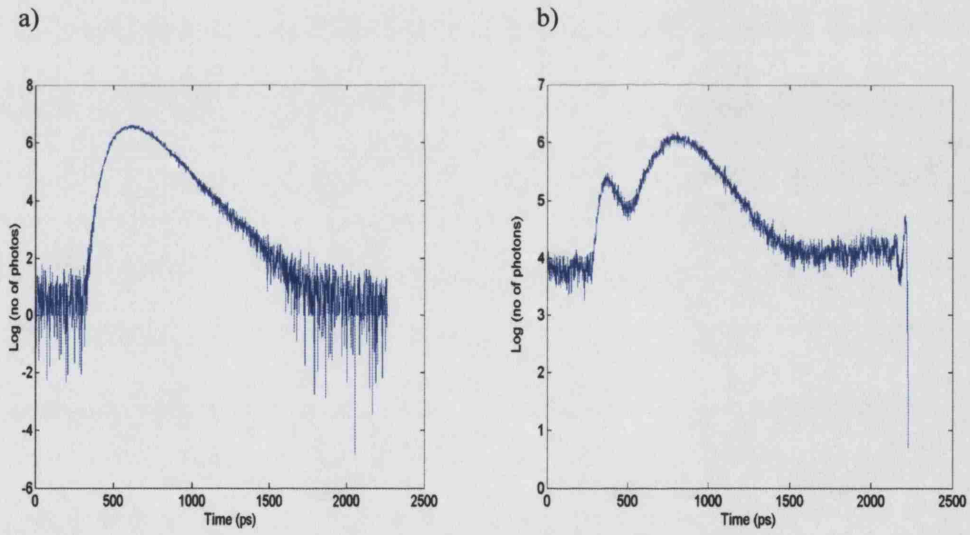

Figure 2.1.2: The effect of light leakage on the TPSF during a volunteer study. a) shows a normal TPSF and b) shows a TPSF affected by light passing directly between adjacent optodes. This effect manifests as a large pre peak and an offset in the measured background counts.

a) b)

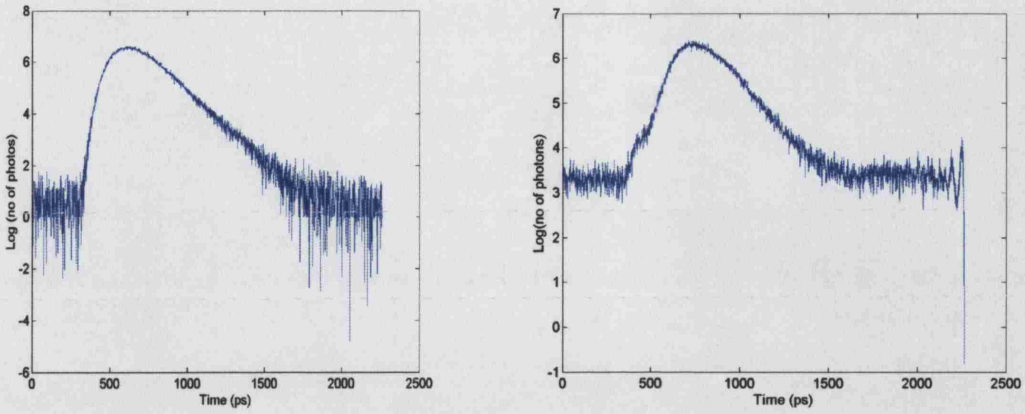

Figure 2.1.3: The effect of cross talk due to an error in the adf file. a) shows a normal TPSF and b) shows a TPSF affected by an inappropriate ADF file. This effect manifests as a large offset in the measured background counts and a distorted TPSF due to contamination by crosstalk from a neighbouring detector channel.

The scan itself is performed in a laboratory with all the lights turned off to minimize the detection of stray light. Surrounding the back of the rings with black cloth further reduces the detection of stray light. During a scan each source location is illuminated for 10 s so that the total scan duration is less than 5 minutes for one ring.

After each scan, data is acquired on a homogenous phantom using the same source and detector positions so that a reference is obtained for difference imaging. This phantom is constructed from epoxy resin machined into a conical shape with a cylindrical base (see section 2.1.3). The slope of the cone is exactly that of the rings (34.5° from the vertical) so that a perfect coupling between the cone and the ring is achieved and no light leakage occurs. The phantom has the properties μ_a = 0.007 mm^{-1} and μ_s' = 0.8 mm^{-1} as these are deemed to be typical average properties of the breast (chapter 1.2).

2.1.2 Reconstruction

It was soon discovered that the geometry of two or all three rings connected together was not suitable for the shape and size of the women volunteers who took part. This included women of various ages with a variety of breast shapes and sizes. Instead, in all cases, just one ring containing 16 fibre bundles was used. When only 16 sources and detectors are used it is possible to reduce cross talk as described in section 1.6.2.3.1 further by using source and detector bundles that, as far as possible, are not next to each other in one MCP-unit.

Image reconstruction for one ring could be considered to be 2D imaging of a single slice through the breast being sampled. This approach would have some advantages, as image reconstruction in 2D requires less computer memory, processing power and time than a 3D reconstruction. A circular finite element mesh for such an approach could be generated with a radius equal to that of the ring. This is a simple mesh that would not require much memory and so would be able to be divided into a greater number of finite elements than might be possible for the same plane in a 3D mesh, and so could provide a better sampling of that slice.

The main problem with using a 2D model is that the breast is a 3D object and so the tissue above and below the slice imaged will have a significant effect on the data obtained. The PMDFs for source and detectors within the 2D ring will extend throughout the 3D volume, and thus measurements will be sensitive to tissues above and below the plane. It is possible to apply an approximate correction for what is termed the 2D-3D effect (Hillman 2002; Schweiger et al 1998), although this correction still includes an element of error. For this reason a mesh was constructed based on a section of a cone that has the same slope as the rings. The mesh was generated using the NETGEN software developed by (Schöberl 1997). The central plane of the mesh is consistent with the plane through the sources and detectors. This is then extended above and below by a thickness of 10 mm to form the cone section. The mesh is made finer at the positions of the sources and detectors as more accurate modelling is required at these points where the density of the PMDFs is greater and so the rate of change of light intensity is greater. The mesh contains 18589 nodes, consisting of 3426 boundary nodes and 15163 internal nodes, and 12325 tetrahedral elements with quadratic interpolation functions and is shown in figure 2.1.4.

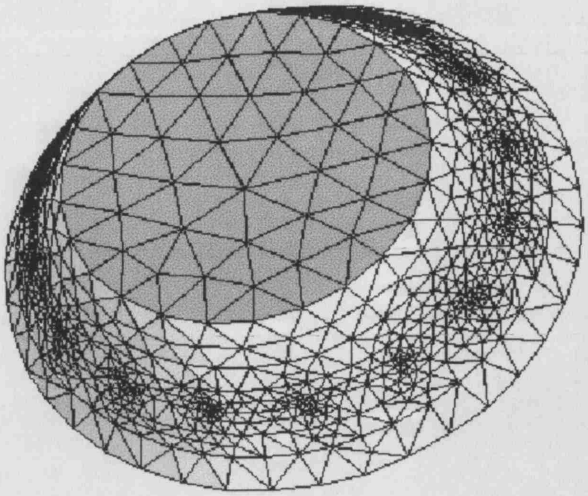

Figure 2.1.4: FEM used to reconstruct images from one ring.

The reconstruction itself is based on a 20 x 20 x 4 pixel basis, a direct solver and Robin boundary conditions (see chapter 1.7). A pixel basis is chosen as this enables the resolution of the images to be altered to allow optimum sampling with minimum reconstruction time and image size and also provides a degree of smoothing of the image. A value of 20 pixels across the plane of the ring was chosen as this suppresses features with a size less than the best spatial resolution of the imaging system (4 mm). The third value (4) defined in the pixel basis determines the number of pixels in the z direction (depth) within the image. Since sampling is constrained to a slice there is no need for high resolution in this direction and so this value can be kept low to reduce reconstruction time.

The use of intensity as a datatype requires the coupling efficiencies between the sources and detectors and the surface of the breast to be known or to be included in the model as a reconstructed parameter (Arridge et al 2000). Furthermore as explained in section 1.6.7 the use of intensity in difference imaging requires that the coupling to the breast is the same as the coupling to the reference media. In most cases the coupling to the breast is highly variable as it depends on such factors as skin tone, hair density, moisture and pressure, and so prevents the use of intensity in difference imaging. Thus images were reconstructed using meantime only (variance contains similar information as meantime, and requires model fitting so was not used).

It has been proven that the use of intensity alone is insufficient to achieve separation of scatter and absorption (Arridge et al 1998). Previous studies suggest that this is probably also the case for the use of meantime only with highly artefactual images of the scatter coefficient often being

obtained. Alternatively images of the absorption coefficient can be obtained by assuming that scatter is constant and uniform across the breast (Hebden et al 2004). In both cases a degree of cross talk between the parameters is inevitable. In most of the cases presented here, scatter was held at a constant value of 0.8 mm^{-1} (the value of the reference phantom) and images of the absorption coefficient were reconstructed.

2.1.3 Phantom study

Conical phantoms were made from epoxy resin mixed with titanium dioxide and an absorbing dye to give a known μ_s' and μ_a within a 10% error. This uses the same recipe as all solid phantoms constructed at UCL (Firbank et al 1995). The background properties of the phantom were $\mu_s' = 0.8$ mm^{-1} and $\mu_a = 0.007$ mm^{-1}. The phantom contained inserts made from the same epoxy resin mixture but with optical properties A: $\mu_s' = 0.8$ and $\mu_a = 0.014$ mm^{-1}, B: $\mu_s' = 1.6$ and $\mu_a = 0.014$ and C: $\mu_s' = 1.6$ and $\mu_a = 0.007$ mm^{-1}. These inserts were cylinders with a radius of 5 mm, and a height of 10 mm, and were placed within the same plane as shown in figure 2.1.5.

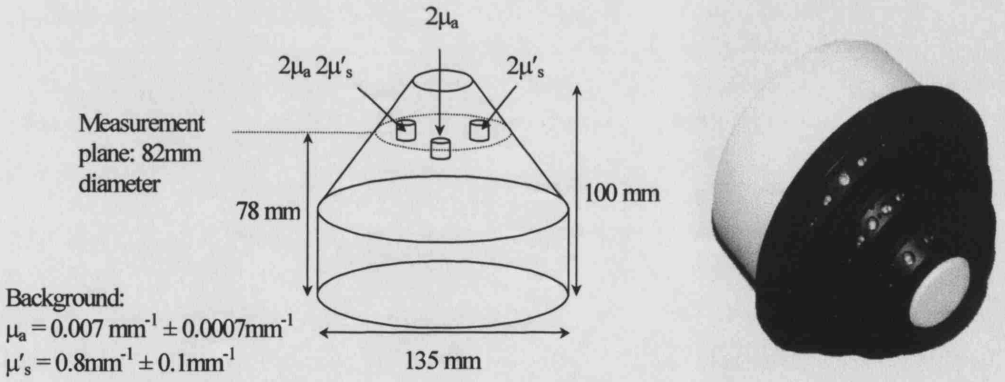

Figure 2.1.5: The cone phantom made and imaged at UCL (Hillman 2002).

A successful 3D reconstruction of this phantom with all three rings connected together and placed over the phantom was performed previously as described by (Hebden et al 2001).

To test the breast imaging protocol and the reconstruction process described above, one ring with the source detector bundles attached was placed around the plane of the phantom where the inserts are located. Black infrared-absorbing material was used to surround the phantom and so minimize stray light reaching the detectors. The homogenous phantom with the same background properties was imaged in the same manner directly afterwards to provide a reference measurement for the reconstruction. The result for λ= 780nm is shown in figure 2.1.6.

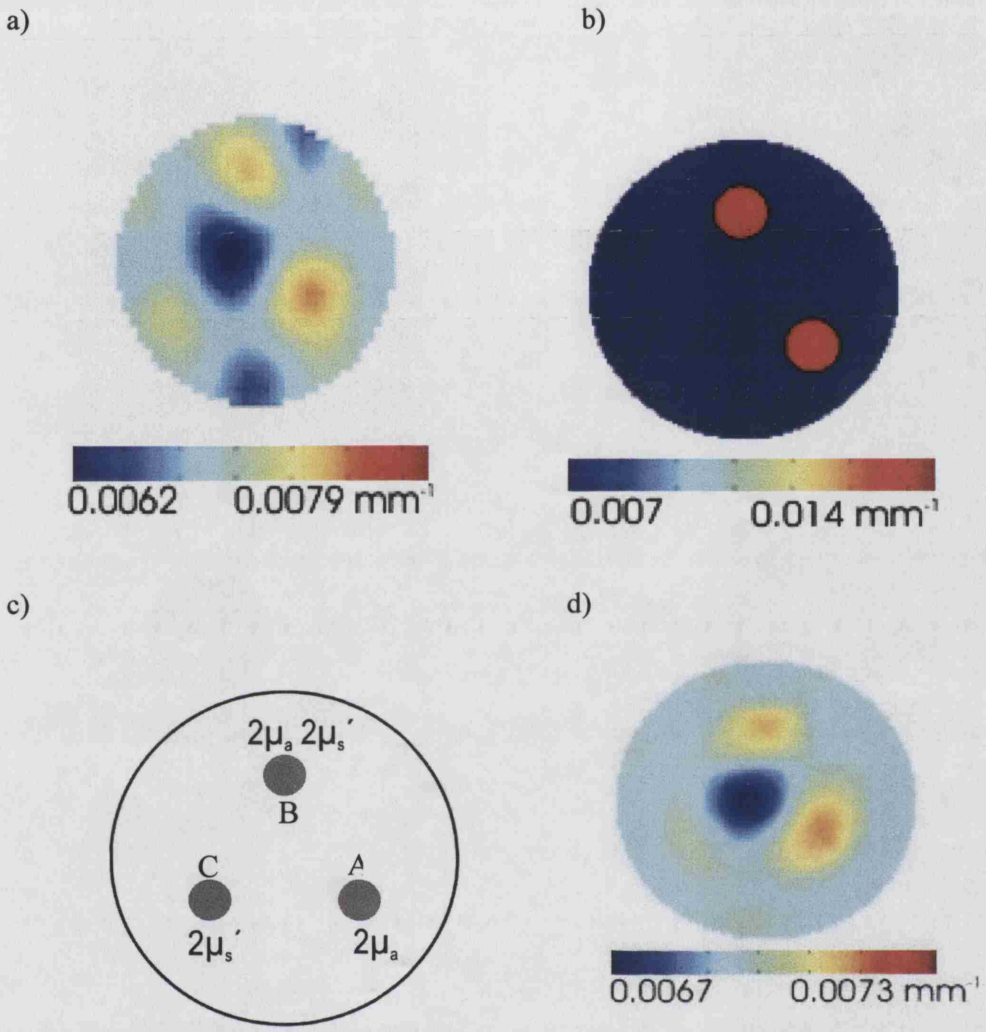

Figure 2.1.6: a) Reconstructed and d) simulated absorption image at 780 nm of the phantom shown in figure 2.1.5. b) and c) are schematic illustrations of target.

The reconstructions took around 4 minutes per iteration on a PC with a 2.2 GHz Xeon processor and used approximately 0.16 GB of RAM. All the images shown in this thesis correspond to the 15th iteration. This was taken as the point at which the objective value of the reconstruction levelled out as shown in figure 2.1.7. The objective value represents the difference between the forward model data from TOAST and the experimental data. Ideally this value should be as low as possible (with a perfect model and noise free data), but the iterations reach a point where no significant improvement is seen. It is possible that certain cases may benefit from further iteration, especially as the differences between the optical properties of the breast and those of the phantom are likely to be greater than between the two phantoms. However in all cases no significant changes to the features in the images were apparent after about the 6th iteration. As can be seen in figure 2.1.7, the objective value actually appears to level out after about 10 iterations so taking the 15th iteration was deemed sufficient in all cases.

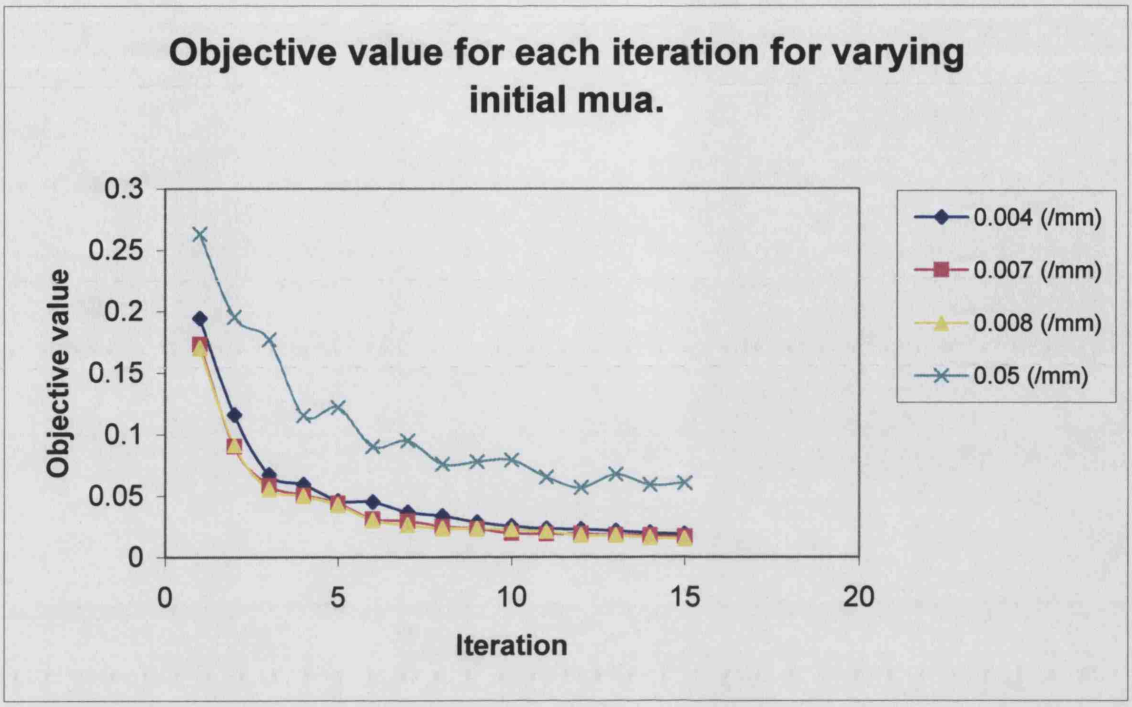

Figure 2.1.7: The objective value vs. iteration number for differing values of assigned reference μ_a.

2.1.3.1 Discussion

Figure 2.1.6 clearly shows regions of high absorption in the location of the two inserts with twice the background absorption (inserts A and B), although the contrast of the feature in the location of the insert which is also twice the background scatter (B) is not as great as for the insert whose scatter is equal to the background. There is, however, also a feature of slight contrast seen corresponding to the insert with only twice the background scatter. The appearance of this image can be explained if we consider how the effect of a local increase in scatter on the mean flight time will be interpreted by the reconstruction algorithm when the scatter is held constant. A local increase in scatter will result in an increased path length for photons travelling through that region and so measurements of mean flight time will be increased. A local decrease in absorption will also lead to an increase in mean flight time and so, when scatter is held constant, the reconstruction algorithm interprets a local increase in scatter as a local decrease in absorption. However, a local increase in scatter near the surface of the object can produce an increase in the number of diffusely reflected photons, which would otherwise have travelled deeper into the object, and so can lead to a decrease in mean flight time for small source-detector separations near the region. This would be interpreted as an increase in absorption. As we employ a variety of source and detector separations it might be expected that the appearance of a scattering insert within images where scatter is assumed constant will

be due to a combination of the two effects described. And indeed, insert C appears to exhibit a bi-polar structure, with a region higher than the background absorption towards the surface and a larger region of lower than background absorption towards the centre. As might be expected, the appearance of insert B appears to be due to a combination of the appearance of inserts A and C. The simulation in figure 2.1.6 d) was generated from a 3D FEM containing targets with the same properties as the phantom. The similarity of this image and that in figure 2.1.6 a) suggests that this is an inherent feature of the method used and not due to experimental errors. Further simulations generated from 3D FEM containing single scattering targets have also confirmed the bi-polar appearance.

The reconstructed values in the image range from 0.0062 to 0.0079 mm^{-1}. This is lower than the expected values of 0.007 mm^{-1} for the background and 0.014 mm^{-1} for the insert. However, difference imaging has been performed and hence the values presented represent the difference between the phantom and the reference phantom added to the estimated value for the reference phantom (chapter 1.6). This means that uncertainty in the optical properties of the reference phantom will lead to an error in the reconstructed values. The optical properties of both the phantom and the reference phantom are known to within ± 10% so although this will have some effect on the reconstructed values this is clearly not the principal cause of the poor quantitation. The principle cause of reduced contrast is the partial volume effect caused by the low spatial resolution. Large source and detector separations result in an inherently lower spatial resolution due to their broad sensitivity functions (PMDFs). The relatively large diameter of the ring used here (82 mm) will therefore contribute to the low contrast seen in the images. Additionally, as described previously, errors will also occur due to the use of a mesh that only models a section of the full three-dimensional volume being imaged.

In summary, phantom studies suggests that this method can be used to distinguish multiple 1 cm objects with absorption twice that of the background. This is of significance for the clinical studies as the lesions to be studied, and in particular malignant lesions, are not likely to have optical properties in excess of twice the background breast tissue properties (chapter 1.2). It should also be noted that it is of utmost importance to be able to detect a 1 cm lesion as the larger the tumour the greater the likelihood it is invasive and so the lower the chance of survival after surgery (chapter 1.3). However, phantom results have also highlighted that any variation in scatter within the breast could lead to features, which may be difficult to interpret.

2.1.4 Image Manipulation

The way in which an image is displayed is an important aspect of medical imaging. The eye is itself an imaging system and as such has various limitations (Blackwell 1946; Cornsweet 1970). For example, our eyes are able to distinguish fewer than 100 shades of grey and so, if an inappropriate threshold is employed, we may not be able to distinguish features of interest. Equally, grey scaling or colour scaling can be used to emphasise a region or small changes in contrast, as is common practise in CT imaging. Thus the choice of colour scale is important when displaying and analysing images.

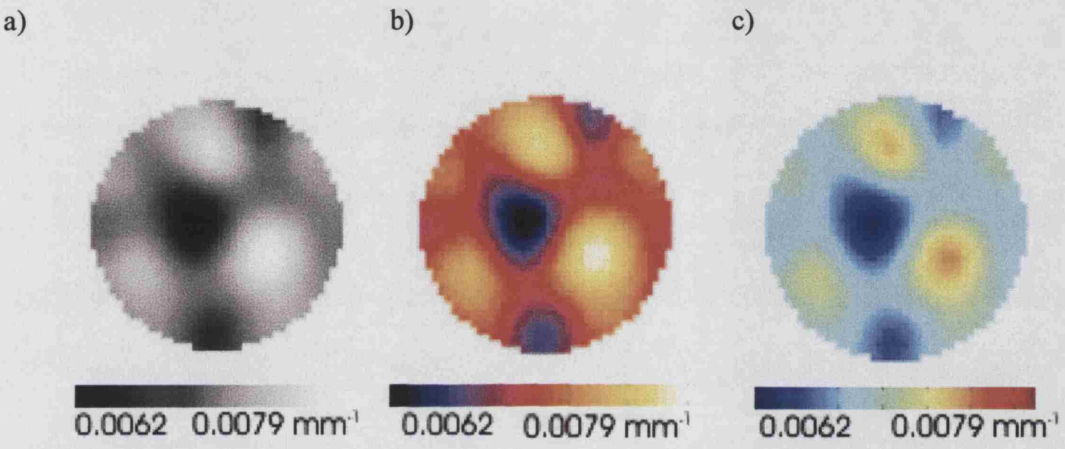

Figure 2.1.8: The same image displayed using different colour scales.

The image of the phantom reconstructed in figure 2.1.6 is shown in figure 2.1.8 using three different colour scales. Figure 2.1.8 a) is displayed on a linear grey scale whereas figures 2.1.8 b) and c) are two different colour scales. The colour scale in figure 2.1.8 c) appears to highlight the areas of contrast due to the inserts as the contrast between the red assigned to the highest absorption values and the surrounding green is more striking than the change from blue to green seen in the background regions. The grey scale, however, appears to show a smoother image as the shade of grey does not vary greatly as the absorption value increases.

Another feature of colour scaling is that it can be adjusted to highlight certain features. For example we know that the background of the phantom was 0.007 ± 0.0007 mm^{-1} so we could assume that any regions below 0.007 mm^{-1} are artefactual. Therefore we can set the colour scale to start at 0.007 mm^{-1} giving all values below that the same colour. This is shown in figure 2.1.9 a) and the areas of contrast are now more clearly defined. Care has to be taken, however, as if the maximum point on the colour scale is now taken to be the known μ_a value of

the inserts i.e. 0.014 then image 2.1.9 b) is obtained. Here the inserts are invisible because the contrast is much lower than would be expected as will be discussed later.

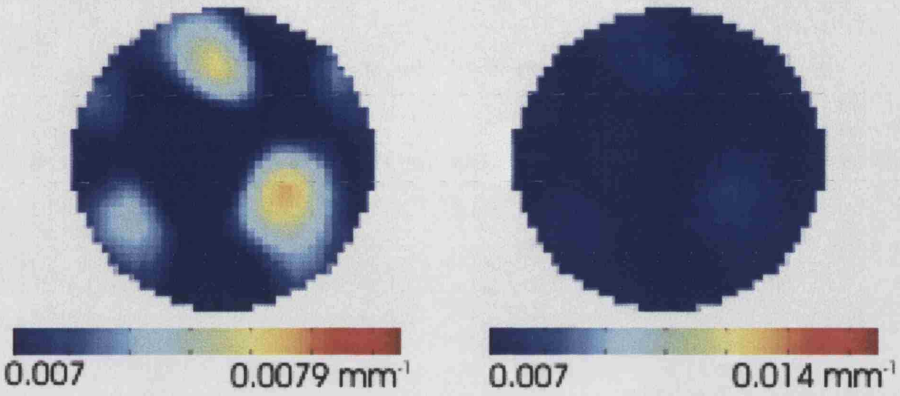

Figure 2.1.9: Changing the contrast of an image can highlight or mask certain features.

It is evident that the colour scale must be taken into account when interpreting an image. In particular it highlights the need to perform extensive validation of the images as is discussed in section 2.1.6. After further work it may be possible to adapt the choice of colour scale to highlight certain features in the image and so aid diagnosis.

The images presented in this thesis are all displayed using either the grey scale shown in figure 2.1.8 a) or the colour scale used in 2.1.8 c). In most cases the scale is applied from the minimum to the maximum node value, although the scales may be adjusted when it is considered necessary to highlight particular features.

2.1.6 Validation of images

It is important for any emerging imaging system to validate the images that are produced. There are various ways in which this can be done. First rigorous testing of the system must be undertaken in the form of phantom studies. These give an indication of the images expected given known properties of an object. In most cases the phantom studies are simplistic objects that are designed to give optimal results for the system. At UCL extensive phantom work to test the capabilities of both the MONSTIR system and the TOAST reconstruction package have been performed (Gibson et al 2003; Hebden et al 2001; Schmidt et al 2000). Additionally, as described in section 2.1.3, phantom work has been performed using the exact protocol used in breast imaging. This work has shown that features with twice the absorbing and scattering properties of a background media can be successfully reconstructed in images, although the

contrast is lower than would be expected. The localisation and spatial resolution of the targets are also less than ideal.

Although phantom work can give an idea of the limitations of the imaging technique and can certainly highlight significant sources of error involved in the data acquisition or image reconstruction, it does not provide complete validation of clinical images. The reason for this is that human breast tissue is more complicated than a phantom due to the physiology and structure of the breast. In these cases we need to compare the images obtained with other imaging modalities for which the limitations and standards are known. As described in chapter 1.4 the gold standard for breast imaging is x-ray mammography and yet the results in this thesis have not been compared with x-ray mammography, as this information has not been available for the volunteers scanned. This is because the majority of volunteers have been young women who have a high proportion of glandular tissue as opposed to adipose tissue within their breast. This tissue is relatively opaque on a mammogram and so often masks a tumour making x-ray mammography unsuitable for such patients. Furthermore it is not advisable to use ionising radiation on younger women where the incidence of cancer is small. Other imaging modalities that could be used for validation are MRI and ultrasound, although MRI is used sparingly due to its expense, and is unsuitable for some patients. This has meant that the only alternative imaging modality that has been available, in most cases, is ultrasound. Ultrasound images, however, are frames taken from a real time image display and so do not convey as much information as the ultrasound scan itself. In addition, interpretation of the ultrasound image is dependent on the operator's expertise. However, it is still possible to gain accurate information of the size and depth of the lesion from the ultrasound image, and the radiographer's report, where a lesion has been detected. What cannot be determined is the accurate location of the lesion within the breast in relation to our images. This is because the breast is supported in a different orientation during an ultrasound scan to that which has been adopted in our optical imaging protocol. Even if mammography or MRI were available, this would still be the case. There would be a particular problem in validating our images with x-ray mammography due to the compression of the breast. For this reason our determination of the position of a lesion has to rely on information given to us from the volunteer and the surgeon at the time of the scan. One way that this could be improved upon is for the volunteer to be imaged simultaneously using MRI and optical mammography, and deriving prior structural information from MRI is currently a matter for further research in our laboratory.

A useful technique to aid validation is to image the other breast of a volunteer. A good example of this will be shown later in figure 2.3.3 where a region of high contrast is shown in the location of a malignant lesion in the right breast that is not present in the image of the left

breast. Such information is evidence that the region seen is due to the abnormality and not a reconstruction artefact. A disadvantage of this approach is the increase in the total imaging time for a volunteer. As each data acquisition takes around 5 minutes it is normally acceptable to acquire two data sets in one session. Initially it was decided to image the breast with the lesion twice to increase the likelihood that a good data set was acquired. This has proved to be unnecessary and so later studies involved imaging both breasts to provide a form of validation for the images. Another validation technique is to scan the volunteer on several occasions and compare the images as is presented in figure 2.4.4. This technique is perhaps not as conclusive as comparing right and left breasts, but the repeatability of images can provide further validation (see section 2.4.1).

A further significant point for validation is determining the origin of other features that are seen within the image such as those in the images for healthy volunteers. Again a structural image of the breast gained with MRI could provide a correlation between these images and some anatomical feature, especially if the MRI image were to be obtained simultaneously with the optical scan. A further complication is that the optical properties displayed are related to physiological and not structural parameters. For this reason it is difficult to completely validate the images using the structural information given by MRI, ultrasound or x-ray mammography. Functional MRI or Doppler ultrasound could be used but again there are subtle differences between the information presented in these images and optical imaging, due to the specific function of the contrast agent used. In conclusion we must accept that it is difficult to validate images that show properties that are unique to that imaging modality. This is a problem that is faced by any new imaging modality.

2.1.7 Analysis of images

In a full clinical trial it is usual practice to assess an imaging system in terms of its sensitivity and specificity, where:

Sensitivity = the probability that a lesion is present (or screening test is positive) given that the person has the disease,

and

Specificity = the probability that a lesion is not present (or screening test is negative) given that the person does not have the disease.

To determine both sensitivity and specificity an extensive trial involving a wide sample of patients must be performed and the system must be assessed on a blinded trial basis. This means that a diagnosis must be made from the images without any prior knowledge of the condition of the volunteer. The diagnosis is then compared to the true condition of the patient. The investigations presented here should be considered preliminary to such a trial. At present the grounds for a diagnosis using optical imaging need to be determined. In particular it is not yet known if there is sufficient contrast between the optical properties of normal and malignant breast tissue in situ for such a diagnosis to be possible. Furthermore ethical approval was only given to image up to 54 volunteers, which is not a sufficient sample to establish the sensitivity and specificity of the system. It is desirable, nevertheless, to provide an indication of the ability of the system to detect lesions from the sample of images obtained. An empirical method of providing a quantitative measure of image quality has been proposed by (Grosenick et al 2003). We have adopted a method based on this where the images are graded from 0 to 5 according to the following categories:

5 – Contrast of lesion dominates image;
4 – Contrast comparable to other inhomogeneities;
3 – Contrast inferior to other inhomogeneities, but still clearly identified;
2 – Weak contrast;
1 – Hardly perceivable inhomogeneity, only detected if position is known;
0 – Not visible;
X – Image not obtained.

For this method any rating of 2 or above is considered to be a positive diagnosis for a tumour. This can be applied to benign lesions but it should be remembered that the expectation for optical mammography is that a malignant lesion will show an increase in absorption compared with healthy breast tissue, and be distinct from a benign lesion. Therefore, we might expect that a benign lesion will not necessarily be the most dominant feature in the image and may not appear at all. Thus a negative diagnosis for a benign lesion may be an indication of a success for optical mammography. The reconstructed images for all the volunteers in this study have been assessed on this basis.

It should be noted that this technique is purely qualitative. It was decided that a more quantitative approach was not appropriate in most cases due to the lack of appropriate validation for the size and location of lesions (see section 2.1.6) and due to the inability to produce true quantitation in the images which is discussed in detail in the following sections.

2.2 Clinical studies I: Healthy and benign tissue.

To be able to distinguish malignant from benign or healthy tissue, the characteristic appearance of both needs to be determined. Therefore, a series of women with pre-diagnosed benign lesions and healthy volunteers have been imaged using MONSTIR and the results have been compared with the medical notes and images from alternative imaging modalities when available.

2.2.1 Healthy Volunteers

Prior to performing scans on patients with known lesions a study of normals has to be performed. This enables us to examine the contrast of optical properties due to healthy breast tissues and also allows us to assess the suitability of the system in terms of patient comfort. A total of three healthy volunteers have been imaged using the ring system described in chapter 2.1. Further information on the appearance of healthy tissue has been gained from imaging the contralateral breast in patients with known lesions. Example images obtained from a 43-year-old healthy volunteer's left breast are shown in figures 2.2.1 for both wavelengths. All the images in this part are displayed as a slice through the plane containing the source detector bundles and are presented as though the volunteer were being viewed from the front (i.e. from the surgeon's point of view).

a) b)

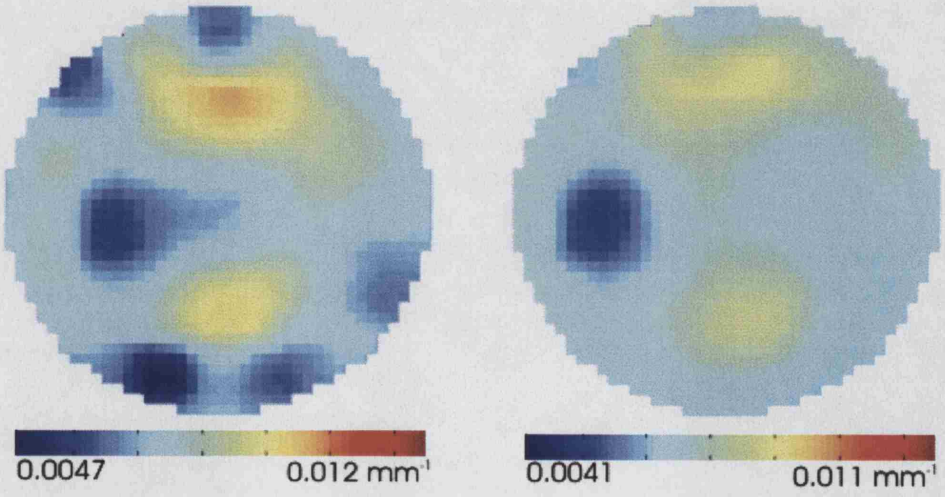

Visibility score = N/A Visibility score = N/A

Figure 2.2.1: The left breast of a 43-year-old healthy volunteer at a) 780 nm and b) 815 nm.

The absorption images of both the left and right breast of a second healthy volunteer aged 32 are shown at both wavelengths in figures 2.2.2 and 2.2.3 respectively

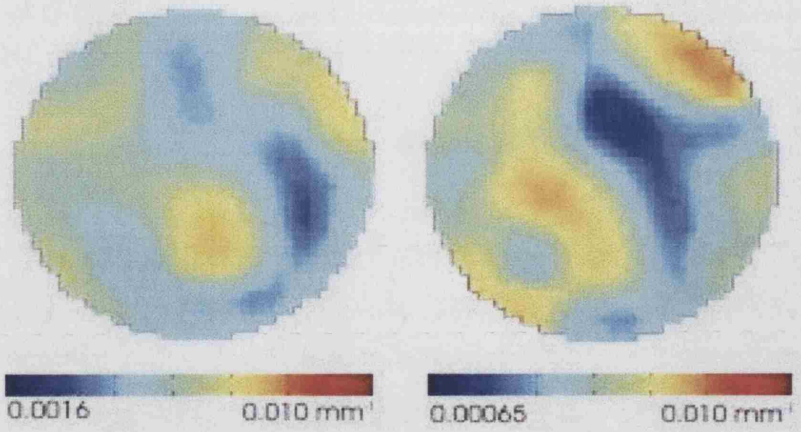

Visibility score = N/A Visibility score = N/A

Figure 2.2.2: The left breast of a 32-year-old healthy volunteer at a) 780 and b) 815 nm.

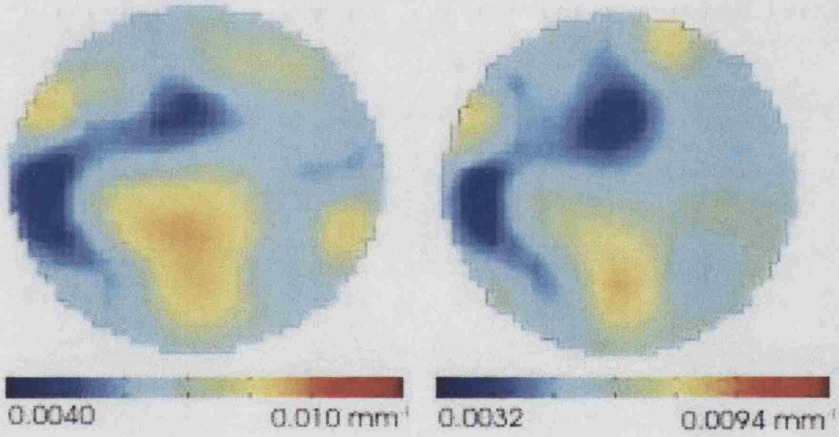

Visibility score = N/A Visibility score = N/A

Figure 2.2.3: The right breast of a 32-year-old healthy volunteer at a) 780 and b) 815 nm.

2.2.1.2 Discussion

The images obtained for healthy volunteers show a highly heterogeneous distribution in the absorption properties of the breast across the image. Healthy breast images typically display one or two highly absorbing features towards the center. The source of these features is unknown, although may be due to some anatomical feature of the breast such as the pectoral muscle (especially as this will be pulled forward by the breast tissue due to the scanning position of the volunteer), internal blood vessels, or the glandular tissue within the breast. Another typical feature of healthy images is a degree of left and right symmetry as is seen in figures 2.2.2 and 2.2.3.

The range of values in each image appears to be similar (except for figure 2.2.2 b)). This consistency across the images and a further correlation with the previous studies reviewed in section 1.2.5 suggests that this range is fairly typical of reconstructed values across healthy breast tissue. These values should, however, be treated with caution, as they are likely to be lower than the absolute values as discussed in the phantom image in figure 2.1.6 and have only been obtained from two healthy volunteers. In particular both volunteers are young and so will have a high proportion of fibrous tissue compared with adipose tissue which is likely to be more dominant in older women. Therefore these values are likely to be higher than might be obtained on an older volunteer.

One additional result of the healthy volunteer studies was that the patient interface was assessed as sufficiently comfortable during the duration of the scan. Some suggestions for further improvements were made, as will be discussed in detail in section 2.5, but overall the impression of volunteers was favourable.

2.2.2 Nodularity

Nodularity is an increased density of breast tissue, most often caused by hormonal changes, which cause the breast to feel lumpy. A 33-year-old woman was diagnosed as having two palpable breast lumps in her left breast. On investigation with ultrasound, the area of the two lesions did not exhibit any abnormality. The surgeon's report of the case states:

> *'Corresponding to the regions of clinical concern, there were prominent areas of breast tissue which appeared entirely normal. No abnormality could be detected.'*

Schematic diagrams indicating the location of specific nodules in both the volunteer's left and right breast are shown in figures 2.2.4 and 2.2.6 respectively. The reconstructed images obtained of her left and right breasts are shown in figures 2.2.5 and 2.2.7.

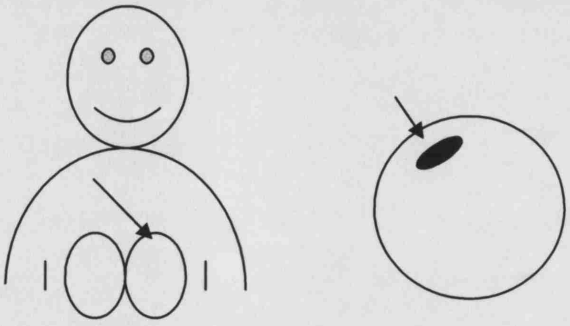

Figure 2.2.4: The location of the palpable lesion in the left breast as indicated by the volunteer.

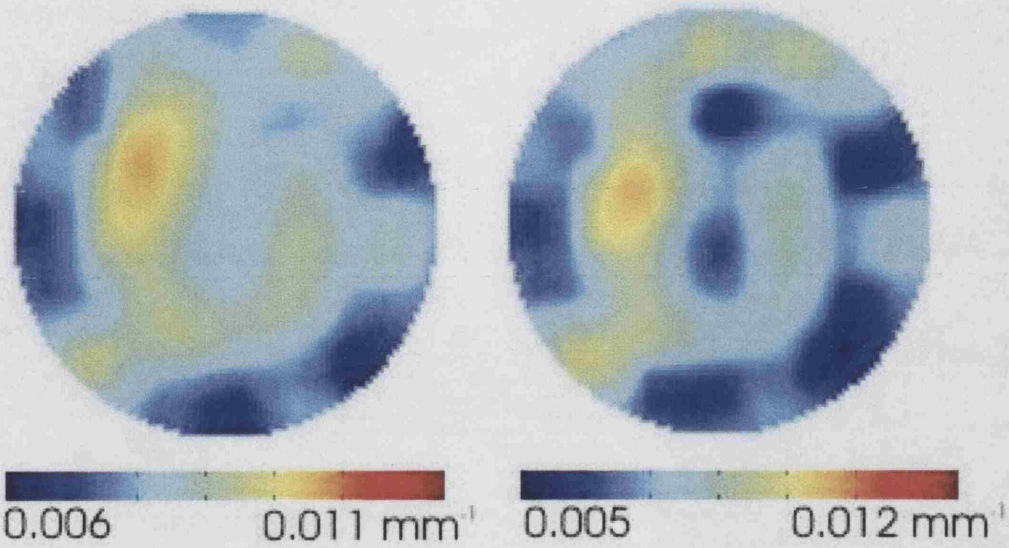

Visibility score = 3 Visibility score = 3

Figure 2.2.5: The absorption images for the left breast at a) λ = 780nm and b) λ = 815nm.

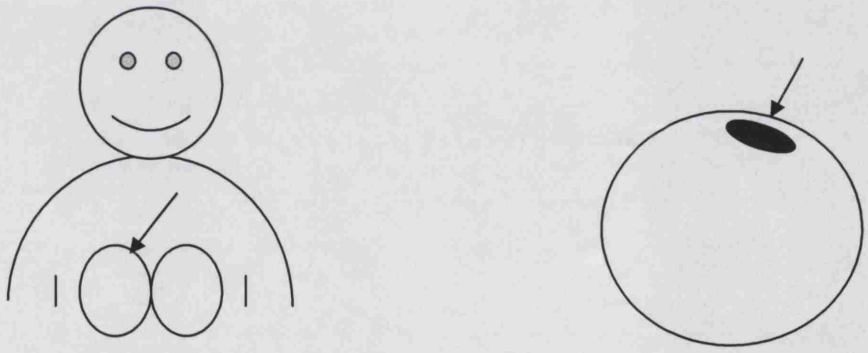

Figure 2.2.6: The location of the palpable lesion in the right breast as indicated by the volunteer.

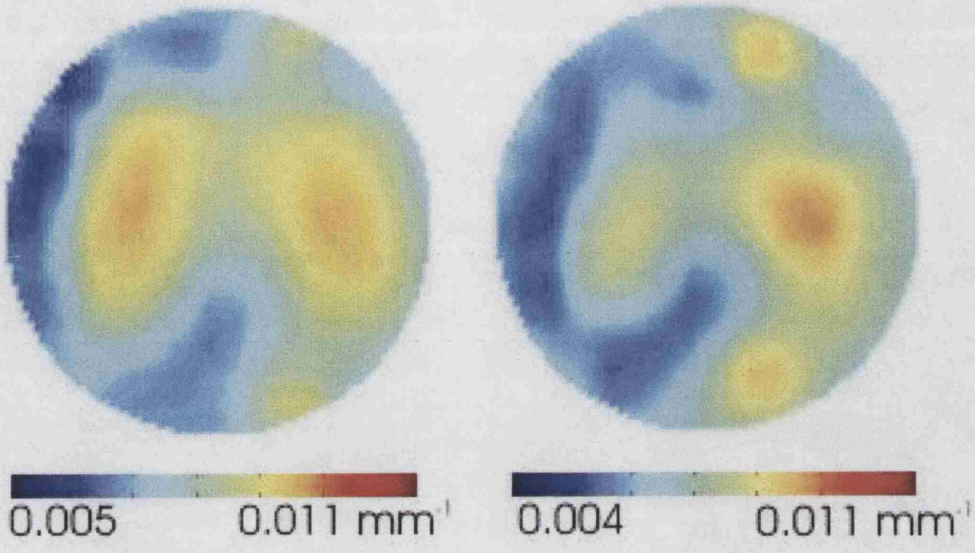

Visibility score = 2 Visibility score = 4

Figure 2.2.7: The absorption images for the right breast at a) λ = 780nm and b) λ = 815nm.

This volunteer returned to the breast clinic 16 months later and on this occasion the ultrasound scan detected a cyst in the right breast and several small cysts in the left breast. The ultrasound report is given below:

> *'The stroma of both breasts was consistent with active glandular tissue.*
> *Right breast*
> *In the UOQ* [Upper Outer Quarter], *there was a cyst measuring 9x9x6mm, 5mms deep to the skin. Nil else of note.*
> *Left breast*
> *There were several cysts scattered throughout the galand disc, ranging in size from 8mms to 5mms.'*

Such a report is consistent with nodularity of the breast. Due to her age, and the results of both ultrasound and physical examination, this volunteer did not undergo further investigative techniques.

2.2.2.1 Discussion

The images of both breasts show a region of contrast in the approximate location of the palpable lumps, although other features are also seen. In the images of the left breast the region is further to the right than was indicated. The positions indicated in figures 2.2.4 and 2.2.6 are, however,

only an estimate based on the information given by the volunteer and so the uncertainty involved is likely to be large. It is interesting to note that this volunteer was described as having 'lumpy breasts' and the images produced appear to coincide with such a description with various regions of high contrast being seen.

Of additional interest is the fact that the first ultrasound image determined the region to be normal and yet our images appear to show areas of contrast in that region, especially as the follow up ultrasound scan gave evidence for cysts. It could therefore be possible that the optical images are showing evidence of a cyst that was missed by ultrasound. If true then this would be a significant finding for optical mammography, although this would require extensive verification (see section 2.1.6).

The visibility scores assigned to these images are notable for two reasons. First, while the visibility score is higher than 2 and therefore a positive diagnosis, in no image is the contrast in the region of the lesion the most dominant feature in the image. Second, the determination of the location of the lesion in this case is arbitrary as no results from an alternative imaging modality are available. As discussed in section 2.1.6, even where MRI or mammography are available, a degree of uncertainty in the localisation of the lesion will exist due to differences in the scanning position of the patient. Thus the area of contrast that is assigned the visibility score may not be due to the lesion, but simply due to an area of healthy tissue in the approximate location of the lesion that has a higher absorption.

In total we have obtained images of four patients with benign nodularity. In all cases the images showed heterogeneities that were comparable in size, contrast and number to those seen in healthy volunteer images. However, where specific areas of nodularity were identified areas of contrast were seen in the corresponding location in the image, although these were generally not the most dominant feature.

2.2.3 Fibroadenoma

Fibroadenomas are discussed in depth in chapter 1.3. They are fibrous lumps with no vascularisation and commonly occur in younger women. The size and shape of a fibroadenoma can cause them to be defined as suspicious on an x-ray mammogram and therefore are often the cause of unnecessary biopsies. A study by (Taroni et al 2004) determined no uniquely defined optical characteristics for fibroadenomas, although it might be expected that they would exhibit similar absorption values to those of healthy breast tissue.

In total we have imaged six patients diagnosed with fibroadenomas. The images obtained from two such patients are shown below.

A palpable lesion was discovered in the upper inner quadrant of the right breast of a 30-year-old woman. An ultrasound investigation was performed and the radiographers report was as follows:

> *'Corresponding to the palpable lump, there was a well-defined hypoechoic structure, measuring 9x14x6 mm, 1 mm deep to the skin, containing homogenous low-level echoes. The overall appearances would seem to be consistent with a fibroadenoma, but other pathology cannot be excluded.'*

Further examination by the surgeon and a fine needle aspiration determined that the lesion was consistent with a fibroadenoma. The absorption image obtained of the right breast at 780 nm is shown in figure 2.2.8.

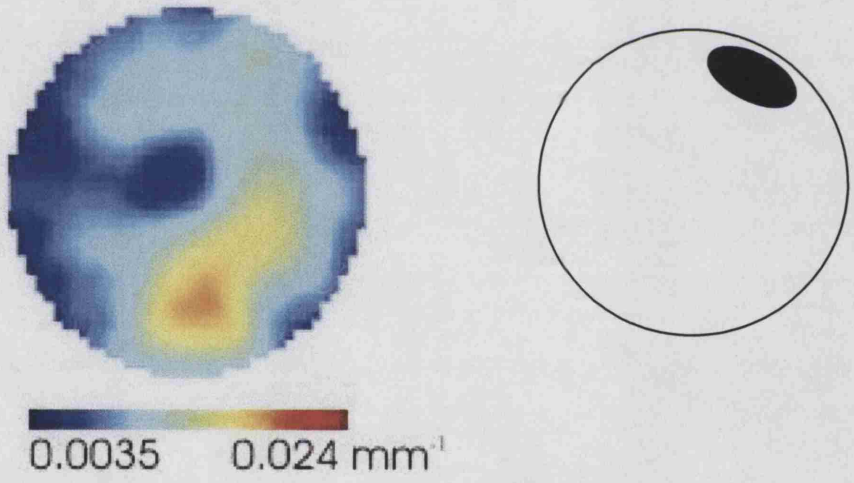

Visibility score = 2

Figure 2.2.8: An image of a volunteer with a fibroadenoma in the right breast at λ = 780nm.

Figure 2.2.9 shows the image acquired for a 26-year-old female with a fibroadenoma located in the right breast. The fibroadenoma was diagnosed via clinical examination, ultrasound and fine needle aspiration. The ultrasound scan (figure 2.2.9 c) indicated a well defined acoustically hypoechoic lesion with estimated dimensions of 17 x 16 x 12 mm, and centred about 2 cm below the surface in the right upper inner quadrant. The fine needle aspiration cytology confirmed the diagnosis of fibroadenoma through the identification of benign epithelial and stromal cells.

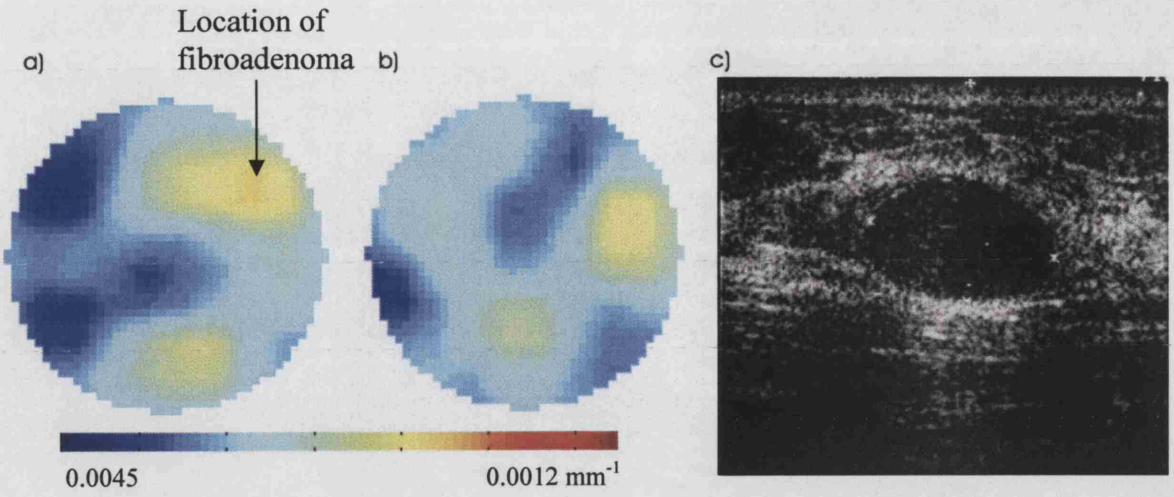

Visibility score = 4.

Figure 2.2.9: Absorption images of a) right breast and b) left breast and c) the ultrasound image of the fibroadenoma located to the top left of the right breast.

2.2.3.1 Discussion

In the first case (figure 2.2.8) the dominant feature is not in the position of the fibroadenoma. It is probable that the most dominant feature is due to some internal structure and is consistent with the presence of other regions of contrast seen in the images for the healthy volunteers and the previous case study. There is, however, a region at the expected location of the fibroadenoma, which has a slightly higher absorption value than that of the rest of the background and it is possible that this is due to the fibroadenoma.

The image obtained of the right breast, in the second case, exhibits no strongly dominant feature, although once again a region of higher absorption seen in the upper inner quadrant is consistent with the expected position of the fibroadenoma. However, the image obtained of the left breast also shows two regions of contrast similar to that seen in the location of the fibroadenoma.

It is difficult to compare the values of the absorption coefficient obtained with previous studies, as no in vivo data is available for the optical properties of a fibroadenoma (see section 1.2.5). The closest study is that by (Taroni et al 2004), where no distinct optical properties for a fibroadenoma were exhibited. Additionally, it is known that the quantitation obtained for our images is inaccurate for several reasons. First, as was observed in the phantom study in section 2.1.3, there will be a reduction in the contrast due to the partial volume effect. Second, the

displayed values are difference values rather than absolute values. And third, once again true separation of absorption and scatter is not possible.

Both cases are typical of what has been observed for fibroadenomas in our study. From a study of 6 volunteers we observe that in most cases the fibroadenoma appears as a region of higher absorption though it is rarely the most dominant feature in the image.

2.2.4 Fibroadenoma with fine needle biopsy

A 31- year -old women was diagnosed as having a fibroadenoma within the upper right quadrant of her right breast. The fibroadenoma had been located by ultrasound and was known to be 13 mm by 6 mm by 3 mm and located 4 mm beneath the skin surface. The position of the fibroadenoma and the ultrasound scan are shown in figure 2.2.10. On the day of the optical scan the volunteer had undergone a fine needle biopsy to provide further diagnosis. This procedure inevitably produces a degree of surface bruising, rupturing minor blood vessels, and so resulting in an increased absorption by blood immediately below the skin. This provides us with a unique case that may provide a large increase in contrast and so enable us to perform further analysis of our images.

Figure 2.2.10: An indication of the position of the fibroadenoma and the ultrasound image of the fibroadenoma.

In this study the volunteer's right breast was imaged twice. The reconstructed images for both scans at both wavelengths are shown in figures 2.2.11 and 2.2.12.

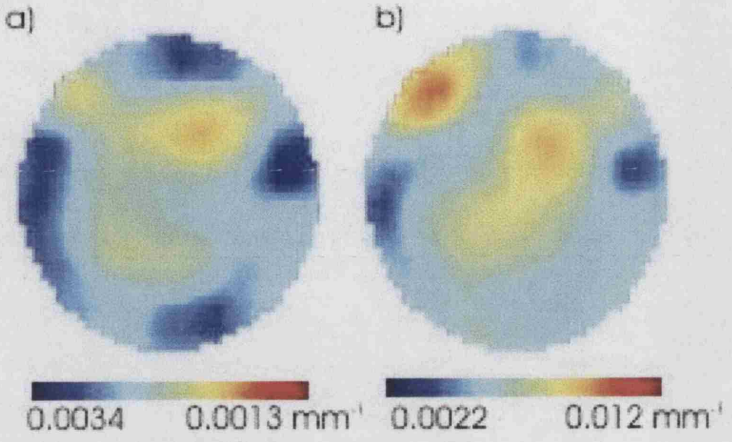

Visibility score = 3 Visibility score = 4

Figure 2.2.11: The right breast of a volunteer with a fibroadenoma in the position indicated in figure 2.2.10. a) is at λ = 780nm, b) λ = 815nm

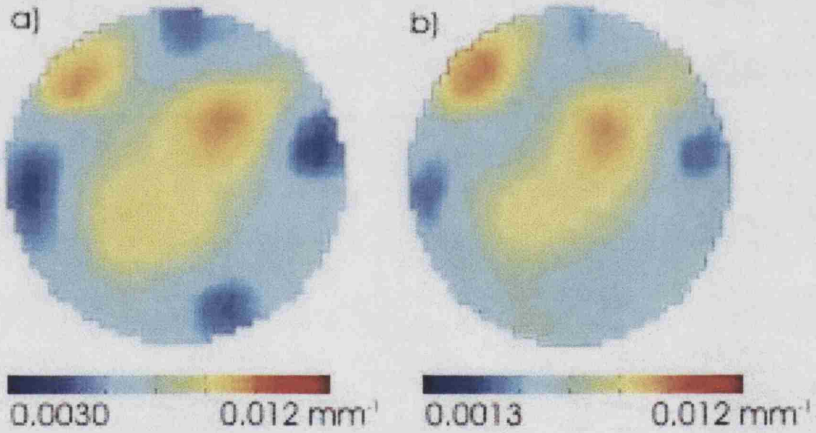

Visibility score = 4 Visibility score = 4

Figure 2.2.12: A second scan of the right breast of a volunteer with a fibroadenoma in the position indicated in figure 2.2.10. a) is at λ = 780nm, b) λ = 815nm

2.2.4.1 Blood volume and oxygen saturation images

For optical tomography to fulfil its potential it is imperative that blood volume and oxygen saturation parameters can be determined. Other groups have investigated the bulk oxygen saturation and blood volume properties of the breast in healthy tissue (Grosenick et al 2003; Heffer et al 2002; McBride et al 1999). Attempts to obtain images representing the blood volume and fractional oxygenation values of the tissue from the absolute values of absorption

coefficient at two wavelengths can be made, assuming that the only wavelength dependent absorbing compounds in the tissue are oxy- and deoxyhaemoglobin. In this study difference values of absorption relative to a homogenous phantom are reconstructed. Providing the initial estimate used in the reconstruction is accurate (the values of reduced scatter and absorption coefficients for the phantom are known to within ± 10%) then the absorption values obtained represent the absolute values and so can be used to produce blood volume and fractional oxygenation maps. A full discussion of the different methods that can be employed for our application is given by (Hillman 2002). The oxygen saturation, *S*, and blood volume, *BV*, can be expressed as follows:

$$S = \frac{[HbO_2]}{[HbO_2]+[Hb]} \times 100 \qquad \textbf{(2.2.1)}$$

$$BV = \frac{V_b}{V_t} \times 100, \qquad \textbf{(2.2.2)}$$

where $[Hb]$ denotes the concentration of deoxy-haemoglobin, $[HbO_2]$ the concentration of oxy-haemoglobin, V_b the volume of whole blood in tissue and V_t the total tissue volume. In order to calculate the fraction of whole blood in tissue, we need to estimate the concentration of haemoglobin in blood, C_{Hb}. A value of ~2mM is given by (Cope 1991) although the value depends on age, sex and the size of the blood vessel from which the blood was extracted. If we now define $\chi_{HbO_2,\lambda 1}$ as the specific absorption coefficient of 100% oxygenated whole blood at wavelength λ_1 multiplied by C_{Hb} and $\chi_{Hb,\lambda 1}$ as the specific absorption coefficient of 100% deoxygenated whole blood at wavelength λ_1 multiplied by C_{Hb}, then we can express the absorption coefficient of a tissue at a particular wavelength in the following way:

$$\mu_{a,\lambda_1} = (1-BV)\mu_{a,bg,\lambda_1} + BV(\chi_{HbO_2,\lambda_1} S + (1-S)\chi_{Hb,\lambda_1})$$
$$\mu_{a,\lambda_2} = (1-BV)\mu_{a,bg,\lambda_2} + BV(\chi_{HbO_2,\lambda_2} S + (1-S)\chi_{Hb,\lambda_2}) \qquad \textbf{(2.2.3)}$$

where μ_{a,bg,λ_1} is the absorption coefficient of the non-blood component of tissue at λ_1. The values of the specific absorption coefficient of oxygenated and deoxygenated blood at 780 nm and 815 nm, taken from figure 1.2.7, are as follows (website 8):

$$\alpha_{HbO_2,780} = 0.16943 \text{ mm}^{-1}\text{mM}^{-1}$$

$$\alpha_{Hb,780} = 0.25437 \text{ mm}^{-1}\text{mM}^{-1}$$

$$\alpha_{HbO_2,815} = 0.22106 \text{ mm}^{-1}\text{mM}^{-1}$$

$$\alpha_{Hb,815} = 0.18158 \text{ mm}^{-1}\text{mM}^{-1}$$

The value of μ_{a,bg,λ_1} includes the absorption of the adipose and glandular tissue in the breast with no blood. The studies presented in chapter 1.2.5 indicate that the wavelength dependence of the absorption of these tissues over the narrow range of 780nm to 815nm is small compared to the changes associated with blood and so we can make the assumption that $\mu_{a,bg,\lambda_1} \approx \mu_{a,bg,\lambda_2}$. Using this assumption and equations 2.2.3 we can thus derive expressions for S and V in terms of $\mu_{a,\lambda 1}$, $\mu_{a,\lambda 2}$ and $\mu_{a,bg}$:

$$S = \frac{(\mu_{a,\lambda_1} - \mu_{a,\lambda_2} + \chi_{Hb,\lambda_2} - \chi_{Hb,\lambda_1})\mu_{a,bg} - \chi_{Hb,\lambda_2}\mu_{a,\lambda_1} + \chi_{Hb,\lambda_1}\mu_{a,\lambda_2}}{(\chi_{HbO_2,\lambda_2} - \chi_{Hb,\lambda_2})(\mu_{a,\lambda_1} - \mu_{a,bg}) - (\chi_{HbO_2,\lambda_1} - \chi_{Hb,\lambda_1})(\mu_{a,\lambda_2} - \mu_{a,bg})} \times 100$$

(2.2.4)

$$BV = 1 + \frac{\chi_{Hb,\lambda_2}\chi_{HbO_2,\lambda_1} - \chi_{Hb,\lambda_1}\chi_{HbO_2,\lambda_2} + \mu_{a,\lambda_1}(\chi_{HbO_2,\lambda_2} - \chi_{Hb,\lambda_2}) - \mu_{a,\lambda_2}(\chi_{HbO_2,\lambda_1} - \chi_{Hb,\lambda_1})}{\chi_{Hb,\lambda_1}\chi_{HbO_2,\lambda_2} - \chi_{Hb,\lambda_2}\chi_{HbO_2,\lambda_1} + \mu_{a,bg}(\chi_{Hb,\lambda_2} - \chi_{Hb,\lambda_1} + \chi_{HbO_2,\lambda_1} - \chi_{HbO_2,\lambda_2})} \times 100$$

(2.2.5)

These equations require an estimate for $\mu_{a,bg}$. In this case the absorption of the breast is estimated to be 0.007 mm^{-1} as this is deemed to be a reasonable estimate for pre-menopausal volunteers (section 1.2.5). According to (van der Zee 1993),(Matcher et al 1993) the background absorption can be estimated to be 70% of the absorption of the tissue and so $\mu_{a,bg}$ is taken to be 0.005 mm^{-1} for this study.

Using equations 2.2.4 and 2.2.5, oxygen saturation maps and blood volume maps can be derived from the absorption images at both wavelengths by calculating the relevant values on a node by node basis. Images derived in this way from the absorption images in figure 2.2.12 are shown in figure 2.2.13.

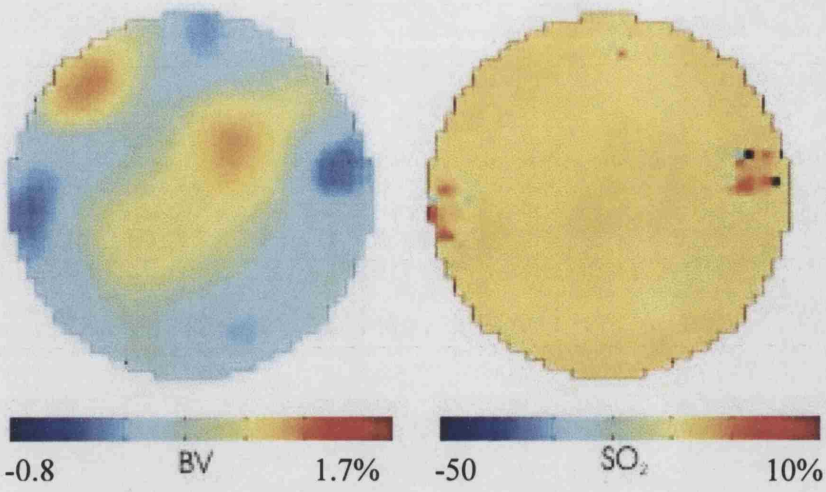

Mean = 0.5 % Mean = - 13.2 %

Figure 2.2.13: Blood volume and scaled oxygen saturation map derived from the images in figure 2.2.12. With an assumed value of $\mu_{a,bg} = 0.005$ mm^{-1}.

2.2.4.2 Discussion

Absorption images were reconstructed which exhibit an area of contrast at the expected location of the fibroadenoma as determined by ultrasound. A fine needle biopsy, being an invasive technique, will lead to the rupture of blood vessels and so a degree of internal bleeding (bruising) will occur. This increase in blood volume will increase the absorption of the affected area and so the increase in the contrast in figure 2.2.11 and 2.2.12 compared with those obtained in figures 2.2.8 and 2.2.9 is likely to be due to this.

There is a second feature of high absorption in the image that does not correspond to the region of the fibroadenoma. This appears to be a similar feature to that seen in the images of the healthy volunteers and so could be one of the anatomical features described previously. An alternative possibility is that this is due to a second fibroadenoma. It is not uncommon for fibroadenomas to occur in clusters and the shape, size and contrast of the lesion is similar to that of the previously described feature at the known location of the fibroadenoma. However, no abnormality was detected in this region with ultrasound, but it is noted that ultrasound has a poor ability to see deep lesions. It should be noted that if this feature does relate to a normal anatomical structure it could prove difficult to differentiate between this feature and a fibroadenoma in a 'blind study'.

Quoted blood volume values for the brain are ~2% (Hebden et al, 2002; Wyatt et al, 1990) therefore the blood volume values obtained in figure 2.2.13 are reasonable given that the blood

volume of the breast is likely to be lower than that of brain tissue. However, unphysical, negative blood volume values are also displayed. The image of blood volume is also similar in appearance to the absorption image presented in figure 2.2.12. This is to be expected as the largest contribution to absorption in the breast comes from the haemoglobin in blood as discussed in chapter 1.2. The values in the oxygen saturation images however are physically impossible. The oxygen saturation must have a value between 0 and 100% and is expected to be of the order of 70% (Durduran et al 2002). There are, however, some limitations of the method employed. First, the images obtained in this manner are entirely reliant on the accuracy to which the absorption values of the subject can be determined. As described in depth else where the scatter coefficient of the tissue will affect the quantitation of the absorption images reconstructed assuming constant scatter and so errors might be expected in the oxygen saturation and blood volume values determined in this way. Second, the values of oxygen saturation and blood volume are reliant on an accurate determination of μ_{abg} and so the estimated value used here may lead to further inaccuracies. However, an investigation showed that using background properties over a range of $\mu_{a,bg}$ = 0.0005 to 0.009 mm^{-1} still yields saturation values outside of the physically viable range. This range of $\mu_{a,bg}$ is consistent with the range of values measured by the published studies discussed in section 1.2.5. One way to potentially overcome both these limitations is to reconstruct the values of oxygen saturation and blood volume directly which was introduced by (Corlu et al 2003), however this approach has not yet been fully implemented within our reconstruction algorithm. Third, it is assumed in the calculations presented in this chapter that the absorption of chromophores other than oxy and deoxy haemoglobin are constant and known. Other groups (McBride et al 1999; Taroni et al 2004) have shown that determination of the absorption of water can lead to increased quantitation of oxygen saturation and blood volume parameters as well as providing additional diagnostic information. In order for this to be achieved acquisition at more than two wavelengths must be performed. In fact a study by (McBride et al 1999) conclude that a minimum of four wavelengths will be needed to produce quantitative images of tissue functional parameters in the breast. At present our system only has the capability to acquire at two wavelengths making the assumptions of a steady background necessary. The addition of other wavelengths is to be a future hardware improvement.

We must conclude, therefore, that it is not possible to obtain accurate values for blood volume and oxygen saturation using this method.

2.2.5 Cysts

As described in section 1.3, cysts are fluid filled sacs that develop within the breast tissue, and are generally quite easy to diagnose during ultrasound examination. Studies reported by (Taroni et al 2004) have shown cysts to typically exhibit low scatter in optical images. A volunteer presented at clinic with an extremely large (11cm) cyst in her left breast and several small cysts in her right breast as shown by ultrasound examination (figure 2.2.14).

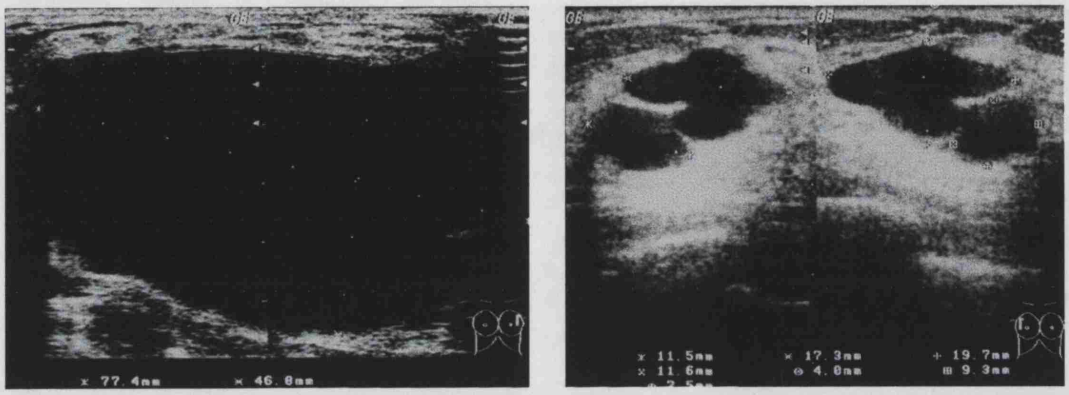

Figure 2.2.14: The ultrasound images of the a) left and b) right breasts of a patient with a large cyst in the left breast and small cysts in the right breast.

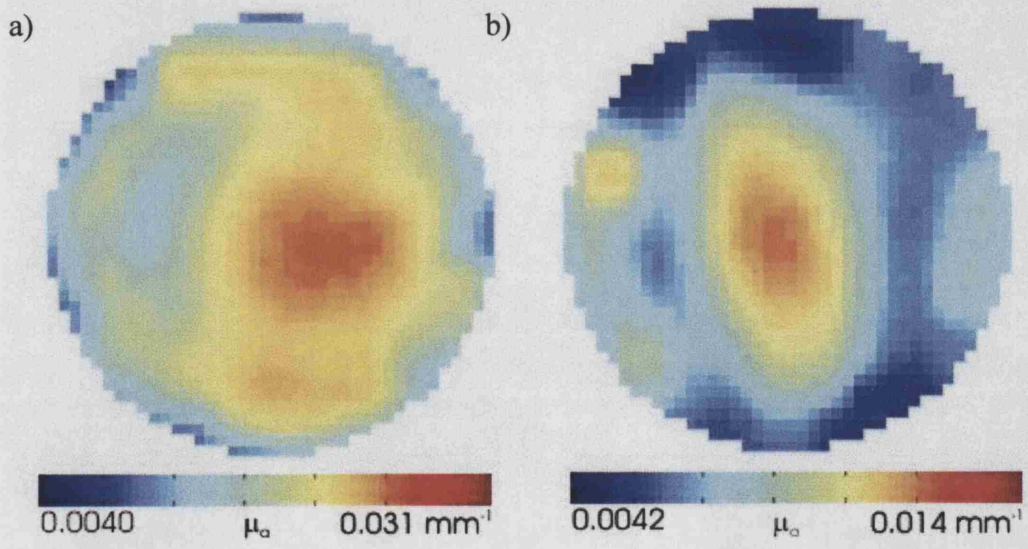

Figure 2.2.15: The absorption images obtained whilst using the single datatype of meantime and assuming constant scatter for a) the left breast and b) the right breast of a patient with cysts in both breasts as indicated in figure 2.2.14.

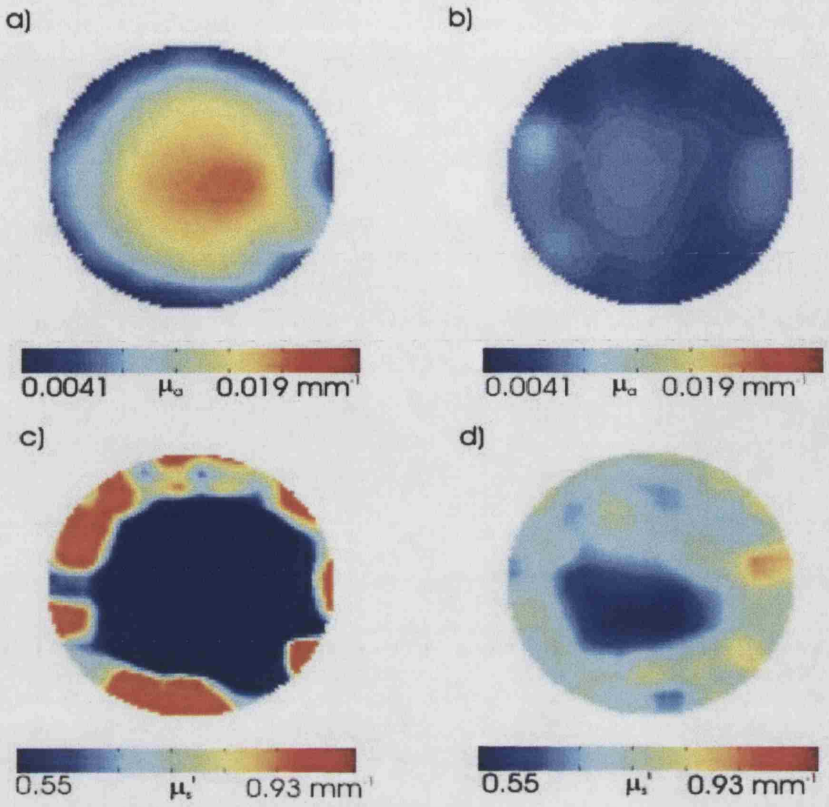

Figure 2.2.16: The absorption and scatter images obtained whilst using the single datatype of meantime for a) and c) the left breast and b) and d) the right breast of a patient with cysts in both breasts as indicated in figure 2.2.14.

The large cyst in the patient's left breast is likely to be the cause of the feature that dominates the absorption image shown in figure 2.2.15 a. A reported case study (Hebden *et al* 2005), which is presented in section 2.3.2, revealed that cysts can provide relatively strong optical contrast as a consequence of their low scatter. The effect of a low scattering region will be the opposite of that described for the high scattering feature in section 2.1.3. A decrease in local scattering causes the measured temporal distribution of photon flight times to become narrower, decreasing the mean photon flight time. Since a local increase in absorption also decreases meantime, absorption images reconstructed assuming constant scatter display regions of low scatter as absorption increases (assuming data is dominated by 'transmission' rather than 'reflection' measurements). This is further verified by the images presented in figure 2.2.16 a and c which were reconstructed for scatter and absorption separately. The scatter image (figure 2.2.16 c) is dominated by a low scatter region due to the cyst although some cross talk into the absorption image (figure 2.2.16 a) remains.

The images of the right breast are not as clear. There are two regions of low scatter in figure 2.2.16 d that correspond to the region of the cysts as defined from ultrasound. However, there are also other regions of similar contrast in the image and a large region in the centre of the image that has a lower scatter value. Neither image of absorption for this breast exhibits distinct regions of contrast in the location of the cysts. It is possible that the cysts in this breast were either too small (~10 mm) to be clearly defined by this system or were located outside the plane of the imaging ring.

2.2.6 Summary

The following table (table 2.2.1) lists the total number of volunteers imaged with healthy or benign tissue and where applicable the visibility score for the images obtained. In all cases the visibility score listed is the best score given out of the images acquired for both wavelengths.

	Number of volunteers/(scans)	Number of images obtained	Score	Average Score
Healthy volunteer	3(7)	4	N/A	N/A
Benign nodularity	4(4)	4	2,2,3,4	2.75
Fibroadenoma	8(8)	6	X,X,1,2,3,3,4,4	2.83
Cyst	1(1)	1	5	5
Total	16(20)	15		Average = 3.0

Table 2.2.1: A summary of the results obtained for different benign conditions

The following has been concluded from the study of healthy and benign tissue:

- Images of healthy volunteers exhibit various inhomogeneties and a degree of right and left symmetry;
- 10 out of 11 benign lesions have been identified but none are the most significant feature in the image;
- Reliable images of blood volume and oxygen saturation cannot be generated using the current method due to a lack of sufficient separation between absorption and scatter;
- Volunteers have found the scans comfortable, although the rings have been unsuitable for some breast sizes.

2.3 Clinical Studies part II: Malignant Conditions

The ultimate goal of optical mammography is to be able to locate and diagnose malignant lesions. To achieve this it is therefore of utmost importance that patients with malignant lesions are scanned to investigate their appearance in optical mammography. A complication unique to this group, however, is that the time window between diagnosis of a malignant lesion and its removal by surgery is ideally only a couple of days. Additionally there is a great anxiety associated with such a diagnosis and the resulting surgery (see section 2.5). For these reasons it was decided that it would be best to approach and scan potential volunteers that had a lesion the surgeon suspected to be malignant but were yet to undergo tests to confirm this, such as a fine needle biopsy, or MRI examination. The problem with this approach, however, is that the time window between initial examination and investigation is still small and so appointments could not be planned in advance. This is a problem, as the electronics in the MONSTIR system need to be switched on for at least 18 hours prior to a scan to reach temporal stability. To overcome this the system was placed 'on standby' for a period of time during the weekly breast clinic at University College London Hospital (UCLH). Potential volunteers were then approached during the clinic and, if consent was given, a scan was performed that day.

2.3.1 Suspected malignant lesion

A 62 year old volunteer was referred to us during a standby session as having a suspect lesion in the lower, inner quadrant of the left breast. The volunteer was asked to indicate the position of the lesion in relation to the imaging ring. This position is illustrated in figure 2.3.1. The volunteer had some scar tissue due to the removal of a malignant lesion by surgery in this region. A recurrence of the malignancy in this region was suspected. The volunteer was scanned and the reconstructed images are shown in figure 2.3.2.

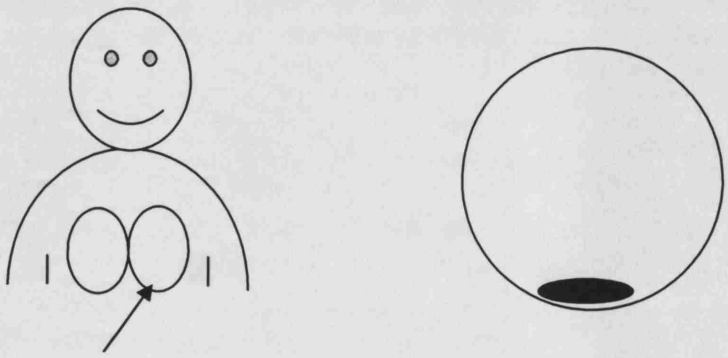

Figure 2.3.1: The location of a suspicious lesion as indicated by the volunteer.

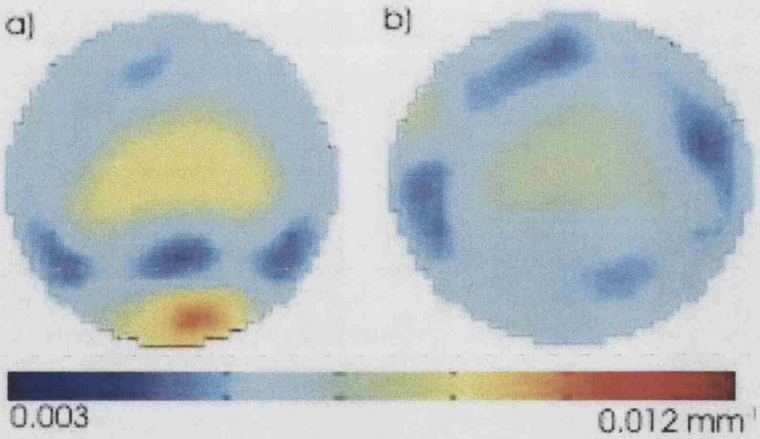

Visibility score = 5

Figure 2.3.2: The absorption images for the a) left breast, and b) right breast of a volunteer with as suspicious lesion in the location presented in figure 2.3.1.

After the optical scan was performed the woman underwent further investigation of the suspicious area in the form of MRI (unsuccessful), contrast enhanced ultrasound and fine needle biopsy. The reports of each of these investigation is presented below:

a) MRI

'This lady attended the department today for an MRI examination of her breast.

Unfortunately, due to her body habitus, she was unable to fit into the scanner. It was therefore not possible to image her today.'

b) Contrast enhanced Doppler ultrasound:

'On baseline scan 3 new nodules (biggest 9.3 x 8.9 x 3 mm) were seen on the anterior/superior wall of the cystic (intruding into) structure seen at last scan. Following contrast injection (2.4 ml Sonovue and further 2 ml of Sonovue) no enhancement was seen (the minimum Colour Doppler scale on this scanner is over 1.6 cm/s). Three core biopsies of area taken and sent for histology.'

c) Fine needle biopsy reports:

I.

'Histological diagnosis:

Breast core biopsies: Scar, radiotherapy changes (B2).

Microscopic Description:

Breast core biopsies showing hyaline fibrosis of stroma suggestive of scar'

B2 is a category given to tissue in a Fine Needle Aspiration that means the sample was benign.

II.

'Histological diagnosis:

Breast core biopsies: Scar, radiotherapy changes (B2).

Microscopic Description:

Breast core biopsies showing hyaline fibrosis of stroma suggestive of scar tissue. Benign ducts showing apocrine metaplasia are present. Within the stroma are occasional clusters of cells with nuclear features that are consistent with previous radiotherapy. Scattered mast cells are seen but these do not appear to be in a perivascular location. There is no evidence of malignancy.'

2.3.1.1 Discussion

Although this case proved to be a benign lesion, it does highlight certain issues when dealing with a clinical study of this nature. First, the protocol used for imaging patients with suspected malignant lesions is inevitably going to mean that some cases will prove to be benign. This is not a particular problem as further investigation of the appearance of benign lesions is always of use, although it is necessary to ensure that a wide sample of patients with malignant lesions are imaged as well.

A second issue is the complexity of diagnosing a lesion and the need for additional information from alternative imaging techniques. In this case, further diagnosis of the lesion was required, as the surgeon remained concerned about this region after the standard ultrasound test. Thus the patient was referred for an MRI investigation, although, as stated in the report, the volunteer was unsuitable for examination by MRI. This highlights a limitation of MRI and also a potential advantage of optical imaging. This volunteer was eventually subjected to a Doppler ultrasound investigation, which involved the injection of a contrast agent, and a fine needle aspiration, both of which suggested the lesion to be benign. Should optical imaging prove successful then this is one case where it would have been the technique of choice over other available modalities, as it is possible to adapt optical imaging for a wide range of body sizes and it does not require the injection of a contrast agent to provide the functional information that was required in this case. It is even possible that optical imaging would have prevented the need for a fine needle aspiration examination in this case, but this will depend on whether the desired sensitivity and specificity can be achieved.

It should be noted that some problems were experienced in imaging this volunteer with our system due to her size. It proved difficult to position the volunteer in the required sitting position and using a single ring meant that large parts of her breast were not sampled. This is something that is to be improved upon in a future design for a patient interface.

The results presented in figure 2.3.2 appear to correspond with the findings of the contrast Doppler ultrasound and fine needle aspiration results. The reconstructed images exhibit a region of high contrast in the location of the scar tissue and potential lesion in the volunteer's left breast. This feature is not seen in the reconstructed image of the volunteer's right breast. The particularly high contrast seen in this image compared to other benign lesions is likely to be a result of the scar tissue in this area, as has been seen in the case of the removal of a fibroadenoma by laser surgery, and the case where a volunteer had undergone a fine needle biopsy on the morning of the optical scan.

2.3.2 Malignant lesion

A 48-year-old lady presented at the breast clinic with a breast mass composed of two separate lumps in the right upper outer quadrant. An MRI scan was performed prior to the optical scan. The lesion was diagnosed as an invasive ductal carcinoma grade III ($T_3N_1M_0$). Lesions of this grade are highly vascularised. During the optical scan her right and left breasts were both imaged. Figures 2.3.3 and 2.3.4 show the absorption images obtained at 780 and 815 nm. Figure 2.3.5 shows the subtracted MRI image, using the contrast agent Magnavist. The MRI image in figure 2.3.5 is shown in a similar orientation to that of the optical scans.

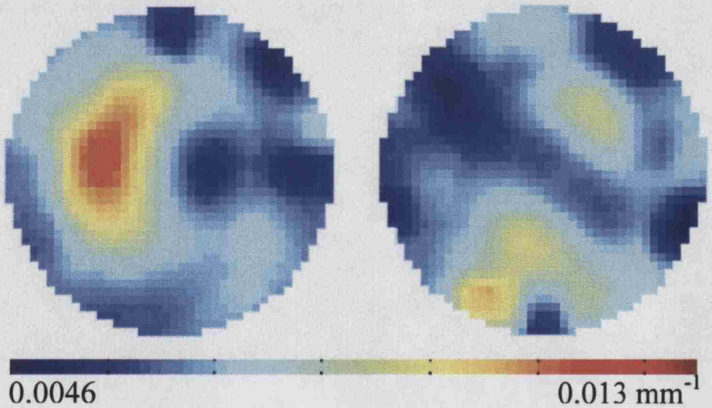

Visibility score = 5.

Figure 2.3.3: The absorption images at 780 nm of the a) right and b) left breast of a patient with an invasive ductal carcinoma located in the right breast.

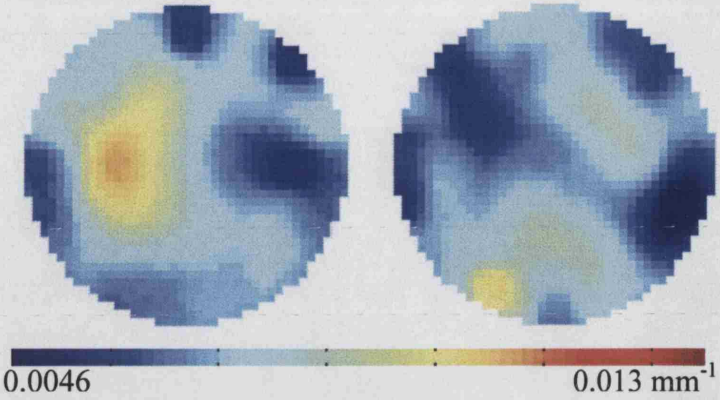

Visibility score = 5

Figure 2.3.4: The absorption images at 815 nm of the a) right and b) left breast of a patient with an invasive ductal carcinoma located in the right breast.

Figure 2.3.5: A subtracted MRI image highlighting the tumour in the right breast.

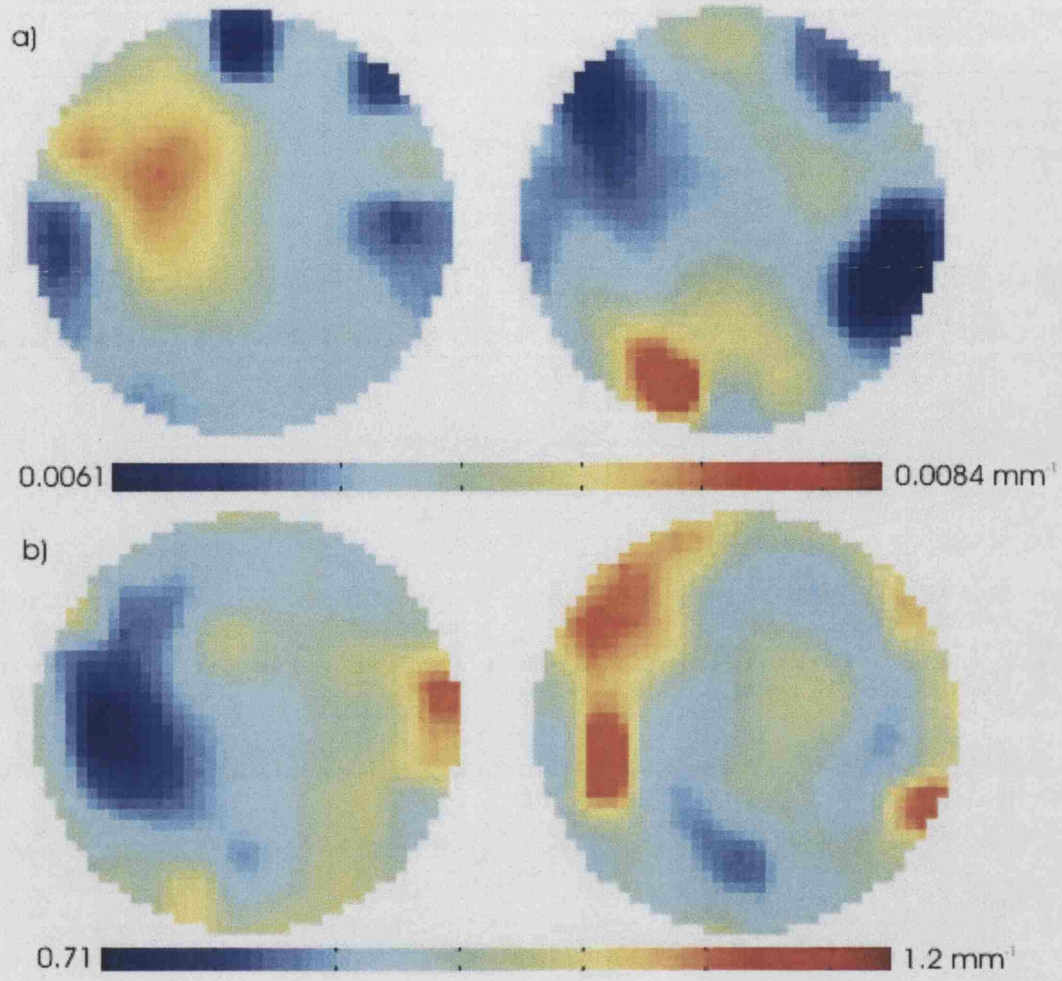

Figure 2.3.6: The a) absorption and b) scatter images for both the right and left breasts at 815 nm using dual parameter reconstruction.

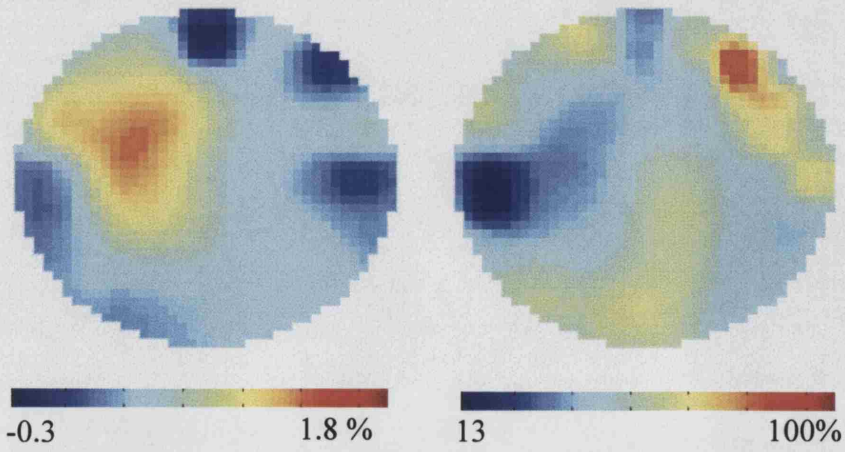

Figure 2.3.7: The a) blood volume and b) oxygen saturation images for the symptomatic breast.

2.3.2.1 Discussion

The optical images obtained in figures 2.3.3 and 2.3.4 show a large absorbing region whose position correlates well with the tumour identified in the corresponding MRI image. The optical contrast is consistent with what we would expect for a highly vascularised malignant lesion. No similar feature is observed in the corresponding absorption image for the left breast although there is a small region of high contrast to the bottom left. This is possibly an artefact caused, for example, by inconsistent coupling at the surface near the feature, but may also be due to a surface blood vessel.

The optical absorption images obtained at a wavelength of 780 nm (figure 2.3.3) are qualitatively very similar to those shown in figure 2.3.4, although there is a slight increase in the absorption maxima in the region of the lesion at 780 nm compared with 815 nm, which would indicate an increased concentration of deoxy haemoglobin in this region. This is consistent with previous studies (Grosenick et al 2003) and with the known physiology associated with increased vascularity in the region of a tumour. Unfortunately without sufficient separation between absorption and scatter, blood volume and oxygen saturation maps cannot be obtained as was shown in section 2.2.4.1.

A degree of separation is achievable using meantime only although the corresponding scatter images are susceptible to artefacts (Hebden et al 2004). In this case the presence of the tumour may invalidate our assumption that scatter in the breast is constant, and so improved image quality and information on the variation of scatter across the breast may be obtained by reconstructing for both parameters separately. The images reconstructed for both absorption and scatter using meantime are shown in figure 2.3.6. The absorption image obtained now exhibits a second smaller feature that merges into the larger feature consistent with the initial clinical diagnosis of two distinct lesions, which are also apparent in the corresponding MRI scan. Meanwhile, the scatter image shows a distinct decrease in scatter in the region of the lesion. There is also a region to the left of the image that exhibits high scatter, which does not appear to relate to any feature seen in the MRI image and is most likely to be artefactual.

As presented in section 2.2.4.1, attempts to obtain images representing the blood volume and fractional oxygenation values were unsuccessful due to the lack of separation obtained between scatter and absorption. An attempt was made to produce such maps for this study using the absorption images obtained with the dual parameter reconstruction presented in figure 2.3.6 and its equivalent image obtained at 780 nm. The image of blood volume obtained is qualitatively similar to the absorption image. This is what we would expect given that we are assuming that

the only wavelength dependent absorbing compounds in the tissue are oxy- and deoxy-haemoglobin. The image of fractional oxygenation, however, shows a decrease in oxygenation in the approximate location of the lesion but an increase in oxygenation to the outer top left of the image. The decrease in oxygenation is consistent with previous studies and the known physiology of a tumour. The cause of the increase in oxygenation, however, is unknown. It is possible that it is due to a surface blood vessel although no such feature is apparent in the corresponding MRI image.

The quantitation in both the haemoglobin volume and the fractional oxygenation images are poor. The haemoglobin value is lower than that obtained by previous researchers for the brain (~2%), however as was mentioned in section 2.2.4.1 this might be expected. Once again unrealistic negative values are present. The values of fractional oxygenation again appear to be outside the physically viable range (i.e. 0 to 100%). Reasons for this lack of quantitation are the inability to completely separate absorption and scatter using one data type, inaccuracies in the values used for the concentration of haemoglobin in blood and the absorption coefficient of the non-blood component.

2.3.3 Other suspect cases

Three other volunteers with malignant lesions were referred to us during standby sessions. Unfortunately these scans were unsuccessful. In two cases it proved impossible to provide a constant coupling between the breast and the sources and detector bundles around the whole circumference of either ring. In both cases the volunteers were older than those imaged with benign lesions and so their breasts were likely to contain a higher proportion of adipose tissue compared with the previous studies. This resulted in a more pendular shaped breast and hence the circular geometry of the ring was not suitable. An additional problem encountered with these older volunteers was that they were less mobile and so it proved more difficult to position them in the upright position required using the adjustable chair, as this requires a degree of manoeuvrability. As shown in figure 1.3.2 the risk of developing cancer increases with age and so it is not a coincidence that the volunteers with benign lesions were younger and so more agile than those with malignant lesions. Thus the geometry and flexibility of the patient interface must be adapted for this older age group.

In the third case the scan was unsuccessful because the suspect lesion was very close to the chest wall and proved to be out of plane of the imaging ring. Given that 50% of malignant lesions (figure 1.3.3) occur in this region this is a further serious limitation of this device.

2.3.4 Summary

	Number of volunteers/(scans)	Image obtained	Score	Average score
Scar tissue as a result of surgery to remove tumour	1(1)	1	5	5
Malignant lesions	4(4)	2	X,X,0,5	2.5
Total	**5(5)**	**3**		**3.33**

Table 2.3.1 A summary of the results obtained for the study of malignant lesions.

The following conclusions can be drawn as a result of the study of patients with malignant lesions:

- The geometry of our system is unsuitable for older woman;
- Scar tissue can provide a high contrast in our images;
- Limited sampling of the breast volume due to the use of one ring means that lesions can be missed;
- A malignant lesion has been imaged as the most dominant feature (based on a single result).

2.4 Clinical Studies part III: Other roles for optical imaging of the breast

At present the role of optical tomography in breast imaging is largely unresolved. Many studies have focused on determining its feasibility as a tool for cancer screening and have met with little success due to poor sensitivity (Drexler et al 1985; Grosenick et al 2003; Ntziachristos et al 2000; Taroni et al 2004). The main focus of the work of this thesis so far has been to determine the appearance of different tissue types in optical images to assess whether such information could be used to distinguish malignant lesions from benign or healthy tissue. There are however other specific applications where optical imaging may be beneficial. For example it has recently been proposed that NIR imaging may be useful for prescreening younger women to identify those at risk of developing disease (Pogue et al 2004; Srinivasan et al 2003). The facility to study tissue function may also make optical imaging a useful tool for detecting response to new and existing forms of therapy. This section looks at the role of optical tomography in the diagnosis of mastalgia and in studying the response of tissue to laser treatment. Both are applications for which current breast imaging modalities have proved unsuitable.

2.4.1 Mastalgia

As described in chapter 1.3, mastalgia (or breast pain) can be related to the menstrual cycle (cyclical mastalgia), with the pain intensifying close to menstruation. It is a condition that is not completely understood and often patients suffering from mastalgia exhibit no abnormal features in images obtained with other modalities (Pierce 2002). However, a large percentage of patients with cyclical mastalgia are referred for an x-ray mammogram to ease anxieties of an association with a malignancy (Duijm et al 1998). Various causes of mastalgia have been proposed such as hormonal influences, water retention, psychoneurosis and a deficiency of essential fatty acids although none have been proven to be the cause of cyclical mastalgia (Pierce 2002). It is possible that the functional information provided by optical mammography could help to identify the unknown physiological processes that cause mastalgia. If this were to be the case then optical mammography could become a valuable tool in the diagnosis, study and management of mastalgia.

A total of four women diagnosed with mastalgia have been imaged using our technique. This includes patients with cyclical and non-cyclical mastalgia.

A 28-year-old woman was diagnosed as having cyclical mastalgia. In order to study the relationship, if any, between the reconstructed images and the degree of pain she was imaged 6 times over an interval of 4 months at specific times corresponding to low and high pain within her cycle. On each occasion her left breast was imaged twice and for two trials her right breast was also imaged as a comparison.

Typical images for the two scans of the left breast and one of the right breast taken in one session are shown for a period of high pain in figure 2.4.1 and low pain in figure 2.4.2. Only the results of a single wavelength, λ=780nm, are presented since the images exhibited no significant wavelength dependence.

As a comparison two different homogenous phantoms were scanned concurrently and images were reconstructed using the data from one phantom relative to the other. The phantom images obtained in this way on two separate occasions are shown in figure 2.4.3.

The mean value for each pixel over both data sets for each scan was calculated and the resulting images are displayed in figure 2.4.4. The mean value of all the pixels in these images was then calculated to study the trend in the bulk absorption of the breast. This is shown in figure 2.4.5.

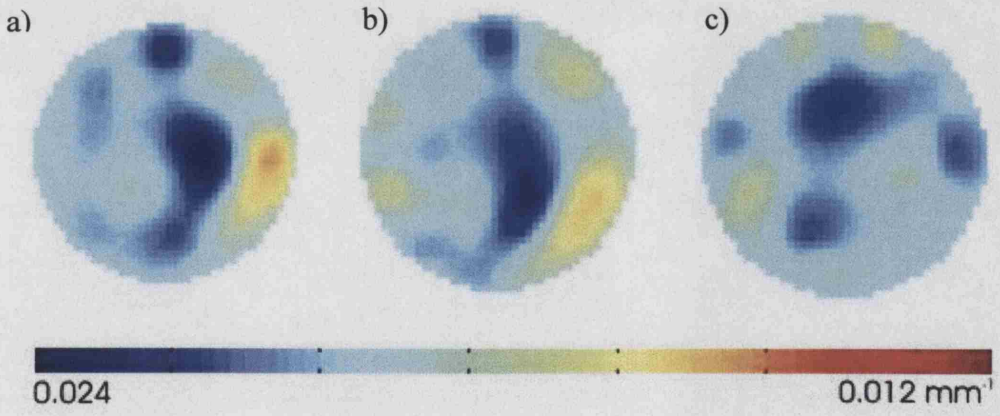

Figure 2.4.1: Images from volunteer's a) and b) left breast and c) right breast at a point of high pain within her cycle.

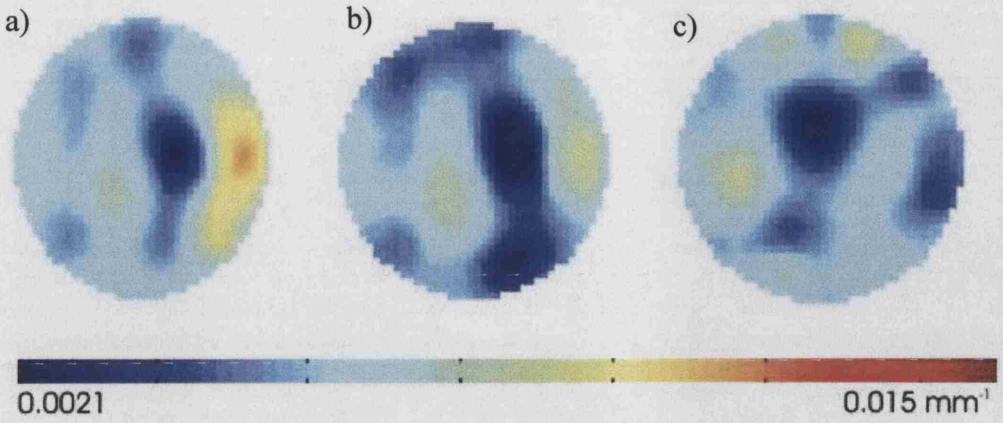

Figure 2.4.2: Images from volunteer's a) and b) left breast and c) right breast at a point of low pain within her cycle.

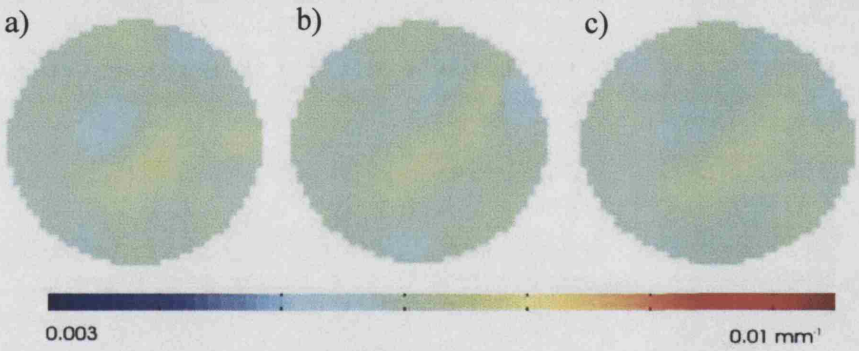

Figure 2.4.3: The reconstructed images of a phantom measured from two separate scans a) and b) and the mean values for those scans c).

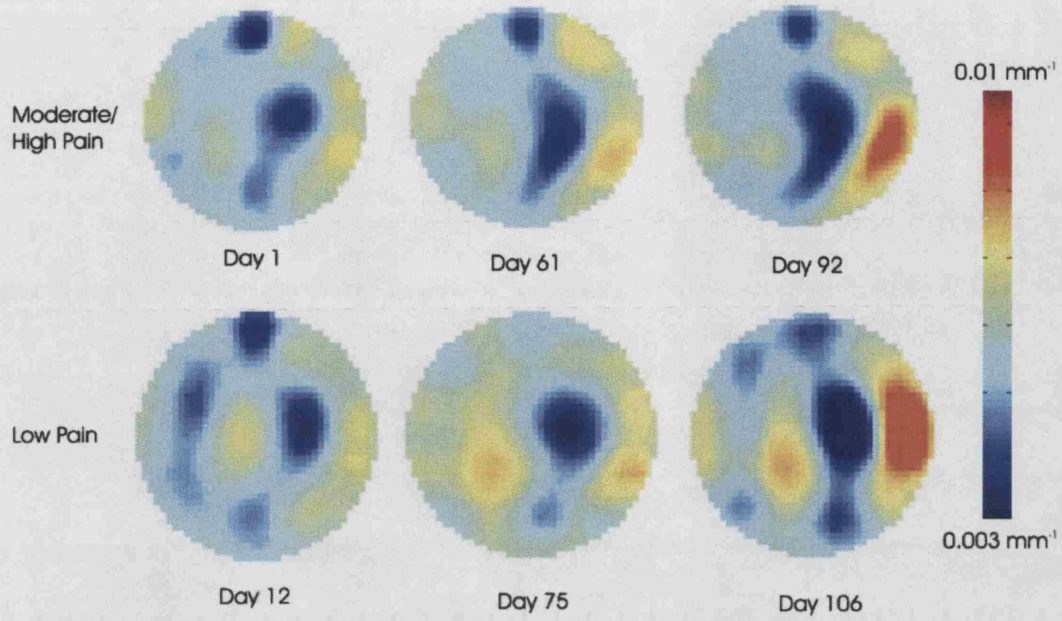

Figure 2.4.4: Images of the left breast of a volunteer suffering from cyclical mastalgia. The images represent the mean values of two data sets collected during the same scan session.

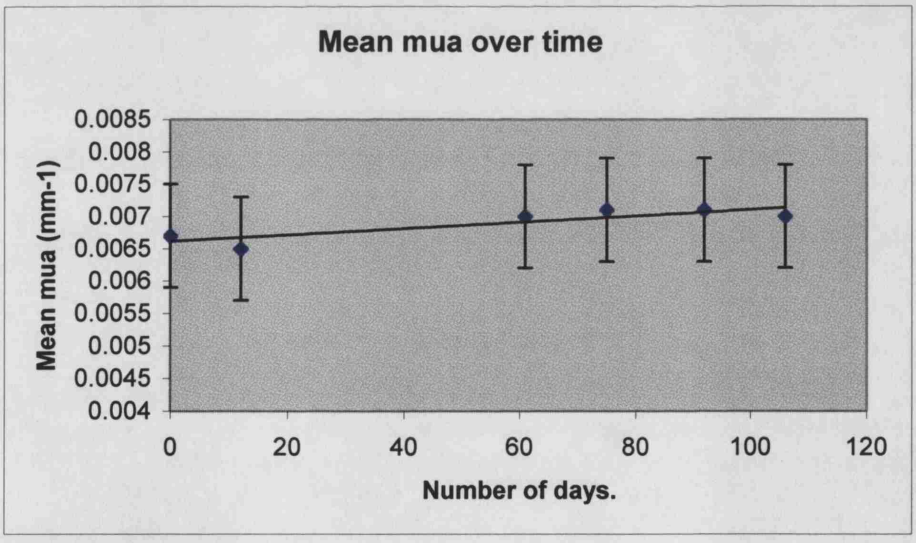

Figure 2.4.5: The mean value of the pixels in the images obtained from a patient with cyclical mastalgia plotted over time.

2.4.1.1 Discussion

Figures 2.4.4 and 2.4.5 reveal no apparent correlation between the time of the scan and the mean value of the pixels within the image. Instead the mean value appears to be constant (within the standard deviation) over time at a value of approximately 0.0068. The fact that no correlation is seen between the mean pixel value and the scan time indicates that the average absorption coefficient of the breast is not related to the menstrual cycle or to the extent of pain within cyclical mastalgia. Furthermore, we have found no link between pain and optical images of a further three patients with mastalgia. This includes 2 non-cyclical cases where the symptomatic and asymptomatic breasts were compared.

A remarkable result of this study is the reproducibility of the images over time. The images in figure 2.4.4 were recorded over an interval of 3 months and yet the same features within the image are apparent. Steps were taken to ensure that this was not due to a feature of the data acquisition or reconstruction. First, the sources and detector bundle positions were changed on successive scans to ensure the images were not a product of a specific source and detector arrangement. Second, the volunteer's right breast was scanned on three occasions and compared with the images obtained for the left breast. In each case the images of the right breast contained different contrast features to those in the left breast, as shown in figures 2.4.1 and 2.4.2, and so provided evidence that the images of the left breast were not systematic artefacts. In fact the images of the right breast appeared to exhibit a degree of mirror symmetry compared with those of the left breast. Third, a homogenous phantom was imaged using exactly the same method as the volunteer. As can be seen in figure 2.4.3 the images obtained appear to be homogenous when represented on the same scale as those from both breasts of the volunteer, again providing further validation of the images obtained.

The reproducibility of the acquired images is a significant result, indicating that the displayed features are due to the optical properties of the breast for this volunteer. The variation between images obtained from different volunteers suggests we can obtain an 'optical print' that is unique to each volunteer. While obviously encouraging, it is not yet possible to interpret this print. Our strategy is to record images on a broad range of breast types in order that we might gain more insight into the origins of tissue contrast using our technique.

2.4.2 Interstitial laser photocoagulation (ILP)

A further potential application of optical mammography is the assessment and monitoring of surrounding healthy tissue following treatment. At UCL, interstitial laser photocoagulation is offered as a routine treatment for fibroadenomas. The procedure involves the application of laser energy to the fibroadenoma, which causes heating of the lesion, coagulative necrosis, and the induction of an inflammatory response, which results in the resorption of the lump over a period of up to 12 months. Overall 89% of patients respond to ILP and it would be advantageous to be able to monitor response to ILP to identify non-responders early. They could then be considered for further laser treatment, or surgical excision. The treatment of fibroadenomas by laser surgery is in itself an experimental procedure (Bown 1998) and a method of monitoring its success would be highly beneficial. At present the most suitable modality is ultrasound due to its use of non-ionising radiation and lack of compression. It is possible, however, that the physiological information provided by optical mammography, which is also non-ionising and does not use compression, could provide a more efficient method of monitoring the recovery of tissue than the structural information provided by ultrasound.

A 26-year-old female with a BMI of 20.9 kgm^{-2} presented to the breast clinic with a painless lump in the right breast. Clinical examination revealed a smooth mobile lump in the right upper outer quadrant. An ultrasound scan (figure 2.4.7 a)) indicated a well defined acoustically hypoechoic lesion with estimated dimensions of 17 x 16 x 12 mm, and centered about 2 cm below the surface. Fine needle aspiration cytology was performed, which showed benign epithelial and stromal cells, confirming the diagnosis of fibroadenoma. The fibroadenoma was treated by interstitial laser photocoagulation under local anesthetic and sedation, and follow-up clinical and ultrasound examinations of the patient were performed at 3 month intervals.

Optical imaging scans of the patient were performed one week before and one week after treatment and immediately after each of the follow-up visits to the breast clinic, so close comparisons between the optical images obtained and clinical notes and/or the results of other diagnostic techniques could be performed.

The optical images were acquired using ring C. Care was taken to ensure that the lesion was located within the plane of the ring and that the position of the breast within the ring was as consistent as possible for each scan.

Figure 2.4.6 shows the absorption images of the right breast, acquired at 780 nm, for each of the six scans.

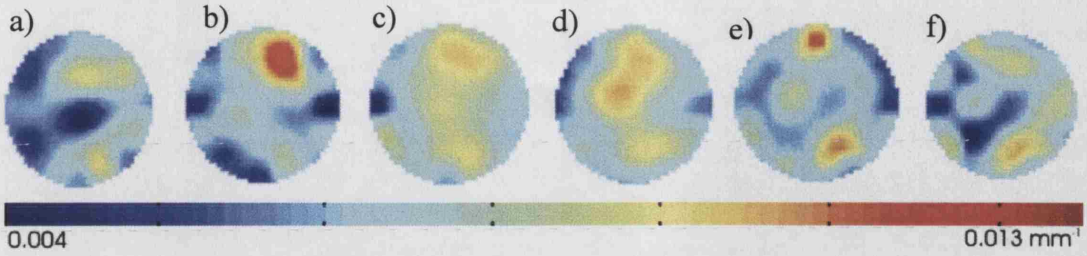

Visibility score = 3 5 4 5 4 3

Figure 2.4.6: The absorption images for a volunteer's right breast a) 1 week before, b) 1 week after and c) 3 months after d) 6months after e) 9 months after and f) 12 months after the removal of a fibroadenoma by laser surgery.

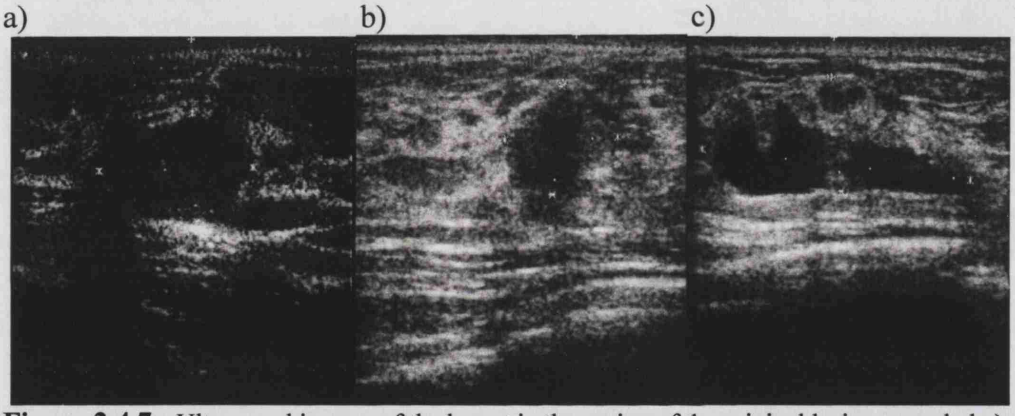

Figure 2.4.7: Ultrasound images of the breast in the region of the original lesion recorded a) one week before treatment b) three months after treatment and c) six months after treatment.

The image obtained prior to surgery exhibits no strongly dominant feature, although a region of higher absorption is seen in the expected position of the fibroadenoma. This is consistent with previous scans of fibroadenomas (section 2.2.3). One week after the surgery the image is dominated by a feature that is almost certainly due to the induction of a significant acute inflammatory response, with its associated increase in blood supply around the site of the recovering tissue. It would be expected that this would disperse over a period of weeks as the tissue recovers and the image obtained three months later does indeed show a reduction in contrast in this region. The image obtained six months post surgery, however, shows the appearance of a second absorbing feature.

In order to interpret the features seen in figure 2.4.6 it is necessary to consider how variation in the scatter coefficient will affect their appearance. A decrease in local scattering will cause the measured temporal distribution of photon flight times to become narrower, which also occurs

with a local increase in absorption. Narrowing of the distribution produces a decrease in the mean flight time. As a consequence, reconstructing absorption images while assuming constant scatter will display regions of low scatter as absorption maxima.

Ultrasound images obtained at 3 months and 6 months post surgery (figure 2.4.7) reveal evidence of a single large cyst at 3 months, which is accompanied by a second smaller cyst after six months. Cysts are fluid-filled and are therefore expected to exhibit low scatter (Taroni et al 2004) and therefore the presence of these cysts are almost certainly responsible for the apparent increase in the absorption seen in the optical images in figure 2.4.6.

During the third follow up session the patient elected to have the larger cyst drained by fine needle aspiration (FNA). The small sample of oily, clear, slightly yellow fluid extracted was analyzed and found to have optical properties consistent with fat. On the following day the fifth optical image in figure 2.4.6 was acquired. The feature corresponding to the larger cyst is now gone and the contrast due to the second smaller cyst has been reduced. Instead the most dominant feature in the image occurs at the surface at the point of entry of the FNA needle. As described in section 2.2.4 this procedure inevitably produces a degree of surface bruising resulting in an increased absorption by blood immediately below the skin. The cause of a second dominant feature at the lower right of the optical images is less certain. It occurs at a region where a local peak is observed in all the previous optical images and it is proposed that this feature is normal healthy breast tissue and that the variability in contrast may be due to differences in the positioning of the breast within the ring.

The images obtained here highlight the need to separate absorption and scatter for the images to be useful clinically. In these images the appearance of a cyst and acute inflamatory response appear to produce similar features within the optical images. As discussed previously to obtain separation of scatter and absorption it is advisable to employ at least two data types in the reconstruction. Specifically it has been proven that the use of intensity alone cannot provide unique separation of these parameters. In order to study the influence of scatter on the absorption images in figure 2.4.6 and so correlate the images to the clinical diagnosis it is therefore useful to study images reconstructed using two datatypes. Figure 2.4.8 shows the images obtained if variance is employed as a second data type in addition to meantime.

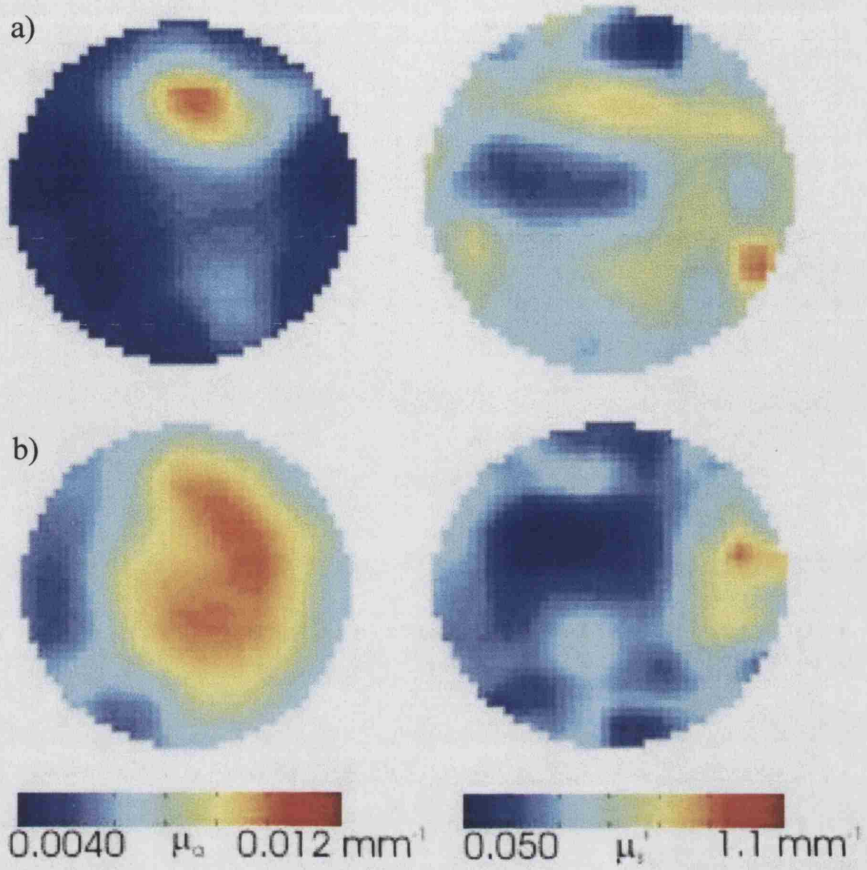

Figure 2.4.8: Absorption and scatter images for a) 1 week after and b) 6 months after treatment reconstructed using meantime and variance datatypes.

The images shown in 2.4.8 illustrate the problems involved with using meantime and variance as a combination of data types. The images produced do show similar features to those seen in figure 2.4.6. However, the absorption image in 2.4.8 b) shows little distinction between the two regions believed to be cysts. The scatter images, however, exhibit significant regions of inconsistent artefact. Previous phantom studies have shown that differences in variance are more susceptible to noise and calibration uncertainties (Hebden et al 2001), which is a likely source of the features seen.

In figure 2.4.9, images of both parameters are reconstructed using meantime alone. While previous experiments on phantoms have indicated that separation between absorption and scatter is likely to be imperfect, a degree of separation is possible, and perhaps sufficient to provide useful diagnostic information in this case.

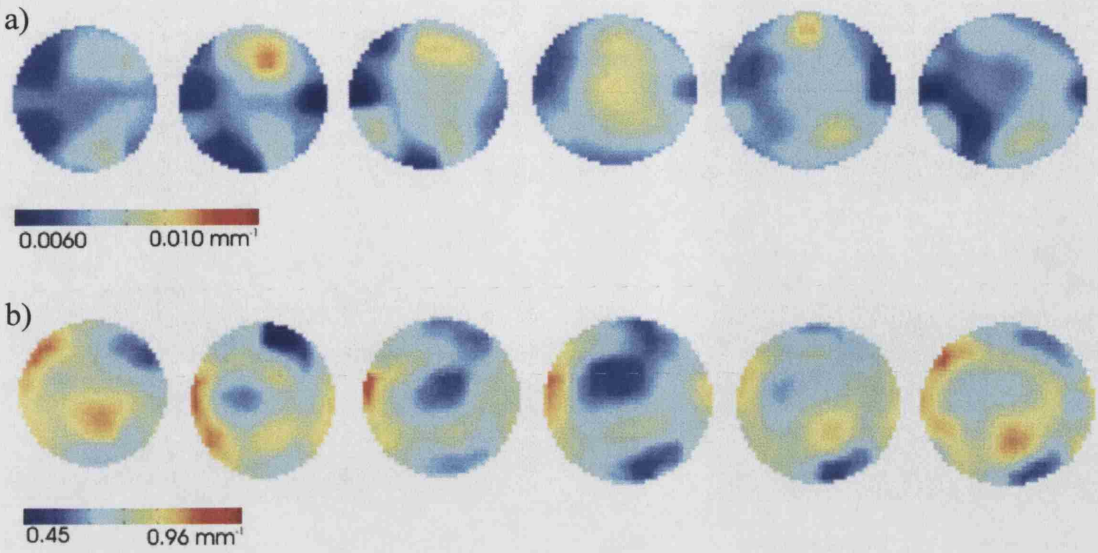

Figure 2.4.9: Images of a) absorption and b) scatter 1 week before, 1 week after and 3/6/9/12 months after surgery reconstructed using only meantime as a datatype.

The absorption images in 2.4.9 are similar in structure to those generated assuming constant scatter (figure 2.4.6). The scatter images exhibit a large variation within each image, although many of the most dominant features are common to all six scatter images. Again, the fibroadenoma does not exhibit high contrast in either absorption or scatter. The images acquired one week after treatment reveal a large local peak in absorption, as before, and the first evidence of an internal region of low scatter, just to the left of centre. At three and six months after treatment the low scatter feature grows significantly in size, although the scatter image at six months does not reveal the binary structure as dramatically as the corresponding absorption image reconstructed assuming constant scatter. After aspiration of the larger cyst the low scatter region is very much reduced. The bruising caused by the FNA needle is evident only as a peak in absorption, which is consistent with a local increase in blood content. It is interesting to note that the variation in amplitude of the feature we attribute to healthy tissue structure at the lower right of each image is now much less in the absorption images, but varies more significantly in the scatter images.

2.4.2.1 Discussion

The features that appear in the images correlate well with known and/or expected behaviour of breast tissue in response to ILP treatment. The images acquired assuming constant scatter provide sufficient resolution and sensitivity to detect regions of increased blood volume and the growth and evolution of cysts. Despite a degree of parameter cross-talk due to the use of a single datatype, we have also demonstrated a distinction between such regions based on their

absorbing and scattering parameters. Attempts to use a second datatype, either that of intensity or variance, have proved unsuccessful and so once again blood volume and oxygen saturation images could not be derived due to the lack of quantitation.

The results from this study so far show that optical tomography has the potential to monitor the recovery of tissue after surgery. If true then this is an encouraging finding as the absence of compression and its use of non-ionising radiation mean that optical mammography is suitable for repetitive imaging of sensitive tissue, whereas x-ray mammography is not. In fact at present there is no satisfactory method for the monitoring of tissue recovery as ultrasound images lack fine detail and functional information and MRI is too expensive to be employed on a long term bases and would require the injection of a contrast agent to provide functional information on the recovery of the tissue. However further studies in this area need to be performed to assess the suitability of optical mammography for this purpose.

2.4.3 Summary

	Number of volunteers/(scans)	Image obtained	Score	Average score
Mastalgia	4(9)	9	N/A	N/A
ILP	2(5)	6	After treatment – 3,3,4,4,5,5	4
Total	6(14)	15		4

Table 2.4.1: A summary of results obtained from specific cases of mastalgia and follow up from treatment of a fibroadenoma with ILP.

The following points have become apparent through the study of specific roles for optical breast imaging:

- Optical images show no correlation with a diagnosis of mastalgia, suggesting that mastlgia is unlikely to be due to an increase in water or blood volume.
- A specific optical print can be obtained for a patient that is reproducible over time.
- A single study suggests optical imaging can be used to monitor the recovery of tissue following ILP treatment.

It is important to note that there may be other specific applications where x-ray mammography or other modalities are inappropriate that may have a role for optical mammography.

2.5 Volunteer reactions to developing technology

An important aspect of the development of a new technique to be used in a clinical environment is the opinions of the volunteers themselves. The reasons for this are two fold. First, if there is an aspect of the imaging system that is intimidating in some way, then a psychological barrier may hinder the introduction of such a technique into routine use. One example of this was the decision to re-name the medical imaging application of nuclear magnetic resonance, 'magnetic resonance imaging' (MRI) and hence dropping the socially unacceptable "nuclear" term. Second, the volunteers first hand experience of the imaging process is necessary to determine the effectiveness of the technique in a clinical environment, especially in relation to comfort.

2.5.1 Collaboration with the Department of Science and Technology Studies

Throughout this project we have been part of a collaboration with Dr. Norma Morris at the Department of Science and Technology Studies at UCL. The purpose of this project has been to test the hypothesis that qualitative data obtained from volunteers can be of practical value in the decision-making about design modifications, development priorities, and improving acceptability to patients and health service professionals. In addition, it is believed that a deeper understanding of the anxieties and preferences of patient-volunteers will help to improve research protocols and possibly also the quality of results.

2.5.2 Format of data collection

Qualitative data on the volunteers' was collected in a one-to-one interview, performed by Norma Morris, directly after (in most cases) the scan has been performed. A standard questionnaire was developed as the basis for the interview but most questions were open-ended. Analysis of the impact of volunteer contributions to the imaging protocol was performed by discussions and consolidation of both volunteer and researcher feedback by Norma Morris. So far data has been collected and analysed from 14 volunteer interviews.

2.5.3 Reactions to date

An in depth review of this study is presented in (Morris et al 2003) which includes discussion of models for the patient researcher interaction. The following provides a summary of the results based on the reactions from volunteers. The feedback from volunteers has been placed into the following categories:

1. Practical suggestions for improvement of the patient interface;
2. Patient/volunteer criteria for acceptance of new instrumentation and process;
3. Social factors affecting the anxieties and satisfaction of patient/volunteers;
4. Volunteer motivation.

Most volunteers experienced some discomfort during the experimental scan sessions from the combination of the position required and the need to keep relatively still for up to 5 minutes. It should be noted, however, that the main concerns over the scan time were focused on the possible strain on staff resources.

Volunteers proved to be eager to offer suggestions for improvements to the patient interface. Examples of suggestions made were to change the angle of the rings, to use flexible rings, to devise a method to bring the machine to the patient rather than the patient to the machine, or to make the interface into a bra. In addition they were able to provide first hand advice as to where more support or padding was required to improve the comfort of the present interface. One point made by several of the volunteers was that the safety goggles made it difficult to rest the head on the padded support and so softer goggles would be more desirable.

The criteria for acceptance of a new procedure appeared to be based on safety, functionality, pain, physical exposure and isolation.

With regards to safety many volunteers stressed the fact that our system does not use x-rays as a major advantage of this technique. Some were already uneasy about the repeated x-ray exposure they had been subjected to in the investigation of their breast condition. Most volunteers accepted the use of light as non-hazardous, with little or no questioning, although a couple of volunteers expressed slight initial concern over the use of lasers. Many volunteers were reassured by the information that the same system is used for imaging the brains of premature babies.

Many volunteers had experienced frustration over the limitations of currently available methods and the uncertainty that resulted and so were prepared to give high priority to the development of new technology if it could offer significant advantages in quality and speed of information. Some volunteers referred explicitly to the optical system's ability to detect differences in blood supply as a potentially significant addition to existing sources of information. Others stated that the possibility for the system to have wider uses than for breast imaging, e.g. for monitoring oxygenation in the brains of premature infants, was an important factor in the priority that this development should have among other health service priorities.

A number of volunteers stated that they would not have wished to take part in the research had it involved any pain. The pain associated with x-ray mammography was notorious amongst the volunteers and anything that might reduce the need for mammograms won firm support. By comparison, no volunteers found the optical procedure painful in any way.

A further concern of particular importance in a breast imaging method is the physical exposure of the technique. Volunteers were impressed by the degree of modesty that was achieved using this technique as compared with other techniques such as ultrasound.

Volunteers also appreciated the fact that the machine operators were present in the room with the volunteer and not behind a shield as in x-ray mammography or outside of the magnet coils as with MRI. This prevented feelings of isolation.

Many of the concerns and anxieties of the volunteers have been covered in the acceptability of the procedure, however one unexpected social aspect was the volunteers concern that they were being a 'good volunteer'. Having agreed to participate most volunteers were anxious to be as useful as possible. This is related in part to the volunteers' motivation for participation in the study. For healthy volunteers this was mainly due to personal connections with either cancer patients or with researchers in the field.

Motivation amongst patient-volunteers included a desire to help others, a scientific or technological curiosity and a hope of personal benefit. It was explained to all volunteers that the technique was experimental and would not directly benefit their diagnosis or treatment. Nonetheless some volunteers stated a desire to know more about their condition as a motivation for participation in the study.

2.5.4 Impact on the project

The first hand reactions of the volunteers had a very valuable impact on the development of the study. Suggested improvements to the comfort of the patient interface have been employed where possible including the use of an armrest and an adjustable chair. The reactions of volunteers along with the limitations on acquiring physical data discussed previously highlighted the need for the development of a new patient interface. The volunteers' views, along with technological constraints and optimum data acquisition, were one element in determining the design of such a system. The new system is described in detail in part 3.

The scan procedure was adapted to take account of the volunteers concerns and anxieties. Physical improvements included the provision of music (if desired) during the scan and rotating the volunteer and apparatus so that they were facing the researchers. Additionally our interaction with the volunteers improved with greater understanding of patients concerns and experience in performing the experiments. It is important to realise that a volunteer who is at ease with the procedure will more readily adopt the required position and is more likely to agree to repeat scans either in the same session or in later ones. Thus it is important to address volunteers' anxieties to achieve optimum data collection. Although the volunteers' reactions regarding the acceptability of the new technology in terms of safety, functionality and pain did not directly influence the scan procedure it is encouraging to see our system is perceived favourably, especially in relation to other modalities, and so it is likely that it would be accepted in a clinical environment if sufficient sensitivity and specificity can be achieved.

Finally, the comments on motivation enable us to tailor our recruitment of potential volunteers accordingly.

2.6 Clinical trials - summary

The data from all of the clinical studies is collected together and presented in table 2.6.1.

	Number of volunteers/(scans)	Image obtained	Score	Average score
Fibroadenoma	8(8)	6	X,X,1,2,3,3,4,4	2.83
Cyst	1(1)	1	5	5
ILP treatment of fibroadenoma	2(6)	6	3,3,4,4,5,5	4
Mastalgia	4(9)	9	N/A	N/A
Benign nodularity	4(4)	4	2,2,3,4	2.75
Suspected malignant lesion	4(4)	2	X,X,0,5	2.5
Healthy volunteer	3(7)	4	N/A	N/A
Total	**24(38)***	**32**		**Average =3.2**

* One volunteer who under went ILP treatment of a fibroadenoma was scanned prior to the treatment and so appears in both the fibroadenoma and ILP categories. One volunteer was diagnosed with mastalgia and benign nodularity so is included in both categories.

Table 2.6.1: A summary of the results obtained for different conditions of the breast

A scan was not obtained if the breast did not conform to the size or shape of either ring. In the case of the healthy volunteers and mastalgia patients the scoring system is not applicable (N/A) as there is no lesion present.

The outcome of patient and volunteer studies performed so far can be summarised as follows:

- The images exhibit heterogeneous features that are unique to an individual volunteer;
- The images for an individual volunteer are reproducible over time;
- Known benign lesions can be identified with a score of 2 or above in 92 % of cases;
- The recovery of tissue after ILP has been successfully monitored over 12 months for one volunteer.
- Scar tissue appears to produce a significant increase in absorption in comparison with healthy breast tissue.

- A malignant lesion has been identified, in one volunteer, with a visibility score of 5.

The results we have obtained to date have been encouraging, suggesting that optical tomography can detect certain types of lesions. Excluding those studies where a lesion is not present we have obtained a visibility score of 2 or above for 9 out of 11 lesions. It should be noted that the majority of these lesions are benign with no vascularisation and so may exhibit optical characteristics that are similar to those of healthy breast tissue. It is more important that such lesions differ in optical characteristics from malignant lesions. The majority of our volunteers have been pre-menopausal women with a higher percentage of glandular tissue compared to post-menopausal women, which may result in a reduction in contrast for some lesions (Cerussi et al 2001). Of the two malignant lesions studied, one was imaged successfully with a visibility score of 5. In the second case the visibility score of 1 is almost certainly due to the lesion being located out of the imaging plane of the ring. From the single study obtained so far it therefore appears that a malignant lesion is seen as the most dominant feature in an absorption image, whereas the benign lesions studied appeared alongside features of equal or more dominant contrast. Thus from this very limited study it appears that a distinction between benign and malignant tissue may be possible. The malignant lesion was also seen to exhibit low scatter and low oxygen saturation, which may be parameters that could further characterise a malignant lesion.

There are however several distinct problems associated with the method that have been identified as a result of these studies:

- Imaging is largely confined to one plane and so full sampling in 3-D is not achieved;
- The mesh used in reconstruction is based on a section of a cone and so is not representative of the whole volume of the breast;
- Intensity cannot be used as a data type preventing true separation of absorption and scatter;
- Oxygen saturation and blood volume maps could not be generated from absorption images at two wavelengths using this method due to an inability to separate absorption and scatter.
- It proved difficult to achieve direct contact between the breast and the sources and detectors in all cases. In particular, the breasts of the older volunteers often did not conform to the shape of the ring and so reasonable data could not be collected.

These deficiencies of the technique must be overcome to ensure that the maximum potential of optical mammography is fulfilled. A second patient interface has been constructed based on a hemisphere filled with a coupling fluid. It is hoped that this system will overcome some of the problems experienced using the ring system. A full description of this system and preliminary results are presented in part 3.

Part 3

A liquid coupled interface

In this part the initial results of an evaluation of a fluid-coupling system are presented. In particular, the spatial resolution, contrast and spatial accuracy are investigated. The knowledge of these parameters will help to validate later clinical studies and to determine the effect of using a matching fluid on the reconstructed images. The first results from a healthy volunteer are also presented.

3.1 The liquid coupled device

As described in part 2 the ring system initially used as a patient interface suffered from the following problems:

1. The geometry did not allow three-dimensional imaging;
2. Intensity could not be used as a datatype as coupling between the breast and the sources and detectors was not constant;
3. Positioning patients as required was not easy especially if the patient was elderly or frail;
4. Contact between the ring and the breast was poor for some women.

These problems need to be overcome in order for optical mammography to be a useful clinical tool. As mentioned in chapter 1.6, other research groups in the field have adopted a variety of acquisition geometries. The main three geometries are slab compression (Grosenick et al 2003; Pifferi et al 2003), a liquid coupled filled geometry (Colak et al 1997; Philips Research laboratories 1997) and an adaptable ring geometry in three planes (Pogue et al 1997; Schmitz et al 2001) (see chapter 1.6 for further details). The compression geometry overcomes problems 3 and 4, although as with compression in x-ray mammography (chapter 1.5), compressing the breast decreases the positional accuracy with which a lesion can be located in three dimensions and there is generally an inconsistent coupling between the breast and the sources and detectors in these systems. Attempts have been made to introduce a coupling fluid into a compression unit but these have so far been unsuccessful (personal communication with Heidrun Wabnitz 2002). Two additional disadvantages of the compression technique are that a reduction in blood volume could potentially lead to a reduction in contrast, and that prolonged compression can produce significant discomfort (Morris et al 2003). The adaptable ring geometry overcomes problems 1,3 and 4 but still may suffer from inconsistent coupling. Additionally this solution involves complex engineering and is expensive in comparison to other approaches. The approach using a coupling fluid filled geometry overcomes all the problems mentioned above in the following ways:

1. It enables full 3-D imaging of the entire breast including tissues adjacent to the chest wall.
2. The liquid surrounding the breast provides a constant coupling between the breast and the sources and detectors.
3. Minimal adjustment is required to position the volunteer. This approach requires the patient to be in a prone position, which may be more acceptable for elderly volunteers.

4. The combination of breast and coupling liquid will always fill the geometry used to its entirety and so contact between the volunteer and the sources and detectors will always be achieved.
5. This approach will benefit the reconstruction as the exterior geometry of the reconstructed volume is known exactly and so an accurate model can be generated.

The potential disadvantages of this approach are that the effects of the choice of the optical properties of the matching fluid on the reconstruction are unknown, and that there may be insufficient restraint on the patient's movement.

A prototype liquid coupled device has been constructed. The coaxial source/detector bundles described in chapter 1.6 are attached to the exterior of an opaque plastic hemispherical shell, 165 mm in diameter with thickness 5 mm (EMA model supplies, Shepperton, UK). Thirty-one bundles are distributed around the hemisphere as shown by the two dimensional representation in figure 3.1.1a. The bundles are positioned within three planes, providing a reasonably even distribution across the surface of the hemisphere.

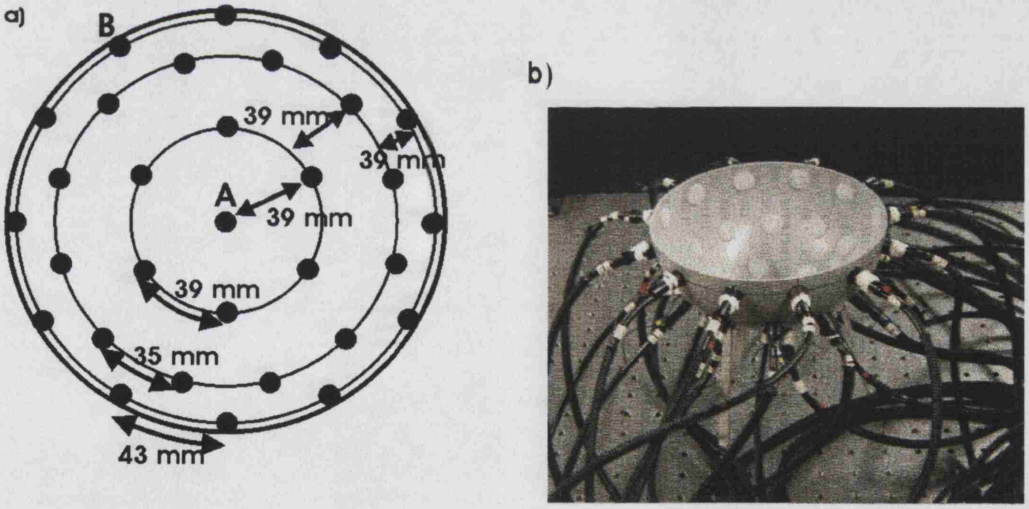

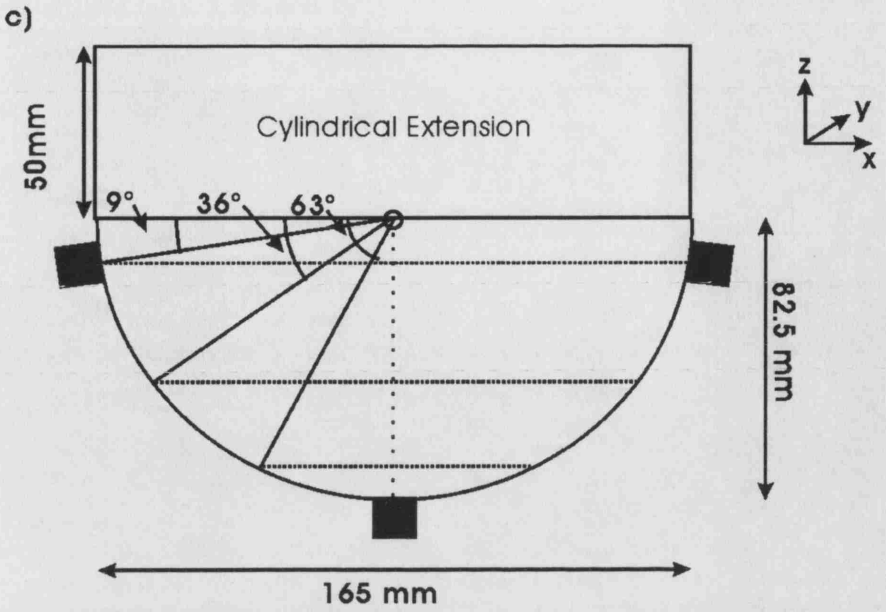

Figure 3.1.1 The positions of the source and detector bundles around the hemisphere. a) A 2D representation of the distribution. b) A photograph of the finished device. c) The angular distribution of the source and detector bundles with an illustration of the extension used for reconstruction purposes.

To allow light to penetrate through the opaque hemispherical shell, holes were drilled in the positions indicated in figure 3.1.1. Epoxy resin, mixed with large amounts of titanium dioxide, was used to make thin windows with very highly scattering properties to create a diffuse source (Firbank et al 1995). These windows were attached to the inner surface of the hemisphere to form a watertight seal across the drilled holes. The use of these windows also ensures that a constant coupling is maintained. The source and detector bundles are held in position using short plastic tubes inserted into the holes on the exterior surface of the hemisphere.

To provide a constant coupling between the fibre bundles and the surface of the breast it is necessary to fill the hemisphere with a liquid. The optimum properties of such a liquid are currently under investigation. In the study performed by the Philips group (Colak et al 1997) the optical properties of the coupling fluid were selected to match the optical properties of the breast. This approach prevents the occurrence of artefacts in the reconstructed images which may arise if the optical properties of the fluid are significantly different from those of the breast. A further consideration is that the coupling fluid must be harmless to skin contact. For the purposes of this preliminary investigation the hemisphere was filled with a solution of intralipid (Driver et al 1989), dye and distilled water with properties of absorption coefficient μ_a = 0.007 mm^{-1} and reduced scattering coefficient μ_s' = 0.8 mm^{-1}. These values were chosen as being representative of the average properties of the breast (see section 1.2.5) (Cerussi et al 2001) and are consistent with those used in previous breast phantom studies at UCL (Hebden et al 2001).

One significant advantage of this approach is that an ideal reference can be created for use in difference imaging. The ideal reference is a homogenous medium with the same average optical properties and external geometry as the object under investigation. Such a reference can be created for this system by filling the hemisphere with the coupling fluid alone. However, in order that reference measurements include a contribution from photons that would travel into the chest wall of a patient, an additional height of liquid above the hemisphere is required. This was achieved by attaching a cylindrical plastic ring, 50 mm in height, to the top of the hemisphere as shown in figure 3.1.1 c.

The repetition rate of the laser (two interlaced trains of pulses at 40 MHz) dictates that the maximum temporal window for each TPSF is 12.5 ns. However, the large diameter of the hemisphere and optical properties of the coupling fluid cause photons to be detected with flight times in excess of the window width. As a consequence it was necessary to acquire data at the two wavelengths successively rather than simultaneously, enabling a temporal window of 25 ns to be used. In the experiments reported below, data were only acquired at a single wavelength of 815 nm. For each study described below the optimum VOA positions were calculated in advance for each source-detector pair.

A 3D finite element mesh was constructed with a Delaunay triangulation method (Schoeberl 2003) to be used in reconstruction of the data obtained using the hemispherical shell. The mesh, shown in figure 3.1.2, was generated as a hemisphere with a 50 mm cylindrical extension to the top. The mesh consists of 23156 tetrahedral elements with quadratic interpolation functions and 35233 nodes. Similarly to the mesh presented in figure 2.1.4 the mesh in figure 3.1.2 was made finer at the positions of the sources and detectors where more accurate modelling is required.

To validate the mesh, forward data was generated from the FEM with a modelled cylinder of 10 mm diameter, placed off centre and with optical properties 10 times greater than the background properties. The mesh was considered acceptable when all the forward fields generated were positive and appeared smooth.

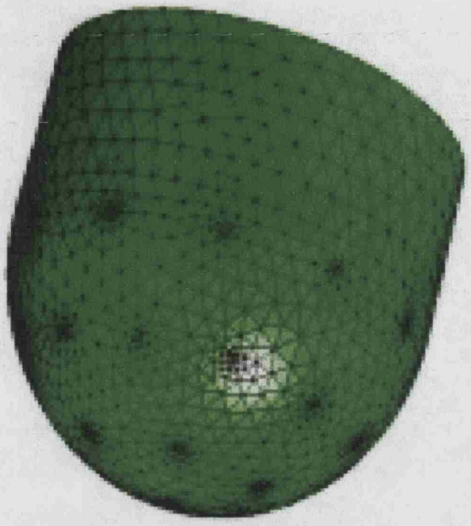

Figure 3.1.2: The surface of the mesh used in the reconstruction of images using the hemisphere.

The image reconstruction was performed using a conjugate gradient solver and Robin boundary conditions. Both meantime and intensity datatypes were utilised to reconstruct images of absorption and scatter. In all cases the 15^{th} iteration was analysed as this was found to be the number beyond which no further improvement to the images was seen. Each iteration required 48 minutes on a 2.2 GHz Xeon processor and used approximately 800 MB of RAM.

3.2 Perturbation experiments

To measure the spatial resolution, spatial accuracy and contrast across the volume of the hemisphere, two resin cylinders with length and diameter of 10 mm were constructed. The optical properties of these are cylinder A: $\mu_a = 0.07$ mm^{-1} (10 x background μ_a) and $\mu_s' = 0.8$ mm^{-1} and cylinder S: $\mu_a = 0.007$ mm^{-1} and $\mu_s' = 8$ mm^{-1} (10 x background μ_s') respectively. The cylinders were each placed at 15 positions within one half-plane of the fluid filled hemisphere as shown in figure 3.2.1. These positions form a grid of equilateral triangles.

Each resin cylinder was suspended in turn, on the end of a thin wire supported by a frame mounted on vertical and horizontal translation stages. The cylinder was initially placed in the centre of the top ring of fibre bundles and was translated relative to this point. Data were acquired for 11 minutes at each position with an acquisition time of 10 seconds per source. Reference data sets were acquired with the cylinder removed, at the end of each row shown in figure 3.2.1, as well as prior to and following the experiment.

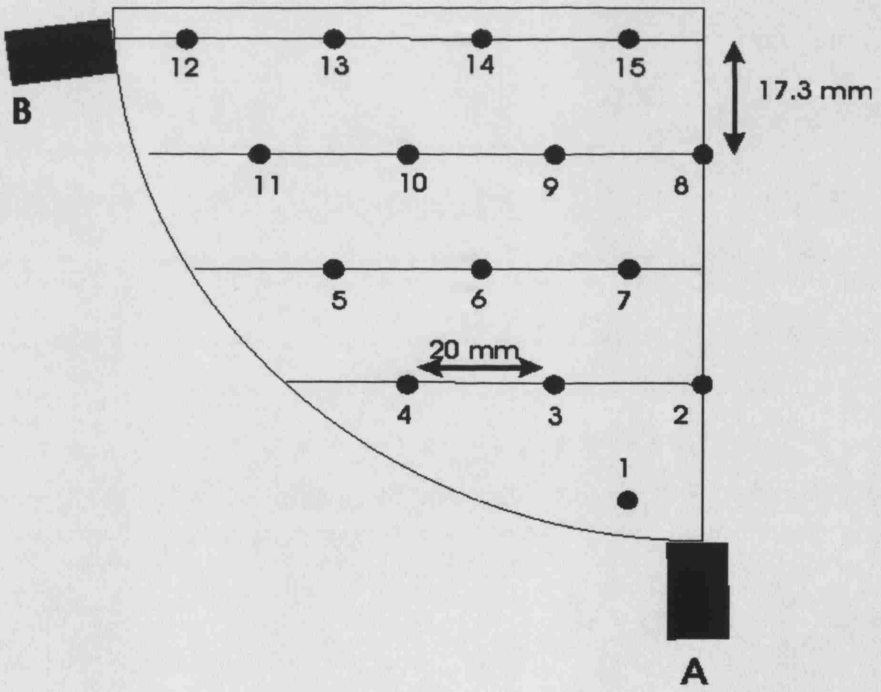

Figure 3.2.1: The positions at which a perturbation was introduced and a measurement set taken.

3.2.1 Analysis

The contrast, spatial resolution and spatial accuracy are determined from detailed analysis of the images obtained for all the 15 positions indicated in figure 3.2.1.

The contrast, C, is calculated using:

$$C = \frac{y_{max} - y_{bg}}{y_{bg}} \quad , \qquad (3.2.1)$$

where y_{max} was taken to be the mean of the top 5% of the values in each image and y_{bg} was the mean background value calculated from the remaining data in the image.

The localisation accuracy was determined from the differences between the positions of the peak value within the images and the expected positions of the cylinder. The position of the peak value was obtained by taking the mean *x, y* and *z* values for the nodes in the mesh which correspond to values above 95% of the maximum value. Any systematic difference between the expected positions and the true positions due to error in the initial positioning of the targets was removed by subtracting the mean expected values and the mean measured values from the corresponding values of *x, y*, and *z*. Any difference between the expected and measured values is then only due to the reconstruction error we wish to quantify.

Each 3D image may be considered to represent the target distribution convolved with a 3D point spread function (PSF). It is conventional to characterise spatial resolution in terms of the width of the PSF. For the analysis presented here, however, we elect to characterise spatial resolution in terms of the *volume* of the PSF. Since the volume of the images of the targets are much greater than that of the targets themselves, we make the approximation that the PSF volume is equal to the volume of the reconstructed target. The 'volume resolution' presented here has been calculated as the volume of the mesh that encompasses all nodes associated with a value greater than or equal to 50% of the maximum value in the image. We call this parameter the full volume at half maximum (FVHM).

The PSF is assumed to have a Gaussian profile. When the volume occupied by the feature in the image becomes greater, the peak value (and therefore the contrast) will be reduced. Hence a decrease in spatial resolution will lead to a direct decrease in contrast. It is proposed that this can be expressed as:

$$V_t h_t = V_i h_i, \tag{3.2.2}$$

where V_t is the true volume of the cylinder, V_i is the volume of the feature in the image, and h_t and h_i are the values of $y_{max} - y_{bg}$ for the cylinder and the image respectively. Thus assuming the background y_{bg} of the image to be equal to the true background of the medium we can express the apparent contrast of the cylinder by:

$$C_i = C_t \frac{V_t}{V_i}, \tag{3.2.3}$$

where C_t is the true contrast of the cylinder. Thus in principle, we should be able to compensate for the reduction in contrast due to the size of the PSF by multiplying the apparent contrast by a factor equal to V_i/V_t. We can estimate V_i from the calculated value of the FVHM by assuming it is a 3D Gaussian. The equation for a Gaussian is given by:

$$y(r) = he^{-\frac{|r-r_o|^2}{2\sigma^2}}, \tag{3.2.4}$$

where σ is the standard deviation, h is the amplitude of the Gaussian, and r_o is the location of the centre of the distribution.

The volume under the Gaussian (V_g) can be obtained from integration of equation 3.2.4:

$$V_g = h(\sqrt{2\pi}\sigma)^3 . \tag{3.2.5}$$

By setting $y(r=f/2) = h/2$ (i.e. half the maximum) in equation 3.2.4 and rearranging we obtain:

$$\sigma = \frac{f}{\sqrt{8\ln 2}}, \tag{3.2.6}$$

where f is the full width at half maximum. Substituting 3.2.6 into 3.2.5 gives:

$$V_g = h\left(\frac{\pi}{4\ln 2}\right)^{3/2} f^3 . \tag{3.2.7}$$

However, our measured value of FVHM represents a sphere of radius $f/2$, which implies:

$$f^3 = \frac{6}{\pi} FVHM . \tag{3.2.8}$$

By combining equations (3.2.7) and (3.2.8) we obtain:

$$V_g = h\left(\frac{\pi}{4\ln 2}\right)^{3/2} \frac{6}{\pi} FVHM \approx 2.3.h.FVHM . \tag{3.2.9}$$

Thus V_i can be estimated from the FVHM by multiplying by a factor of 2.3.

3.2.2 Results

Figure 3.2.2 shows typical images reconstructed from the data acquired for cylinders A and S in position 11 in figure 3.2.1. These images represent a slice taken in the x-z and x-y planes (see figure 3.1.1c) through the plane of interest. In each case the 15th iteration is shown. Although the targets are displayed in the expected location we also observe the crosstalk between absorption and scatter that occurs when both parameters are reconstructed simultaneously. The images appear to exhibit a degree of crosstalk between the scatter and absorption parameters, although the largest perturbation is identified in the correct parameter. It is likely that one source of this cross talk is the refractive index mismatch between the coupling fluid (n=1.33) and the resin cylinders (n=1.56). The equivalent image for cylinder A reconstructed using only the intensity datatype is shown in figure 3.2.3 to illustrate that intensity is a robust datatype containing useful information using the liquid coupled device.

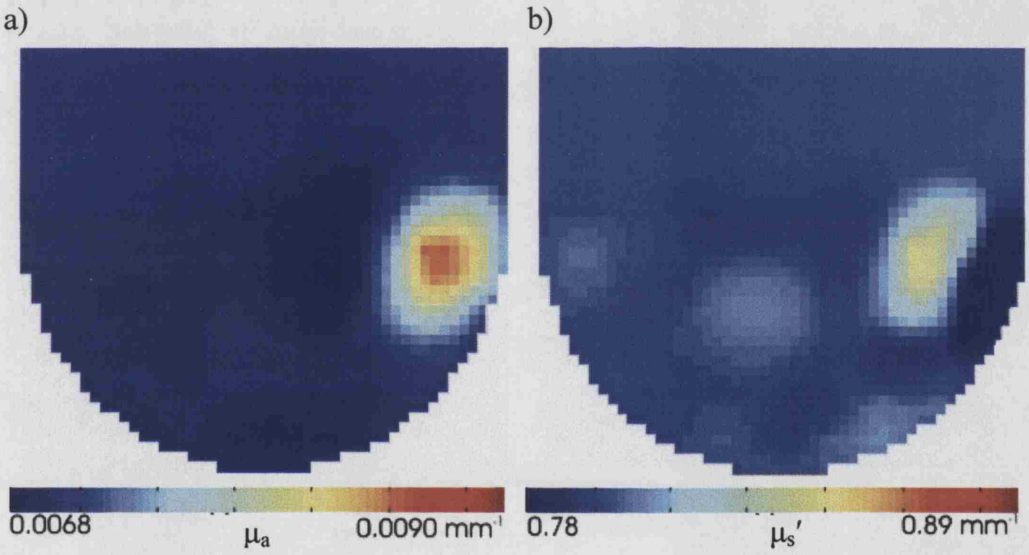

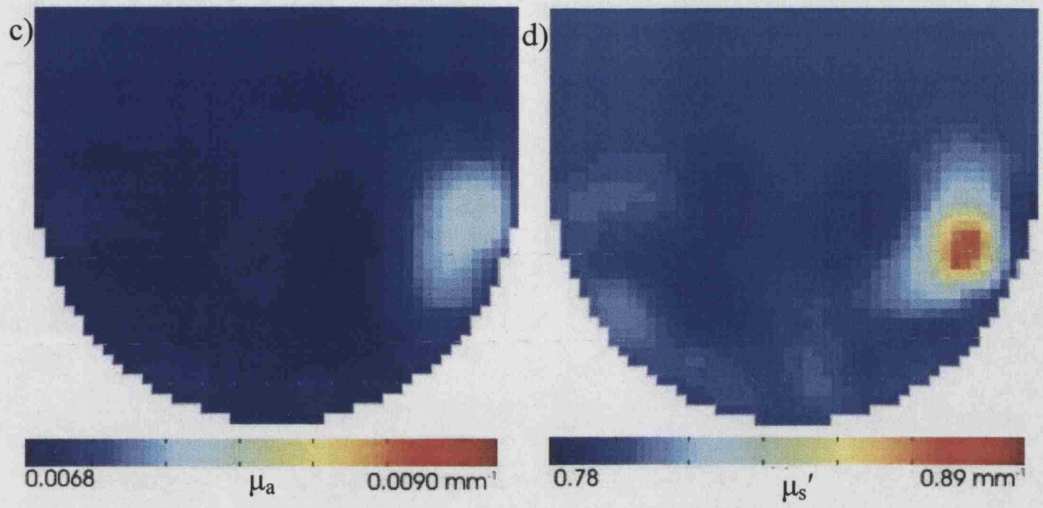

Figure 3.2.2 The reconstructed a) absorption and b) scatter images with cylinder A placed in position 11 from figure 3.2.1. Figures c) and d) show the corresponding images for cylinder S.

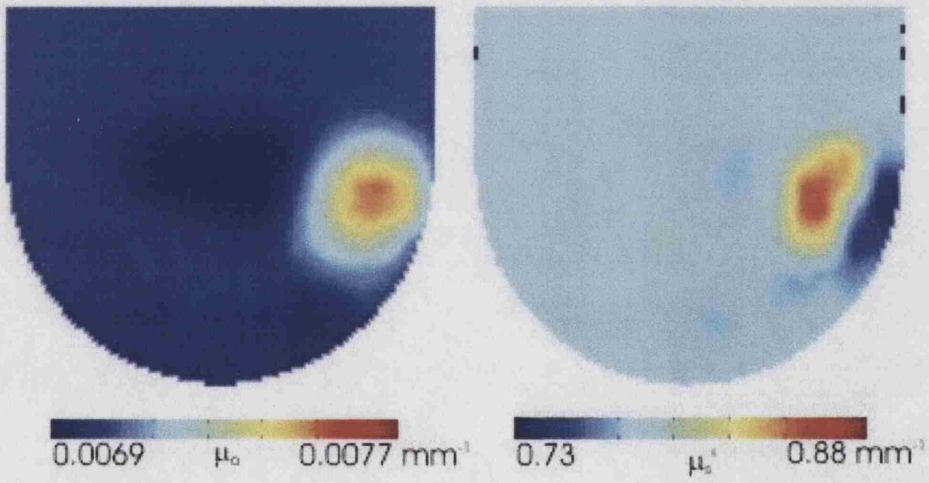

Figure 3.2.3: The reconstructed absorption image with cylinder A placed in position 11 from figure 3.2.1 using intensity as the only data type.

Plots of the variation in contrast, localisation accuracy and FVHM (as defined in section 3.2.2) with distance from position O (figure 3.1.1 c) are shown in figures 3.2.4, 3.2.5 and 3.2.6 respectively. A linear trend line was fitted to the data in each of the plots using a least squares regression. All three plots show strong dependency on the position of the cylinder from the edge of the hemisphere.

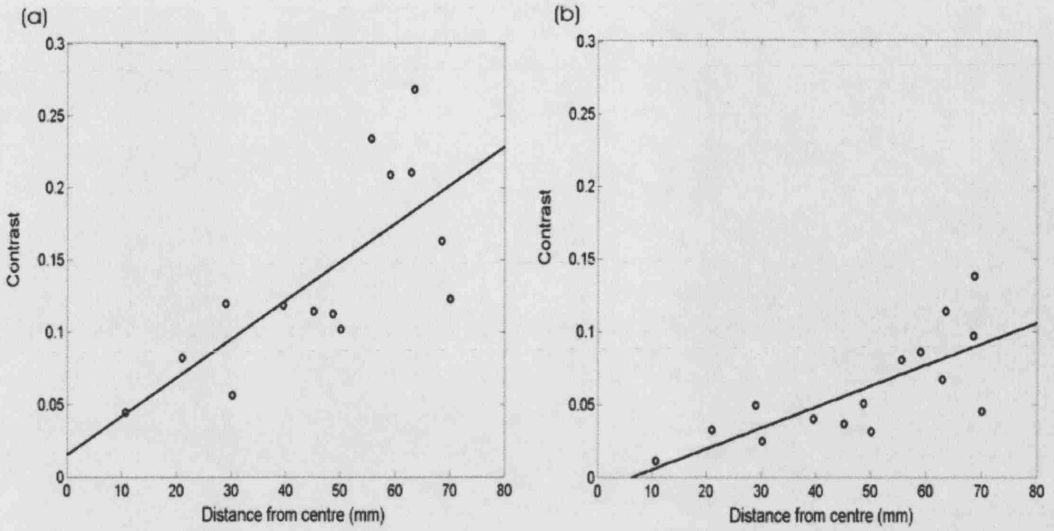

Figure 3.2.4: The contrast for the 15th iteration of images constructed of a) cylinder A and b) cylinder S with distance from position O.

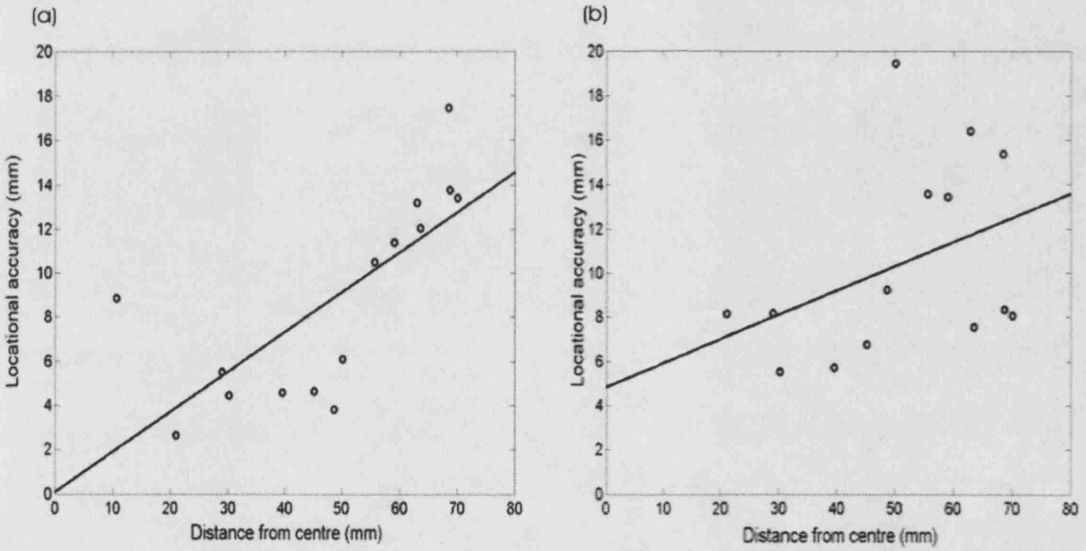

Figure 3.2.5: The spatial accuracy for the 15th iteration of images constructed of a) cylinder A and b) cylinder S with distance from position O.

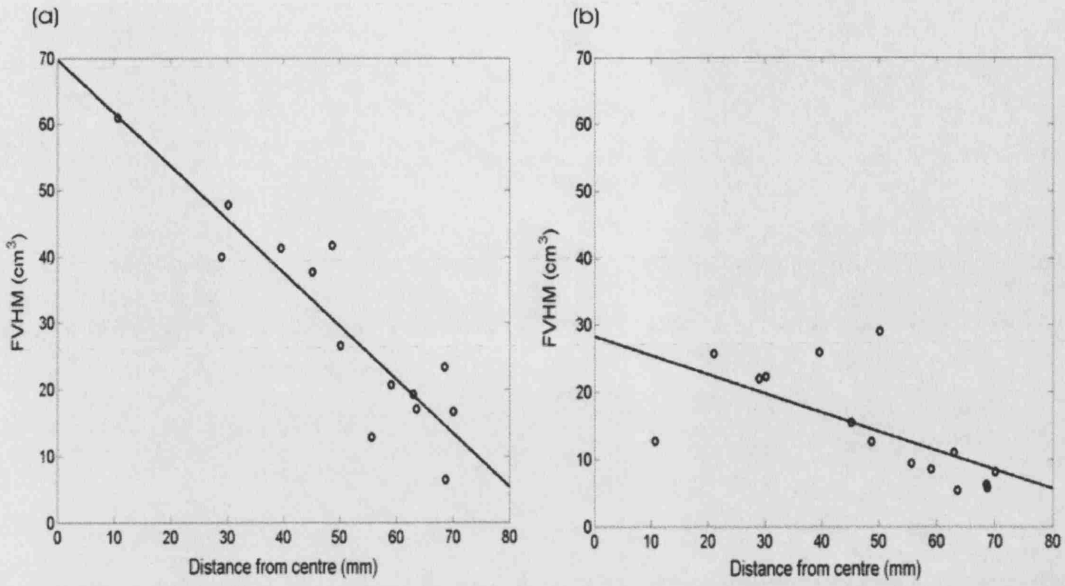

Figure 3.2.6: The full volume at half maximum for the 15th iteration of images constructed of a) cylinder A and b) cylinder S with distance from position O.

A plot of the adjusted contrast (V_iC_i/V_i) against distance from position O is shown in figure 3.2.7. As discussed in section 3.2.3 below, the values obtained are closer to the true contrast of 9 and so suggests that this method could be used to improve quantitation of optical tomography.

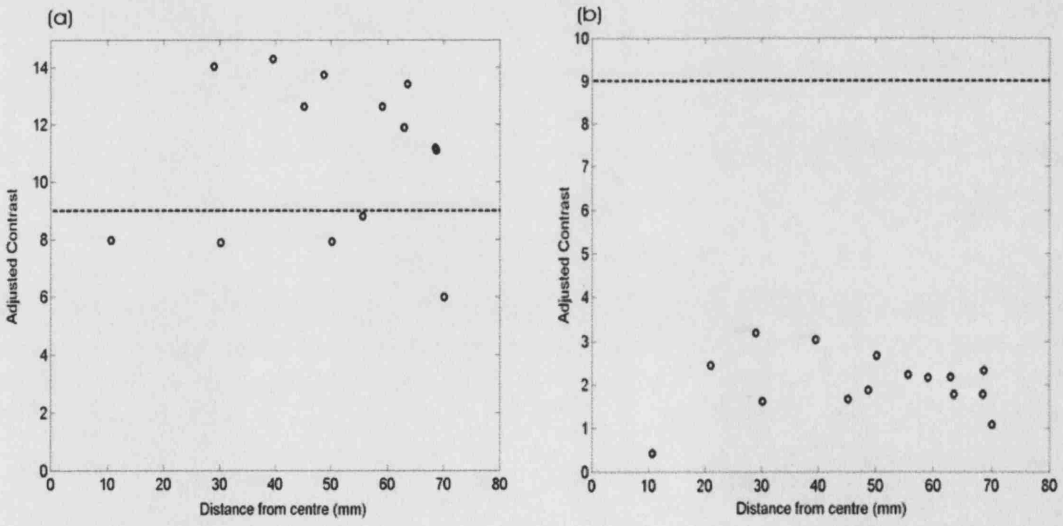

Figure 3.2.7: Values of contrast following compensation for the partial volume effect plotted against distance from position O for a) cylinder A and b) cylinder S. In both a) and b) the dashed line represents the true contrast value.

3.2.3 Discussion

The use of the coupling fluid in the manner described above enabled both intensity and meantime measurements to be used to reconstruct 3D images for both absorption and scatter. This is an improvement on earlier breast imaging studies performed at UCL (Hebden et al 2002; Yates et al 2005) where intensity was unavailable due to inconsistent coupling between the breast and the fibre bundles. This technique also has the advantage that a simple generic mesh can be used in the reconstruction and so prevent the difficulties involved with using a more complex patient-specific mesh.

The spatial resolution, presented here as a value of FVHM (figure 3.2.6), decreases from 60 to 6 cm^3 for cylinder A, and from 30 to 5 cm^3, for cylinder S, as the cylinders are placed closer to the edge of the hemisphere. In an ideal imaging system the FVHM would be equal to the true volume of the cylinder, i.e. 0.8 cm^3, and be independent of position. Our results show that first, the mean FVHM is substantially higher than the true volume and second, the FVHM is decreased by up to a factor of 10 when the cylinder is positioned at the edge of the cylinder compared with a position towards the centre.

Large source and detector separations (up to 165 mm) result in an inherently lower spatial resolution due to their broad sensitivity functions (PMDF's, see chapter 1.7). Information about the centre of the hemisphere is derived only from measurements taken with large source and detector separations, and consequently the spatial resolution is lower towards the centre of the hemisphere. The obvious impact of this on imaging the breast is that smaller superficial lesions can be seen more easily than deeper ones.

The contrast across the hemisphere for cylinder A exhibits an upward trend from 0.045, close to the centre of the hemisphere, to 0.27 at the edge of the hemisphere (figure 3.2.4). A similar trend is seen for cylinder S with a contrast range from 0.011 to 0.14. The true contrast, as defined by equation (3.2.1), of a cylinder with optical properties of 10 times the background properties would be 9.0, and should be independent of position. Overall we observe a much lower contrast than the true contrast throughout the volume, but a general improvement as the cylinder is positioned closer to the edge of the hemisphere.

Underestimation of contrast is largely due to the partial volume effect caused by limited spatial resolution. We can compensate for this effect by using a multiplication factor of $(2.3FVHM/V_i)$ as presented in figure 3.2.7. The contrast values adjusted in this way now have a mean value of 11.0 and 2.03 for cylinders A and S respectively. The discrepancy between the mean adjusted

contrast values (11.0 and 2.3) and the true contrast (9.0) is possibly due to the crosstalk described earlier in section 3.2.2. In general, we observe better separation between parameters for absorbing targets than for scattering targets, which is consistent with the larger discrepancy in the adjusted contrast observed for the scattering target. An analysis of the images in figure 3.2.2, for example, reveals that the absorption contrast is nearly three times higher than the scatter contrast for the absorbing target, while the absorption contrast is roughly equal to the scatter contrast for the scattering target. Furthermore, the graph in figure 3.2.7 illustrates that the adjusted contrast values plotted against the distance from the centre of the hemisphere show virtually no dependence on the target position. We note that the method involved in deriving this multiplication factor relies on the assumption that the profile of the PSF is Gaussian. This method could potentially provide a technique by which the decrease in contrast due to the partial volume effect could be partially compensated for and greater quantitative accuracy can be achieved.

The error in target localisation, as illustrated in figure 3.2.5, has surprisingly large mean values of 8.7 mm for cylinder A and 11 mm for cylinder S. This error is largely a consequence of the automated method of determining the centre of each target image. We note that the peak value in the image (determined by calculating the centroid of the nodes in the mesh with the top five percent of values) does not generally agree well with the centre of the feature identified by inspection. We also find that adjusting the threshold for selecting the volume from which the centre position is calculated does not significantly reduce the localisation error. It is particularly interesting to note that the localisation error increases as the target moves away from the centre, even though spatial resolution improves. There are two potential contributing factors. First, the region between a given source and detector to which the measurements are sensitive (the banana-shaped "photon measurement density function" or PMDF (Arridge 1995)) has a cross-section which changes fastest nearest the source and detector. This will inevitably produce an asymmetry in the reconstructed target image. Second, the external region of the hemisphere is more sparsely sampled, and consequently there is likely to be a tendency for the reconstructed targets to be displaced away from their true positions towards the centre of the nearest PMDF.

Although the parameters investigated are plotted against distance from the centre of the hemisphere, we note that the relevant factor may actually be the distance from the sources and detectors. It is the movement of the absorbing and scattering cylinders towards the sources and detectors that leads to the improvement in spatial resolution and contrast, rather than the distance from the centre of the hemisphere. The data was presented in the manner shown for simplicity, but this discrepancy may account for some of the scatter from the fit seen in the data presented in figures 3.2.4, 3.2.5 and 3.2.6.

3.3 Intralipid properties simulation.

The optimal optical properties of the coupling solution is an issue which requires a careful investigation. (Colak et al 1997) matched their coupling solution to the average properties of the breast. The advantage of adopting this method for our system would be that large differences between the tissue and the reference media, which are difficult to reconstruct, would be avoided. However, reducing the absorption and/or scatter of the liquid would allow a greater intensity of photons to sample the breast and so could produce data with a higher signal-to-noise ratio. In order to study the affects of varying the absorption and scattering properties of the coupling fluid a series of simulations using the forward solver in TOAST have been performed (section 1.7).

In this study the breast is modelled as a hemisphere of radius 60 mm and properties of μ_a = 0.007 mm^{-1} and μ_s' = 0.8 mm^{-1} (figure 3.3.1). The chest wall is modelled as a block across the top of the mesh and is again given properties of μ_a = 0.007 mm^{-1} and μ_s' = 0.8 mm^{-1} to avoid any features that may result due to a mismatch. The remainder of the mesh is representative of the coupling fluid and is assigned the optical properties as shown in table 3.3.1 for each simulation. It must also be considered that a mismatch in the refractive index between the coupling solution (which is close to that of water) and the tissue may result in significant reflection at the liquid/tissue boundaries which is not modelled in the reconstruction algorithm. However, in this study both the breast and coupling fluid are modelled with a constant refractive index of 1.4 which is an accepted estimate of the refractive index of tissue (Bolin et al 1989).

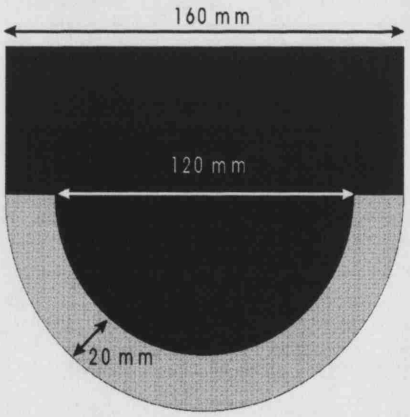

Figure 3.3.1: The regions of the mesh as tissue (black) and coupling fluid (grey) during simulations of different optical properties of the coupling solution.

In each case data is simulated on a finite element mesh that has the same geometry as that shown in section 3.1 but with 51795 nodes and 35068 elements to allow accurate modelling of the data. The simulated data is then reconstructed using the mesh shown in figure 3.1.2 to be

consistent with the reconstruction method used in clinical or phantom imaging. The initial parameters for the reconstruction were the optical parameters of the simulated coupling fluid (i.e. the values in table 3.3.1). However a further investigation into the effect of varying the initial parameters was also performed using the simulated data for a coupling solution with μ_a = 0.006 mm^{-1} and $\mu_s' = 0.8$ mm^{-1}. In this study the initial μ_a was varied from 0.002 to 0.01 mm^{-1}. The results from this investigation were compared with those obtained by varying the properties of the coupling solution to determine whether it is more important to know the properties of the coupling solution exactly than to match the properties closely to those of the breast.

To analyse the images the mean pixel value within the volume of the mesh that represents the breast (i.e. a hemisphere of radius 60 mm) is calculated and compared to the expected value of 0.007 mm^{-1}. By plotting the difference between the two against the value of the absorption coefficient assigned to the coupling fluid in the simulation an assessment of the quality of the reconstructed image for each value can be made.

Image	μ_a of coupling solution (mm^{-1})	μ_s' of coupling solution (mm^{-1})
a)	0.0001	0.8
b)	0.001	0.8
c)	0.002	0.8
d)	0.003	0.8
e)	0.004	0.8
f)	0.005	0.8
g)	0.006	0.8
h)	0.008	0.8
i)	0.009	0.8
j)	0.007	0.1
k)	0.007	0.2
l)	0.007	0.3
m)	0.007	0.4
n)	0.007	0.5
o)	0.007	0.6
p)	0.007	0.7
q)	0.007	0.9
r)	0.007	1.0

Table 3.3.1: The values of μ_a and μ_s' assigned to the coupling fluid during a series of simulations.

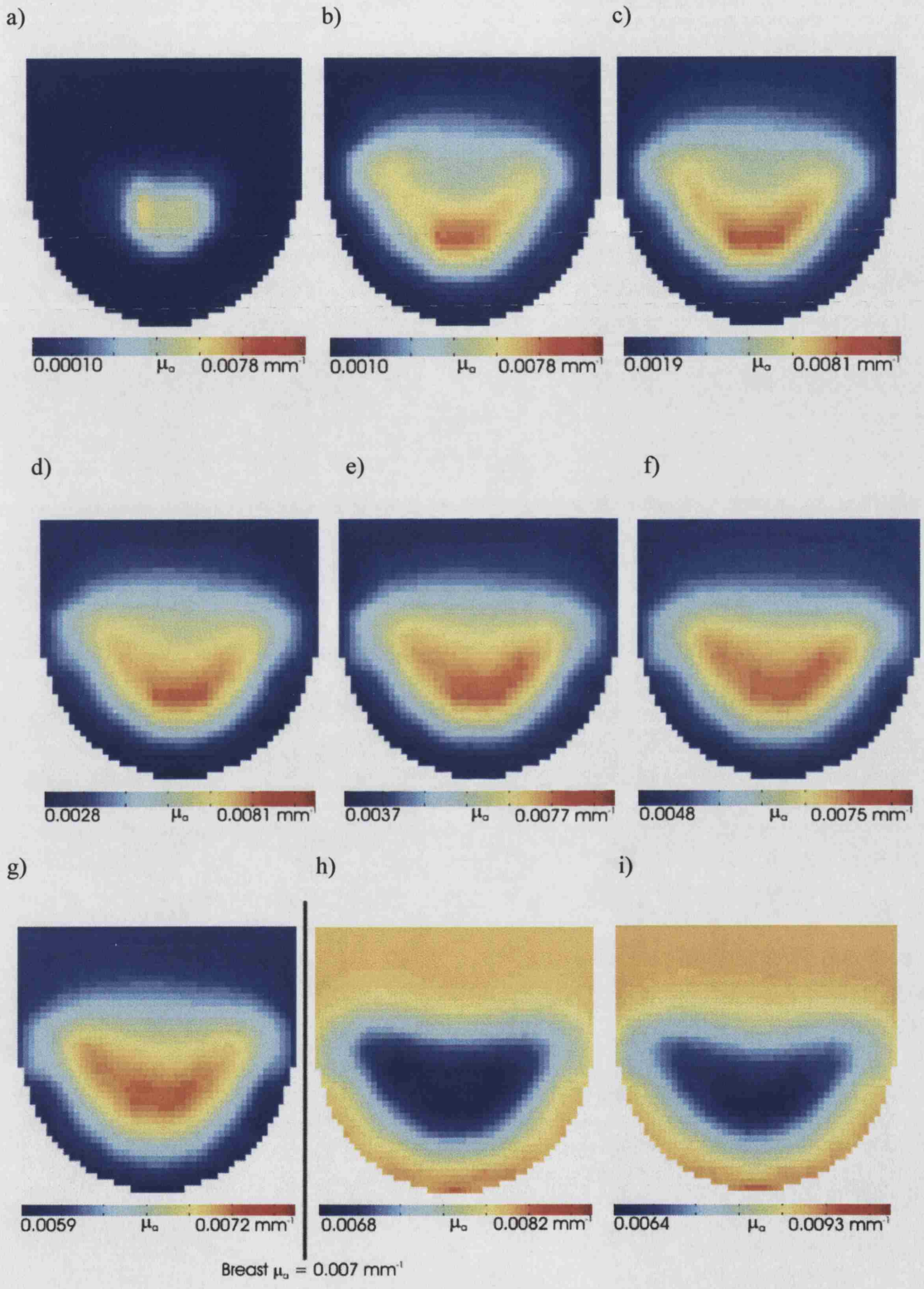

Figure 3.3.2: The absorption images for various simulated absorption coefficients of the coupling fluid as listed in table 3.3.2.

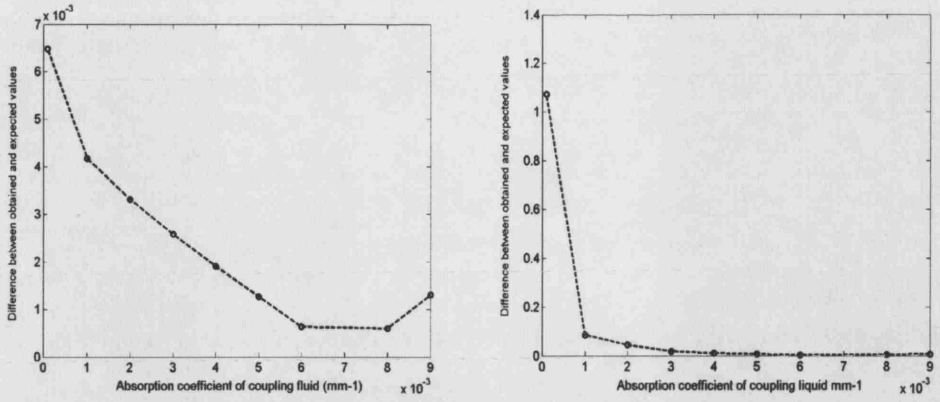

Figure 3.3.3 A plot of the difference between the mean value in the reconstructed region of the breast and the assigned value for images of a) absorption coefficient and b) scatter coefficient for varying values of the absorption coefficient of the coupling fluid.

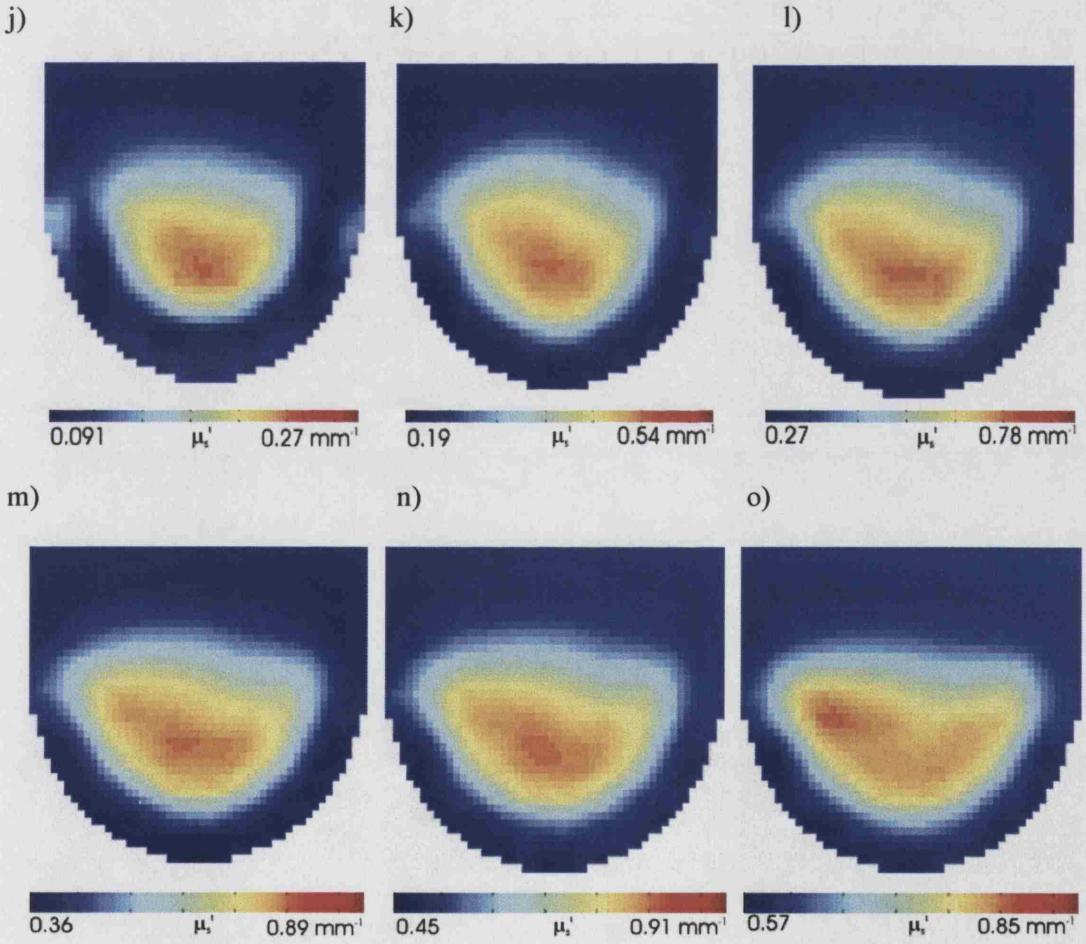

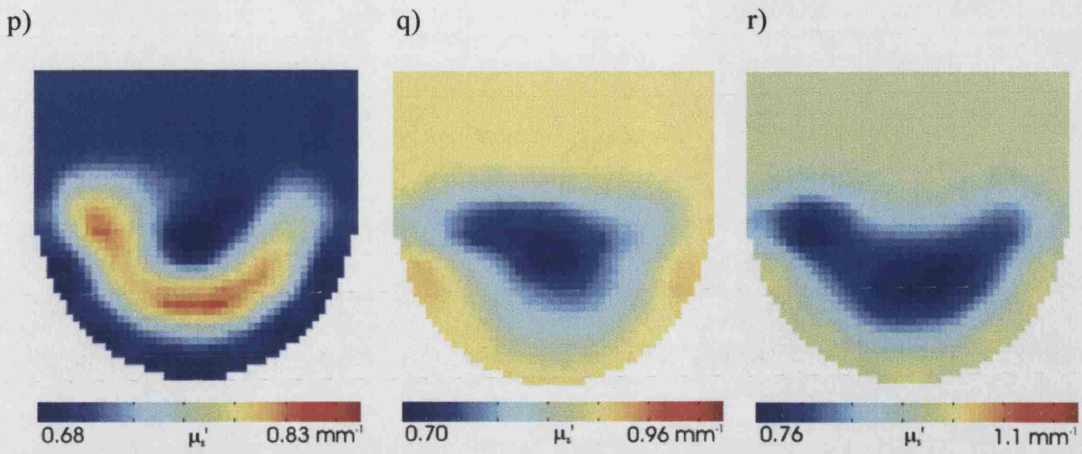

Figure 3.3.4: The scatter images for various simulated scatter coefficients of the coupling liquid as listed in table 3.3.1

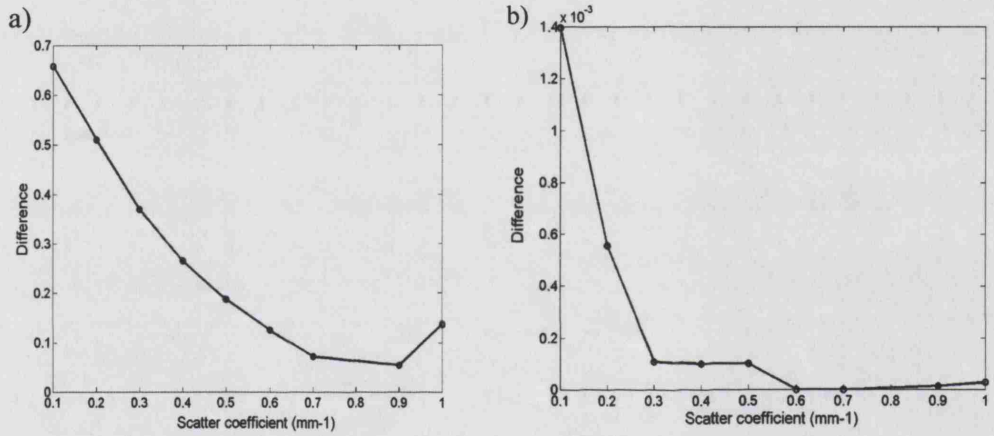

Figure 3.3.5 A plot of the difference between the mean value in the reconstructed region of the breast and the assigned value for images of a) absorption coefficient and b) scatter coefficient for varying values of the scattering coefficient of the coupling fluid.

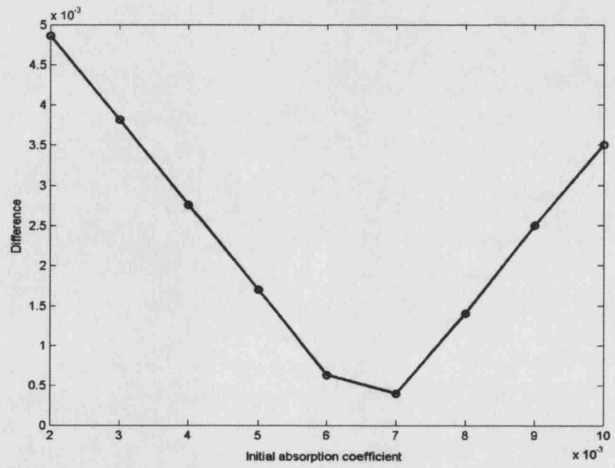

Figure 3.3.6 A plot of the difference between the mean value in the reconstructed region of the breast and the assigned initial absorption coefficient for images of the absorption coefficient.

3.3.1 Discussion

In both the absorption and scattering cases the difference between the mean value within the region of the breast and the assigned value for the breast is reduced as the assigned coupling fluid properties approach the optical properties of the breast. This suggests that it is necessary to match the properties to those of the breast. It is worth noting, however, that there is little difference in the appearance of the images with up to a 40% variation in the optical properties of the coupling fluid from those of the breast. This is encouraging for clinical studies where the exact optical properties of the breast are unknown. The exception to this trend is figure 3.3.3 p). In this figure the optical properties of the coupling solution ($\mu_a = 0.007$ and $\mu_s' = 0.7$ mm^{-1}) were close to those of the breast ($\mu_a = 0.007$ and $\mu_s' = 0.8$ mm^{-1}) and yet the image appears to have a very low scattering region towards the centre. It is possible that this is a result of the small differences being reconstructed in this case resulting in an ambiguous solution.

Figure 3.3.6 indicates that the initial starting parameter used in the reconstruction has a significant effect and that the closer the starting parameter is to the real values the more accurate the reconstruction. It is interesting to note that in the case investigated the difference between the mean absorption of the reconstructed breast volume and the assigned value for absorption is lowest when the initial absorption for the reconstruction is assigned as the value of the breast as opposed to the value of the coupling fluid. This suggests that it is important that the properties of the coupling fluid are known as accurately as possible and that they are matched to the properties of the breast.

One limitation of this study is that the data used is not subjected to noise. Experimental TPSFs contain a variety of sources of noise that will potentially affect the reconstructed images. It is possible that reducing the absorption or scatter of the coupling fluid will increase the signal to noise ratio, especially for large source and detector separations, and so may improve image quality. Thus further experimental investigations into the properties of the coupling fluid may be necessary to determine the optimum optical properties of the coupling fluid.

There are also other factors that may need to be investigated to identify the ideal properties of the coupling fluid. As mentioned previously the effect of a refractive index mismatch on the reconstruction is unknown and so may produce a significant source of error. Additionally the dye used to match the optical properties of the coupling fluid to that of the breast needs to be chosen with care. A dye is required which has significant absorption at 780 and 815 nm and preferably with the same wavelength dependence of tissue across these values. A further

consideration for our study is that the breast is to be submerged in the liquid for up to around 11 minutes at a time and so it is essential that the dye is not an irritant or of sufficient strength to cause colouration to the skin.

3.4 Calculating the Jacobian (J) of a system.

As seen in chapter 1.7 the reconstruction of images from the data requires calculation of the sensitivity matrix J [5]. This matrix is usually obtained numerically from a theoretical model but can also be derived empirically. It is possible that the empirically derived sensitivity matrix will provide a more accurate representation of the true sensitivity across the object as it is not based on any assumptions regarding the state of the object. In this section three alternative techniques for determining sensitivity matrices are compared:

1. Calculated from a theoretical model.
2. Constructed from experimental perturbation data acquired in the manner described in section 3.2.
3. Constructed from data acquired from simulations of each perturbation measurement made.

A comparison of the matrices can be achieved by viewing the matrices directly with the use of an appropriate finite element mesh, or by using each individual matrix to reconstruct an image and comparing the results. The latter provides an indication of whether the experimental matrix can be used in simple linear reconstructions to produce images. Such a method may have an advantage over using a calculated sensitivity matrix, as systematic errors in the data collection could be eliminated. A linear reconstruction method could also be used as a quick initial indicator of a data set's reliability as the computational time for reconstruction using such a matrix could be reduced to a few seconds.

3.4.1 Numerical FEM matrix

As described in chapter 1.7 TOAST constructs a sensitivity matrix using a finite element method to determine the PMDF for each source and detector combination (Arridge et al 1995). This sensitivity matrix is an $N \times M$ matrix, where N is the number of pixels and M is the number of measurements.

3.4.2 Empirical derivation of the Jacobian

If we introduce an isolated perturbation into an otherwise homogenous medium then as described in chapter 1.7, we can assume that the corresponding change in measurement can be expressed as follows:

$$J_{n,m}(x_0(r),\omega) = \frac{Y_{n,m}(x_1(r),\omega) - Y_{n,m}(x_0(r),\omega)}{x_1(r) - x_0(r)} = \frac{\partial Y_{n,m}(x_0(r),\omega)}{\partial x} .$$

(3.4.1)

The values of $J_{nm}(x_0(r),\omega)$ plotted over the volume of the object of interest represents the so-called photon measurement density function (PMDF) which describes the magnitude of the change in the measurement $Y_{nm}(x,\omega)$ that will result from a unit change in optical properties x at position r for a given source detector pair n,m. The sensitivity matrix is then composed from all the derivatives of $J_{nm}(x_0(r),\omega)$ for all source and detector combinations at all mesh nodes. Thus an experimental sensitivity matrix can be constructed by inserting a small perturbation of different scattering or absorbing properties within a homogenous volume. Measurements are recorded for both the initial homogenous state and the state inclusive of the perturbation. Thus:

$$J_{n,m}(x_o(r),\omega) = \frac{\textit{Measured datatype for object - Measured datatype for homogenous reference}}{\textit{Optical property of object - Optical property of homogenous reference}}$$

(3.4.2)

For the experiment presented in section 3.2 a perturbation of ten times the background absorption and scatter was introduced to a homogenous system and data were collected for both the perturbed and homogenous states. We can therefore use this data to construct an empirical sensitivity matrix. The data acquired represents the sensitivity for one half plane of the hemisphere (figure 3.2.1). The sources and detectors are positioned around the hemisphere in a pattern that exhibits 6-fold symmetry (figure 3.1.1 a). This means that the same sensitivity will be seen in 5 other identical half planes. Thus we can build a sensitivity matrix that incorporates data from 114 positions in the hemisphere. This method has been used previously to construct the sensitivity matrix of other imaging systems (Sevick et al 1994).

3.4.3 Numerical perturbation matrix

The forward solver in TOAST was used to simulate the measurements for the isolated perturbations, and the model predictions were used to generate a second sensitivity matrix. Both the numerical perturbation and empirical sensitivity matrices are $N \times M$ matrices, where N is the number of different positions of the perturbation and M is the number of measurements recorded (or simulated) at each position. It should be noted that as M is the same value for all of the sensitivity matrices to be studied, JJ^T should be the same size for all three (an $M \times M$ matrix).

In order to view the three different sensitivity matrices, appropriate meshes must be produced. The numerical FEM sensitivity matrix can be displayed using the mesh shown in figure 3.1.2

with the images produced representing the sensitivity at every node of the mesh. To display both the empirical and numerical perturbation matrices a mesh is used where the nodes represent the positions of the perturbations (shown in figure 3.2.1). Performing a Delaunay triangulation on the coordinates of the nodes creates the elements. This was achieved using the Delaunay3 triangulation function in MATLAB.

3.4.4 Results

All three sensitivity matrices are displayed for a particular source and detector combination in figures 3.4.1 to 3.4.4. The values for both intensity and meantime measurements for both μ_a (figures 3.4.1 and 3.4.2) and κ (figures 3.4.3 and 3.4.4) data are shown.

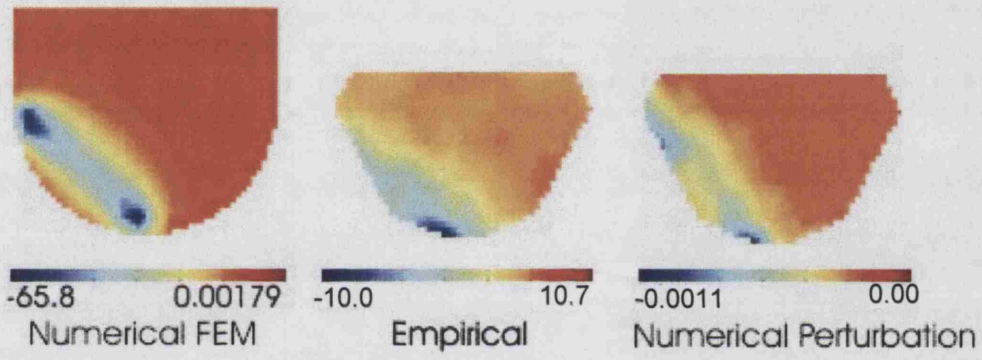

Figure 3.4.1: The Numerical FEM, empirical and numerical perturbation matrices for intensity measurements and μ_a data.

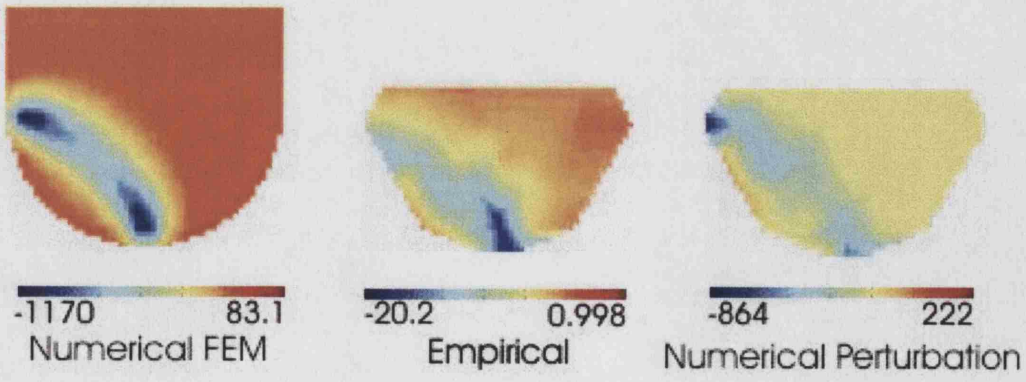

Figure 3.4.2: The numerical FEM, empirical and numerical perturbation matrices for mean time measurements and μ_a data.

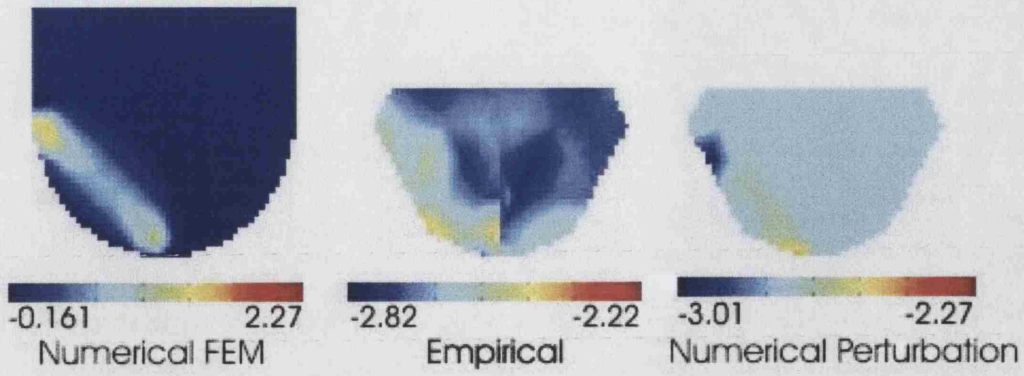

Figure 3.4.3: The numerical FEM, empirical and numerical perturbation matrices for intensity measurements and κ data.

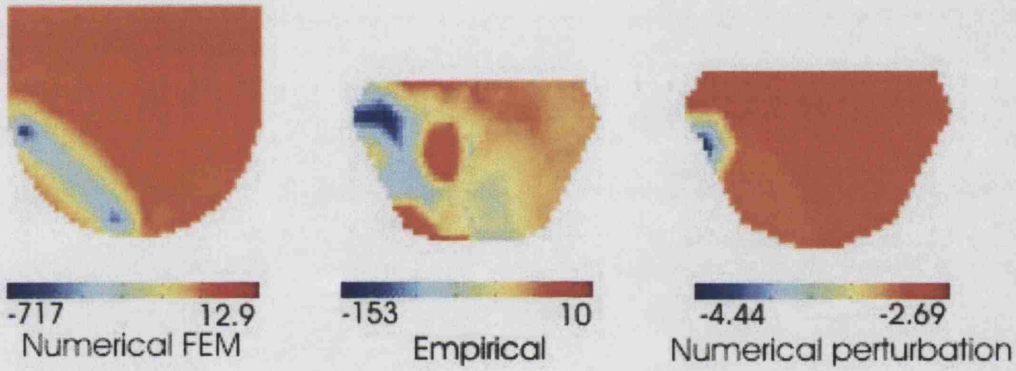

Figure 3.4.4: The numerical FEM, empirical and numerical perturbation matrices for meantime measurements and κ data.

3.4.5 Discussion

In all cases the empirical matrix appears to agree qualitatively with the numerical FEM matrix. There are, however, significant discrepancies between the two. In particular the numerical FEM matrices appear to show a degree of symmetry across the PMDF that is not seen in the empirical matrices. Additionally the numerical FEM matrix is smoother than the empirical matrix. There are two main reasons for these discrepancies. The first is due to noise in experimental data. As seen in figures 3.2.3, 3.2.4, and 3.2.5 the spatial resolution, spatial accuracy and contrast of the reconstructed images using the experimental data are less than ideal. In particular the large errors seen on the spatial accuracy of the system will affect the results of a sensitivity matrix constructed from such measurements. The second is due to a difference in the number of positions across the volume that are sampled by each sensitivity matrix. The mesh used to calculate and display the numerical FEM sensitivity matrix contains 35233 nodes, in comparison the mesh used to display the empirical matrix contains just 114. Consequently the

images presented of the different sensitivity matrices appear to have slightly different geometries. If data were to be collected at the position of every node in the mesh used to display the numerical FEM matrix then this would not be a factor. However, given that a measurement for one position takes around 11 minutes to acquire, this is not feasible even through manipulation of the 6-fold symmetry. Furthermore, given the close correlation between the matrices produced it is perhaps not necessary to sample at every node.

A more direct comparison can be made between the empirical and the numerical perturbation matrices as the same mesh has been utilised in both cases. Once again the two matrices appear to exhibit a reasonable qualitative agreement.

Quantitatively, however, there appears to be poor agreement between the empirical and numerical FEM matrices with a ratio of up to 600 being seen. This could be due in part to the errors in the experimental data as discussed, but the largest discrepancy is again likely to be due to the large difference in the number of positions that have been sampled by the two methods. This is supported by the fact that there appears to be much closer correlation between the intensity measurements for the empirical and numerical perturbation matrices. It should be noted, however, that there is a variation in the meantime measurements, of the empirical and numerical perturbation matrices, of up to a factor of 800. It should also be noted that positive values are obtained within the empirical matrix for absorption and intensity data. This is the reverse of what would be expected as the introduction of an absorbing perturbation should lead to a decrease in intensity. This discrepancy is due to laser fluctuations between the acquisition of the perturbation data and the homogenous data.

3.4.6 Reconstruction using the empirical matrix.

As seen above, construction of a sensitivity matrix from experimentally measured perturbations to a system produces a more irregular result than one generated from a theoretical approach. This is because the numerical FEM matrix can be used to include the values at many more nodes and it is not subject to the experimental constraints of the system. It is possible, however, that an empirical matrix could be more appropriate for a real system as the matrix is acquired on the medium to be imaged itself rather than a model, which will only approximate the true properties and geometry of the medium. For this reason it is of interest to study the reconstructed images that can be obtained using the empirical matrix. Although unlikely to be superior to the numerical FEM matrix, it is feasible that such images could be used as a quick reference before more complicated reconstruction has been performed.

Figure 3.4.5 shows the images obtained for the absorbing perturbation in position 3 shown in figure 3.2.1 using a sensitivity matrix constructed from empirical measurements and the numerical FEM matrix. In both cases a linear reconstruction method as described in chapter 1.7 is used. A Tikhonov regularisation number of 0.0001 was used. Linear reconstruction is used in this case because it is the simplest method to reconstruct a small change relative to a homogenous background (see chapter 1.7).

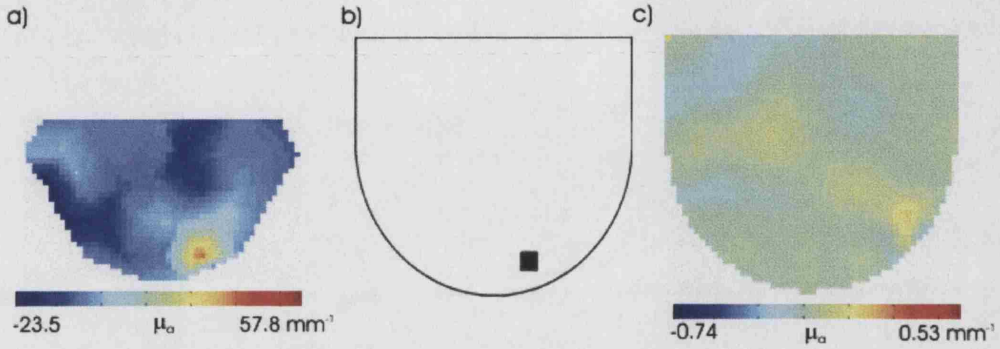

Figure 3.4.5: A linear reconstruction of an absorbing perturbation placed in the position indicated b) using a sensitivity matrix constructed from a) experimental and c) theoretical values.

3.4.7 Discussion

Images of the absorbing perturbation placed at different positions within the hemisphere have been successfully reconstructed using an empirically constructed sensitivity matrix. The images produced contain very few artefacts and appear to exhibit good localisation of the perturbations. In comparison the image obtained using the numerical FEM matrix is surprisingly poor. The contrast and localisation of the perturbation in figure 3.4.5 c) being inferior to that seen in figure 3.4.5 a).

However, the reconstructed values of the change in μ_a relative to the homogenous state (μ_a = 0.007 mm^{-1}) in figure 3.4.5 vary from –23.5 to 57.8 mm^{-1} for the numerical matrix and -0.74 to 0.53 for the numerical FEM matrix. The ranges of both are unrealistic. We would expect a positive increase of around 10 times due to the absorbing perturbation. Although it should be noted that some negative changes might be expected due to experimental differences in the measured optical properties of the coupling liquid between the homogenous measurement and that of the perturbation measurement, such changes would be expected to be minimal. Thus the range exhibited for the image of the numerical FEM matrix is in fact more realistic than that of the empirical matrix.

It should be noted that neither image compares to the clarity of the images and the range of values reconstructed for the images shown in figure 3.2.2 where non-linear reconstruction (TOAST) and a numerical FEM matrix are employed. However, the advantage of such a method is that it takes considerably less time to reconstruct an image. Therefore it is conceivable that this technique could be used to obtain a degree of prior structural information in a few seconds that could then be used in a longer (several hours) TOAST reconstruction.

3.6 Preliminary trials on healthy volunteers.

As with the previous patient interface described in part 2 it is important to assess the liquid coupled interface on a sample of healthy volunteers in order to determine the appearance of images obtained for the normal healthy breast. Trials on healthy volunteers are also important to establish the suitability of the system in a clinical environment.

3.6.1 Patient interface.

For the system to be evaluated on volunteers, a custom made bed has been built. The structure of the bed consists of a wooden frame, treated with a water resistant sealant, and a lower shelf for the storage of necessary equipment. The hemisphere is attached to a plastic ring secured firmly into an aperture in the bed as shown in figure 3.6.1. A channel is cut into the ring, which enables any coupling fluid that overflows from the hemisphere to be drained away via plastic tubing. The hemisphere is filled with coupling fluid from below using a peristaltic pump. The addition of a heating element to the pump system will ultimately provide a means of ensuring the liquid is maintained at a constant temperature. To ensure maximum comfort for the patient the table is covered with a layer of foam padding and a pillow is provided. Towels are available as required.

Figure 3.6.1 The hemisphere incorporated into a custom built bed and overflow system to be used in clinical studies.

To ensure optimum sampling of the breast, the breast must fill as much of the reconstructed volume as possible. Our imaging system is limited to just 32 source and detector positions, and the sampling of the surface is therefore limited. Therefore we intend to produce a range of hemispheres with the smallest possible diameter being used in all cases. A method has been developed to make a range of different sized breast cups.

3.6.2 Preliminary studies on healthy volunteers

Initial studies on three healthy volunteers have been performed to date. Prior to the investigation, the coupling fluid was prepared at an ambient room temperature of 23°C. Data were acquired on each of the volunteers' breasts for a total scan time of 11 minutes, or 10 seconds per source. The procedure was then repeated with the resin cylinders described in section 3.2 attached to the medial and lateral sides of each breast using micropore tape. This enabled us to see if a perturbation of 10 times the background μ_a and μ_s' can be reconstructed in the presence of the complex structure of the breast. This simulates a patient with a high contrast lesion, although this contrast is in excess of that seen between malignant and healthy tissue (see chapter 1.2).

3.6.2.1 Initial images using the system on a healthy volunteer

The reconstructed absorption images of the first healthy volunteer's left breast with and without cylinder A attached are shown in figure 3.6.2. The corresponding scatter images are shown in figure 3.6.3.

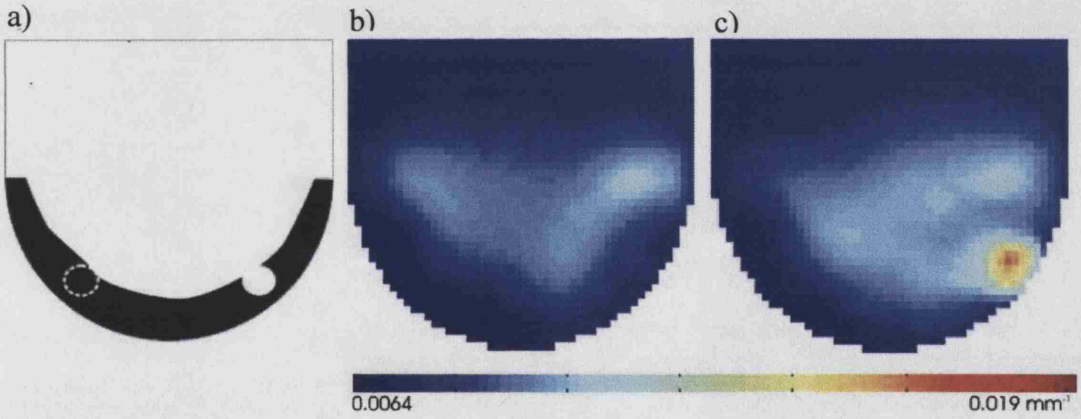

Figure 3.6.2: The reconstructed images of μ_a for b) a healthy volunteer's left breast c) the same breast with cylinder A attached in the position indicated in a)

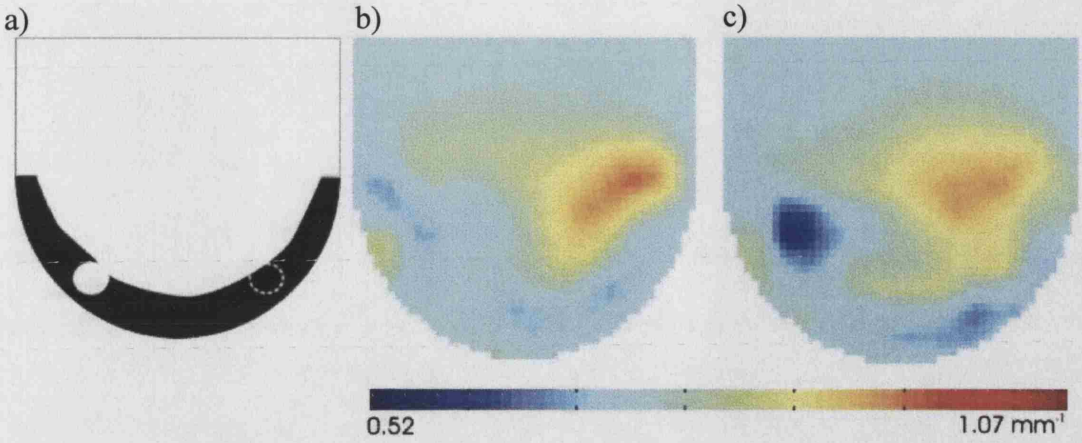

Figure 3.6.3: The reconstructed images of μ_s' for b) a healthy volunteer's left breast c) the same breast with cylinder S attached in the position indicated in a).

3.6.2.3 Discussion

The first human images obtained using the liquid coupled interface are shown in figures 3.6.2 and 3.6.3. The absorption images obtained exhibit an area of higher contrast which corresponds to the size and location of the breast. This shows that the inevitable differences between the properties of the coupling solution and the breast can be reconstructed. The absorption image obtained with the cylinders attached to the breast shows an area of high absorption that corresponds to the position of cylinder A. The contrast and spatial resolution are again low, but are consistent with the values obtained in the phantom studies shown in section 3.2.

The scatter images also contain a large region of high contrast in the approximate location of the breast, although the contrast is higher than would be expected from the previous phantom studies. However a distinct area of contrast corresponding to cylinder S is not seen. It was considered that a reason for both these anomalies might be that the value of $\mu_s' = 0.8$ mm^{-1} for the coupling solution is an insufficiently accurate reference for the high scatter of the ribs ($\mu_s' \sim$ 2 mm^{-1}) (Firbank et al 1993). As a consequence we have significantly different boundary conditions for the volunteers as compared to those for the homogenous reference. A possible effect of this on the reconstruction is that these differences are projected back into the image, masking any other features. Due to this, alternative methods of providing a suitable reference, which includes the high scatter of the chest wall, need to be investigated. Alternatively prior knowledge of the properties of the chest wall could be involved in the reconstruction.

The studies on healthy volunteers also suggested that patients could be positioned with more ease than for the 2D system, and that a scan time of 11 minutes is acceptable.

3.6.3 Alternative reference media for the liquid coupled breast imaging device

In section 3.6.2 it was postulated that the dominant scatter feature seen in the first healthy volunteer images obtained using the liquid coupled system is caused by a mismatch in the scattering properties between the chest wall and the reference used. In order to test the hypothesis and to attempt to remove this feature, a further series of scans involving a healthy volunteer was performed. In this study data were acquired on the volunteer's right breast only and two separate data sets, with the volunteer repositioned each time, were acquired on the right breast with cylinders A and S attached (figure 3.6.4).

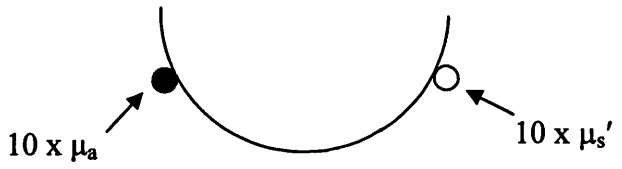

Figure 3.6.4: The positions, on the breast, of the cylinders described in section 3.2.

Additionally, five separate reference measurements were acquired, interspersed with the volunteer measurements to ensure that the effects of slight temporal variation in the system between a data and reference acquisition were minimised. It was anticipated that the selection of an appropriate reference medium would reduce or eliminate the dominant feature observed in earlier scatter images and further knowledge of the transport of light in this specific situation would be derived. Additionally, we were keen to identify an alternative to the previous reference medium of a column of liquid extended above bench level, which requires the use of a watertight detachable container and is therefore technically challenging to implement.

The five references investigated were as follows:

a) The liquid extension:

This reference is the same as that used earlier in section 3.6.2.

Figure 3.6.5: A picture of the extension added to the hemisphere to be filled with liquid in order to be used as a reference.

b) Resin block:

This reference consists of a cylindrical block made from an epoxy resin mixture identical to that used to produce the solid tissue-equivalent conical phantoms described earlier (section 2.1.3). The block was placed over the top of the liquid filled hemisphere in contact with the liquid. The block has a diameter of 200 mm and a thickness of 65 mm. The optical properties of the block are $\mu_a = 0.007$ mm^{-1} and $\mu_s' = 2.0$ mm^{-1}. The high scatter coefficient was chosen to represent the high scattering tissues within the chest wall, such as bone and muscle. It should also be noted that the refractive index of the block, $n = 1.56$, is higher than that of the coupling liquid, $n = 1.33$.

Figure 3.6.6: Photograph of the resin block that can be placed over the hemisphere filled with coupling fluid to provide a reference.

c) The volunteers back:

The volunteer was asked to lie on her back over the hemisphere and the pump was used to fill the hemisphere to the point of overflow so that the liquid was in contact with the volunteer's back.

d) Bag of coupling solution (higher scattering properties):

A large 4 litre water carrier, made of a thin transparent plastic, was filled with a solution containing intralipid, distilled water and dye in concentrations to yield an absorption coefficient of 0.007 mm^{-1} and a transport scattering coefficient of 2 mm^{-1} to be consistent with the estimate of the scatter coefficient of chest wall tissues used for the resin block.

Figure 3.6.7: A photograph of the water carrier that can be placed over the hemisphere filled with coupling solution to provide a reference.

e) Male volunteer:

In this case the scan of a male volunteer, with the hemisphere filled with coupling fluid up to the chest wall, was employed as a reference. In principle this measurement provides an ideal reference for difference imaging of the breast since it should represent very similar optical properties within the chest wall, but without the breast present.

The advantages and disadvantages of each reference are outlined in table 3.6.1.

Reference	Optical Properties	Advantages	Disadvantages
a) Liquid Extension	$\mu_s' = 0.8$ mm^{-1} $\mu_a = 0.007$ mm^{-1} $n = 1.33$	Reproducible No refractive index mismatch.	Difficult to implement whilst maintaining a water tight seal. Homogenous optical properties through out the whole of the reference.
b) Resin Block	$\mu_s' = 2.0$ mm^{-1} $\mu_a = 0.007$ mm^{-1} $n = 1.56$	Easy to use Reproducible Homogenous	Need to ensure perfect contact with liquid. Refractive index mismatch.
c) Volunteers Back	unknown – likely to be close to front of volunteer.	Close match with optical properties of chest wall at front of body.	Longer scanning time for patient. Difficult to ensure no air is trapped. Back is concave Inhomogeneous
d) Bag of Liquid	$\mu_s' = 2.0$ mm^{-1} $\mu_a = 0.007$ mm^{-1} $n = 1.33$	Ease of use Reproducible No refractive index mismatch with coupling fluid	The wall of the bag may create a clear layer in which light can travel unscattered. Air bubbles may be trapped beneath the bag leading to image artefacts.
e) Male volunteer	unknown – simulation of chest wall.	Close match in optical properties to female chest wall.	Not clinically viable

Table 3.6.1: The advantages and disadvantages of 5 different references for imaging the breast using a liquid coupled device.

3.6.3.1 Results

In the following images both a vertical and horizontal plane through the cylinders is displayed. The following diagram illustrates the approximate position of the cylinders within these images:

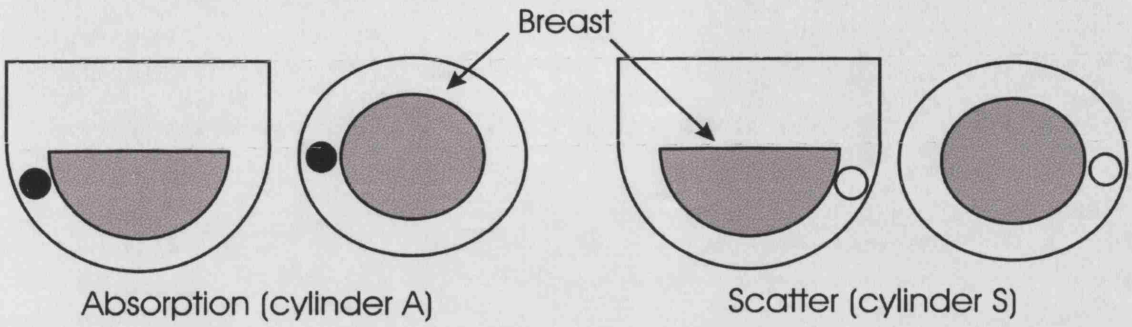

Figure 3.6.8: The expected positions of the cylinders in the images.

The following images were obtained using each separate reference.

a) Liquid Extension

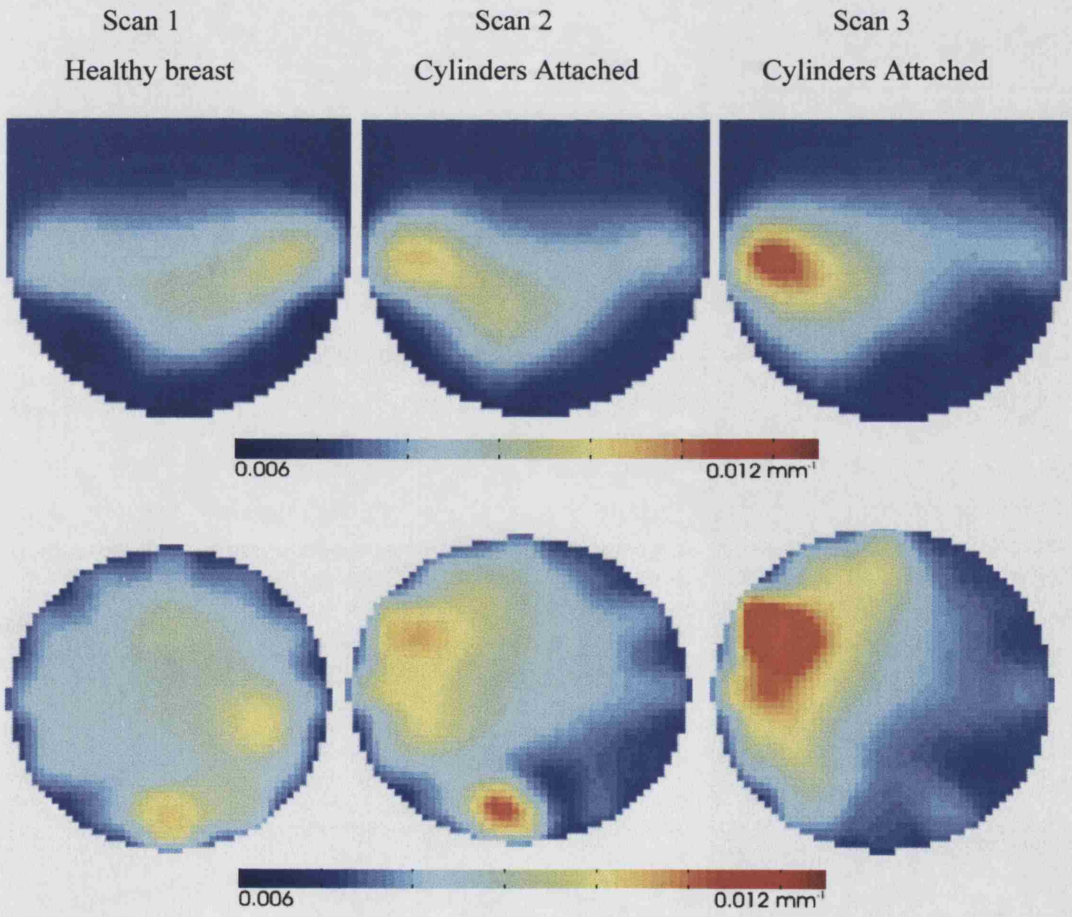

Figure 3.6.9: The images of μ_a obtained using the liquid extension as a reference.

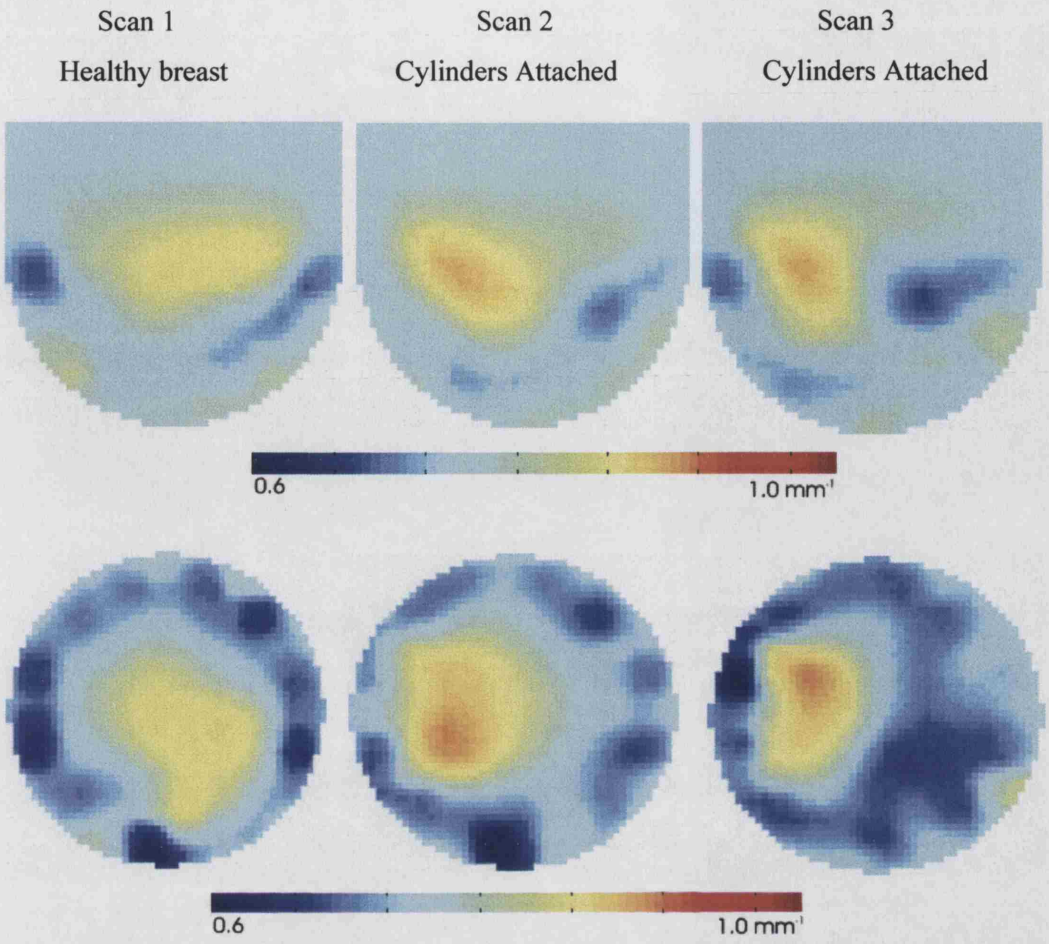

Figure 3.6.10: The images of μ_s' obtained using the liquid extension as a reference.

The liquid extension was the reference used in previous studies (section 3.6.2), which exhibited a large dominant feature in the scatter images. The images acquired here (figure 3.6.10) also clearly show a large dominant feature in all three scatter images (with or without cylinders), although the feature does exhibit a slightly higher contrast in the images with the cylinders attached. This is most likely due to a change in position of the breast (following attachment of the cylinders) and it should be noted that the scattering feature also moves after the breast is repositioned. This suggests that the high scatter region is due to the breast tissue itself rather than the chest wall as postulated. The absorption images (figure 3.6.9) are similar to those acquired previously. The increase in contrast of the cylinder in the image of the second scan (with cylinders attached) suggests that the volunteer may have been positioned closer to the edge of the hemisphere during this data acquisition than in the first scan.

b) Resin block

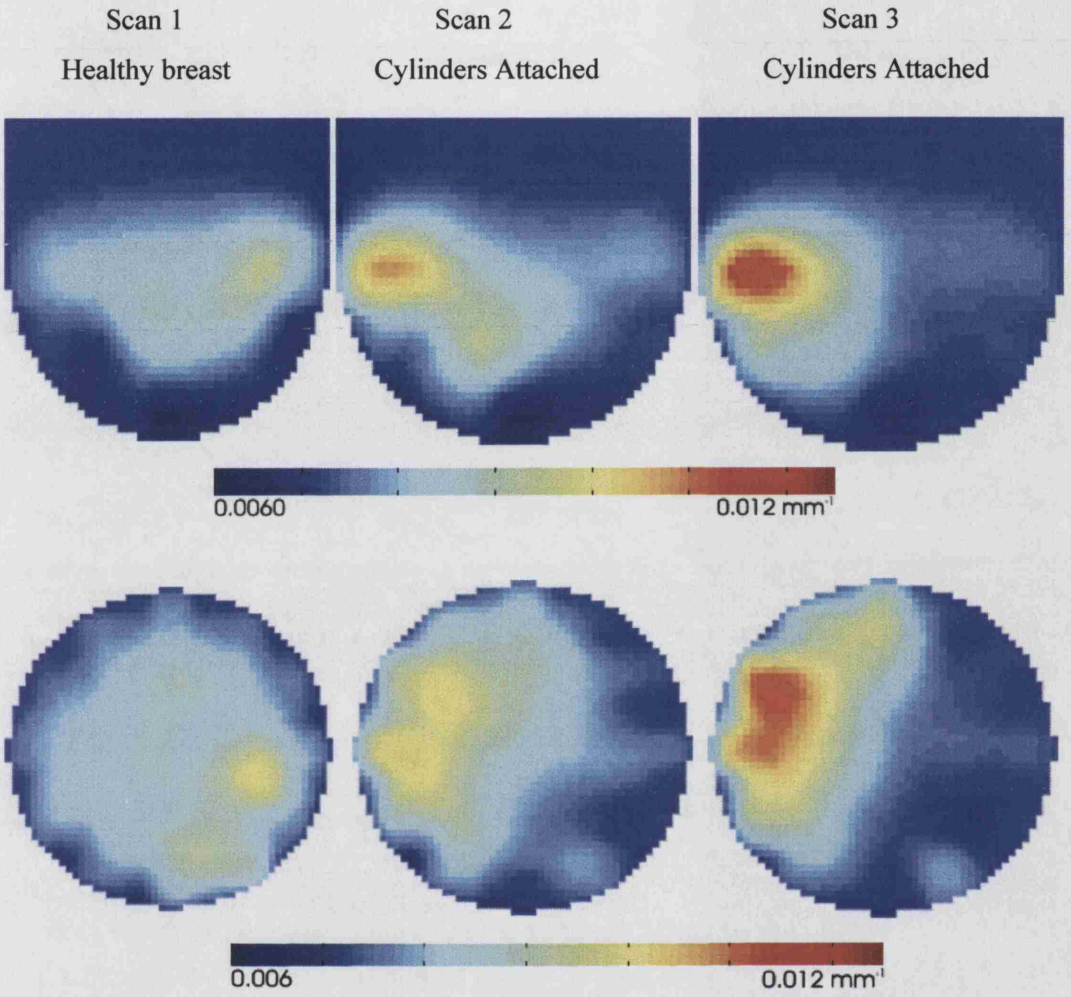

Figure 3.6.11: The images of μ_a obtained using the resin block as a reference.

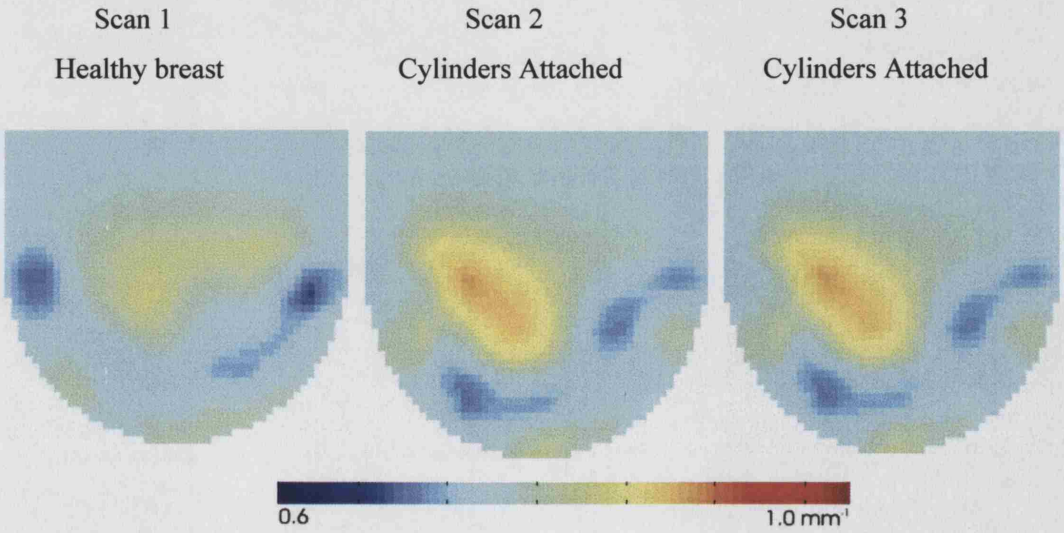

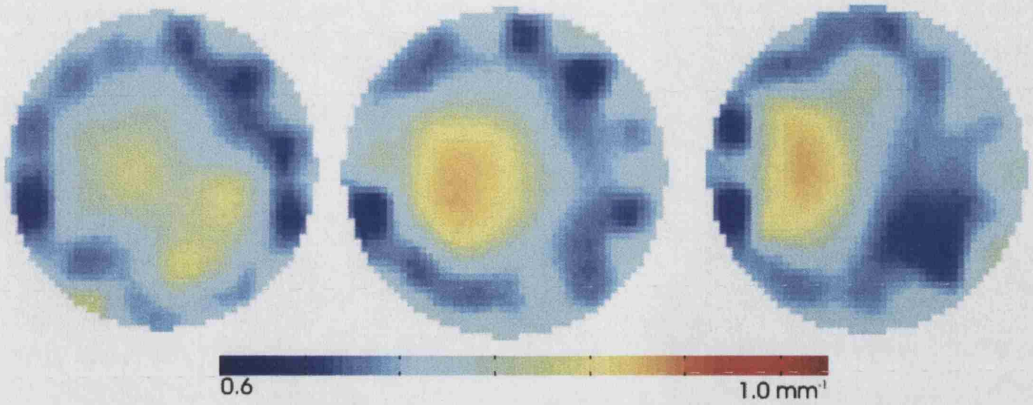

Figure 3.6.12: The images of μ_s' obtained using the resin block as a reference.

The images obtained using the resin block as a reference are similar in appearance to those obtained using the liquid extension. There does not appear to be a significant reduction in the dominant feature in the scatter image. However, there are two main advantages of using the resin block over the liquid extension. First, the liquid extension requires a watertight seal, which is difficult to employ in a clinical situation, and second, the optical properties of the resin block can be altered independently of the coupling fluid and so could be matched more accurately to the properties of the chest wall.

c) Volunteer's Back

Scan 1	Scan 2	Scan 3
Healthy breast	Cylinders Attached	Cylinders Attached

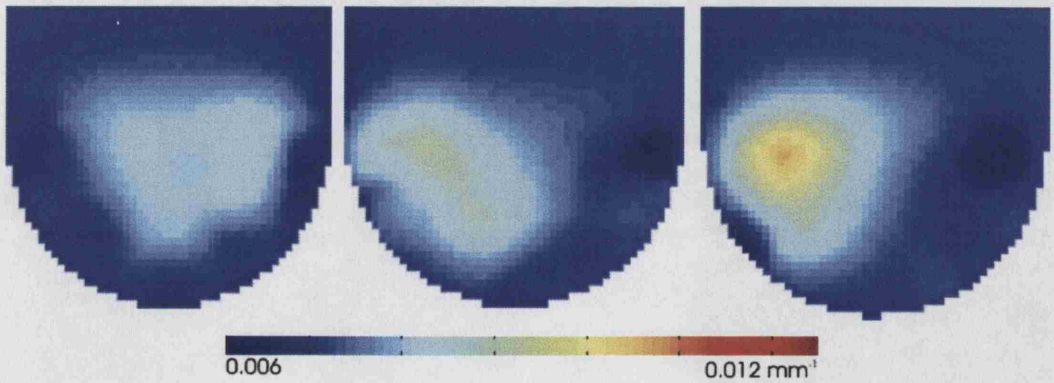

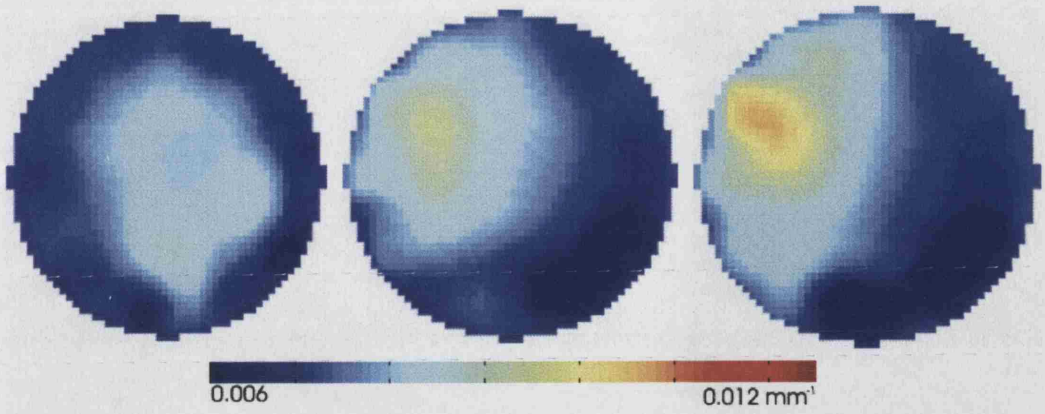

Figure 3.6.13: The images of μ_a obtained using the volunteer's back as a reference.

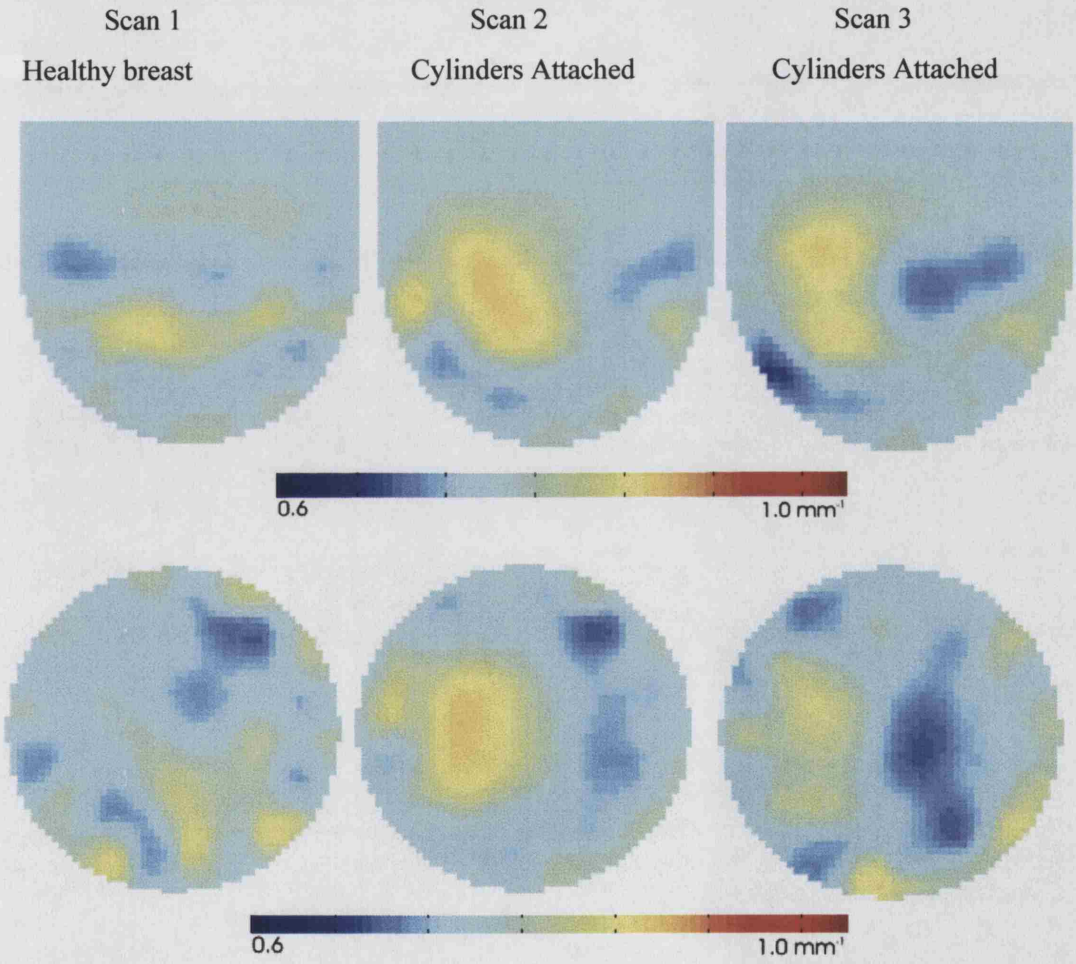

Figure 3.6.14: The images of μ_s' obtained using the volunteer's back as a reference.

The images shown in figure 3.6.13 are similar in appearance to the absorption images obtained using the previous references. The images shown in figure 3.6.14 appear to be dominated by artefact. Once again a large dominant scatter region is seen towards the centre, which is surprising given that this reference method was chosen to provide close optical properties to the

chest wall. The images also contain several smaller artefacts towards the edge of the images. These features may be a result of poor contact between the liquid in the hemisphere and the back due to its concave shape.

d) Bag of Liquid

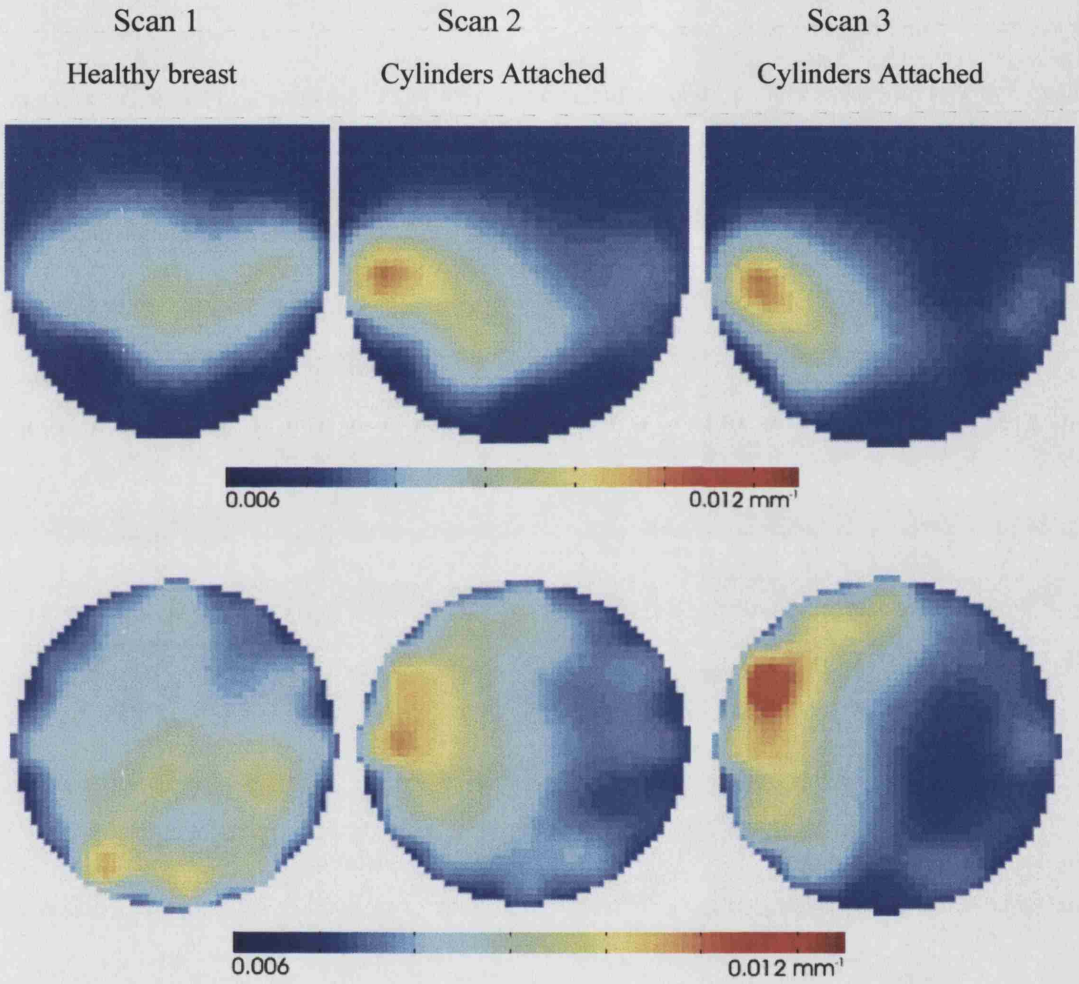

Figure 3.6.15: The images of μ_a obtained using the bag of liquid as a reference.

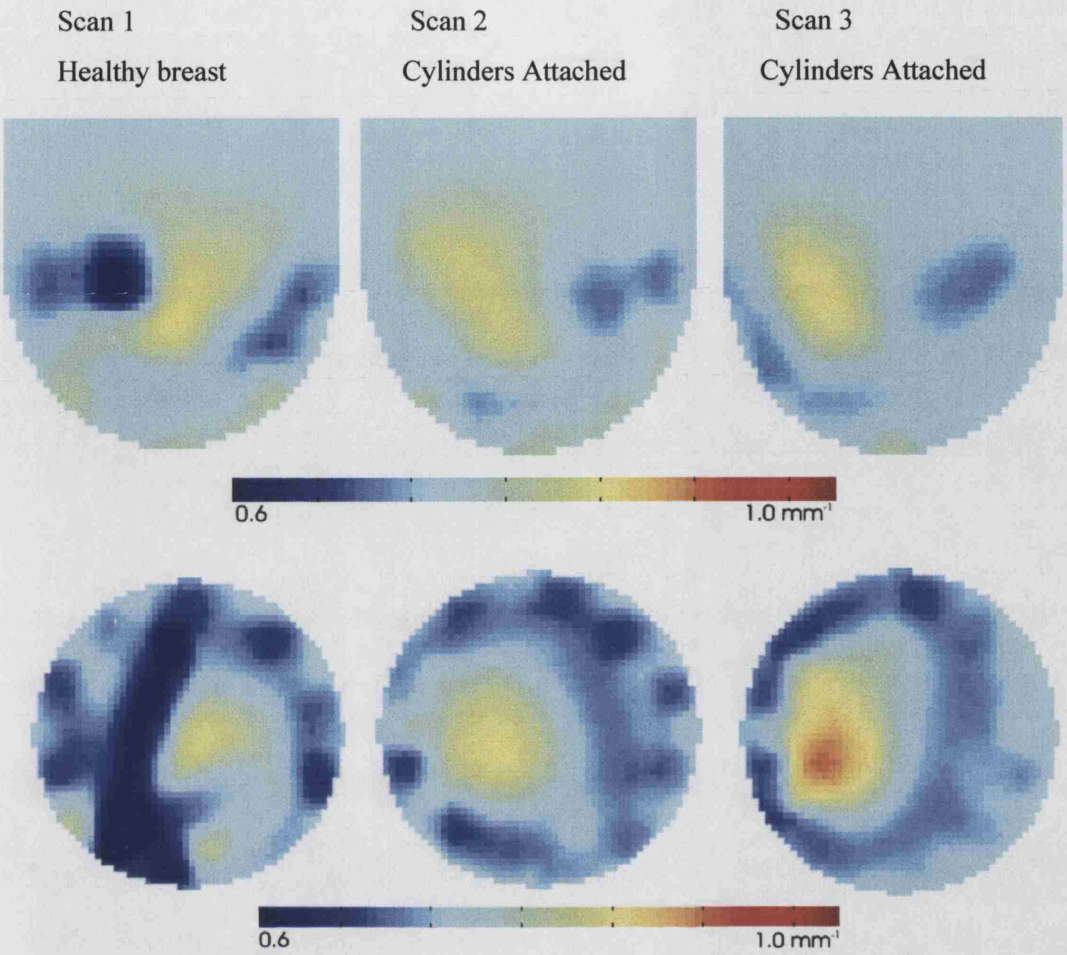

Figure 3.6.16: The images of μ_s' obtained using the bag of liquid as a reference.

In this case the contrast of the dominant feature in the scatter image appears to have been reduced. However there are several regions of low scatter towards the centre and there is a large dominant region of low scatter across the centre of the image acquired for the breast only. Once again the absorption images are very similar to those obtained using other reference media. It is possible that the increase in artefact, especially in the scatter images, is due to light being able to travel unscattered through a clear layer between the two liquid volumes created either by the wall of the bag, or by air being trapped under the bag.

e) Male volunteer

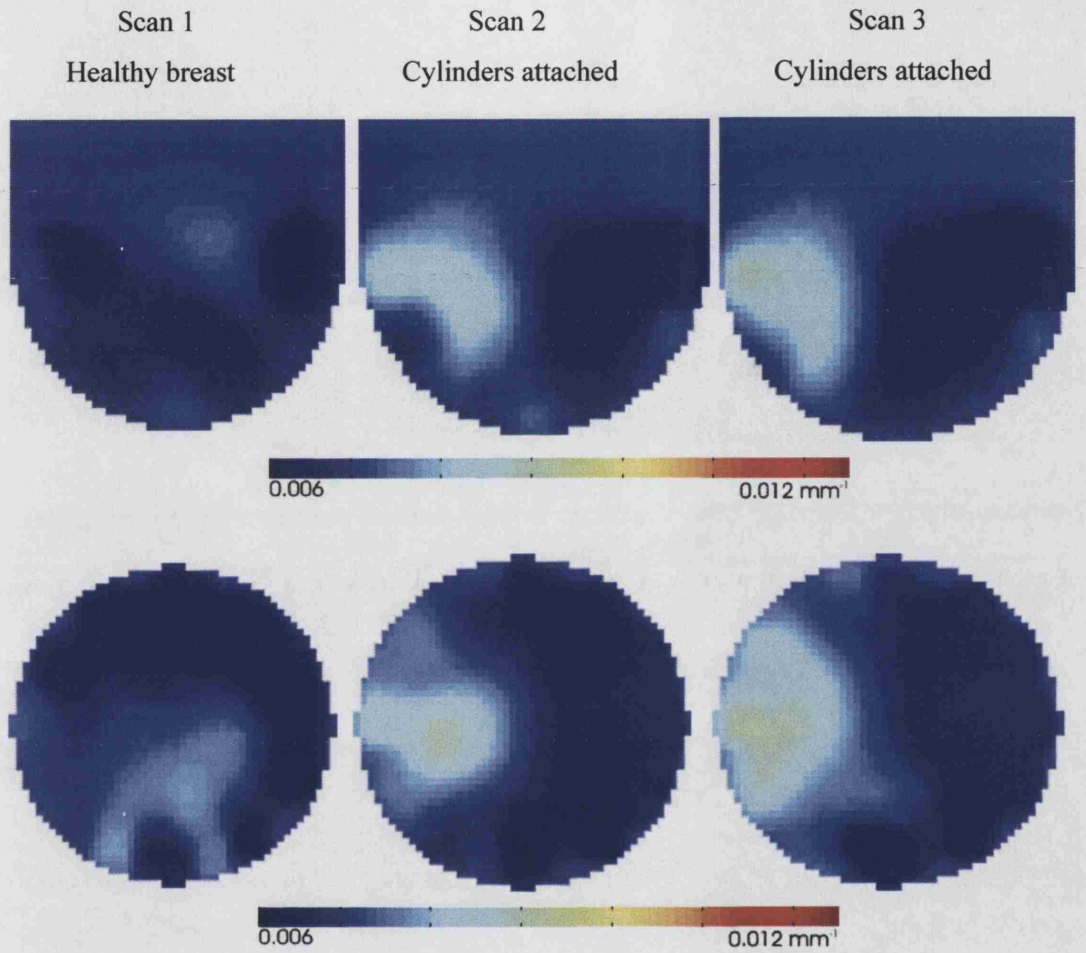

Figure 3.6.17: The images of μ_a obtained using a male volunteer as a reference.

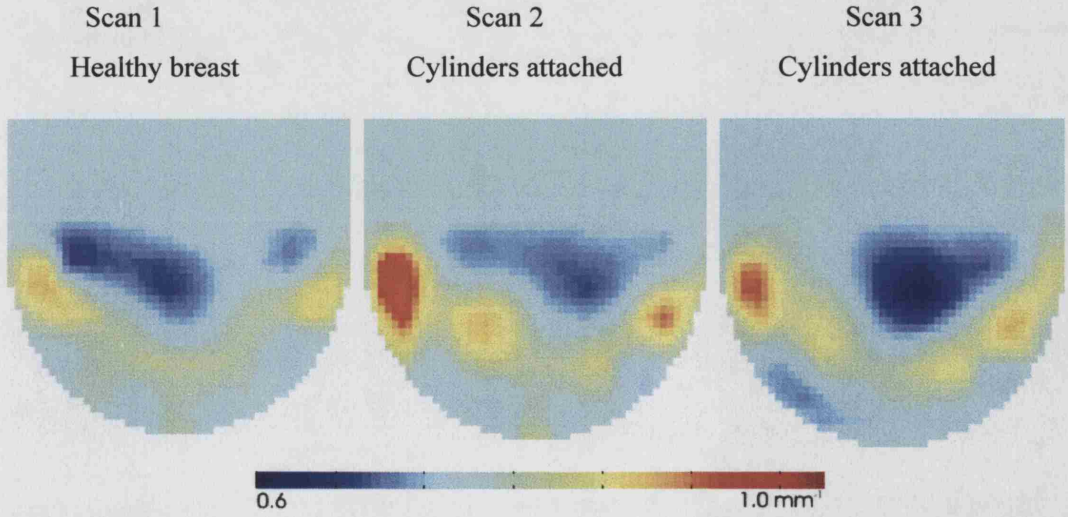

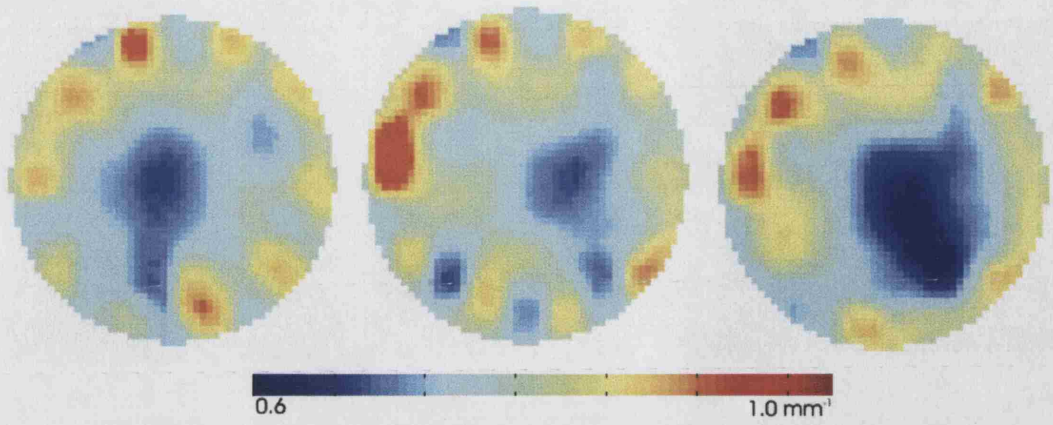

Figure 3.6.18: The images of μ_s' obtained using a male volunteer as a reference.

In this case the large scatter feature does not appear. However, the scattering cylinder is also not seen and the images are dominated by artefact. It appears that the contrast obtained for the absorption images is less than that obtained using the other references.

3.6.3.2 Images obtained from a male volunteer

In addition to being a potentially useful reference, reconstructing the images obtained from these male volunteers provides us with images of the chest wall with minimal breast tissue and so can be used to study the effect of this region. Two studies have been performed on male volunteers. Example absorption and scatter images from one male volunteer are shown in figure 3.6.19.

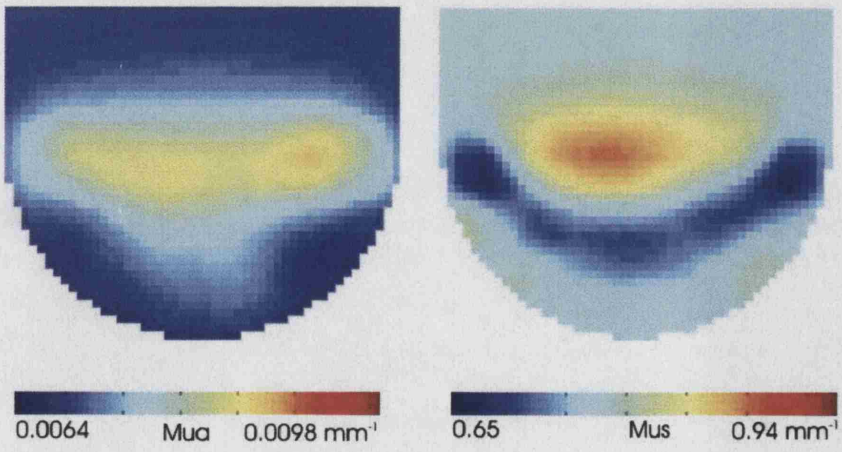

Figure 3.6.19: The reconstructed images of μ_a and μ_s' for a male volunteer.

The reconstructed images of the male volunteer do have a large dominant scatter region, however this region is not as large as the feature seen in the images of the female volunteer

figure 3.6.3. It is possible that a small amount of breast tissue extended into the hemisphere from the male volunteer, especially due to the adopted patient position, which may account for this feature.

3.6.3.3 Simulation

In order to investigate the limitations of the reconstruction when small features of high contrast are reconstructed in the presence of a large feature such as the breast the above experiment was simulated using a FEM method. For simplicity the cylinders were modelled as spheres with a radius of 6 mm with the same optical properties (i.e. μ_a = 0.07 mm^{-1} and μ_s' = 0.8 mm^{-1} for sphere A whereas μ_a = 0.007 mm^{-1} and μ_s' = 8.0 mm^{-1} for sphere S). The volunteer was modelled as described in section 3.3 with optical properties μ_a = 0.008 mm^{-1}, μ_s' = 0.85 mm^{-1}, which were estimated as being reasonable properties for the breast whilst providing a contrast to the background optical properties which were set at μ_a = 0.007 mm^{-1} and μ_s' = 0.8 mm^{-1}. The spheres were placed in positions to correspond with those in the experiment described above.

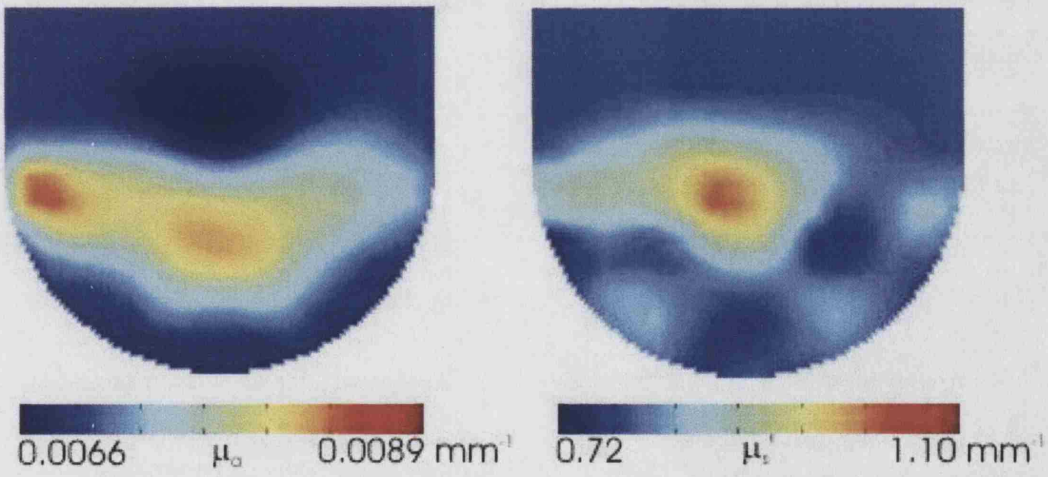

Figure 3.6.20: a) absorption and b) scatter images reconstructed from simulated data representative of a breast with both an absorbing and a scattering cylinder attached.

As has been seen experimentally the absorbing sphere is the dominant feature in the reconstructed image of absorption, but the scattering cylinder cannot be identified. These simulations, therefore, suggest that this discrepancy is a limitation of the reconstruction.

3.6.3.4 Reconstruction using prior knowledge from an inhomogeneous reference

For all the images presented so far the initial parameters for the reconstruction were taken as the best estimate of the properties of the coupling fluid. These were μ_a = 0.007 mm^{-1} and μ_s' = 0.8

mm^{-1}. However many of the references included in this study have defined regions of different optical properties. Previous simulations and studies on head phantoms have shown that the use a prior information of separate regions with similar optical properties can be beneficial to the reconstruction (Gibson et al 2003; Schweiger et al 1999). In the case using a resin block as a reference we know that the region on top of the hemisphere will have different optical properties to those of the hemisphere itself and importantly those properties are known to within ± 10 %. Thus reconstructing for these regions separately may yield more accurate results. The following images were obtained using this region-based reconstruction. In this case the mesh displayed in figure 3.1.2 was used. The 50 mm cylinder at the top of the mesh was assigned the initial starting parameters μ_a = 0.007 mm^{-1} and μ_s' = 2.0 mm^{-1} to be consistent with the properties of the resin block. The hemispherical bottom to the mesh was assigned the initial starting parameters μ_a = 0.007 mm^{-1} and μ_s' = 0.8 mm^{-1} to be consistent with the properties of the coupling fluid. Each region was assigned using MESHMOD a specialised mesh editing tool contained within the TOAST package.

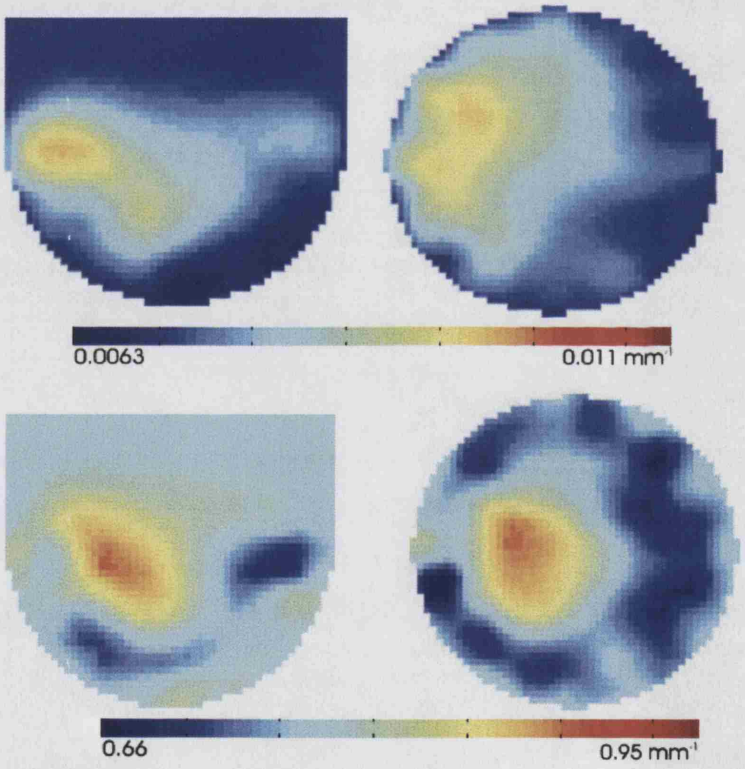

Figure 3.6.21: Absorption and scatter images from a region based reconstruction of the breast with the cylinders attached.

There is very little difference between the images shown in figure 3.6.21 and the equivalent images in figures 3.6.11 and 3.6.12 indicating that using different starting parameters for each region in the reconstruction does not appear to improve image quality in this case. The use of a prior information can also be implemented in the form of a region based reconstruction. This

process involves segmenting the mesh into sections of similar optical properties and performing an initial reconstruction to derive starting parameters for these areas. This information is then used in a second reconstruction which allows the defined regions to be reconstructed independently of each other. In the case presented here, the improvement that may be obtained from employing this method is likely to be insignificant due to the limited sampling of the region above the hemisphere. It should be noted, however, that if the surface of the breast is known then region-based reconstruction could be used to reconstruct the volume of the breast independently of the region of coupling fluid and superior images may be obtained. This requires further investigation (see future work).

3.6.3.5 Discussion

It has been seen that for each type of reference measurement the absorbing cylinder was successfully imaged against the complex structure of the breast. However, a cylinder with high scattering properties was not. It is noted that the contrast exhibited for the scattering cylinder in the perturbation experiments in section 3.2 was considerably lower than that of the absorption cylinder and it is likely that this intrinsically low contrast in the presence of a large feature such as the breast would prove difficult to distinguish. This has been shown to be the case in the simulations shown in figure 3.6.20, where, once again, the absorbing feature can be identified in the presence of the breast whilst the scattering feature cannot. The results of this simulation suggest that this is a limitation of the reconstruction. This result is disappointing for the development of this system. Its impact on breast imaging is that we are unlikely to be able to distinguish small ($< 1cm^3$) scattering features using the hemisphere described in this chapter. To overcome this limitation a series of smaller hemispheres are to be developed (see section 4.1.2). Using smaller hemispheres will result in smaller source and detector separations and so, as described in section 3.2, may result in increased spatial resolution and contrast. Such smaller sized hemispheres are likely to be suitable for the majority of women, but may mean that larger women can not be imaged using this technique without a compromise on the amount of information available.

The attempts to reduce the large dominant scattering feature seen in the initial images obtained for a healthy volunteer through the use of a more appropriate reference have been largely unsuccessful. The results obtained indicate that this feature is actually a real feature and not a result of a mismatch between the reference and the chest wall as first believed. The patient position adopted in this method acts to pull the pectoral muscle down into the hemisphere. The high scatter region appears to correlate with the position the pectoral muscle is likely to adopt. This does not agree with previously published results which give the scatter coefficient of

muscle as 0.7 mm^{-1} at 780 nm (Simpson et al 1998), that of glandular tissue as 1.4 mm^{-1} and adipose as 0.8 mm^{-1} (Peters et al 1990), although these later results were obtained in vitro and so may not be representative of the in vivo properties, which will include the effects of blood. The appearance of the pectoral muscle within the images is analogous with the absorption results obtained in part 2 where a central feature that is believed to be the pectoral muscle was occasionally apparent.

Despite these problems we concluded that the most practical reference, in a clinical situation, is the resin block and so this will be employed for all future studies.

3.7 Summary of 3D system

In the summary of part 2, four problems with the tomographic ring system were identified. As previously discussed, it was anticipated that the liquid coupled interface would overcome these problems. Following from the preliminary investigations of this system, presented in this part, we can now examine whether the initial expectations have been realised.

1. Three-dimensional images of both phantom studies and healthy volunteers have now been performed. However, it has not yet been possible to reconstruct a scattering feature attached to the side of a healthy breast.
2. Intensity has been employed as a datatype and, by employing both intensity and meantime, images have been reconstructed of both scatter and absorption parameters although a degree of crosstalk remains.
3. Although only three studies have been performed so far, positioning the volunteer has proven to be substantially easier using this technique than using the ring system. Additionally volunteers commented on the comfort of the scanning bed. There were, however, some perceived disadvantages in terms of patient comfort. The temperature of the liquid was considered cold on initial contact, and overflow of the liquid from the hemisphere caused the top surface of the bed to become damp and to require a thorough clean following the scan. Additionally there may be insufficient restraint on the patient's movement, which could produce significant artefact over an 11 minute scan time.
4. Contact between the edge of the hemisphere and the breast could be achieved in all cases using the coupling liquid.

There are, however, some important issues that remain to be investigated. First, a change in the temperature of the liquid used could result in a change of blood volume. If the temperature is lower than the breast surface temperature then the blood volume in the breast could be reduced over the time of the scan. Keeping the coupling fluid at a constant temperature using a heating filament incorporated into the pump system should prevent this. However, it should be noted that this could be exploited in future by purposely changing the temperature of the liquid to acquire a difference image where the reference data is that acquired at a lower temperature. Such an image could perhaps be used to highlight the distribution of blood within the breast. Second, the effect of refractive index mismatch between the coupling fluid and the breast is unknown. Third, improvements to the spatial resolution and contrast may be needed in order for the system to be clinically viable.

4.1 Summary and Future Work

4.1.1 Summary

The purpose of the work in this thesis was to investigate the potential for optical tomography to be used in the detection and specification of breast cancer. The first section of this thesis focused on the preliminary clinical investigations using a simple patient interface based on a single ring of source and detector bundles. This work showed that distinct signals due to variations in the absorption of healthy tissue could be imaged and that these patterns were repeatable for an individual over time. The appearance of various benign lesions was investigated and although visible in most cases, they proved difficult to distinguish from other features in the image. A malignant lesion was imaged with a large contrast compared to the background breast tissue. Although, as yet, the facility to routinely distinguish between malignant and benign lesions has not been demonstrated, preliminary results have been encouraging. Finally, in part 2, novel applications of optical tomography in imaging the breast were investigated. In particular optical tomography was shown to successfully monitor the recovery of breast tissue over a period of a year after the removal of a fibroadenoma by ILP treatment in one patient. By examining specific clinical problems where other imaging modalities have proved unsuccessful, new applications for optical tomography may be identified where the technique may prove to be uniquely effective.

To optimise the data collected in clinical investigations a second patient interface was designed and constructed. Investigations performed using this interface showed that the spatial resolution and contrast were poor, but improved as features became closer to the sources and detectors. It was also seen that intensity could be used as a reliable datatype using this interface and so potentially improved separation of scatter and absorption images can be achieved. Initial volunteer studies showed that the outline of the breast could be distinguished from the coupling fluid and that a cylindrical absorbing feature with 10 times the contrast of the coupling fluid and a diameter of 10 mm could be reconstructed when attached to the complex structure of the breast. Unfortunately, the equivalent scattering feature could not.

Thus, although the role of optical imaging in the detection and specification of breast disease has not yet been completely defined, potential applications have been identified due to successful preliminary patient studies and future system developments have been initiated in order for this potential to be achieved.

4.1.2 Development of different sized hemispheres

The majority of future developments are focused on improvement of the liquid coupled interface. To attempt to overcome the problems encountered so far, it is important that the breast fill as much of the reconstructed volume as possible. The imaging system is limited to just 32 source and detector positions, and the sampling of the surface is therefore limited. In the volunteer studies performed so far the breast has filled between a half to three quarters of the volume of the hemisphere and so optimal sampling has not been achieved. To overcome this, a range of containers of different volumes and possibly different shapes are to be produced and the most appropriate container for each individual is to be used. It is hoped that by imaging across smaller source and detector distances the contrast will be improved and that both scattering and absorbing features can be determined. The development of such containers has already begun by Louise Enfield supported by a three year grant funded by Cancer Research UK. The hemispheres are built up of repeated layers of epoxy resin mixed with a black paint placed over a hemispherical mould. The materials used were chosen as being suitable for the bonding of adhesives in order to achieve watertight attachment of sources and detectors. A photograph of a finished hemisphere with a diameter of 140 mm is shown in figure 4.1.

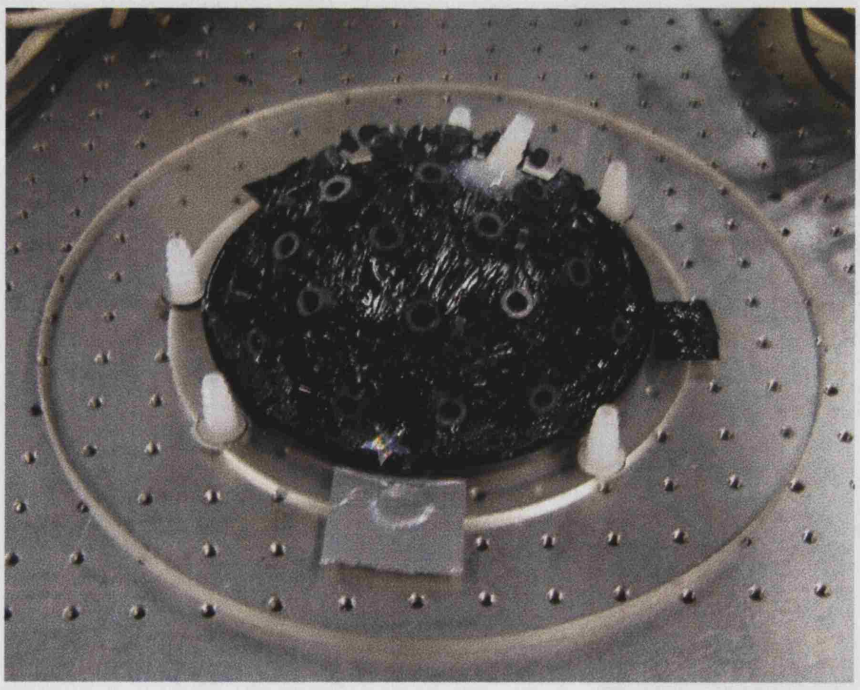

Figure 4.1: The latest model of the liquid coupled device made from epoxy resin.

The windows over the source detector bundles, for this prototype, are created from clear epoxy resin. Investigations on a healthy volunteer are to be performed shortly.

4.1.3 Future Clinical Studies

An extensive clinical study of 100 patients is planned with the liquid coupled interface. This work will build on the clinical study presented in part 2 of this thesis and incorporate patients with a variety of conditions. It is anticipated that the focus of this work will be patients with malignant lesions in order to establish the appearance of these lesions in our optical images. Future studies of patients who have undergone ILP treatments will also be a focus of this work. This work is also being undertaken by Louise Enfield funded by Cancer Research UK.

4.1.4 Combined Optical and MRI breast imaging

Due to the limited spatial resolution seen in optical tomography both within this project and the work of other groups the use of optical imaging of the breast is limited. However, as has been highlighted in the work presented in this thesis, optical tomography does have a strong potential to provide information on the functionality of breast tissue and so provide additional diagnostic information to that available with current imaging modalities. This has lead to the proposal by many groups to combine optical imaging with a standard imaging modality that can provide *a prior* structural information of the breast. One group has developed a system to combine x-ray mammography and optical imaging (Li et al 2003) other groups are investigating the possibility of combining MRI and optical imaging device (personal communication with Herbert Rinneberg 2004)(Brooksby et al 2003) and equally it may be possible to acquire information from ultrasound transducers placed alongside optical sources and detectors. At UCL the superior structural information obtained with MRI has been seen as a significant advantage over other imaging modalities for combination with optical imaging. In addition optical imaging does not require the use of any metallic components to be placed within the field of the MRI magnets and so is one of the very few modalities that can be combined with MRI for that reason. Finally the system described in part 3 of this thesis adopts a similar patient position to that used in MRI of the breast see section 1.4 and so inclusion of the optical patient interface within an MRI coil should be relatively straight forward. Preliminary investigations into combining MRI and optical imaging are to be performed by Adam Gibson in the near future following from the award of an EPSRC fellowship to fund this work.

Appendix A

Other benign breast conditions not presented in this thesis:

1. Breast Calcifications.

Calcifications are small deposits of calcium salts. They develop naturally as the breast ages and changes, and can occur with other benign breast conditions such as fibro adenomas and cysts. They can also occur as a reaction to inflammation and foreign bodies such as implants or stitches. Calcifications are very common and in most cases are harmless. Occasionally, however, they can be a sign of breast cancer. Calcifications are very small and are not palpable. This means they are usually first discovered on an x-ray mammogram where they show up as white spots, due to the high atomic number of calcium compared with normal breast tissue (see chapter 1.4).

2. Duct Ectasia and Periductal Mastitis

During the menopause it is normal for the ducts behind the nipple to become dilated. This is known as duct ectasia. A result of this is that fluid can collect in the ducts and so block them. In addition the lining of the ducts can become ulcerated, causing pain. This can lead to inflammation or infection in the ducts and bloody or clear discharge from the nipple. Duct ectasia can often be identified by a palpable lump behind the nipple or by the appearance of scar tissue behind the nipple, which can eventually cause the nipple to invert. Periductal mastitis affects younger women. It occurs when the ducts around the nipple become inflamed or infected and has similar symptoms to duct ectasia.

3 Fat Necrosis

Fat necrosis is a condition in which the neutral fats in the cells of adipose tissue break down into fatty acids and glycerol. It causes the formation of a firm, round lump and mainly occurs in an area of fatty breast tissue that has been damaged. The lump is usually painless, and the skin around it may look red, bruised or dimpled.

4 Hyperplasia.

Hyperplasia is caused by increased growth in the size and number of normal cells within a part of the breast. It can occur in the ducts (ductal hyperplasia) or the lobes (lobular hyperplasia).

Sometimes the cells develop an irregular pattern and these are known as atypical ductal hyperplasia and atypical lobular hyperplasia. If these cell changes in the lobes are very irregular, the condition is known as lobular carcinoma in situ (LCIS). This is not a true cancer (carcinoma) but an intermediate stage where the abnormal cells fill up the lobes.

As the abnormal cells in the ducts or lobes have the potential to spread to the surrounding tissue, atypical hyperplasia and LCIS have been shown to slightly increase the risk of developing breast cancer in the future. This risk is further increased when there is a history of breast cancer in the family.

5 Intraductal papilloma

An intraductal papilloma is a benign wart-like lump within a duct just behind the areola. Symptoms can include a small lump under the areola or discharge of clear, sticky or bloodstained fluid from the nipple. Intraductal papillomas can occur in both breasts at the same time and are sometimes found by chance following breast surgery. Women reaching the menopause are more likely to have a single intraductal papilloma, while younger women often have more than one.

6 Phyllodes Tumour

Phyllodes tumours are a rare type of breast lesion that can grow to be very large. They can affect a woman at any time in her life, but mostly occur in women between 40 and 50 years old who have not yet been through the menopause. Phyllodes tumours are usually benign but occasionally they can be malignant. They are classified into three groups: benign, borderline malignant and malignant.

7 Sclerosing Adenosis

Sclerosing Adenosis is a benign condition where extra tissue grows within the breast lobules. This can cause recurring pain (which may be cyclical) or result in a small, firm lump in the breast.

Appendix B

A description of the stage and TNM classifications of tumours.

Stage 1

- The tumour is no more than 2 centimetres across.
- The lymph nodes in the armpit are not affected.
- The cancer has not spread.

Stage 2

- The tumour is more than 2 centimetres, but less than 5 centimetres across.
- And/or the lymph nodes in the armpit are affected.
- The cancer has not spread anywhere else

Stage 3

- The tumour is more than 5 centimetres across
- The lymph nodes in the armpit are affected
- There is no further spread

Stage 4

- The tumour can be any size
- The lymph nodes in the armpit are often affected
- The cancer has spread or metastasised to other parts of the body (for example, lymph nodes above the collar bone or distant organs such as the lungs, liver or bones)

Tumour (T)

T1 – The tumour is no more than 2 cm across
T2 – The tumour is more than 2 cm, but no more than 5 cm across.
T3 - The tumour is bigger than 5 centimetres across
T4a - The tumour is fixed to the chest wall
T4b - The tumour is fixed to the skin
T4c - The tumour is fixed to both the skin and the chest wall
T4d - Inflammatory carcinoma. This is a cancer in which the overlying skin is red, swollen and painful to the touch.

Nodes (N)

N0 - Nodes not involved
N1 - Nodes in axilla involved but not stuck to other structures
N2 - Nodes in axilla involved and stuck to each other and other structures
N3 - Nodes under the breast bone (intramammary nodes) involved

Metastases (M)

M0 - No distant spread
M1 - Spread outside the breast and local lymph glands

Appendix C

Developing techniques to improve x-ray mammography

1 Digital Mammography

Digital mammography is similar to conventional mammography in most aspects and from the patients point of view the procedure is the same. The difference is that digital mammography is equipped with a digital receptor and computer instead of a film cassette. There are two different types of detector technology that are used in digital mammography. The early systems employed indirect-conversion with a scintillator layer such as caesium iodide doped with thallium [CsI(Tl)], to capture the x-ray energy and convert it to light. An array of thin-film diodes then converts the photons to electronic signals that are captured using thin-film transistors. More recent systems however use a direct- conversion method where a photoconductor such as amorphous selenium (a-Se), absorbs the x-rays and directly generates the signal(Smith 2003,Yaffe 2001). The ability to view the image on a PC enables the radiologist to manipulate the magnification, orientation, brightness and contrast of the image to study areas in more detail. A digital mammogram and conventional mammogram of the same breast are shown in figure A.

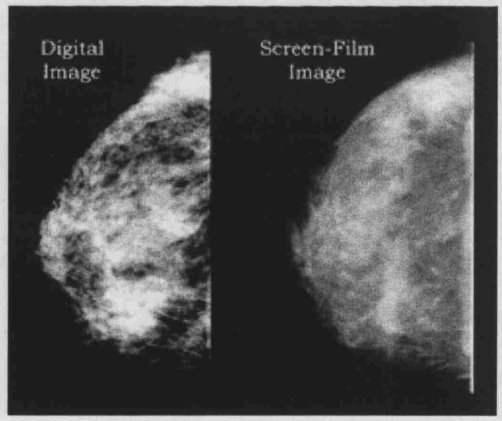

Figure A A comparison of a digital mammogram and conventional mammogram of the same breast (www.rk4cure.org/ images/mam.jpg)

The benefits of digital mammography over conventional mammography are that it allows easier manipulation of images for more accurate detection of breast cancer and without the need to repeat mammograms, the image processing is faster, the images can be stored and retrieved

more easily and it is possible to send the images over telephone lines or a network for remote consultation.

At present studies have indicated that the specificity of digital mammography is comparable with conventional mammography (D'Orsi 2002) although digital mammography systems currently cost four to five times more than conventional mammography. The decrease in procedural time over conventional mammography does justify this cost to some extent for a system involved in screening vast numbers of women a year, but the potential benefits in terms of breast cancer detection as opposed to extra cost are still being investigated and techniques are being improved upon. For this reason digital mammography systems are currently not widely available for routine use.

2 Computer Aided detection CAD

Computer aided detection (CAD) is a recent advance in mammography which helps to identify abnormalities within the breast (website 1,Brem et al 2003). CAD technology works by reviewing digitised mammograms and marking areas of suspected abnormalities. To use the CAD technology, mammogram films are first loaded into a processing unit that digitises the mammogram images. The digital images are then run through a neural network to analyze the images and highlight abnormalities. For example a computer algorithm can be written to search for bright points that exceed a given threshold. These spots could be representative of microcalcifications and so a cluster (three or more) of these spots is identified to draw the attention of the radiographer to that area (Winn Hardin 1999). The digitised mammograms are displayed on monitors on a motorized film viewer so the radiologist can compare the original film to the digitised mammogram image on the small monitor. The radiologist reviews whether the marked areas are suspicious and require additional tests or biopsy. When using a CAD system the radiologist always makes the final interpretation of the mammogram.

CAD can enhance the radiologist's performance by drawing attention to suspicious areas that may have been missed. It can improve the rate of detection of small breast abnormalities, which increase the chances of successful treatment (Freer et al 2001). It performs consistently, reducing variability due to fatigue, distraction and workload and it reduces site-to-site variability. However, until the use of digital mammography is more widespread, it requires a lot of time and effort to digitise mammogram films. CAD currently marks a significant number of normal areas on mammograms as abnormal, which could lead to unnecessary additional breast imaging and biopsies and distracts the reporting radiologist. Furthermore CAD systems are currently very expensive.

References

Arridge, S R 1995 Photon measurement density functions part 1: analytic forms *Appl Opt* **34** 7395-7409

Arridge, S R and Lionheart, W R B 1998 Nonuniqueness in diffusion-based optical tomography *Opt.Lett.* **23** 882-884

Arridge, S R and Schweiger, M 1995 Photon measurement density functions part II: finite element method calculations *Appl Opt* **34** 8026-8037

Arridge, S. R. 1999 Optical Tomography in Medical Imaging *Inverse Problems* **15** R41-R93

Arridge, S. R. and Hebden, J. C. 1997 Optical imaging in medicine: II. Modelling and reconstruction *Phys.Med.Biol.* **42** 841-853

Arridge, S. R., Hebden, J. C., Schweiger, M., Schmidt, F. E. W., Fry, M. E., Hillman, E. M. C., Dehghani, H., and Delpy, D. T. 2000 A method for 3D time-resolved optical tomography *Int.J.Imag.Sys.Tech* **11** 2-11

Arridge, S. R. and Schweiger, M. 1993 The use of multiple data types in time-resolved optical absorption and scattering tomography (TOAST) *Proc.SPIE* **2035** 218-229

Barker, M C J 1996 Medical Imaging *Physics Education* **31** 70-75

Barrett, H H and Swindell, W 1981 Radiological imaging - detection and processing *New York: Academic* Press **1**

Belliveau, N and Keyserlingk, J 1998 Infrared Imaging of the Breast: Initial Reappraisal Using high-Resolution Digital Technology in 100 Successive Cases of Stage I and II Breast Cancer *Breast Journal* **4**

Bennett, A H, Osterburg, H, Jupnitz, H, and Richards, O W 1951 Phase microscopy, *New York: Wiley*

Bevilacqua, F, Marquet, P, Coquoz, O, and Depeursinge, C 1997 Role of tissue structure in photon migration through breast tissues *Appl Opt* **36** 44-48

Blackwell, H R 1946 Contrast Thresholds of the Human Eye *Journal of the optical society of america* **36** 642-643

Boas, D. A., Culver, J. P., Stott, J J, and Dunn, A K 2002 Three dimensional Monte Carlo code for photon migration through a complex heterogenous media including the adult human head. *Optics Express* **10** 159-170

Bohren, C F and Huffman, D R 1983 Absorption and scattering of light by small particles *Wiley, New York*

Bolin, F P, Preuss, L E, Taylor, R C, and Ference, R J 1989 Refractive index of some mammalian tissues using a fiber optic cladding method *Appl Opt* **28** 2297-2303

Bone, B, Pentek, Z, Perbeck, L, and Veress, B 1997 Diagnostic accuracy of mammography and contrast-enhanced MR imaging in 238 histologically verified breast lesions. *Acta Radiol* **38** 489-496

Bown, S G 1998 New techniques in laser therapy.(Science, Medicine and the Future) *British Medical Journal* **316** 754-757

Brem, R F, Baum, J, Lechner, M, Kaplan, S, Souders, S, Naul, L G, and Hoffmeister, J 2003 Improvement in sensitivity of screening mammography with computer -aided detection: a multiinstitutional trial *Am J Roentgenol* **181** 687-693

Brenner, R J 1982 X-ray mammography and diaphanography in screening for breast cancer *J Reprod Med* **1982** 679-684

Brooksby, B A, Dehghani, H, Pogue, B W, and Paulsen, K D 2003 Near-infrared (NIR) tomography breast image reconstruction with a priori structural information from MRI: algorithm development for reconstructing heterogeneities *IEEE J Quant Elec* **9** 199-209

Bundred, N, Levack, P, Watmough, D J, and Watmough, J A 1987 Preliminary results using computerized telediaphanography for investigating breast disease *Br J Hosp Med* **37** 70-71

Cerussi, A E, Berger, A J, Bevilacqua, F, Shah, N, Jakubowski, D, Butler, J, Holcombe, R F, and Tromberg, B J 2001a Sources of absorption and scattering contrast for near-infrared optical mammography *Acad.Radiology* **8** 211-218

Cerussi, A E J A, Bevilacqua, F, Shah, N, Jakuboxski, D, Butler, J, Holcombe, R F, and Tromberg, B J 2001b Sources of Absorption and Scattering Contrast for Near-Infrared Optical Mammography *Acad Radiol* **8** 211-218

Cerussi, A E, Jakubowski, D, Shah, N, Bevilacqua, F, Lanning, R, Berger, A J, Hsiang, D, Butler, J, Holcombe, R F, and Tromberg, B 2002 Spectroscopy enhances the information content of optical mammography *J Biomed Opt.* **7** 60-71

Chance, B, Cope, M, Gratton, E, Ramanujam, N, and Tromberg, B 1998 Phase measurement of light absorption and scatter in human tissue *Rev Sci Instrum* **69** 3457-3481

Cheng, X, Mao, J, Bush, R, Kopans, D B, Moore, R H, and Chorlton, M 2003 Breast cancer detection by mapping hemoglobin concentration and oxygen saturation *Applied Optics* **42** 6412-6421

Cheong, W, Prahl, S A, and Welch, A J 1990b A Review of the optical properties of Biological Tissues *IEEE J Quant Elec* **26** 2166-2185

Cheung, K L 1999 Management of cyclical mastalgia in oriental women: pioneer experience of using gamolenic acid (Efamast) in Asia. *Aust N Z J Surg.* **69** 492-494

Colak, S B, Papaioannou, D G, Hooft, G W 't, Mark, M B, Schomberg, H, Paasschens, J C J, Melissen, J B M, and Asten, N 1997 Tomographic image reconstruction from optical projections in light-diffusing media *Applied Optics* **36** 180-213

Conway, J M, Norris, K H and Bodwell, C E 1984 A new approach for the estimation of body composition, infrared interactance, *Am. J. Clin. Nutr.***40** 1123-1130

Cope, M 1991 The development of a near infrared spectroscopy system and its application for non invasive monitoring of cerebral blood and tissue oxygenation in the newborn infant *Phd Thesis*

Cornsweet, T N 1970 Visual Perception *Acad.Press New York*

Cubeddu, R, D'Andrea, C, Pifferi, A, Taroni, P, Torricelli, A, and Valentini, G 2000 Effects of the menstrual cycle on the red and near-infrared optical properties of the human breast *Photochem.Photobiol.* **72-73** 383-391

Culver, J P, Choe, R, Holboke, M J, Zubkov, L, Durduran, T, Slemp, A, Ntziachristos, V, Chance, B, and Yodh, A G 2003 Three-dimensional diffuse optical tomography in the parallel plane transmission geometry: Evaluation of a hybrid frequency domain/continuous wave clinical system for breast imaging. *Med.Phys.* **30** 235-247

Cutler, M 1929 Transillumination as an aid in the diagnosis of breast lessions *Surg Gynecol Obstet* **48** 721-729

Dehghani, H, Pogue, B W, Poplack, S P, and Paulsen, K D 2003 Multiwavelength three-dimensional near-infrared tomography of the breast: initial simulation, phantom, and clinical results *Applied Optics* **42** 135-145

Dershaw, D D 2000 Mammographic screening of the high-risk women *Am J Surg* **180** 288-289

Douglas, S W, Williamson, H D 1980 Principles of Veterinary Radiography 3rd Ed. *Bailliere Tindall*

Drexler, B, Davis, J L, and Schofield, G 1985 Diaphanography in the diagnosis of breast cancer *Radiology* **157** 41-44

Driver, I, Feather, J W, King, P R, and Dawson, J B 1989 The optical properties of aqueous suspensions of Intralipid, a fat emulsion *Phys.Med.Biol.* **34** 1927-1930

Duijm, L E M, Guit, G L, Hendicks, J H C L, Zaat, J O M, and Mali, W P T M 1998 Value of breast imaging in women with painful breasts: observational follow up *BMJ* **317** 1492-1495

Durduran, T, Choe, R, Culver, J P, Zubkov, L, Holboke, M J, Giammarco, J, Chance, B, and Yodh, A G 2002 Bulk optical properties of healthy female breast tissue *Phys.Med.Biol.* **47** 2847-2861

Eda, H, Oda, I, Ito, Y, Wada, Y, Oikawa, Y, Tsunazawa, Y, Takada, M, Tsuchiya, Y, Yamashita, Y, Oda, M, Sassaroli, A, Yamamda, Y, and Tamura, M 1999 Multichannel time-resolved optical tomographic imaging system *Rev.Sci.Instrum.* **70** 3595-3602

Fantini, S, Walker, S A, Francheschini, M A, Kashke, M, Schlag, P M, and Moesta, K T 1998 Assessment of the size, position, and optical properties of breast tumors in vivo by noninvasive optical methods *Appl Opt* **37** 1982-1989

Ferlay, J, Bray, F, Pisani, P, and Parkin, D M 2001 GLOBOCAN 2000: Cancer Incidence, Mortality and Prevalence Worldwide **Version 1.0. IARC CancerBase No. 5**

Firbank, M, Hiraoka, M, Essenpreis, M, and Delpy, D T 1993 Measurement of the optical properties of the skull in the wavelength range 650-950 nm *Phys.Med.Biol.* **38** 503-510

Firbank, M, Oda, M, and Delpy, D T 1995 An improved design for a stable and reproducible phantom material for use in near-infrared spectroscopy and imaging *Phys.Med.Biol.* **40** 955-960

Foster, R S 2003 Breast Cancer detection and Treatment *American Medical Association Archives* **138** 397-408

Francheschini, M A, Moesta, K T, Fantini, S, Gaida, G, Gratton, E, Jess, H, Mantulin, W W, Seeber, M, Schlag, P M, and Kaschke, M 1997 Frequency-domain techniques enhance optical mammography: initial clinical results *Proc.Natl.Acad.Sci.* **94** 6468-6473

Gayen, S K and Alfano, R R 1999 Sensing lesions in tissues with light *Opt.Exp.* **4** 475-480

Gibson, A P, Yusof, R Md, Dehghani, H., Riley, J, Everdell, N, Richards, R, Hebden, J. C., Schweiger, M., Arridge, S. R., and Delpy, D. T. 2003 Optical tomography of a realistic neonatal head phantom *Appl.Opt.* **42** 3109-3116

Götz, L, Heywang-Köbrunner, S, Schütz, O, and Siebold, H 1998 Optical mammography on preoperative patients *Akt.Radiol* **8** 31-33

Gros, C and Gautherie, M 1980 Breast Thermography and Cancer Risk Prediction. *Cancer* **45** 51-56

Grosenick, D, Moesta, K T, Wabnitz, H, Mucke, J, Stroszczynski, C, Macdonald, R, Schlag, P M, and Rinneberg, H H 2003 Time-domain optical mammography: initial clinical results on detection and characterization of breast tumors *Applied Optics* **42** 3170-3186

Grosenick, D, Wabnitz, H, Rinneberg, H H, Moesta, K T, and Schlag, P M 1999 Development of a time-domain optical mammograph and first in vivo applications *Applied Optics* **38** 2927-2943

Hall-Craggs, E C B 1995 Anatomy as a basis for clinical medicine *Lippincott Williams and Wilkins* **3rd ed**

Hawrysz, D J and Sevick-Muraca, E M 2000 Developments towards diagnostic breast cancer imaging using NIR optical measurements and fluorescent contrast agents *Neoplasia* **2** 388-417

He, P, Kaneko, M, Takai, M, Baba, K, Yamashita, Y, and Ohta, K 1990 Breast cancer diagnosis by laser transmission photoscanning with spectro-analysis *Radiation Med.* **8** 1-5

Hebden, J. C. 2003 Advances in optical imaging of the newborn infant brain *Psychophysiology* **40** 501-510

Hebden, J. C., Arridge, S. R., and Delpy, D. T. 1997 Optical imaging in medicine: I. Experimental techniques *Phys.Med.Biol.* **42** 825-840

Hebden, J C, Bland, T D, Hillman, E M C, Gibson, A P, Everdell, N, Delpy, D T, Arridge, S R, and Douek, M 2002 Optical Tomography of the breast using a 32-channel time-resolved imager *OSA Technical Digest, Biomedical Topical Meetings* 187-189

Hebden, J. C., Gibson, A P, Yusof, R Md, Everdell, N, Hillman, E. M., Delpy, D. T., Austin, T, Meek, J, and Wyatt, J S 2002 Three-dimensional optical tomography of the premature infant brain *Phys.Med.Biol.* **47** 4155-4166

Hebden, J. C., Gonzalez, F M, Gibson, A P, Hillman, E. M., Yusof, R Md, Everdell, N, Delpy, D. T., Zaccanti, G, and Martelli, F 2003 Assessment of an in situ temporal calibration method for time-resolved optical tomography *J.Biomed.Opt* **8** 87-92

Hebden, J. C. and Kruger, R A 1990 Transillumination imaging performance: spatial resolution simulation studies. *Appl.Opt.* **30** 788-794

Hebden, J. C., Veenstra, H., Dehghani, H., Hillman, E. M., Schweiger, M., Arridge, S. R., and Delpy, D. T. 1-7-2001 Three-dimensional time-resolved optical tomography of a conical breast phantom *Appl.Opt.* **40** 3278-3287

Hebden, J C, Yates, T D, Gibson, A, Everdell, N, Arridge, S R, Chicken, D W, Douek, M, and Kashtgar, M R S 2004 Monitoring recovery following laser surgery of the breast using optical tomography: a case study *Appl Opt* **In Press**

Heffer, E L and Fantini, S 2002 Quantitative oximetry of breast tumors: a near-infrared method that identifies two optimal wavelengths for each tumor *Appl Opt* **41** 3827-3839

Hillman, E M C 2002 Development of optical tomography techniques for functional imaging of the neonatal brain *PhD Thesis*

Hillman, E M C, Arridge, S R, Hebden, J C, and Delpy, D T 2001 *Processing multi-wavelength time-resolved optical tomography data to derive functional parameters. OSA Technical Digest* **Biomedical Topical Meetings (OSA)**

Hillman, E. M. C., Hebden, J. C., Schmidt, F. E. W., Arridge, S. R., Schweiger, M., Dehghani, H., and Delpy, D. T. 2000 Calibration techniques and datatype extraction for time-resolved optical tomography *Rev.Sci.Instrum.* **71** 3415-3427

Holder D S 1995 Design and electrical characteristics of an electrode array for electrical impedance tomography of the female breast *Innov.Tech.Biol.Med.* **16** 144-150

Hollis, V S, Binzoni, T, and Delpy, D T 2001 Noninvasive monitoring of brain tissue temperature by near-infrared spectroscopy. **3194** 184-190

Hoogeraad, J H, van der Mark, M B, Colak, S B, Hooft, G W, and van der Linden, E S 1997 First results from the Philips optical mammoscope *Photon Propagation of tissues III* **3194** 184-190

Houssami, N, Irwig, L, Simpson, J M, McKessar, M, Blome, S, and Noakes, J 2003 Sydney Breast Imaging Accuracy Study: Comparative sensitivity and specificity of mammography and sonography in young women with symptoms. *Am J Roentgenol* **180** 935-940

Hughes, S 2001 Medical ultrasound imaging *Physics Education* 468-474

Isaacson, D, Cheney, M, and Newell, J C 1992 Comments on reconstruction algorithms *Clin Phys Physiol Meas* **13** 83-89

Ishimaru, A 1978 Wave propagation and scattering in random media *Academic press, Orlando* **1 and 2**

Jennions, D K, Gibson, A P, Everdell, N, and Hebden, J 2003 Variable Optical Attenuation for Time-resolved Optical Tomography **The International Conference on Advanced Laser Technologies**

Jiang, S, Pogue, B W, McBride, T O, and Paulsen, K D 2003 Quantitative analysis of near-infrared tomography: sensitivity to the tissue-simulating precalibration phantom *Journal of Biomedical Optics* **08** 308-315

Jossinet, J 1996 Variability of impedivity in normal and pathological breast tissue *Med Biol Eng Comput* **34** 346-350

Jöbsis, F F 1977 Noninvasive, infrared monitoring of cerebral and myocardial oxygen sufficiency and circulatory parameters *Science* **198** 1264-1267

Kaneko, M, Hatakeyama, M, and He, P 1989 Construction of a laser transmission photo-scanner: pre-clinical investigation *Radiat.Med.* **7** 129-134

Kang, K A, Chance, B, Zhao, S, Srinivasan, S, Patterson, E, and Trouping, R 1993 Breast tumour characterization using near-infra-red spectroscopy *Photon Migration and Imaging in Random Media and Tissues* **1888** 487-499

Kaschke, M, Jess, H, Gaida, G, Kaltenbach, J, and Wrobel, W 1994 Transillumination imaging of tissue by phase modulation techniques *Advances in Optical Imaging and Photon Migration* **24** 88-92

Keevil, S F 2001 Magnetic resonance imaging in medicine *Physics Education* **36** 476-485

Keith, L G, Oleszczuk, J J, and Laguens, M 2002 Are Mammography and Palpation Sufficient for Breast Cancer Screening? A Dissenting Opinion *Journal of Women's Health and Gender- based Medicine* **11** 17-25

Kerlikowske, K, Grady, D, Barclay, J, Sickles, E A, Eaton, A, and Ernster, V 1993 Positive predictive value of screening mammography by age and family history of breast cancer. *JAMA* **270** 2444-2450

Keyserlingk, J 1997 Time to Reassess the value of Infrared Breast Imaging? *Oncology News Int.* **6**

Koizumi, H, Yamamoto, T, Maki, A, Yamashita, Y, Sato, H, Kawaguchi, H, and Ichikawa, N 2003 Optical topography: practical problems and new applications *Appl Opt* **42** 3054-3062

Kopans, D B 1994 Screening for Breast Cancer and Mortality Reduction Among Women 40 - 49 Years of Age *Cancer* **74** 311-322

Kopans, D B 1999 The Breast Cancer Screening Controversy and the National Institutes of Health Consensus Development Conference on Breast Cancer Screening for Women ages 40-49 *Radiology* **210** 4-9

Kothari, M 2003 Benign breast disorders *Chemist and Druggist* 19-22

Lafreniere, R, Ashkar, F S, and Ketcham, A S 1986 Infrared light scanning of the breast *Am Surg* **52** 123-128

Lakowicz, J R and Berndt, K 1990 Frequency domain measurement of photon migration in tissue *Chem Phys Lett* **166** 246-252

Leung, T S, Elwell, C E, Henty, J R, and Delpy, D T 2002 Simultaneous measurement of cerebral tissue oxygenation over the adult frontal and motor cortex during rest and functional activation. *Advances in Experimental Medicine and Biology* **540** 13-18

Li, A, Miller, E L, Kilmer, M E, Brukilacchio, T J, Chaves, T, Stott, J, Zhang, Q, Wu, T, Chorlton, M, Moore, R H, Kopans, D B, and Boas, D A 2003 Tomographic optical breast imaging guided by three-dimensional mammography *Applied Optics* **42** 5181-5190

Lionheart, W R B 2004 EIT reconstruction algorithms: pitfalls, challenges and recent developments *Physiol Meas.* **25** 125-142

Matcher, S J, Cope, M, and Delpy, D T 1993 Use of the water absorption spectrum to quantify tissue chromophore changes in near-infrared spectroscopy *Phys Med Biol* **38** 177-196

McBride, T O, Pogue, B W, Gerety, E D, Poplack, S B, Osterberg, U L, and Paulsen, K D 1999 Spectroscopic diffuse optical tomography for the quantitative assessment of hemoglobin concentration and oxygen saturation in breast tissue. *Appl Opt* **38** 5480-5490

Miller, J C 2003 Screening Mammography - Who Needs It? What are the Benefits? *Radiology Rounds (A news letter for referring physicians, Massachusetts general hospital, department of radiology)* **1** 1-3

Mitic, G, Kölzer J, Otto J, Plies, E, Sölkner, G, and Zinth, W 1994 Time-gated transillumination of biological tissues and tissuelike phantoms *Appl.Opt.* **33** 6699-6710

Moesta, K T, Fantini, S, Jess, H, Totkas, S, Franceschini, M A, Kashke, M, and Schlag, P M 1998 Contrast features of breast cancer in frequency-domain laser scanning mammography *J Biomed Opt.* **3** 129-136

Morris, N, Hebden, J C, Bland, T D, and Balmer, B 2003 Role of patient feedback in the design and implementation of clinical trials of optical tomography of the breast *Proc SPIE* **5138** 12-22

Nair, M S, Ghosh, N, Raju, N S, and Pradhan, A 2002 Determination of optical parameters of human breast tissue from spatially resolved fluorescence: a diffusion theory model. *Appl Opt* **41** 4024-4034

Nioka, S, Yung, Y, Shnall, M, Zhao, S, Orel, S, Xie, C, Chance, B, and Solin, L 1997 Optical Imaging of breast tumor by means of continuous waves *Adv.Exp.Med.Biol.* 227-232

Ntziachristos, V and Chance, B 2000 Probing and molecular function using optical imaging: applications to breast cancer *Biomed* **3**

Ntziachristos, V, Yodh, A G, Schnall, M, and Chance B 14-3-2002 Concurrent MRI and diffuse optical tomography of breast after indocyaninie green enhancement *Proc.NY Acad.Sci.* **97** 2767-2772

Nyirjesy, I 1986 Clinical Evaluation, Mammography and Thermography in the Diagnosis of Breast Carcinoma *Thermology* **1** 170-173

Ohlsson, B, Gundersen, J, and Nilsson, D M 1980 Diaphanography: a method for evaluation of the female breast *World J.Surg.* **4** 701-705

Osterman, K S, Kerner, T E, Williams, D B, Hartov, A, Poplack, S P, and Paulsen, K D 2000 Multifrequency Electrical Impedance Imaging: Preliminary In Vivo Experience in the Breast *Jour Phys Meas* **21** 67-77

Patterson, M S, Wilson, B C, and Wyman, D R 1992 The propagation of optical radiation in tissue 1: models of radiation transport and their application *Lasers Med Sci* **6** 155-168

Pavic, D D, Koomen, M D, Kuzmiak, C D, and Pisano, E D 2003 Ultrasound in the management of breast disease *Current Women's Health Reports* **3** 156-164

Peebles, D M, Edwards, A D, Wyatt, J S, Cope, M, Delpy, D T, and Reynold, E O R 1992 Changes in human fetal cerebral oxygenation and blood volume during delivery *Am.J.Obstet.Gynecol.* **167** 1916-1917

Peña, M, Maki, A, Kovacic, D, Dehaene-Lambertz, G, Koizumi, H, Bouquet, F, and Mehler, J 2003 Sounds and silence: An optical topography study of language recognition at birth *PNAS* **100** 11702-11705

Perkins, G H and Middleton, L P 2003 Breast cancer in men *BMJ* **327** 239-240

Peters, M E, Voegeli, D R, Scanlan, K A 1989 Breast Imaging *Churchill Livingstone*

Peters, V G, Wyman, D R, Patterson, M S, and Frank, G L 1990 Optical properties of normal and diseased human breast tissue in the visible and near infrared *Phys Med Biol* **35** 1317-1334

Philips Research laboratories 1997 User Manual for Philips Optical Mammoscope, *Philips*

Pierce, P K 2002 Cyclic Mastalgia: Primary Care Management *Clinical Excellence for Nurse Practitioners* **6** 45-48

Pifferi, A, Taroni, P, Torricelli, A, Messina, F, Cubeddu, R, and Danesini, G 2003 Four-wavelength time-resolved optical mammography in the 680 - 980 nm range *Optics letters* **28** 1138-1140

Pogue, B W, Jiang, S, Dehghani, H, Kogel, C, Soho, S, Srinivasan, S, Song, X, Tosteson, T D, Poplack, S B, and Paulsen, K D 2004 Characterization of hemoglobin, water, and NIR scattering in breast tissue: analysis of intersubject variability and menstrual cycle changes. *J Biomed Opt.* **9** 541-552

Pogue, B W, Poplack, S P, McBride, T O, Wells, W A, Osterman, K S, Osterberg, U L, and Paulsen, K D 2001 Quantitative hemoglobin tomography with diffuse near infrared spectroscopy: pilot results in the breast *Radiology* **218** 261-266

Pogue, B W, Testorf, M, McBride, T, Osterberg, U, and Paulsen, K 1997 Instrumentation and design of a frequency-domain diffuse optical tomography imager for breast cancer detection *Opt.Express* **1** 391-403

Pope, J 1999 Medical Physics: Imaging, *Heineman Educational Books*, 4-26

Press, W H, Teukolsky, S A, Vetterling, W T, and Flannery, B P 1992 Numerical Recipes in C **Second edition**

Profio, A E, Navarro, G A, and Sartorious, O W 1989 Scientific basis of breast diaphanography *Med.Phys* **16** 60-65

Quaresima, V, Matcher, S J, and Ferrari, M 1998 Identification and quantification of intrinsic optical contrast for near-infrared mammography *Photochem.Photobiol.* **67** 4-14

Radai, M M, Abboud, S, and Rosenfeld, M 1999 Evaluation of impedance technique for detecting breast carcinoma using a 2-D numerical model of the torso *Ann N Y Acad Sci* **873** 360-369

Riley, J, Dehghani, H, Schweiger, M., Arridge, S. R., Ripoll, J, and Nieto-Vesperinas, M 2000 3D optical tomography in the presence of void regions *Optics Express* **7** 462-467

Sainsbury, J R C, Anderson, T J, and Morgan, D A L 2000 ABC of breast diseases: Breast cancer *BMJ* **321** 745-750

Säbel, M and Aichinger, H 1996 Recent developments in breast imaging *Phys Med Biol* **41** 315-368

Schmidt, F. E. 2000 Development of a Time-resolved Optical Tomography System for Neonatal Brain Imaging *PhD thesis*

Schmidt, F. E. W., Fry, M. E., Hillman, E. M. C., Hebden, J. C., and Delpy, D. T. 2000 A 32-channel time-resolved instrument for medical optical tomography *Rev.Sci.Instrum.* **71** 256-265

Schmidt, F. E. W., Hebden, J. C., Hillman, E. M. C., Fry, M. E., Schweiger, M., Dehghani, H., Delpy, D. T., and Arridge, S. R. 2000 Multiple-slice imaging of a tissue-equivalent phantom by use of time-resolved optical tomography *Appl.Opt.* **39** 3380-3387

Schmitz, C. H., Graber, H. L., Luo, H., Arif, I., Hira, J., Pei, Y., Bluestone, A., Zhong, S., Andronica, R., Soller, I., Ramirez, N., Barbour, S-L. S., and Barbour, R. L. 2000 Instrumentation and calibration protocol for imaging dynamic features in dense-scattering media by optical tomography. *Appl.Opt.* **39** 6466-6486

Schmitz, C. H., Löcker, M, Lasker, J M, Hielscher, A H, and Barbour, R L 2001 Instrument for fast functional optical tomography *Rev.Sci.Instrum.* **73** 429-439

Schnall, M D 2000 Application of magnetic resonance imaging to early detection of breast cancer *Breast Cancer Research* **3** 17-21

Schöberl, J. 1997 NETGEN - An advancing front 2D/3D-mesh generator based on abstract rules. *Comput.Visual.Sci* **1** 41-52

Schoeberl, J 2003 NETGEN - an automatic 3D tetrahedral mesh generator http://www.hpfem.jku.at/netgen/

Schweiger, M. and Arridge, S. R. 1999 Application of temporal filters to time-resolved data in optical tomography *Phys.Med.Biol.* **44** 2703-2721

Schweiger, M. and Arridge, S. R. 1999 Optical tomographic reconstruction in a complex head model using a priori region boundary information *Phys.Med.Biol.* **44** 2703-2721

Schweiger, M. and Arridge, S. R. 1998 Comparison of two-- and three- dimensional reconstruction methods in optical tomography *Appl.Opt.* **37** 7419-7428

Severinghaus, J W 1986 Pulse Oximetry, *Springer-Verlag, Heidelberg*

Sevick, E M, Burch, C L, Frisoli, J K, and Lakowicz, J R 1994 Localization of absorbers in scattering media by use of frequency-domain measurements of time-dependent photon migration *Appl.Opt.* **33** 3562-3571

Sickles, E A 1984 Breast cancer detection with transillumination and mammography *Am J Roentgenol* **142** 841-844

Simpson, C R, Kohl, M, Essenpreis, M, and Cope, M 1998 Near infrared optical properties of ex-vivo human skin and sub-cutaneous tissues measured using the Monte-Carlo inversion technique *Phys Med Biol* **43** 2465-2478

Sinha, S and Sinha, U 2002 Functional magnetic resonance of human breast tumors: diffusion and perfusion imaging *Ann N Y Acad Sci* **980** 95-115

Srinivasan, S, Pogue, B W, Jiang, Shudong, Dehghani, H, Kogel, C, Soho, S, Gibson, J J, Tosteson, T D, Poplack, S P, and Paulsen, K D 2003 Interpreting hemoglobin and water concentration, oxygen saturation, and scattering measured in vivo by near-infrared breast tomography *PNAS* **100** 12349-12354

Strangman, G, Boas, D. A., and Sutton, J P 2002 Non-Invasive Neuroimaging Using Near-Infrared Light *Biological Psychiatry* **52** 679-693

Suzuki, K, Yamashita, Y, Ohta, K, Kaneko, M, Yoshida, M, and Chance, B 1996 Quantitative measurement of optical paramters in normal breasts using time-resolved spectroscopy: in vivo results of 30 Japanese women. *J Biomed Opt.* **1** 330-334

Tabar, L, Yen, M F, Vitak, B, Tony Chen, H H, Smith, R A, and Duffy, S W 2003 Mammography service screening and mortality in breast cancer patients: 20-year follow-up before and after introduction of screening *Lancet* **361** 1405-1410

Taroni, P, Danesini, G, Torricelli, A, Pifferi, A, Spinelli, L, and Cubeddu, R 2004a Clinical trial of time-resolved scanning optical mammography at 4 wavelengths between 683 and 975 nm. *J Biomed Opt.* **9** 464-473

Taroni, P, Torricelli, A, Spinelli, L, Pifferi, A, Arpaia, F, Danesini, G, and Cubeddu, R 2004b Time-resolved optical mammography between 637 and 985 nm: Clinical study on the detection and identification of breast lesions. *Phys.Med.Biol.* **Under review**

Tetlow, R L and Hubbard, A E 2000 Preliminary results of a pilot study into the diagnostic value of T scan in detecting breast malignancies *Breast Cancer Research* **2**

Tromberg, B, Coquoz, O, Fishkin, J, Pham, T, Anderson, E R, Butler, J, Cahn, M, Gross, J D, Venugopalan, V, and Pham, D 1997 Non-invasive measurements of breast tissue opitcal properties using frequency-domain photon migration *Philosophical Transactions of the Royal Society of London Series B - Biological Sciences* **352** 661-668

Tromberg, B, Shah, N, Lanning, R, Cerussi, A E, Espinoza, J, Pham, T, Svaasand, L, and Butler, J 2000 Non-invasive in vivo characterization of breast tumors using photon migration spectroscopy *Neoplasia* **2** 26-40

Troy, T L, Page, D L, and Sevick-Muraca, E 1996 Optical properties of normal and diseased breast tissue: prognosis for optical mammography *J Biomed Opt.* **1** 342-355

van der Zee, P 1993 Measurement and modelling of the optical properties of biological tissues in the near infrared *PhD Thesis*

Villringer, A, Planck, J, Hock, C, Schleinkofer, L, and Dirnagl, U 1993 Near infrared spectroscopy (NIRS): A new tool to study hemodynamic changes during activation of brain function in human adults *Neuroscience Letters* **154** 101-104

Webb, S 1993 The Physics of Medical imaging *IOP*

Website 1 http://www.imaginis.com/breasthealth/breast_anatomy.asp

Website 2 http://www.breastdoctor.com/breast/anatomy.htm

Website 3. "Dartmouth instrumentation" http://www-nml.dartmouth.edu/nir/research.html

Website 4 "EIT" www.eit.org.uk/about.html

Website 5 "EPSRC funded public awareness project" www.cmp.uea.ac.uk/mammores

Website 6 "Hitachi system" http://www.hitachimed.com/products/optical_examples.asp#

Website 7 "Medcyclopaedia Professional Edition" www.Amershamhealth.com

Website 8 "Spectra"
http://www.medphys.ucl.ac.uk/research/borl/research/NIR_topics/spectra/spectra.htm

Yates, T, Hebden, J C, Gibson, A, Everdell, N, Arridge, S R, and Douek, M 2005 Optical tomography of the breast using a 32-channel time-resolved imager *Phys Med Biol* **Under review**

Yodh, A and Chance, B 1995 Spectroscopy and imaging with diffusing light *Physics Today* **48** 34-40

Zacharakis, G, Zolindaki, A, Sakkalis, V, Filippidis, G, Papazoglou, T, G, Tsiftsis, D,D, Koumantakis, E, 2001, In vitro optical characterization and discrimination of female breast tissue during near infrared femtosecond laser pulses propagation *J. Biomed. Opt.* **6**(4) 446-449